dortmund university

Dissertation

submitted for the academic degree
Doctor rerum naturalium (Dr. rer. nat.)

Spin dynamics in interacting semiconductor quantum dots

by
Andreas Fischer

2022

Department of Physics
TU Dortmund University

Accepted by the Department of Physics, TU Dortmund University, Germany

Date of the oral examination: December 7, 2022

Examination Board:
Prof. Dr. Frithjof B. Anders
Prof. Dr. Götz S. Uhrig
Dr. Anton Savitsky
Prof. Dr. Carsten Westphal

External Reviewer:
Prof. Dr. Michael Potthoff (Universität Hamburg)

Abstract

We study the spin dynamics in an ensemble of singly charged semiconductor quantum dots. The spin of the confined charge carriers can be polarized by coherent laser pulses. Due to the strong localization of the charge carrier, the hyperfine interaction with the local nuclear spin bath is the main contribution to the electron spin decoherence. Two-color pump-probe experiments indicate a coherent long-ranged interaction between the electron spins in different quantum dots. In this thesis, we develop a semiclassical approach based on spin-coherent states that allows for the efficient simulation of large spin systems and in addition preserves quantum mechanical properties on the level of single spins. We extend the semiclassical approach to open quantum systems using a quantum jump approach. We perform an in-depth analysis of the coherent optical manipulation of an interacting quantum dot ensemble employing pulse sequences with tailored spectra. Moreover, we study the cross-correlation spectra of second and fourth order to obtain complementary information about the spin system. Finally, we examine the intertwined dynamics of the electron spin and the nuclear spins at low temperatures to study the formation of a highly correlated nuclear-spin polaron state.

Kurzfassung

Wir untersuchen die Spindynamik in einem Ensemble einfach geladener Halbleiterquantenpunkten. Aufgrund der starken Lokalisierung des Ladungsträgers wird die Dekohärenz des Elektronenspins vorwiegend durch die Hyperfeinwechselwirkung mit den umliegenden Kernspins bestimmt. Pump-Probe Experimente mit zwei verschiedenen Laserspektren zeigen, dass eine kohärente langreichweitige Wechselwirkung zwischen den Elektronenspins verschiedener Quantenpunkte existiert. In dieser Arbeit entwickeln wir einen semiklassischen Ansatz basierend auf kohärenten Spinzuständen, der die effiziente Simulation vieler wechselwirkender Spins im Quantenpunktensemble ermöglicht und die quantenmechanischen Eigenschaften der einzelnen Spins erhält. Wir erweitern den semiklassischen Ansatz für offene Quantensysteme unter Verwendung von Quantensprüngen. Mit Hilfe des erweiterten Ansatzes betrachten wir die kohärente Manipulation des Quantenpunktensembles mittels verschiedener optischer Pulsfolgen bestehend aus Laserpulsen mit maßgeschneiderten Spektren. Des weiteren untersuchen wir Kreuzorrelationsspektren zweiter und vierter Ordnung, die ergänzende Informationen über die Spinwechselwirkungen liefern. Schließlich betrachten wir die gekoppelte Dynamik des Elektronenspins und der Kernspins bei tiefen Temperaturen und untersuchen die resultierende Formation eines nuklearen Spinpolaronzustandes.

List of publications

Major parts of the thesis reuse or are adapted from the author's contributions to the following publications:

- N. Jäschke, A. Fischer, E. Evers, V. V. Belykh, A. Greilich, M. Bayer and F. B. Anders
  Nonequilibrium nuclear spin distribution function in quantum dots subject to periodic pulses
  Phys. Rev. B **96** 205419 (2017)
- A. Fischer, E. Evers, S. Varwig, A. Greilich, M. Bayer and F. B. Anders
  Signatures of long-range spin-spin interactions in an (In,Ga)As quantum dot ensemble
  Phys. Rev. B **98** 205308 (2018)
- A. Fischer, I. Kleinjohann, F. B. Anders and M. M. Glazov
  Kinetic approach to nuclear-spin polaron formation
  Phys. Rev. B **102** 165309 (2020)
- A. Fischer, I. Kleinjohann, N. A. Sinitsyn and F. B. Anders
  Cross-correlation spectra in interacting quantum dot systems
  Phys. Rev. B **105** 035303 (2022)
- I. Kleinjohann, A. Fischer, M. M. Glazov and F. B. Anders
  Nuclear-spin polaron formation: Anisotropy effects and quantum phase transition
  Phys. Rev. B **105** 195309 (2022)
- F. Vonhoff, A. Fischer, K. Deltenre and F. B. Anders
  Microscopic origin of the effective spin-spin interaction in a semiconductor quantum dot ensemble
  Phys. Rev. Lett. **129** 167701 (2022)

Contents

Chapter 1

Introduction

Semiconductors have electrical and optical properties that can be tailored by their material composition, doping, and structure. Their versatile technical applications range from cell phones and household appliances to lasers, sensors, and power applications. Classical information technology is based on the development and miniaturization of semiconductor transistors, where the core element of information processing is the intrinsic charge of the electrons. In addition to charge, electrons have another intrinsic property, the spin, which is barely used in today's electronics. Stern and Gerlach were the first to provide direct evidence for an electron spin in their seminal silver beam experiment in 1922 [1]. Uhlenbeck and Goudsmit postulated that the electron spin is an intrinsic property of the electron with exactly two states [2, 3]. In 1928, Dirac was able to derive the electron spin from the combination of quantum mechanics and special relativity [4]. New technologies that use the spin as a key element for information processing are discussed under the term spintronics [5–7]. The utilization of the spin promises to overcome the limitations of charge-based technologies. For example, the switching frequency is no longer limited by the capacitance [8]. Furthermore, spin-based transistors are expected to generate significantly less heat, overcoming theoretical limits of the field-effect transistor (FET) miniaturization [9]. Among the currently employed spin-based technologies are spin-valve sensors [10–12], used in hard disk read heads, and magnetoresistive random-access memory (MRAM) [13–15].

Aside from the advantages in classical information processing, the electron spin constitutes a promising candidate for the realization of a quantum bit (qubit) [16–20]. While a classical bit has two states 0 and 1, the spin 1/2 of an electron may be in a superposition of the two quantum mechanical spin states $|\uparrow\rangle$ and $|\downarrow\rangle$. As a result, the spin state can be described by a vector on a spherical surface which is called Bloch sphere [21]. Moreover, several qubits may form an entangled state enabled by the quantum mechanical superposition. This entanglement is essential for quantum parallelism [22], which can significantly reduce the complexity of certain computational problems. Examples of such tasks are the simulation of quantum mechanical systems [23], the prime factorization of large numbers [24], or

searching unsorted databases [25]. The quantum threshold theorem states that a quantum computer with an error rate below a certain threshold can keep logical errors arbitrarily small by using quantum error correction [26–30]. Even though the rapid progress in the development of commercial quantum technologies [31, 32] leads to quantum processors with 50 to a few hundred qubits, these devices operate in the noisy intermediated-scale quantum (NISQ) regime [33]. The first fault-tolerant quantum computer with two logical qubits was presented in 2022 [34]. To realize a universal and fault-tolerant quantum computer, DiVincenzo established five criteria that a quantum computer must fulfill [35]. One of these criteria requires a long coherence time compared to the duration of the computational operations. For a localized electron spin in a semiconductor quantum dot (QD), the major source of decoherence is the interaction with surrounding nuclear spins [36–39]. Dynamical decoupling [40, 41] can drastically increase the coherence time. Alternatively, the nuclear spins can be driven into a tailored state using dynamic nuclear polarization [42, 43], optical cooling [44, 45], or the spin-mode locking effect [46–49]. The two latter effects are investigated in more detail in this thesis.

Another criterion of DiVincenzo requires a universal set of quantum gates. Single qubit operations can be realized in QDs with high fidelity by ultrafast optical stimulation [50–52]. To obtain a universal set of quantum gates, additional two-qubit gates are necessary [53]. For example, a set of controlled-NOT (CNOT) gates linking all pairs of qubits, directly or indirectly, fulfills the requirement. The realization of two-qubit gates is challenging for spin qubits since two-qubit gates cannot be implemented solely by optical means. A controllable coherent spin-spin interaction between the qubits is necessary. The first implementation of two spin-qubits was presented in 2015 [54, 55], a three spin-qubit processor followed in 2021 [56]. These realizations employ a direct spin-exchange interaction for the two-qubit gates. With regard to potential applications in spintronics and quantum technologies, there is a high demand for the exploration of the interaction of electron spins of adjacent QDs.

Two-color pump-probe experiments report a long-range inter-QD interaction in InGaAs QD ensembles that is in the order of a few μeV [57, 58]. The microscopic origin of this interaction has not been finally resolved. One objective of this thesis is the investigation of the effect of this long-range spin-spin interaction. We demonstrate that a Ruderman-Kittel-Kasuya-Yosida (RKKY) interaction mediated by the charge carriers in the wetting layer is compatible with the experimental observations in Ref. [57]. We provide a microscopic explanation for the experimental findings [59]. Furthermore, we show that the interaction, on the one hand, has a substantial effect on the spin dynamics on the time scale of nanoseconds and, at the same time, is indistinguishable from other effects in pump-probe and spin-noise experiments with a single fixed laser spectrum [46, 60]. Therefore, our theory

remains compatible with the literature where inter-QD interactions are usually neglected [48, 61–64].

For the description of the spin dynamics, we employ an extended central spin model (CSM) [65]. The CSM describes the interaction of the electron spin, the central spin, with the surrounding nuclear spins and captures a single QD. For a QD ensemble, we extend the model to include further interactions, such as the external magnetic field, nuclear quadrupolar interactions, and inter-QD spin-spin interactions. To efficiently calculate the time evolution of a system with a large number of spins, we employ a semiclassical approach (SCA). In the SCA each spin is parameterized by a classical vector, which represents a spin-coherent state. For the evaluation of correlation functions, we map the quantum mechanical time evolution onto a quaternionic representation, which was originally introduced independently by Rodrigues [66] and Hamilton [67, 68] more than 150 years ago. This approach preserves the quantum mechanical properties of the correlation function on the single spin level. The spin system interacts with its environment via spin-light and spin-lattice interaction. We extend the SCA to account for open quantum systems using quantum trajectory theory, which describes system-environment interactions by non-deterministic quantum jumps.

By means of the extended SCA, we study the signatures of inter-QD interactions for various types of experiments. In pump-probe experiments, the spins can be manipulated coherently. In Voigt-geometry, the optically generated electron spin polarization oscillates coherently in the external magnetic field. These dynamics are superimposed by a dephasing produced by the fluctuating nuclear spins. Based on experiments [57, 58, 69], we study various pulse protocols ranging from two-color pumping with optional rotation pulses to pulse sequences with spectrally tailored laser pulses. By tuning the excitation spectrum of the laser, different QD subsets of the ensemble can be addressed. These QD subsets interact with each other, such that phase shifts of the coherent electron spin oscillations arise and the dephasing time is changed. We link these effects to the varying g factors of the electron spins in the ensemble and demonstrate that the spin-spin interaction can lead to either the prolongation or the shortening of the dephasing time depending on the pulse protocol. Moreover, we examine the synchronization of the spin dynamics in the coupled QDs under long periodic pulse sequences that induce the spin mode-locking effect. Here, the nuclear spins adjust in such a way that the electron spin performs an integer or half-integer number of revolutions between two pulses. We demonstrate that the inter-QD interaction leads to an additional selection rule: Two electron spins do not favor the same precession mode. This mode repulsion generates strong correlations between nuclear spins of adjacent QDs.

In addition to the pump-probe scheme, we investigate spin noise spectroscopy which

was originally proposed by Aleksandrov and Zapasskii [70, 71]. Spin-noise spectroscopy enables the non-perturbing study of the spin system in thermal equilibrium. The power spectrum of the electron spins allows for extracting the different interactions [60, 72–76]. Here, we focus on the cross-correlation spectrum [77] and demonstrate that it is, in contrast to the power spectrum, sensitive to inter-QD interactions. In addition to the conventional second-order correlation spectra, higher-order correlations raised attention recently [78–84]. Higher-order correlation spectra can be obtained either from spin-noise or spin-echo experiments and promise access to quantum effects that do not appear in second-order correlation functions. In this thesis, we address the cross-correlation bi-spectrum, which is a fourth-order correlation function, and obtain information about the correlations between nuclear spin baths of different QDs.

Cross-correlations arise also between the electron spin and the nuclear spins in a single QD due to the hyperfine interaction. Low temperatures enhance the correlations and the electron spin and the nuclear spins align antiparallel to minimize the hyperfine energy. The nuclear-spin polaron formation was first predicted by Merkulov [44] who used a mean-field approach with two effective spin temperatures. While the electron spin is strongly coupled to the environment and maintains the lattice temperature, the nuclear spins are assumed to have a much lower effective spin temperature achieved by optical cooling. The mean-field approach predicts the spin-polaron formation in a shallow donor center for nuclear spin temperatures below $10^{-7}\,\mathrm{K}$ at cryostatic electron spin temperatures of 4 K. While experimental efforts of realizing a nuclear-spin polaron state are ongoing [45, 85], it is still not observed. Theoretical investigations, that assume a ferromagnetic coupling of the electron spins predict a long-range ferromagnetically ordered state involving both electrons and nuclei [86] for negative effective nuclear spin temperatures. In this thesis, we restrict ourselves to the hyperfine interaction for the investigation of the nuclear-spin polaron state and present an in-depth analysis of the Ising limit of the hyperfine interaction using kinetic rate equations.

This thesis is structured as follows. In Chapter 2, we review the experimental background and discuss the properties of singly charged QDs. In Chapter 3, we introduce the CSM and extend it to include the interactions between QDs as well as further relevant spin interactions. We present the derivation of the SCA from a saddle point approximation of the quantum mechanical path-integral formalism in Chapter 4 and extend the SCA to open quantum systems in Chapter 5. In Chapter 6, we address two-color pump-probe experiments [57, 58] and demonstrate that the experimental results can be described by a wetting-layer mediated RKKY interaction [59]. Based on experiments with tailored laser pulses [69], we investigate the influence of the laser bandwidth on the dephasing time in Chapter 7. In Chapter 8, we study the second-order cross-correlation function in equilibrium and reveal the influence

of the various spin interactions on the cross-correlation spectrum. In Chapter 9, we continue with the study of cross-correlation spectra in non-equilibrium. Here, we examine the fourth-order cross-correlation bi-spectrum after periodic optical excitation. The spin dynamics at low temperatures and the nuclear-spin polaron formation are addressed in Chapter 10. In Chapter 11, we summarize the results and present an outlook for future investigations.

Chapter 2

Experimental background

The theoretical investigations in this thesis are closely related to recent experiments on semiconductor QD ensembles [46, 57, 58, 69, 77]. We consider indium gallium arsenide (InGaAs) QDs as a model system, even though the model and the methods used can be generalized to other systems, like gated QDs [87], nitrogen-vacancy centers in diamond [88] or donor-bound electrons [89, 90]. Self-assembled InGaAs QDs are characterized by their optical properties and have been extensively studied experimentally [91]. In this chapter, we address the basic properties of semiconductor QDs and their growth process (Sec. 2.1), the optical properties (Sec. 2.2), as well as the experimental setups (Sec. 2.3) relevant for the investigations in the later chapters.

2.1 Ensemble of singly charged quantum dots

Three classes of materials are distinguished with regard to their electrical conductivity [92], which is characterized by the energy gap between the valence band and the conduction band. These are insulators with a large band gap, semiconductors with a small band gap, and metals without a band gap. Metals have good conductivity while in insulators electrical conductivity is strongly suppressed. Semiconductors represent a special situation in between. In semiconductors, electrical transport is only possible if charge carriers are added via thermal excitation, optical excitation, or doping of the material. In semiconductor nanostructures, materials with different band gaps are assembled in such a way that the band gaps form an artificial potential landscape. For example, a potential well can be formed by a semiconductor with a small band gap surrounded by a semiconductor with a large band gap. This concept can be used to confine either an electron in the conduction band or an electron hole in the valence band. Depending on the number of spatial dimensions that are not confined, we refer to a bulk (3D), quantum well (2D), quantum wire (1D), or quantum dot (0D). In a QD, all spacial dimensions are confined. Lateral confinement discretizes the energy spectrum, see Fig. 2.1(a). Although QDs can

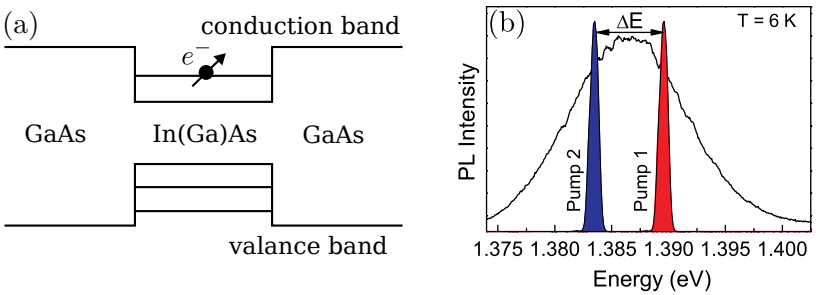

Figure 2.1: (a) Scheme of the conduction and valence bands in an In(Ga)As /GaAs nanostructure. Due to the spatial confinement of the electron, discrete energy levels emerge. (b) Photoluminescence spectrum of an In(Ga)As/GaAs QD ensemble. QD subsets can be optically selected by spectrally narrow laser pulses. Panel (b) is taken from Ref. [57].

appear naturally in thin quantum wells due to potential fluctuations [93–95], QDs are usually fabricated by molecular beam epitaxy [96], lithography [97] or wet chemical methods [98]. In the case of gated QDs, at least one of the three confinements is realized by a tunable gate voltage [99].

In this thesis, we focus on self-assembled InGaAs/GaAs QD ensembles as a model system and, therefore, discuss the QD growth in molecular beam epitaxy in more detail. In the growth process, InAs is vapor-deposited onto a GaAs substrate. Initially, a thin wetting layer [100–102] of InAs forms, which is only a few atomic layers thick. However, the lattice constants of GaAs and InAs differ by about 7 %, so strains arise [91]. As a consequence, InAs islands form on the wetting layer which is called Stranski-Krastanov growth [103]. These InAs islands are covered by GaAs and form the actual QDs. By additional heating, the In partially diffuses from the QDs, which allows a precise adjustment of the band gap. Electrons, donated by a silicon (Si) layer near the QDs, can be trapped in the QDs. If there is already an electron in the QD, much more energy is required to add another electron because of the Coulomb repulsion. Therefore, the QDs are predominantly singly charged if the number of donated electrons and the number of QDs matches. However, due to imperfections, empty and doubly charged QDs are possible [57]. QDs produced by the Stranski-Krastanov method are spatially randomly arranged and differ slightly in size and shape. Also, other properties, such as the excitation energy and the effective g factor of the resident electron, vary between the QDs [104].

Figure 2.1(b) shows the photoluminescence spectrum (PL) of an InGaAs QD ensemble. The PL represents the optical excitation spectrum of the resident electron spins. While a single QD has a narrow excitation line, the spectrum of an inhomogeneous ensemble is significantly broadened [77]. Experimentally, this can be used to excite

and probe distinct subensembles of the QDs, as it is proposed in Ref. [57], where two energetically shifted narrow band lasers are applied to excite two disjoint QD subensembles. Alternatively, the bandwidth of the laser can be varied to change the size of the excited subensemble [69]. The QDs of the subensembles are spatially randomly arranged. While the spin dynamics of different QDs are independent of each other in a first approximation, a closer examination reveals interactions between the QDs [57, 58, 69], where the wetting layer may serves as a channel for possible interactions between QDs [59].

2.2 Optical excitation and readout

To understand the optical excitations in semiconductor QDs, we first refer to the bulk material and then discuss the additional effects that arise in QDs. Of particular interest for optical experiments are direct semiconductors such as InAs or GaAs. In direct semiconductors, the maximum of the valence band and the minimum of the conduction band are located at the same wave vector. Due to the direct band gap, a photon with resonant energy can generate an electron-hole pair without generating an additional phonon to transfer the momentum [105].

Typical III-V semiconductors, such as GaAs and InAs, have the direct band gap at the Γ point ($\vec{k} = 0$). The lowest conduction band results from the twofold degenerate s-orbitals while the upper valence band originates from the sixfold degenerate p-orbitals. The band structure around the Γ point arises from the symmetry of the lattice and can be derived from $\vec{k} \cdot \vec{p}$ perturbation theory [105, 106]. Close to the Γ point, the bands are assumed to be parabolic. The originally sixfold degenerate valence band splits into a light-hole, heavy-hole, and split-off band, with the light-hole band and heavy-hole band being degenerate at the Γ point (see Fig. 2.2(a)). Because of the large splitting energy Δ_{SO} caused by spin-orbit coupling, the split-off band is neglected in the following. The curvature of the bands is inverse proportional to the effective mass of the charge carriers.

In QDs, the bands reduce to discrete energy levels, and the degeneracy of heavy and light holes at $\vec{k} = \vec{0}$ is lifted by the spatial confinement and growth-induced strain [107]. In this thesis, we restrict ourselves to the lowest resonant excitation energy and neglect a potential mixing of the heavy and light hole states. Circularly polarized light can generate a pair of an electron and a heavy hole (see Fig. 2.2(b)). Light with σ^+ polarization generates a heavy hole $|\Uparrow\rangle$ and an electron spin $|\downarrow\rangle$ due to the conservation of angular momentum. If the QD is singly charged by an electron, an electron-hole pair can only be generated if the resident electron has the spin $|\uparrow\rangle$, due to the Pauli principle. Thus, the excitation with σ^+ polarized light induces the

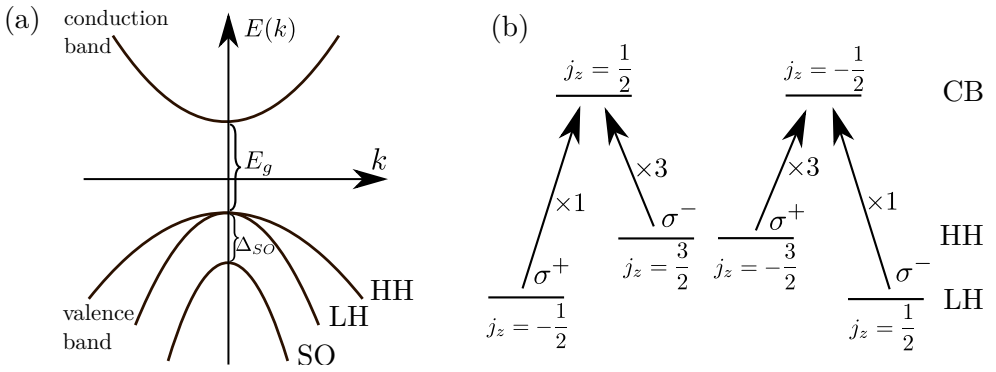

Figure 2.2: (a) Scheme of the conduction band (CB) and the valence band (VB) in GaAs-like semiconductors with a band gap E_g and a spin-orbit splitting Δ_{SO}. The valence band splits into a heavy-hole (HH), light-hole (LH), and split-off (SO) band. (b) Energy levels relevant for the optical excitation of QDs. Only transitions conserving the total angular momentum are allowed. The numbers $\times 1$ and $\times 3$ indicate the relative weights of the transitions.

transition $|\uparrow\rangle \rightarrow |\Uparrow\uparrow\downarrow\rangle$ while σ^- polarized light produces the transition $|\downarrow\rangle \rightarrow |\Downarrow\uparrow\downarrow\rangle$. The bound state consisting of a hole and two electrons is called trion or charged exciton. Emitting a photon, the heavy hole and the electron recombine, and a single electron spin is left. This decay process occurs on a the time scale of $100 - 400\,\mathrm{ps}$ [46, 62].

The same mechanism can be utilized to read out the electron spin polarization. For this purpose, the sample is irradiated with linearly polarized light of low intensity, such that the measurement does not manipulate the system. The linearly polarized light is a superposition of σ^+ and σ^- polarized light with equal weight. If the electron spins in the QDs are unpolarized, σ^+ and σ^- polarized light are equally absorbed. If the electron spin is aligned in the state $|\uparrow\rangle$, σ^+ polarized light is absorbed more efficiently and the transmitted light becomes elliptically polarized. The Faraday ellipticity is a measure of the electron spin polarization along the optical axis. Due to the inhomogeneous broadening in a QD ensemble, not all the dots have an excitation energy resonant to the laser. Thus, the total ellipticity signal is the sum of the contributions of the individual QDs weighted by the spectral sensitivity $g(\Delta E)$ parameterized by the energy detuning ΔE [108, 109] (see Fig. 2.3).

As an alternative to the Faraday ellipticity, the Faraday rotation of the transmitted linearly polarized light can be measured. The magneto-optic Faraday effect is caused by differing refraction indices of the circularly polarized light components in a magnetized sample [110]. The varying refraction indices cause a phase shift between the σ^+ and σ^- polarized light, which generates a rotation of the polarization plane.

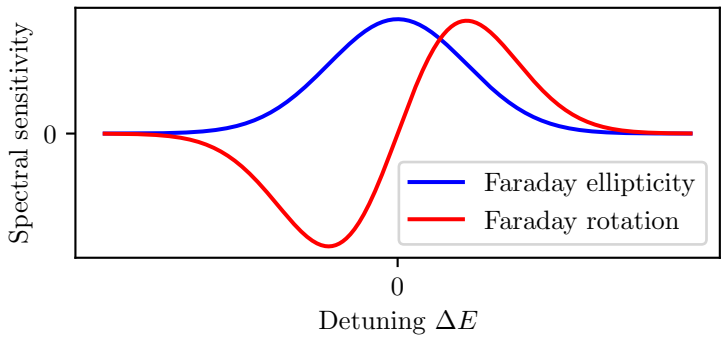

Figure 2.3: Scheme of the spectral sensitivity of Faraday ellipticity and Faraday rotation [108]. While the spectral sensitivity of the ellipticity has its maximum at zero detuning, the spectral sensitivity of the Faraday rotation has a zero crossing at resonant excitation with a negative and positive wing to the left and right, respectively.

The spectral sensitivity of the Faraday rotation is shown in Fig. 2.3 as a red curve. Unlike the Faraday ellipticity, the Faraday rotation has a zero crossing at resonant excitation, such that an energy detuning between the optical excitation and readout is necessary [111].

2.3 Experimental setup

There are various experimental setups for the optical measurement of the spin dynamics in QDs. In this thesis, we mainly focus on pump-probe and spin-noise setups. In pump-probe experiments, the system is driven out of equilibrium by periodic pulse sequences, and the resulting spin dynamics are measured with time resolution. In spin-noise experiments, the system remains in equilibrium, and the correlation functions are measured from the noise signal of the temporal spin fluctuations.

In its pure form, a pump-probe experiment consists of a periodic sequence of two laser pulses. First, a circularly polarized pump pulse generates spin polarization along the optical axis. After a time Δt, a much weaker linearly polarized probe pulse reads out the spin polarization by measuring either the Faraday ellipticity or rotation. Typical repetition rates are in the order of 76 MHz to 1 GHz, and the signal is averaged over many periods [47, 111–113]. The variation of Δt enables the measurement of the time-resolved spin dynamics relative to the incidence of the pump pulse. The

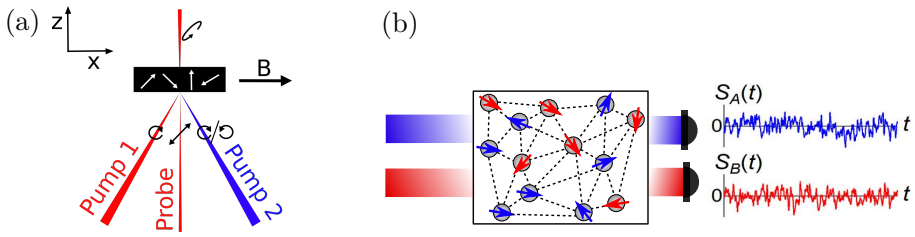

Figure 2.4: Scheme of two-color experiments. (a) Schematic pump-probe setup for the investigation of interacting QDs. Two circularly polarized pump pulses with energy detuning are used to generate spin polarization in disjoint subensembles of QDs. The probe pulse is used to detect the spin polarization of a selected subensemble. (b) Scheme of a two-color spin-noise experiment. Two continuous wave laser detect the spin fluctuation of the respective spin subensembles. The spin-noise signal can be used to calculate various correlation functions.

maximum time Δt is limited by the repetition time. Extended pump-probe schemes circumvent this limit by selecting and sorting out individual laser pulses [114, 115]. Various extensions for the manipulation of the sample are possible: Additional radio-frequency pulses can drive specific nuclear spin species [115]. Moreover, pump pulses with tailored frequency spectrum [69, 116] can be employed to select different subensembles of the QDs [57, 58] enabling the investigation of inter-QD interactions (see Fig. 2.4(a)).

While in pump-probe experiments the system is driven out of equilibrium, a spin-noise measurement allows for studying the system in thermal equilibrium [60, 72–76, 117, 118]. Continuous wave (CW) lasers are used to read out the spin polarization. As the system is unpolarized, only noise is measured. However, the fluctuation-dissipation theorem links the noise signal to correlation functions. For example, the Fourier transform of the noise signal reveals the so-called power spectrum, a second-order correlation function. It describes the intensity of different frequency components in the spin dynamics and allows for the identification of different interactions in the QDs. Recently, higher-order correlation functions attracted attention as they provide additional information about the system [80, 84, 119] not included in the power spectrum. In this thesis, the extension of spin-noise experiments with two CW lasers of different frequencies (see Fig. 2.4(b)) is of particular interest [77, 120], as it allows to measure the cross-correlation function which is sensitive to spin-spin interactions [120]. In addition to spin-noise measurements, spin-echo experiments provide higher-order correlation functions by applying an increasing number of pulses [79, 121, 122].

Chapter 3

Extended central spin model

Due to the spatial confinement of the charge carriers in the QDs, we restrict our description of the spin degrees of freedom. The charge carrier can be either an electron or an electron-hole. For better readability, we will omit this distinction in the following and write electron spin in general when no further distinction is necessary. In addition to the electron spin, the nuclear spins in the vicinity of the QD are relevant since they interact via the hyperfine interaction with the electron spin. In this chapter, we introduce all interactions relevant to the spin dynamics of a single QD. The spin dynamics of a single semiconductor QD are well-studied and follow a strict time hierarchy [91, 105]. The short-time dynamics is governed by the hyperfine interaction (Sec. 3.1) and the external magnetic field (Sec. 3.2). Together they form the central spin model (CSM) or Gaudin model [65]. Besides its relevance in the description of spin dynamics in semiconductor QDs [46, 47] or nitrogen-vacancy centers in diamond [123–127], the CSM is also of theoretical interest [61, 62, 118, 128] due to its dedicated star-topology: While the electron spin is coupled to all nuclear spins, a direct interaction between the nuclear spins is absent.

On longer time scales, however, additional interactions become relevant. In this thesis, we extend the CSM by the nuclear-electric quadrupolar interactions (Sec. 3.3) which lead to a disorder of the nuclear spins on the time scale of 100 ns [73, 74]. The nuclear dipole-dipole interactions, in contrast, are relevant on time scales of ms and therefore are neglected [129]. The ultrafast optical excitation of the electron spin is discussed in Sec. 3.4. In Sec. 3.5, we complement the model to account for a QD ensemble. The ensemble is characterized by an additional interaction between the electron spins of different QDs. Since the microscopic mechanism of the inter-QD interaction is not known, we focus on a minimal model that reproduces experimental results and discuss possible microscopic candidates.

3.1 Hyperfine interaction

The hyperfine interaction stems from the interaction of the nuclear magnetic dipole moment with the effective magnetic field generated by the electron [105, 129]. Under the assumption of a localized nucleus, we obtain the Hamiltonian for electron-nuclear interaction,

$$H_{n,e} = \frac{2\mu_B\mu_N}{I}\vec{I}\left[\frac{\vec{l}}{r^3} - \frac{\vec{S}}{r^3} + 3\frac{\vec{r}(\vec{S}\vec{r})}{r^5} + \frac{8\pi}{3}\vec{S}\delta(\vec{r})\right] , \tag{3.1}$$

with the electron spin $\vec{S}$, the nuclear spin $\vec{I}$, the Bohr magneton μ_B, the nuclear magneton μ_N, the relative position operator $\vec{r}$, and the Dirac delta $\delta(\vec{r})$. The Hamiltonian comprises three contributions, which can be interpreted separately. The first term is associated with the orbital angular momentum $\vec{l}$ of the charge carrier and can be disregarded in our case since we do not include rotational modes within the QD. The second and third terms comprise the dipole-dipole interaction between the nuclear magnetic moment and the magnetic moment of the electron spin. The last contribution is called Fermi contact interaction [130]. It is isotropic and is only relevant if the electron wave function is not vanishing at the position of the nucleus. It is the major hyperfine contribution for electron spins in the conduction band due to the *s*-type orbital. For hole spins, the Fermi contact interaction is irrelevant due to the *p*-type orbital with a zero probability density at the position of the nucleus, and the main hyperfine contribution results from the weaker dipole-dipole interaction.

The different contributions can be included in the general Hamiltonian,

$$H_{\mathrm{HF}} = \sum_k \sum_{\alpha,\beta} A_{k,\alpha\beta} S_\alpha I_{k,\beta}, \tag{3.2}$$

where $k \in [1, N_I]$ labels the N_I nuclear spins in the QD, and $\alpha, \beta \in \{x, y, z\}$ denote the spatial direction. S_α and $I_{k,\beta}$ are the spin operators of the electron respectively nuclear spin. The hyperfine tensor $A_{k,\alpha\beta}$ in its most general form summarizes the relevant terms of Eq. (3.1). In this thesis, we restrict ourselves to the case $A_{k,\alpha\beta} = \delta_{\alpha,x}\delta_{\beta,x}\lambda A_k + \delta_{\alpha,y}\delta_{\beta,y}\lambda A_k + \delta_{\alpha,z}\delta_{\beta,z}A_k$ with the hyperfine anisotropy factor λ and the Kronecker δ. This coupling captures systems with uniaxial symmetry such as singly charged self-assembled QDs grown on the [001] crystallographic plane [105]. For this scenario, the hyperfine Hamiltonian reduces to

$$H_{\mathrm{HF}} = \sum_k A_k S_z I_{k,z} + \lambda A_k (S_x I_{k,x} + S_y I_{k,y}) . \tag{3.3}$$

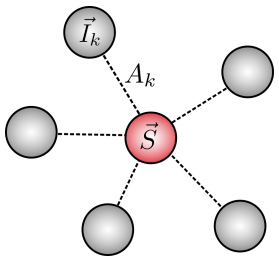

Figure 3.1: Scheme of the central spin model. The electron spin $\vec{S}$ is coupled to the nuclear spin $\vec{I}_k$ via hyperfine interaction with the coupling constant A_k. While the electron spin is coupled to all nuclear spins, the nuclear spins do not interact with each other.

Depending on λ, different physical systems can be described [131]. The electron spin couples to all nuclear spins while the nuclear spins do not interact with each other. This special topology, see Fig. 3.1, is called the central spin model and is the subject of many investigations [37, 65, 132, 133]. Except for Chapter 10, we will study the isotropic case $\lambda = 1$ which is relevant for an electron spin. However, for a hole spin, λ differs from the isotropic case: $\lambda = -2$ was found for the light hole, and the Ising limit $\lambda = 0$ accounts for a heavy hole [131]. Though the hyperfine coupling constants A_k have a different physical origin for electrons and holes, their value is proportional to the squared absolute value of the envelope wave function $|\psi(\vec{R}_k)|^2$ of the electron (hole) spin at the position of the nucleus.

Due to the imbalance of the number of spins, a single electron spin and N_I nuclear spins, the hyperfine interaction introduces different energy and time scales. The nuclear spins are affected by the Knight field $\vec{B}_{K,k} = A_k \vec{S}$, which induces the slowest time scale. The electron spin is affected by the Overhauser field $\vec{B}_N = \sum_k A_k \vec{I}_k$. The associated time scale varies depending on the temperature regime. In the high-temperature limit, all nuclear spins are randomly aligned and the expectation value of $\vec{B}_N$ vanishes. The relevant time scale,

$$T^* = \frac{1}{\sqrt{\sum_k A_k^2 \left\langle \vec{I}_k^2 \right\rangle}} , \tag{3.4}$$

is, therefore, given by the fluctuations $\langle \vec{B}_N^2 \rangle$ and governs the dephasing time of the electron spin subject to a disordered nuclear spin bath. In the low-temperature limit, all nuclear spins are fully aligned and the relevant energy scale is given by $A_S = \sum_k A_k$. This energy scale corresponds to the electron precession frequency in a fully polarized Overhauser field. The total hyperfine constant A_S is independent of the shape of the wave function due to the relation $A_k \propto |\psi(\vec{R}_k)|^2$ in combination

with the normalization of the wave function and is, therefore, a material constant. For GaAs, A_S is in the order of several Tesla [91, 105, 134, 135]. The dephasing time T^*, in contrast, varies depending on the size of the QDs. For a typical semiconductor QD ensemble, the dephasing time is in the order of nanoseconds [111]. In this thesis, we mostly focus on the electron spin dynamics in the high-temperature limit and, therefore, employ T^* as the characteristic time scale of the system. At cryostatic temperatures of 1 K, the thermal energy $k_B T$ is larger than the hyperfine splitting, and a high-temperature description is indicated.

3.2 External magnetic field

For large external magnetic fields, the Zeeman splitting of the electron spin becomes the dominant energy scale. The Zeeman effect is included in the Hamiltonian

$$H_{\mathrm{SZ}} = g_{\mathrm{e}} \mu_B \vec{B}_{\mathrm{ext}} \vec{S} \,, \tag{3.5}$$

where g_e is the g factor of the electron, μ_B is the Bohr magneton, and $\vec{B}_{\mathrm{ext}}$ is the external magnetic field. The electron spin precesses about the external magnetic field with the Larmor frequency, $\omega_{\mathrm{L}} = g_{\mathrm{e}} \mu_B B_{\mathrm{ext}}$. Due to the spin-orbit coupling in the crystal field, g_e is an effective g factor and is approximately 0.55 for electron spin in self-assembled InGaAs QDs [47]. While the g factor anisotropy is negligible for electron spins, it becomes relevant for heavy holes [60]. In a self-assembled QD ensemble, the g factor varies between the QDs and, due to the Lax-Zwergling relation, is correlated with the excitation energy [69, 104, 109].

The effect of the external magnetic field on the nuclear spins is three orders of magnitude weaker compared to the electron due to the large mass of the nuclei. The Hamiltonian for the nuclear Zeeman effect reads

$$H_{\mathrm{NZ}} = \sum_k g_{N,k} \mu_N \vec{B}_{\mathrm{ext}} \vec{I}_k, \tag{3.6}$$

where $g_{N,k}$ is the nuclear g factor, μ_N is the nuclear magneton, and $\vec{I}_k$ is the nuclear spin operator. In InGaAs QDs, three elements with different isotopes occur. They differ in the spin length I_k and the g factor $g_{N,k}$. The spin length is 3/2 for Ga and As and 9/2 for In. Instead of treating all isotopes separately, it is convenient to use a weighted average of isotopes in the semiconductor [136], resulting in an approximate ratio between the Larmor frequencies,

$$z = \frac{g_N \mu_N}{g_e \mu_B} \approx \frac{1}{800} \,. \tag{3.7}$$

3.3 Nuclear-electric quadrupolar interactions

The growth process of self-assembled QDs relies on the mismatch of the lattice constants of the substrate and the deposited material, which results in strain in the material. This strain produces electric field gradients that affect the nuclear spin dynamics. Since the charge distributions of the nuclei do not have a dipole moment, the quadrupole moment is relevant in leading order, see Fig. 3.2(a). The quadrupole moment couples to electric field gradients in the material [137, 138] and, thus, affects the dynamics of the nuclear spins. The effect of the nuclear-electric quadrupolar interactions on a single nuclear spin is described by the Hamiltonian [105, 129, 139]

$$H_Q = \sum_k q_k \left[\left(\vec{I}_k \vec{n}_k \right)^2 + \frac{\eta}{3} \left(\vec{I}_k \vec{n}_{k,x} \right)^2 - \frac{\eta}{3} \left(\vec{I}_k \vec{n}_{k,y} \right)^2 \right] . \tag{3.8}$$

Here, q_k is the quadrupolar coupling strength and $\vec{n}_k$ the easy axis. The biaxiality η enters the interaction along the auxiliary axes $\vec{n}_{k,x}$ and $\vec{n}_{k,y}$ which in combination with $\vec{n}_k$ form an orthonormal basis. Since the Hamiltonian, Eq. (3.8), is quadratic in the spin operators, it produces an effect only for spin lengths $I \geq 1$.

The local easy axis of the nuclei in the QDs is predominantly oriented in the growth direction of the sample, although significant deviations are possible. In the following, we assume that the axes $\vec{n}_k$ are uniformly distributed on a cone along the optical axis with an apex angle of 35°, see Fig. 3.2(b). This angle reproduces the mean

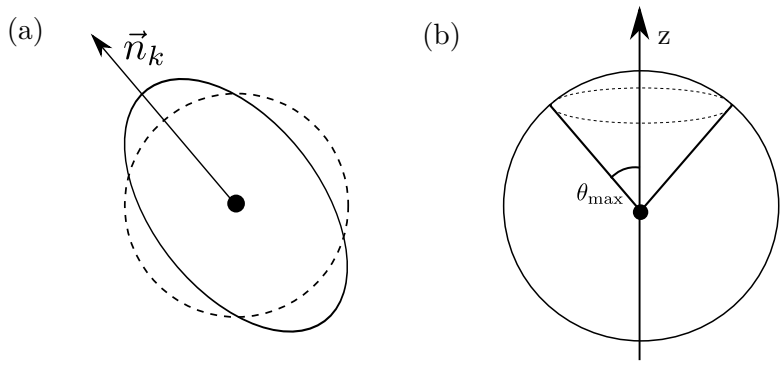

Figure 3.2: (a) Charge distribution of a nucleus in a material with strain. Due to the deviation from a spherical shape, the nucleus carries a non-zero quadrupole moment. The symmetry axis defines the easy axis $\vec{n}_k$. (b) Scheme of the random orientations of the easy axis $\vec{n}_k$. The easy axes are randomly oriented on an upper dome of the unit sphere with maximum deviation angle $\theta_{\max}$ from the growth direction (z direction).

deviation angle for $In_{0.4}Ga_{0.6}As$ [138]. The quadrupolar interactions provide an additional dephasing mechanism for the electron spin on the time scale of µs and, therefore, are relevant when considering times $t \gg T^*$ [74, 119].

3.4 Optical excitation

A singly charged QD can be optically excited by using circularly polarized light, where a σ^+ pulse drives the transition $|\uparrow\rangle \rightarrow |\Uparrow\downarrow\uparrow\rangle$ while the down-spin $|\downarrow\rangle \rightarrow |\downarrow\rangle$ remains unaltered [107]. For for a σ^- polarized pulse, we obtain an analog relation with reversed spin directions, see Sec. 2.2. For simplicity, we restrict ourselves to the case of σ^+ polarization and introduce the abbreviation $|T\rangle = |\Uparrow\downarrow\uparrow\rangle$.

In the following consideration, we exploit that the photon energy is in the order of eV, which is many orders of magnitude larger than any energy scale of the Hamiltonian of the system. Moreover, the envelope function of the laser pulse has a duration of a few ps, so the spin dynamics can be approximated as frozen during the optical excitation. Only at large magnetic fields $B_{\text{ext}} > 10\,\text{T}$ [63] or for laser pulses of long duration $T_P > 30\,\text{ps}$ [116], the electrons Larmor precession period comes into the order of the pulse duration. Here, we disregard these special cases, the laser pulse is described by an instantaneous unitary transformation. As a consequence, each QD is treated separately and the nuclear spin dynamics can be neglected during the pulse. The energy levels of the three involved states $|\uparrow\rangle, |\downarrow\rangle, |T\rangle$ are depicted in Fig. 3.3(a) where we omit the level splitting of $|\uparrow\rangle$ and $|\downarrow\rangle$.

In a rotating wave approximation, the Hamiltonian of light-matter interaction is given by

$$\begin{aligned} H_L(t) &= \epsilon_T \left|T\right\rangle \left\langle \mathrm{T}\right| \\ &\quad + \frac{\Omega(t)}{2}\Big(\exp\left(-\mathrm{i}\epsilon_L t\right)\left|T\right\rangle\left\langle\uparrow\right| + \exp\left(\mathrm{i}\epsilon_L t\right)\left|\uparrow\right\rangle\left\langle T\right|\Big)\,, \end{aligned} \tag{3.9}$$

where ϵ_T is the trion excitation energy. A laser field with photon energy ϵ_L drives the dipole transition between the spin-up state $|\uparrow\rangle$ and the trion state $|T\rangle$, while the spin-down state $|\downarrow\rangle$ is left unaffected [69]. The envelope function $\Omega(t)$ reflects the time-dependent variation of the amplitude of the laser pulse whereby the fast oscillations are determined by the photon energy ϵ_L. By means of a unitary transformation into the rotating frame of the laser field

$$U_L = \exp(-\mathrm{i}\epsilon_L t)\left|T\right\rangle\left\langle T\right|\,, \tag{3.10}$$

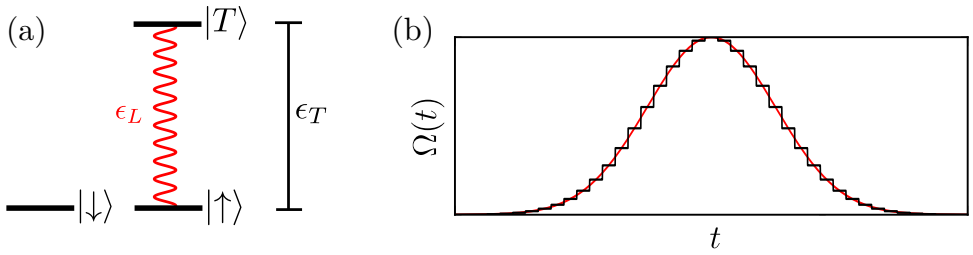

Figure 3.3: (a) Energy levels in a singly charged QD with the transition energy ϵ_T driven by a laser field with the photon energy ϵ_L. (b) Decomposition of the slowly varying envelope function of a laser pulse into short periods with approximately constant envelope.

we obtain the Hamiltonian

$$\begin{aligned}\tilde{H}_L(t) &= U_L^\dagger \left(H_L(t) - \epsilon_L \left|T\right\rangle \left\langle T\right|\right) U_L \\ &= \Big(\epsilon_T - \epsilon_L\Big) \left|T\right\rangle \left\langle T\right| + \frac{\Omega(t)}{2}\Big(\left|T\right\rangle \left\langle\uparrow\right| + \left|\uparrow\right\rangle \left\langle T\right|\Big),\end{aligned} \tag{3.11}$$

where the fast oscillations with frequency ϵ_L vanish and only the time dependency of $\Omega(t)$ persists. The time dependency of the Hamiltonian $\tilde{H}_L(t)$ is relatively slow compared to the fast oscillatory components entering $H_L(t)$. Therefore, the time evolution governed by $\tilde{H}_L(t)$ is numerically calculated by a Trotterization of the unitary time-evolution operator with time steps t_l of duration $\Delta_t = t_{l+1} - t_l$, see Fig. 3.3(b),

$$U_P \approx U_L \left(\prod_l \exp\left(-\mathrm{i}\,\tilde{H}_L(t_l)\,\Delta t\right)\right) U_L^\dagger\,. \tag{3.12}$$

For the limit of short time steps $\Delta t \to 0$ and a finite pulse duration T_p, this expression becomes exact.

Since the electron spin-down state $|\downarrow\rangle$ is an eigenstate of the pulse Hamiltonian $H_L(t)$, it is not affected by the laser pulse. The matrix representation of the pulse operator in the basis $|\uparrow\rangle$, $|\downarrow\rangle$, and $|T\rangle$ reduces to

$$U_P = \begin{pmatrix} a & 0 & b \\ 0 & 1 & 0 \\ c & 0 & d \end{pmatrix} \tag{3.13}$$

with the complex parameters a, b, c, and d. If we assume that the trion state is vacant before the laser pulse, the parameters b and d are irrelevant, as they are responsible for the process $|T\rangle \to |\uparrow\rangle$. In addition, U_P is unitary and, therefore,

$|a|^2 + |c|^2 = 1$. Thus, the effect of the pulse is completely determined by the three real parameters $|a|$, $\arg(a)$, and $\arg(c)$. In Chapter 5, we will show that $\arg(c)$ only generates a complex phase of the trion state, which is decoupled from the remaining spin dynamics and can be neglected as well. Accordingly, the effect of the laser pulse on an electron spin is described by a single complex number a with $|a| \leq 1$. We can interpret a by defining the pulse efficiency $Q^2 = (1 - |a|^2)$, which is the probability of exciting a spin up to a trion [109]. The geometric phase $\varphi = \arg(a)$ generates a rotation of the spin about the optical axis and can be utilized for spin-echo experiments [50–52] or optical spin tomography [58].

In the case of a resonant pulse, $\epsilon_L = \epsilon_T$, with the pulse area $\Theta = \int \Omega(t)dt = \pi$, we obtain $a = 0$ and $c = 1$, which correspond to a complete transition $|\uparrow\rangle \rightarrow |\Uparrow\downarrow\uparrow\rangle$. For a general pulse area Θ and detuning $\delta = \epsilon_L - \epsilon_T$, the pulse parameter a can be calculated numerically using Eq. (3.12). In a QD ensemble, a has to be determined individually for each QD since the QDs may differ in their excitation energies ϵ_T.

3.5 Inter quantum-dot interactions

In pump-probe experiments by Spatzek et al. [57], spin interactions between the electron spins in different QDs were observed for an ensemble of InGaAs quantum dots. This interaction was confirmed in further experiments [58, 69]. However, the microscopic mechanism behind the inter-QD interaction has not been clarified yet. A Heisenberg coupling was proposed as an effective interaction, whose coupling constant is estimated to be in the order of a few µeV. We introduce the Hamiltonian for the QD ensemble,

$$H_{\mathrm{Ens}} = \sum_i H_1^{(i)} + \sum_{i>j} J_{ij} \vec{S}^{(i)} \vec{S}^{(j)} \,, \tag{3.14}$$

where $H_1^{(i)}$ is the Hamiltonian for a single QD with index $i \in [1, N_{\mathrm{QD}}]$ and J_{ij} is the interaction strength between the electron spins i and j. The Hamiltonian of a single QD $H_1^{(i)}$ is composed of the various contributions introduced in the Secs. 3.1, 3.2, and 3.3,

$$H_1^{(i)} = H_{\mathrm{HF}}^{(i)} + H_{\mathrm{SZ}}^{(i)} + H_{\mathrm{NZ}}^{(i)} + H_Q^{(i)} \tag{3.15}$$

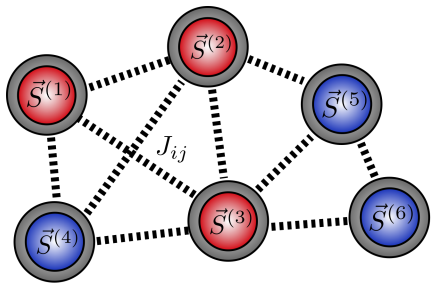

Figure 3.4: Scheme of an ensemble of interacting QDs. All electron spins $\vec{S}^{(i)}$ interact with each other via a Heisenberg interaction with coupling constant J_{ij}. The QDs are grouped by their excitation energy into two subensembles as would be the case in optical two-color experiments.

with

$$H_{\mathrm{HF}}^{(i)} = \sum_k A_k^{(i)} S_z^{(i)} I_{k,z}^{(i)} + \lambda A_k^{(i)} \left(S_x^{(i)} I_{k,x}^{(i)} + S_y^{(i)} I_{k,y}^{(i)} \right) \tag{3.16a}$$

$$H_{\mathrm{SZ}}^{(i)} = g_e^{(i)} \mu_B \vec{B}_{\mathrm{ext}} \vec{S}^{(i)} \tag{3.16b}$$

$$H_{\mathrm{NZ}}^{(i)} = \sum_k g_{N,k}^{(i)} \mu_N \vec{B}_{\mathrm{ext}} \vec{I}_k^{(i)} \tag{3.16c}$$

$$H_Q^{(i)} = \sum_k q_k^{(i)} \left[\left(\vec{I}_k^{(i)} \vec{n}_k^{(i)} \right)^2 + \frac{\eta}{3} \left(\vec{I}_k^{(i)} \vec{n}_{k,x}^{(i)} \right)^2 - \frac{\eta}{3} \left(\vec{I}_k^{(i)} \vec{n}_{k,y}^{(i)} \right)^2 \right] \tag{3.16d}$$

constitutes the sum of Eqs. (3.3), (3.5), (3.6), and (3.8) with an additional superscript i for the respective QD. The Heisenberg couplings J_{ij} in Eq. (3.14) couple all QDs with each other so that a complex network of $N_{\mathrm{QD}} N_I$ interacting spins is formed. Since the microscopic origin of the inter-QD interaction is not clear, we choose the J_{ij} to mimic the known experimental results as closely as possible. In the following, we discuss the most important candidates for the microscopic mechanism.

Dipole-dipole interaction

A potential candidate for a spin-spin interaction between the electron spins of different QDs is the magnetic dipole-dipole interaction [140]. According to classical electrodynamics, a magnetic dipole $\vec{\mu}_1$ of a spin labeled by the index 1 generates a distance-dependent magnetic field,

$$\vec{B}(\vec{r}) = \frac{\mu_0}{4\pi r^2} \frac{3(\vec{\mu}_1 \vec{r})\vec{r} - r^2 \vec{\mu}_1}{r^3} \,, \tag{3.17}$$

with the vacuum permeability μ_0 and the distance vector $\vec{r}$. Adding a second magnetic moment $\vec{\mu}_2$ into the field $\vec{B}(\vec{r})$, we obtain the dipole energy,

$$H_{\mathrm{DD}} = \frac{\mu_0}{4\pi r^2} \frac{3(\vec{\mu}_1\vec{r})(\vec{\mu}_2\vec{r}) - r^2\vec{\mu}_1\vec{\mu}_2}{r^3} \,, \tag{3.18}$$

where $\vec{r}$ is the distance vector between the two magnetic moments. In the case of electron spins, the magnetic moments are given by

$$\vec{\mu}_i = -g_e\mu_B\vec{S}_i \,. \tag{3.19}$$

As a result, we obtain the typical energy scale

$$\Delta E_{\mathrm{DD}} \approx \frac{\mu_0}{4\pi} \frac{g_e^2\mu_B^2}{r^3} \,. \tag{3.20}$$

For a typical QD distance of 100 nm, this results in the energy scale $\Delta E_{\mathrm{DD}} = 13\,\mathrm{feV}$ whereas a distance of 0.25 nm would be required to obtain a relevant dipole-dipole splitting of $\Delta E_{\mathrm{DD}} = 1\,\mu\mathrm{eV}$. The latter distance is well below the typical diameter of a QD. Consequently, the magnetic dipole-dipole interaction can be ruled out as a candidate for the spin-spin interaction between QDs.

Wetting layer mediated RKKY interaction

A promising candidate for an inter-QD spin-spin interaction is an RKKY interaction [141–143] mediated in the wetting layer [59]. Here, we assume that the electron doping of the sample charges the QDs as well as the conduction band of the wetting layer. The wetting layer can be approximated as a two-dimensional free electron gas,

$$H_{\mathrm{WL}} = \sum_{\vec{k}} \frac{k^2}{2m^*} c^\dagger_{\vec{k},\sigma} c_{\vec{k},\sigma} \,, \tag{3.21}$$

where m^* is the effective mass, and $c_{\vec{k},\sigma}$ is the annihilation operator for an electron with the wave vector $\vec{k}$ and the spin σ. For the QD ensemble, we employ the Hamiltonian

$$H_{\mathrm{QD}} = \sum_i^{N_{\mathrm{QD}}} \sum_\sigma \epsilon_i^d d^\dagger_{i,\sigma} d_{i,\sigma} + U_i n^d_{i,\uparrow} n^d_{i,\downarrow} \,, \tag{3.22}$$

where ϵ_i^d is the single particle energy of a bound electron with a spin σ in the QD i. Thus, $d_{i,\sigma}$ is the associated annihilation operator, and $n^d_{i,\sigma}$ is the corresponding

number operator. The energy U_i describes the Coulomb repulsion of two electrons in the same QD. Therefore, H_{QD} only takes into account the energetically lowest orbital in the QD. The chemical potential μ determines the filling of both the QDs and the wetting layer. A QD is singly charged when $\epsilon_i^d < \mu < \epsilon_i^d + U_i$. The interaction between the QD orbitals and the wetting layer can be described via the hybridization,

$$H_{\mathrm{Hyb}} = \sum_i^{N_{\mathrm{QD}}} \sum_m \sum_\sigma \left(V_m^i d_{i\sigma}^\dagger c_{m\sigma} + h.c. \right) \tag{3.23}$$

where $c_{m\sigma}$ is the annihilation operator of the Wannier orbital at the location $\vec{R}_m$ and is related to $c_{\vec{k},\sigma}$ via a spatial Fourier transformation. The parameter V_m^i corresponds to the hopping element between the QD i and the Wannier orbital m. Taking into account all three contributions,

$$H_{\mathrm{MIAM}} = H_{\mathrm{QD}} + H_{\mathrm{WL}} + H_{\mathrm{Hyb}} \tag{3.24}$$

yields a multi-impurity Anderson model (MIAM) [144–146] for the QD ensemble. The MIAM can be mapped to an effective Heisenberg model in a two-step process, first with a Schrieffer-Wolff transformation to a Kondo ensemble [147], and in a second perturbation step to a Heisenberg model by introducing effective spin-spin interactions [148]. For the interaction strength between the spins i and j, Fischer and Klein [148] determined

$$J_{ij}^{\mathrm{RKKY}} = -J_{K,i} J_{K,j} \rho_0 \frac{\overline{v} k_F^2}{4\pi} \left[J_0(k_F R_{ij}) N_0(k_F R_{ij}) + J_1(k_F R_{ij}) N_1(k_F R_{ij}) \right] \ . \tag{3.25}$$

Here, $J_{K,i}$ is the local Kondo interaction strength obtained by the Schrieffer-Wolff transformation, ρ_0 is the constant density of states of the wetting layer, $\overline{v}$ is the mean unit cell volume, k_F is the Fermi wave vector, R_{ij} is the QD distance, $J_l(x)$ is the Bessel function, and $N_l(x)$ is the Neumann function. However, in the parameter regime considered in this thesis, relevant terms might be neglected in the two-step perturbation process especially at short distances [59, 144, 149]. By means of the numerical renormalization group (NRG) [150, 151], the interaction strength, Eq. (3.25), can be evaluated directly [59] overcoming the problems of the two-step perturbation theory.

In Fig. 3.5, we show the distance dependency of the wetting layer induced RKKY interaction for a realistic set of parameters calculated with the NRG using $N_{\mathrm{QD}} = 2$ QDs. We assume the QDs to be equal and use $\epsilon_i = -1.5\,\mathrm{meV}$, $\epsilon_F = 0.5\,\mathrm{meV}$, $U_i = 4\,\mathrm{meV}$, and introduce the hybridization strength $\Gamma_0 = \pi V_0^2 \rho_0^2 = 0.14\,\mathrm{meV}$ with the QD hopping parameter $V_0 = V_i = \sum_m V_m^i$. These parameters are within a

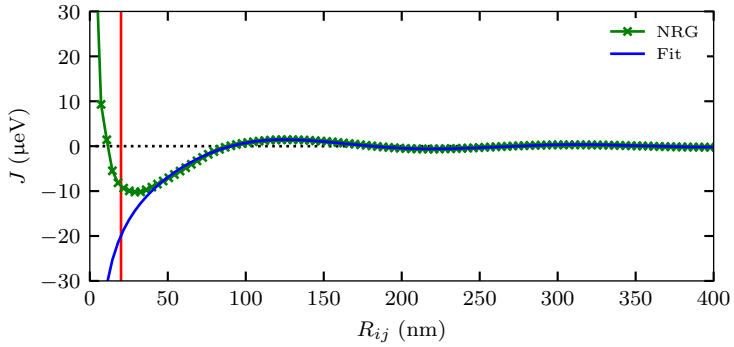

Figure 3.5: Distance dependency of the wetting layer mediated RKKY interaction. The green x markers depict the NRG results, and the green lines are linear interpolations as a guide to the eye. The blue curve is a fit using Eq. (3.25) with the amplitude as a fit parameter. The red vertical line marks a QD diameter of 20 nm, which determines the minimal distance. The data was provided by Frederik Vonhoff and has been published in Ref. [59].

realistic range for self-assembled InGaAs QDs [59] and were adjusted to reproduce the phase shift reported by Ref. [57], see Sec. 6.3. Furthermore, we add a fit according to Eq. (3.25) with the amplitude as a fit parameter. While the distance dependence is similar for large distances, relevant deviations appear for short distances where the perturbation theory yields a ferromagnetic coupling and the NRG an antiferromagnetic coupling.

Optically induced RKKY interaction

Piermarocchi et al. [57, 152] introduced an optical RKKY interaction between charged semiconductor QDs. This inter-QD coupling is generated via the virtual excitation of excitons in the wetting layer. Therefore, the mechanism is related to the previous one with the difference that the charge carriers in the wetting layer are optically generated. The excitons are optically induced by a CW laser and, therefore, can be coherently controlled. For the experiment by Spatzek et al. [57], an optical RKKY interaction can be ruled out since the laser pulse duration is in the order of ps and the optically induced excitons would decay rapidly, which is not compatible with the observed coherent interaction in the order of several ns. In summary, an RKKY interaction mediated by charge carriers in the wetting layer can be considered the most promising candidate for a microscopic explanation of inter-QD interactions in semiconductor QDs.

Chapter 4

Semiclassical approach

The central spin model is integrable, and an exact analytical solution can be determined by a Bethe ansatz [65, 153–156]. For general initial states, however, the effort of solving the initial value problem scales exponentially with the system size and restricts the evaluation to small spin baths. Through a stochastic evaluation of the Bethe approach, the bath size can be increased up to 48 nuclear spins [157, 158]. Several quantum mechanical approaches based on exact diagonalization [17, 22, 49, 63, 84, 119], Chebychev polynomials [118, 159, 160], perturbation theory [61, 136] and non-Markovian master equations [36, 128, 161–165] have been developed. All of them are equally limited to a small number of spins due to the exponentially growing Hilbert space dimension. Methods based on time-dependent density-matrix renormalization-group (TD-DMRG) can handle significantly larger spin baths but are limited to short time scales [166–169].

A semiclassical approach (SCA) provides an alternative route [37, 48, 62, 118, 168, 170–173]. Each spin is represented by a classical vector with three components. This allows the treatment of very large systems for long time scales with the drawback that quantum entanglement is excluded by construction. In the CSM, a semiclassical treatment is justified by a large number of nuclear spins. In the case of interacting QDs, this argument is strengthened. However, when the Knight field becomes relevant, deviations between semiclassical and quantum mechanical treatments are expected [61, 62]. SCAs exist in various forms and can be derived from the Ehrenfest theorem as dynamics of expectation values [75], via the time-dependent variational principle [174], or a Wigner truncation [175, 176]. In the following, we present a derivation via the saddle-point approximation of the quantum mechanical path integral using spin-coherent states [171, 173]. In this procedure, the quantum mechanical properties at the level of a single spin can be fully preserved. Furthermore, the approach is rather flexible and can be extended beyond the CSM and allows for the treatment of open quantum systems.

4.1 Spin-coherent states

To derive the SCA, we follow the route by Chen et al.[171] where spin coherent states [177–180] are used to represent the quantum state. While the derivation in Ref. [171] is restricted to the CSM, we derive an SCA for arbitrary spin interactions. Employing the spin basis $|s, m\rangle$ with

$$\vec{S}^2 |s, m\rangle = s(s+1) |s, m\rangle \ , \tag{4.1a}$$

$$S_z |s, m\rangle = m |s, m\rangle \ , \tag{4.1b}$$

we can define the spin-coherent state,

$$|\vec{s}\rangle = e^{-\mathrm{i}\vec{\theta}\vec{S}} |s, s\rangle \, , \tag{4.2}$$

which is parameterized by a classical vector of the length $|\vec{s}| = s$. The spin-coherent state describes a spin fully aligned along the quantization axis $\vec{n}_0 = \vec{e}_z$, which is rotated by the angle $\cos(\theta) = \vec{s}\vec{n}_0$ around the axis $\vec{\theta}/\theta = \vec{s} \times \vec{n}_0/|\vec{s} \times \vec{n}_0|$. Spin-coherent states represent an over-complete basis of the Hilbert space. The completeness relation is given by

$$\mathbb{1} = \int d\mu(\vec{s}) \, |\vec{s}\rangle \, \langle\vec{s}| \tag{4.3}$$

with the identity matrix $\mathbb{1}$ and the integration measure

$$d\mu(\vec{s}) = \left(\frac{2s+1}{4\pi} \right) \delta(\vec{s}^2 - s^2) d^3 s \, . \tag{4.4}$$

Spin-coherent states can be interpreted as the "most classical" states since they have the expectation value

$$\langle\vec{s}| \, \vec{S} \, |\vec{s}\rangle = \vec{s} \tag{4.5}$$

with the minimal possible fluctuation

$$\langle\vec{s}| \, \vec{S}^2 \, |\vec{s}\rangle - (\langle\vec{s}| \, \vec{S} \, |\vec{s}\rangle)^2 = s \, . \tag{4.6}$$

We note that the expectation values of higher powers of $\vec{S}$ are less trivial. Only in the limit of long spins, we obtain the relation

$$\lim_{S \to \infty} \langle\vec{s}| \, S_\alpha^p \, |\vec{s}\rangle = s_\alpha^p \qquad \text{with} \ \ \alpha \in \{x, y, z\}, p \in \mathbb{N} \, . \tag{4.7}$$

The reason lies in the spin commutator

$$\frac{1}{s^2}[S_\alpha, S_\beta] = \frac{1}{s^2} \mathrm{i} \sum_\gamma \epsilon_{\alpha\beta\gamma} S_\gamma = \mathcal{O}\left(\frac{1}{s} \right) \tag{4.8}$$

which is of the order of $\frac{1}{s}$.

4.2 Quantum mechanical path-integral formalism

In the following, we combine the information about all electron and nuclear spins in a coupled QD system into the product state

$$|\{\vec{s}_j\}\rangle = \bigotimes_j |\vec{s}_j\rangle \ , \tag{4.9}$$

where the index j labels the individual nuclear and electron spins. The transition from quantum mechanics to the classical limit can be approached within the path-integral formalism. We start with the propagator

$$K(\{\vec{s}_{j,f}\},\{\vec{s}_{j,i}\},t) = \langle\{\vec{s}_{j,f}\}|\, e^{-\mathrm{i}Ht}\, |\{\vec{s}_{j,i}\}\rangle \ , \tag{4.10}$$

which provides the transition amplitude from an initial state $|\{\vec{s}_{j,i}\}\rangle$ at time 0 to a final state $|\{\vec{s}_{j,f}\}\rangle$ at time t. We use a Trotterization to decompose the time evolution operator into N small time intervals $\Delta t = t/N$,

$$K(\{\vec{s}_{j,f}\},\{\vec{s}_{j,i}\},t) = \lim_{N\to\infty} \langle\{\vec{s}_{j,f}\}| \prod_{n=0}^{N-1} e^{-\mathrm{i}H\Delta t}\, |\{\vec{s}_{j,i}\}\rangle \ . \tag{4.11}$$

Inserting the completeness relation, Eq. (4.3), between all infinitesimal time evolution operators, we obtain infinitesimal transition amplitudes,

$$K(\{\vec{s}_{j,f}\},\{\vec{s}_{j,i}\},t) = \lim_{N\to\infty} \int \prod_{n=1}^{N-1} d\mu(\{\vec{s}_{j,n}\}) \prod_{n=0}^{N-1} \langle\{\vec{s}_{j,n+1}\}|\, e^{\mathrm{i}H\Delta t}\, |\{\vec{s}_{j,n}\}\rangle \ , \tag{4.12}$$

where the boundaries are $|\vec{s}_{j,i}\rangle = |\{\vec{s}_{j,0}\}\rangle$ and $|\{\vec{s}_{j,f}\}\rangle = |\{\vec{s}_{j,N}\}\rangle$. We rewrite the last equation in a more comprehensive form by a Taylor expansion of the exponential function in first order of Δt, where we identify the time derivative of $\frac{d}{dt}|\{s_{j,n}\}\rangle \approx |\{\vec{s}_{j,n+1}\}\rangle - |\{\vec{s}_{j,n}\}\rangle / \Delta t$ and perform the Taylor expansion backwards again,

$$\begin{aligned} K(\{\vec{s}_{j,f}\},\{\vec{s}_{j,i}\},t) &= \lim_{N\to\infty} \int \prod_{n=1}^{N-1} d\mu(\{\vec{s}_{j,n}\}) \prod_{n=0}^{N-1} \langle\{\vec{s}_{j,n+1}\}|\, (1+\mathrm{i}H\Delta t)\, |\{\vec{s}_{j,n}\}\rangle \\ &= \lim_{N\to\infty} \int \prod_{n=1}^{N-1} d\mu(\{\vec{s}_{j,n}\}) e^{\mathrm{i}\sum_{n=0}^{N-1}\left(\mathrm{i}\langle\{\vec{s}_{j,n}\}|\frac{d}{dt}|\{\vec{s}_{j,n}\}\rangle + \langle\{\vec{s}_{j,n}\}|H|\{\vec{s}_{j,n}\}\rangle\right)\Delta t} \ . \end{aligned} \tag{4.13}$$

At this point, the transition amplitude can be comprehensively written as a path integral,

$$K(\{\vec{s}_{j,f}\},\{\vec{s}_{j,i}\},t) = \int \mathcal{D}[\{\vec{s}_j\}]\; e^{\mathrm{i}S[\vec{s},\{\dot{\vec{s}}_j\}]} \tag{4.14}$$

with the action

$$S[\{\vec{s}_j\},\{\dot{\vec{s}}_j\}] = \int \left(\mathrm{i}\,\langle\{\vec{s}_j\}|\,\frac{d}{dt}\,|\{\vec{s}_j\}\rangle + \langle\{\vec{s}_j\}|\,H\,|\{\vec{s}_j\}\rangle\right) dt \tag{4.15}$$

and the integration measure

$$\mathcal{D}[\{\vec{s}_j\}] = \lim_{N\to\infty} \prod_{n=1}^{N-1} d\mu(\{\vec{s}_{j,n}\})\;. \tag{4.16}$$

The action can be separated into two parts: the topological or kinetic action which only depends on the topology of the Hilbert space,

$$\begin{aligned} S_{\mathrm{top}}[\{\vec{s}_j\},\{\dot{\vec{s}}_j\}] &= \int L_{\mathrm{top}}(\{\vec{s}_j\},\{\dot{\vec{s}}_j\})dt \\ &= \int \mathrm{i}\,\langle\{\vec{s}_j\}|\,\frac{d}{dt}\,|\{\vec{s}_j\}\rangle\,dt\;, \end{aligned} \tag{4.17}$$

and the contribution from the Hamiltonian,

$$\begin{aligned} S_H[\{\vec{s}_j\},\{\dot{\vec{s}}_j\}] &= \int \langle\{\vec{s}_j\}|\,H\,|\{\vec{s}_j\}\rangle\,dt \\ &= \int \tilde{H}(\{\vec{s}_j\})dt\;. \end{aligned} \tag{4.18}$$

For the latter contribution, we define the classical Hamilton function,

$$\tilde{H}(\{\vec{s}_j\}) := \langle\{\vec{s}_j\}|\,H\,|\{\vec{s}_j\}\rangle\;. \tag{4.19}$$

The path integral, Eq. (4.14), provides a physical understanding: The system propagates from the initial to the final state using every possible path. The paths are weighted with a complex phase $e^{\mathrm{i}S}$, which only depends on its action S. For large systems, a small variation of the path leads to a strong variation of the action S so that fast oscillating phases cancel each other out (destructive interference). However, there is one path, where the variation δS is zero, so that neighboring paths interfere constructively with each other and produce the most weight for the transition amplitude K. The path with $\delta S = 0$ is called the classical path and is investigated in the following.

4.3 General equations of motion

To obtain the classical path, we variate the trajectories $\{\vec{s}_j(t)\}$ under the constraint of fixed lengths of all spins,

$$\vec{s}_j^{\,2} = s_j^2 \; . \tag{4.20}$$

We define the restricted Lagrangian,

$$L_{\text{res}}(\{\vec{s}_j\},\{\dot{\vec{s}}_j\}) = L_{\text{top}}(\{\vec{s}_j\},\{\dot{\vec{s}}_j\}) + \tilde{H}(\{\vec{s}_j\}) + \sum_j \frac{\lambda_j}{2}(\vec{s}_j^{\,2} - s_j^2) \tag{4.21}$$

with the Lagrange multiplier λ_j to calculate the functional derivative,

$$\frac{\delta L_{\text{res}}}{\delta \vec{s}_j} = \frac{\partial L_{\text{res}}}{\partial \vec{s}_j} - \frac{d}{dt}\frac{\partial L_{\text{res}}}{\partial \dot{\vec{s}}_j} = 0 \; . \tag{4.22}$$

The functional derivative of the topological part [181] results in

$$\frac{\partial L_{\text{top}}}{\partial \vec{s}_j} - \frac{d}{dt}\frac{\partial L_{\text{top}}}{\partial \dot{\vec{s}}} = \frac{\vec{s}_j \times \dot{\vec{s}}_j}{s_j} \; . \tag{4.23}$$

The functional derivatives of the other two terms in Eq. (4.21) do not depend on $\dot{\vec{s}}_j$ such that we obtain the equation

$$\begin{aligned} \frac{\vec{s}_j \times \dot{\vec{s}}_j}{s_j} + \frac{\partial \tilde{H}(\{\vec{s}_j\})}{\partial \vec{s}_j} + \lambda_j \vec{s}_j = 0 \\ \Rightarrow \left[\frac{\vec{s}_j}{s_j}\right]_\times \dot{\vec{s}}_j = -\frac{\partial \tilde{H}(\{\vec{s}_j\})}{\partial \vec{s}_j} - \lambda_j \vec{s}_j \; , \end{aligned} \tag{4.24}$$

with the cross-product matrix defined as $[\vec{a}]_\times \vec{b} = \vec{a} \times \vec{b}$. Cross-product matrices have the rank two and therefore are not invertible. To solve Eq. (4.24) for $\dot{\vec{s}}_j$, we require the information of an additional linear independent equation given by the conservation of the spin length,

$$\begin{aligned} \vec{s}_j^{\,2} = s_j^2 \\ \Rightarrow \left(\frac{\vec{s}_j}{s_j} \otimes \frac{\vec{s}_j}{s_j}\right) \dot{\vec{s}}_j = \vec{0} \; , \end{aligned} \tag{4.25}$$

with the dyadic product $\otimes$. Equation (4.25) yields that the projection of the derivative $\dot{\vec{s}}_j$ along the spin axis $\vec{s}_j$ is zero. The Eqs. (4.24) and (4.25) can be summed up to

$$\left(\left[\frac{\vec{s}_j}{s_j}\right]_\times + \frac{\vec{s}_j}{s_j} \otimes \frac{\vec{s}_j}{s_j}\right) \dot{\vec{s}}_j = -\frac{\partial \tilde{H}(\{\vec{s}_j\})}{\partial \vec{s}_j} - \lambda_j \vec{s}_j \; . \tag{4.26}$$

We identify the left-hand side with a rotation matrix in $\mathbb{R}^3$ which is defined by

$$R_{\vec{n}}(\alpha) = (1 - \cos(\alpha))\vec{n} \otimes \vec{n} + \cos(\alpha)E + \sin(\alpha)[\vec{n}]_\times \ . \tag{4.27}$$

Using the angle $\alpha = \pi/2$,

$$R_{\vec{n}}\left(\frac{\pi}{2}\right) = \vec{n} \otimes \vec{n} + [\vec{n}]_\times \ , \tag{4.28}$$

we reproduce the left-hand side of Eq. (4.26). A rotation matrix is trivially inverted by $R_{\vec{n}}^{-1}(\alpha) = R_{\vec{n}}(-\alpha)$, which yields

$$\dot{\vec{s}}_j = -\vec{s}_j \times \frac{\partial \tilde{H}(\{\vec{s}_j\})}{\partial \vec{s}_j} + \left(-\frac{\partial \tilde{H}(\{\vec{s}_j\})}{\partial \vec{s}_j}\vec{s}_j - \lambda_j\right)\vec{s}_j \ . \tag{4.29}$$

Finally, we choose the Lagrange multiplier λ_j as

$$\lambda_j = -\frac{\partial \tilde{H}(\{\vec{s}_j\})}{\partial \vec{s}_j}\vec{s}_j \ , \tag{4.30}$$

which takes on the role of a generalized force along the spin direction that guarantees spin length conservation. We end up with the general equation of motion (EOM),

$$\dot{\vec{s}}_j = \frac{\partial \tilde{H}(\{\vec{s}_j\})}{\partial \vec{s}_j} \times \vec{s}_j \ . \tag{4.31}$$

This equation allows the derivation of semiclassical EOM for any spin Hamiltonian as outlined in the next section.

4.4 Equations of motion for the quantum dot ensemble

The EOM, Eq. (4.31), is form-invariant for different types of spins, such as nuclear or electron spins, though their distinction is encoded in the Hamilton function $\tilde{H}(\{\vec{s}_j\})$. For a Hamiltonian that is linear in the spin operators, we can replace each spin operator $\vec{S}_j$ by its classical counterpart $\vec{s}_j$ using Eq. (4.5). However, for a non-linear Hamiltonian like H_Q in Eq. (3.8), the evaluation of the classical Hamilton function has to be performed rigorously.

Following Eq. (4.31), the EOMs of the full Hamiltonian, Eq. (3.14), read

$$\dot{\vec{s}}^{(i)} = \vec{b}_{\text{eff}}^{(i)} \times \vec{s}^{(i)} \ , \tag{4.32a}$$

$$\dot{\vec{i}}_k^{(i)} = \vec{b}_{\text{eff},k}^{(i)} \times \vec{i}_k^{(i)} \ , \tag{4.32b}$$

with the classical electron spin vectors $\vec{s}^{(i)}$ and the nuclear spin vectors $\vec{i}_k^{(i)}$. The spins are subject to the effective magnetic fields,

$$\vec{b}_{\text{eff}}^{(i)} = \vec{b}_{\text{ext}}^{(i)} + \vec{b}_N^{(i)} + \vec{b}_J^{(i)} \,, \tag{4.33a}$$

$$\vec{b}_{\text{eff},k}^{(i)} = \vec{b}_{\text{ext},k}^{(i)} + \vec{b}_{K,k}^{(i)} + \vec{b}_{Q,k}^{(i)} \,. \tag{4.33b}$$

The different interactions of the Hamiltonian are reflected by the magnetic fields $\vec{b}_{\text{eff}}^{(i)}$ and $\vec{b}_{\text{eff},k}^{(i)}$ which in general can be time-dependent.

The hyperfine interaction appears twice: as the Overhauser field

$$\vec{b}_N^{(i)} = \sum_k A_k^{(i)} \vec{i}_k^{(i)} \tag{4.34}$$

acting on the electron spin and the much weaker Knight-field

$$\vec{b}_{K,k}^{(i)} = A_k^{(i)} \vec{s}^{(i)} \tag{4.35}$$

acting on the nuclear spins. The inter-QD interactions generate the field

$$\vec{b}_J^{(i)} = \sum_j J_{ij} \vec{s}^{(j)} \tag{4.36}$$

which is the sum over all electron spins $\vec{s}^{(j)}$ weighted by the interaction strength J_{ij}.

The quadrupolar fields,

$$\begin{aligned} \vec{b}_{Q,k}^{(i)} = 2q_k^{(i)} \left(1 - \frac{1}{2I}\right) \Bigg\{ & \left(\vec{i}_k^{(i)} \vec{n}_k^{(i)}\right) \vec{n}_k^{(i)} \\ & + \frac{\eta}{3} \left[\left(\vec{i}_k^{(i)} \vec{n}_{k,x}^{(i)}\right) \vec{n}_{k,x}^{(i)} - \left(\vec{i}_k^{(i)} \vec{n}_{k,y}^{(i)}\right) \vec{n}_{k,y}^{(i)} \right] \Bigg\} \,, \end{aligned} \tag{4.37}$$

cannot be obtained by a replacement $\vec{I}_k^{(i)} \to \vec{i}_k^{(i)}$ since H_Q is quadratic in the nuclear spin operators. The prefactor $(1 - 1/2I)$ ensures that the quadrupolar interactions vanish for spin 1/2 as required by quantum mechanics. In contrast to the external magnetic field, $\vec{b}_{Q,k}^{(i)}$ is time-dependent as it depends on the nuclear spin itself.

To obtain the field $\vec{b}_{Q,k}^{(i)}$, we calculate the classical Hamilton function $\tilde{H}(\vec{i}_k^{(i)})$ via Eq. (4.19) with the classical vector $\vec{i}_k^{(i)}$. Since the quadrupolar Hamiltonian consists of three similar terms, we omit the indices k and i and evaluate a term of the general form

$$\begin{aligned} \langle \vec{i} | \, (\vec{I}\vec{m})^2 \, | \vec{i} \rangle &= \langle I, I | \, e^{\mathrm{i}\vec{\theta}\vec{I}} (\vec{I}\vec{m})^2 e^{-\mathrm{i}\vec{\theta}\vec{I}} \, | I, I \rangle \\ &= \langle I, I | \, (\vec{I}\tilde{\vec{m}})^2 \, | I, I \rangle \ . \end{aligned} \tag{4.38}$$

From the first to the second line, we applied a rotation that rotates the spin-coherent state $|\vec{i}\rangle$ to the spin state with a maximum spin quantum number in the z component. The same rotation is applied to the orientation vector $\vec{m}$ producing $\tilde{\vec{m}}$ result of the above equations remains the same. In the next step, we substitute the spin operator,

$$\vec{I} = (I_x, I_y, I_z)^T = \left(\frac{1}{2}\left(I_+ + I_-\right),\ \frac{1}{2\mathrm{i}}\left(I_+ - I_-\right),\ I_z \right)^T \ , \tag{4.39}$$

and obtain the expression

$$\begin{aligned} \langle \vec{i}| \left(\vec{I}\vec{m}\right)^2 |\vec{i}\rangle = \langle I, I| \Bigg[& \frac{1}{4}\tilde{m}_x^2 \left(I_+^2 + I_+I_- + I_-I_+ + I_-^2\right) \\ & - \frac{1}{4}\tilde{m}_y^2 \left(I_+^2 - I_+I_- - I_-I_+ + I_-^2\right) \\ & + \tilde{m}_z^2 I_z^2 \Bigg] |I, I\rangle \ , \end{aligned} \tag{4.40}$$

where all contributions with I_+ acting on the spin state $|I, I\rangle$ with the maximum spin z component vanishes. The contributions containing I_-^2 result in two orthogonal spin states and, therefore, vanish as well. Hence, Eq. (4.40) reduces to

$$\langle \vec{i}| \left(\vec{I}\vec{m}\right)^2 |\vec{i}\rangle = \langle I, I| \frac{1}{4}\left[\tilde{m}_x^2 + \tilde{m}_y^2\right] I_+I_- + \tilde{m}_z^2 I_z^2 \, |I, I\rangle \ . \tag{4.41}$$

We insert $I_+I_- \, |I, I\rangle = 2I \, |I, I\rangle$ and $I_z^2 \, |I, I\rangle = I^2 \, |I, I\rangle$ and obtain

$$\begin{aligned} \langle \vec{I}| \left(\vec{I}\vec{m}\right)^2 |\vec{I}\rangle &= \frac{1}{2}\left(\tilde{m}_x^2 + \tilde{m}_y^2\right) I + \tilde{m}_z^2 I^2 \\ &= \frac{I}{2} + \left(1 - \frac{1}{2I}\right) \left(\tilde{\vec{m}}\vec{e}_z I\right)^2 \ , \end{aligned} \tag{4.42}$$

where we made use of the normalization of $\tilde{\vec{m}}$, i.e., $\tilde{m}_x^2 + \tilde{m}_y^2 = 1 - \tilde{m}_z^2$. After rotating back, the final result reads

$$\langle \vec{i}| \left(\vec{I}\vec{m}\right)^2 |\vec{i}\rangle = \frac{I}{2} + \left(1 - \frac{1}{2I}\right) \left(\vec{i}\vec{m}\right)^2 \ . \tag{4.43}$$

For the semiclassical EOM according to Eq. (4.31), we have to differentiate the Hamilton function with respect to $\vec{i}$ yielding the field $\vec{b}_{Q,k}^{(i)}$ in Eq. (4.37).

4.5 Configuration averaging

In the previous sections, we derived the semiclassical trajectory from a saddle-point approximation of the quantum mechanical path integral. This generates EOMs for the dynamics of spin-coherent product states. In this thesis, we generally consider the high-temperature limit since, at cryostatic temperatures, $k_B T = 100\,\mu\text{eV}$ exceeds any energy scale of the Hamiltonian, Eq. (3.14). The spin system in thermal equilibrium is described by the density operator $\rho = \mathbb{1}/D$ with Hilbert space dimension D. Using the completeness relation for spin-coherent states, Eq. (4.3), we calculate the initial density matrix,

$$\begin{aligned} \rho &= \frac{1}{D} \int d\mu(\{\vec{s}_j\}) \, |\{\vec{s}_j\}\rangle \langle\{\vec{s}_j\}| \\ &\approx \frac{1}{N_C} \sum_{\mu} |\{\vec{s}_{j,\mu}\}\rangle \langle\{\vec{s}_{j,\mu}\}| \ , \end{aligned} \tag{4.44}$$

by an integration over all spin-coherent product states. In the last step, instead of integrating over all spin-coherent states on the Bloch sphere, we perform a Monte Carlo integration. We choose N_C representations of spin-coherent product states, which we draw uniformly distributed on the Bloch sphere. These representations are labeled by the index μ. The dynamics of the configurations can be evaluated independently employing the semiclassical EOMs. When the expectation value of a general observable O is calculated,

$$\langle O(t) \rangle = \frac{1}{N_C} \sum_{\mu} \langle\{\vec{s}_{j,\mu}\}(t)| \, O \, |\{\vec{s}_{j,\mu}\}(t)\rangle \ , \tag{4.45}$$

the different configurations have to be merged. The independent configurations allow for a massive parallelization of the SCA. The statistical error arising from the Monte Carlo integration scales with $1/\sqrt{N_C}$ and can be controlled by the number of configurations N_C. In this theses, we typically choose $N_C = 10^5$ to $N_C = 10^6$. When the coupling constants of the Hamiltonian, such as $A_k^{(i)}, J_{ij}$, and $g_e^{(i)}$, are drawn from a random distribution, it is advantageous to draw these parameters independently for each configuration μ. This way, the results are independent of the specific realization of the coupling constants in the limit of large N_C. The averaging over the configurations μ, thus, represents not only different realizations of the initial conditions $\{\vec{s}_{j,\mu}(0)\}$, but also different realizations of the coupling constants of the Hamiltonian. To simplify the notation, we neglect the configuration index μ in general.

4.6 Reduction to an effective ensemble size

In a self-assembled QD ensemble, a laser spot with a typical diameter of 100 µm covers 10^5 to 10^6 QDs and each QD contains 10^5 to 10^6 nuclear spins. To access such a system numerically, it is helpful to reduce the number of QDs in such a way that the dynamics of the system remain unchanged. To this end, we note that the effect on an electron spin induced by the surrounding QDs is given by the classical field $\vec{b}_J^{(i)}$. When reducing the number of interacting QDs, we have to rescale the coupling constants J_{ij} ensuring that the total field $\vec{b}_J^{(i)}$ remains the same. Depending on the physical scenario, different scaling rules can apply. In the following, three scenarios, which lead to different scaling rules, will be discussed:

(i) the inter-QD interaction is a short-range interaction,

(ii) subsets of electron spins are synchronized,

(iii) all electron spins are randomly aligned.

In the first scenario, the nearest QD has the most relevant effect on QD i, while the coupling to more distant QDs is negligible. Therefore, we define the nearest-neighbor interaction strength,

$$J_{\mathrm{NN},i} = \max_j J_{ij} \ . \tag{4.46}$$

In the second scenario, we assume that the QDs are grouped into two subsets A and B. All spins of the same subset are synchronized so that $\vec{s}^{(i)} = \vec{s}^{(j)}$ if either $i, j \in A$ or $i, j \in B$ holds but not for $i \in A, j \in B$ or vice versa. This scenario is realized in two-color pump-probe experiments [57]. We assume that all electron spins in the subset A have the spin $\vec{s}^A$ and all spins of the subset B have the spin $\vec{s}^B$. The effective field of QD $i \in A$ is

$$\begin{aligned} \vec{b}_J^{(i)} &= \sum_j J_{ij} \vec{s}^{(j)} \\ &= \sum_{j\in A} J_{ij} \vec{s}^A + \sum_{j\in B} J_{ij} \vec{s}^B \\ &\approx \sum_{j\in B} J_{ij} \vec{s}^B = J_{\mathrm{sync},i} \vec{s}^B \ . \end{aligned} \tag{4.47}$$

From the second to the last line, we omit the summand including $\vec{s}^A \parallel \vec{s}^{(i)}$ due to the cross product in Eq. (4.32a). From the remaining contributions produced by subensemble B, we can identify the effective coupling constant

$$J_{\mathrm{sync},i} = \sum_{j\in B} J_{ij} \ . \tag{4.48}$$

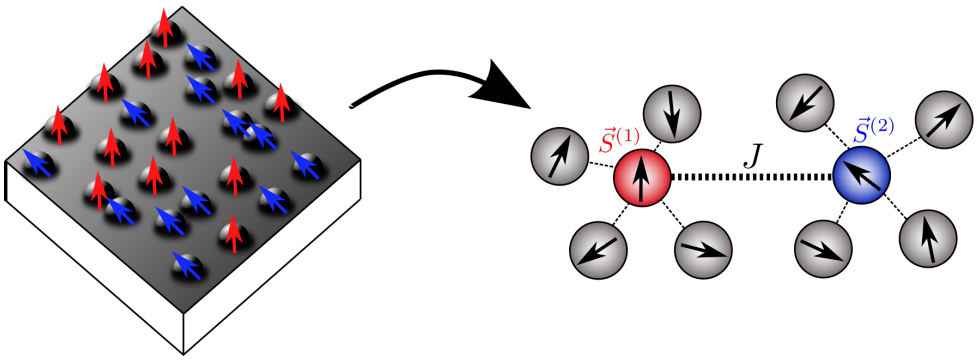

Figure 4.1: Reduction of the QD ensemble to an effective two-QD model.

In the third scenario, all electron spins $\vec{s}^{(i)}$ are randomly aligned which corresponds to the high-temperature equilibrium. The average value of $\langle \vec{b}_J^{(i)} \rangle = 0$ is zero and the fluctuations $\langle (\vec{b}_J^{(i)})^2 \rangle \neq 0$ become relevant. In the high-temperature limit, all spins are independent, so the fluctuations,

$$\begin{aligned} \left(\vec{b}_J^{(i)}\right)^2 &= \sum_j J_{ij}^2 \left(\vec{s}^{(j)}\right)^2 \\ &= J_{\mathrm{fluc},i}^2 \vec{s}^2 \,, \end{aligned} \tag{4.49}$$

can be simplified by replacing the spin length $\left(\vec{s}^{(j)}\right)^2 = \vec{s}^2$ and using the definition of an effective coupling constant

$$J_{\mathrm{fluc},i} = \sqrt{\sum_j J_{ij}^2} \,. \tag{4.50}$$

All three scenarios have in common that we can define an effective interaction strength ($J_{\mathrm{NN},i}$, $J_{\mathrm{sync},i}$, or $J_{\mathrm{fluc},i}$). As a result, the coupling of the electron spin to the effective field $\vec{b}_J^{(i)}$ complies with the analytical form of the electron spin coupling to another single electron spin. Depending on the scenario, the other electron spin corresponds to (i) the nearest-neighbor electron spin, (ii) a representative spin of the second subensemble, or (iii) another randomly fluctuating electron spin. Supported by this analytical structure, we can reduce the QD ensemble with $N_{\mathrm{QD}} = 10^6$ QDs to a pair of $N_{\mathrm{QD}} = 2$ QDs coupled with the corresponding effective interaction strength (see Fig. 4.1).

Under the assumption that we have a microscopic model that provides the interaction strength $J_{ij} = J(\vec{R}_i, \vec{R}_j)$ as a function of the QD locations $\vec{R}_i$ and $\vec{R}_j$, we can

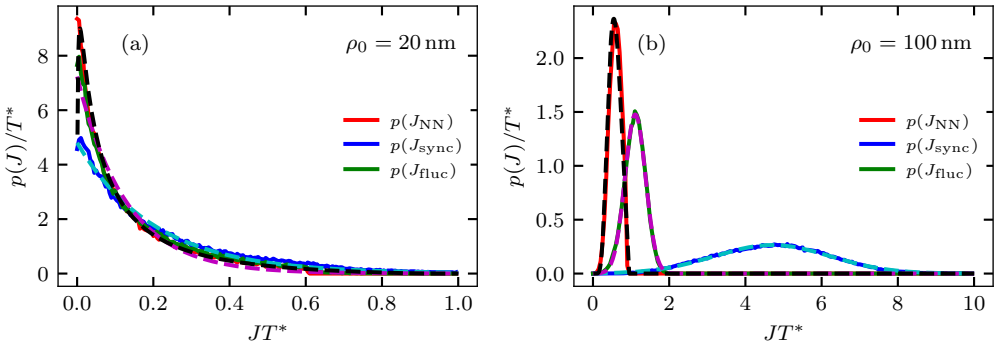

Figure 4.2: Distribution $p(J)$ of the three effective coupling constants $J_{\mathrm{NN},i}$, $J_{\mathrm{sync},i}$ and $J_{\mathrm{fluc},i}$ for an interaction length of (a) $\rho_0 = 20\,\mathrm{nm}$ and (b) $\rho_0 = 100\,\mathrm{nm}$ obtained with $N_{\mathrm{QD}} = 10^5$. The dashed magenta and cyan lines are (a) exponential or (b) Gaussian fits. The dashed black line depicts the analytical prediction, Eq. (4.55).

determine the effective interaction strength for each QD i and thus obtain the distributions $p(J_{\mathrm{NN},i})$, $p(J_{\mathrm{sync},i})$, and $p(J_{\mathrm{fluc},i})$. In the SCA, we mimic the ensemble by a QD pair with an effective coupling strength $J = J_{12}$ drawn from one of the distribution p for each classical configuration μ.

In the following, the distribution of the effective inter-QD coupling strength J shall be discussed in more detail. We assume, that N_{QD} QDs are distributed randomly on a square with an edge length $L = \sqrt{N_{\mathrm{QD}}} \times 100\,\mathrm{nm}$, which corresponds to a QD density of $n = (100\,\mathrm{nm})^{-2}$. The minimum distance between the centers of the QDs is restricted to $R_0 = 20\,\mathrm{nm}$. For the sake of simplicity, we assume an exponentially decreasing coupling constant,

$$J(r) = \alpha \exp\left(-\frac{r}{\rho_0}\right) , \tag{4.51}$$

with the QD distance r, a prefactor α defining the interaction strength, and the parameter ρ_0 controlling the distance dependency.

We randomly draw the centers of the QDs $\vec{R}_i$ one after the other uniformly distributed on the given square. If a QD center is too close to another QD, the position is rejected and redrawn. After drawing the positions $\vec{R}_i$, we can calculate the matrix elements $J_{ij} = J(|\vec{R}_i - \vec{R}_j|)$ as well as the effective coupling constants $J_{\mathrm{NN},i}$, $J_{\mathrm{sync},i}$, and $J_{\mathrm{fluc},i}$ using the Eqs. (4.46), (4.48), and (4.50). The values of the effective coupling constants are processed in a histogram to obtain the corresponding distribution function (see Fig. 4.2). In Fig. 4.2(a), we address a short range interaction with

$\rho_0 = 20\,\mathrm{nm}$. Due to the short range of the interaction, in essence, only the next neighbors interact with each other, and all three distributions become similar. For all three effective coupling constants, $p(J)$ decreases monotonically and can be approximated by an exponential function. In Fig. 4.2(b), we examine a long-range interaction with $\rho_0 = 100\,\mathrm{nm}$. In this case, many QDs contribute to the effective magnetic field and, due to the central limit theorem, the distributions $p(J_{\mathrm{sync}})$ and $p(J_{\mathrm{fluc}})$ become Gaussian.

The distribution $p(J_{\mathrm{NN}})$ of the nearest-neighbor coupling is accessible analytically and can be used as an approximation for J_{sync} and J_{fluc} for short-range interactions. To calculate $p(J_{\mathrm{NN}})$, we first derive the probability $\tilde{p}(r)$ to find the next neighbor at the distance r. We calculate $p(r, \Delta r)$ as the product of the probability to find zero QDs within the distance r and the probability to find at least one QD within the range $[r, r + \Delta r]$,

$$p(r, \Delta r) = e^{-n\pi r^2}(1 - e^{-n\pi((r+\Delta r)^2 - r^2)}) \,, \tag{4.52}$$

using the Poisson distribution. In the limit

$$\tilde{p}(r)dr = \lim_{\Delta r \to dr} p(r, \Delta r) = 2\pi n r e^{-n\pi r^2} dr \,, \tag{4.53}$$

we obtain the desired distribution $\tilde{p}(r)$. The inverse transformation method,

$$p(J_{\mathrm{NN}})dJ_{\mathrm{NN}} = \tilde{p}(r)dr \,, \tag{4.54}$$

yields the distribution $p(J_{\mathrm{NN}})$,

$$p(J_{\mathrm{NN}}) = 2\pi n \rho_0^2 J_{\mathrm{NN}}^{-1} \ln\left(\frac{\alpha}{J_{\mathrm{NN}}}\right) \exp\left(-n\pi\rho_0^2 \ln^2\left(\frac{J_{\mathrm{NN}}}{\alpha}\right)\right) \,. \tag{4.55}$$

We added this distribution in Fig. 4.2 as a dashed black line. This analytical form is rather complex but for short distances, it can be well approximated by an exponential function.

4.7 Frozen Overhauser-field approximation

Due to their complexity, the semiclassical EOM in general must be evaluated numerically. For the special case of non-interacting QDs, an analytical solution for short time scales was found by Merkulov et al. [37]. The basic idea is a separation of the time scales. While the electron spin interacts with many nuclear spins and precesses about an almost frozen Overhauser field, the nuclear spins are affected by the Knight field, which is smaller in magnitude by a factor of $\sqrt{N_I}$ at high

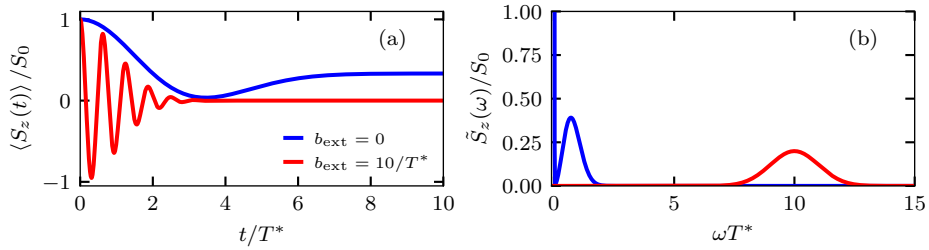

Figure 4.3: Solution of the FOA for a single QD in the time domain (a) and frequency domain (b) for an initial spin polarization in $\vec{S}_0 \parallel \vec{e}_z$. In time domain (a), we use Eq. (4.57) for $b_{\rm ext} = 0$ and Eq. (4.59) for $b_{\rm ext} = 10/T^*$. In frequency domain (b), Eq. (4.58) is used for $b_{\rm ext} = 0$ and Eq. (4.60) for $b_{\rm ext} = 10/T^*$. Both panels share the same legend.

temperatures. The nuclear spin dynamics become relevant on the time scale of µs and thus can be neglected for the short-time dynamics of the electron spins. Therefore, we employ the frozen Overhauser field approximation (FOA) in the following. The electron spin precesses about a constant field $\vec{b} = \vec{b}_{\rm ext} + \vec{b}_N$, where $\vec{b}_{\rm ext}$ and $\vec{b}_N$ are the external magnetic field and the Overhauser field. The dynamics of the electron spin are given by

$$\vec{S}(t) = \left(\vec{S}_0\vec{n}\right)\vec{n} + \left[\vec{S}_0 - \left(\vec{S}_0\vec{n}\right)\right]\cos(bt) + \vec{S}_0 \times \vec{n}\sin(bt) \tag{4.56}$$

with the magnitude $b = |\vec{b}|$ and the direction $\vec{n} = \vec{b}/b$ of the total magnetic field. The vector $\vec{S}_0$ is the spin state at time $t = 0$. The Overhauser field is calculated as the sum of many randomly oriented nuclear spins and, therefore, follows a three-dimensional normal distribution with zero mean value and standard deviation $(T^*)^{-2}/3$ in each direction. For the expectation value of the electron spin averaged over all possible Overhauser fields, we obtain

$$\langle\vec{S}(t)\rangle = \frac{\vec{S}_0}{3}\left\{1 + 2\left[1 - \frac{1}{3}\left(\frac{t}{2T^*}\right)^2\right]e^{-\frac{1}{6}\left(\frac{t}{2T^*}\right)^2}\right\}. \tag{4.57}$$

This curve with the universal time scale t/T^* starts at $\vec{S}_0$ for $t = 0$ and asymptotically approaches $\vec{S}_0/3$, see the blue curve in Fig. 4.3(a). Interestingly, only the characteristic time T^* enters the analytical solution while details about the hyperfine coupling constants are irrelevant due to the averaging over many nuclear spin configurations. Furthermore, we examine the Fourier transform of Eq. (4.57),

$$\tilde{\vec{S}}(\omega) = \frac{1}{2\pi}\int_{-\infty}^{\infty}\langle\vec{S}(t)\rangle\, e^{-{\rm i}\omega t}dt = \frac{\vec{S}_0}{3}\delta(\omega) + 2\sqrt{3}\vec{S}_0\frac{\omega^2(2T^*)^3}{\sqrt{2\pi}}e^{-\frac{3}{2}(2\omega T^*)^2}, \tag{4.58}$$

which is depicted as a blue curve in Fig. 4.3(b). The frequency spectrum of the electron spin dynamics comprises two contributions: The Dirac-delta corresponds to the non-decaying part, while the second term arises from the Overhauser field fluctuations and produces an approximately Gaussian-shaped peak around $\omega T^* = 1$.

In the case of a strong transversal field, $\vec{b}_{\text{ext}} = b_{\text{ext}}\vec{e}_x$ with $b_{\text{ext}} \gg (T^*)^{-1}$, and an initial electron spin polarization in z direction, we obtain the averaged solution,

$$\langle S_z(t)\rangle = S_{z,0}\cos(b_{\text{ext}}t)e^{-\frac{1}{6}\left(\frac{t}{T^*}\right)^2}\,, \tag{4.59}$$

which corresponds to a spin precession with the frequency b_{ext} and a dephasing on the time scale of T^*, see the red curve in Fig. 4.3(a). The Fourier transform yields a combination of two Gaussian functions,

$$\tilde{S}_z(\omega) = S_{z,0}\frac{\sqrt{3}T^*}{2\sqrt{2\pi}}\left(e^{-\frac{3((\omega-b_{\text{ext}})T^*)^2}{2}} + e^{-\frac{3((\omega+b_{\text{ext}})T^*)^2}{2}}\right)\,, \tag{4.60}$$

centered around $\pm b_{\text{ext}}$ with their width governed by $(T^*)^{-1}$, see the red curve in Fig. 4.3(b).

4.8 Nuclear-spin trajectories

In the following, the nuclear spin dynamics disregarded in the FOA will be investigated in more detail. In the SCA, the nuclear spins experience the effective field $\vec{b}^{(i)}_{\text{eff},k}$, Eq. (4.33b), that consists of three components: the external magnetic field $\vec{b}^{(i)}_{\text{ext},k}$, the nuclear-quadrupolar field $\vec{b}^{(i)}_{Q,k}$, and the Knight field $\vec{b}^{(i)}_{K,k}$. Here, we study the trajectories of the nuclear spins when neglecting the Knight field. This is justified because, on the one hand, the Knight field is very small in magnitude, and on the other hand, the nuclear spins cannot follow the fast dynamics of the electron spin. A relevant effect of the Knight field is expected on the time scale of seconds, while the quadrupolar interactions are already relevant on the µs time scale.

By neglecting the Knight field, all nuclear spins decouple and precess independently in their effective field. The semiclassical EOM for a single nuclear spin according to Eq. (4.32b) is of the form

$$\partial_t\vec{i} = \left(b\vec{n}_b + 4q\left(\vec{n}_q\vec{i}\right)\vec{n}_q\right)\times\vec{i} \tag{4.61}$$

with the external magnetic field, $\vec{b} = b\vec{n}_b = z\vec{b}_{\text{ext}}$ and the easy axis $\vec{n}_q$. Here, we neglect the quadrupolar biaxiality ($\eta = 0$) and omit the indices k and i as the nuclear spins are independent. To find a solution to the EOM, we first focus on conserved

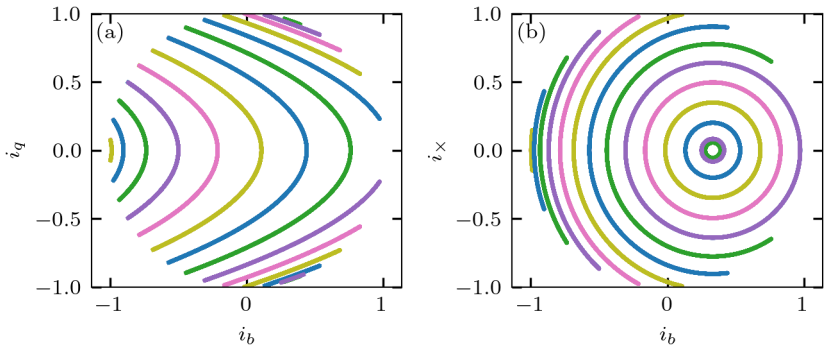

Figure 4.4: Nuclear-spin trajectories from different perspectives for the ratio $b/q = 2$. The various colors correspond to different starting conditions. (a) Trajectories projected to the $(i_b,\ i_\times)$. The surfaces of constant energy form parabolas. (b) Trajectories projected to the (i_b, i_q) plane form circles corresponding to Eq. (4.64).

quantities. By determining two conserved quantities, we reduce the problem to a single first-order equation, which can be solved in a closed formula.

The first conserved quantity is the spin length. Due to the cross product on the right-hand side of Eq. (4.61), the time derivative $\partial_t \vec{i}$ is always perpendicular to $\vec{i}$. The trajectories of $\vec{i}$ are restricted to the surface of a sphere with radius I. The second conserved quantity is the energy,

$$E = b(\vec{n}_b\vec{i}) + 2q(\vec{n}_q\vec{i})^2 \ . \tag{4.62}$$

The conservation of energy is reflected in the cross product of the EOM as well. The time derivative $\partial_t \vec{i}$ is perpendicular to the vector field

$$\vec{V}(\vec{i}) = \left(b\vec{n}_b + 4q\left(\vec{n}_q\vec{i}\right)\vec{n}_q\right) \ . \tag{4.63}$$

The vector field $\vec{V}$ determines the normal vector $\vec{V}/V$ of the surfaces of constant energy E. The surfaces of constant energy are given by parabolas in the plane spanned by $\vec{n}_b$ and $\vec{n}_q$. As a result, the trajectories of $\vec{i}$ can be interpreted as a section between a sphere with radius i and a parabolic surface with the curvature $2q/b$, see Fig. 4.4(a).

In the following, we focus on the dynamic for the case of perpendicular magnetic and quadrupolar easy axis, $\vec{n}_b \perp \vec{n}_q$. This situation is realized in the Voigt geometry of the setup, for which the quadrupolar easy axis is directed approximately along the growth axis of the sample and the external magnetic field is applied perpendicularly.

For completeness, we define the third axis $\vec{n}_\times = \vec{n}_b \times \vec{n}_q / |\vec{n}_b \times \vec{n}_q|$. Let $i_\alpha = \vec{i}\vec{n}_\alpha$ with $\alpha \in \{b, q, \times\}$ be the projection of $\vec{i}$ on the specific axis. The spin length conservation and the energy conservation can be combined to the cylindrical equation,

$$i_\times^2 + \left(i_b - \frac{b}{4q}\right)^2 = I^2 - \frac{E}{2q} + \frac{b^2}{16q^2} =: R^2 \tag{4.64}$$

with the radius R. We present the trajectories projected to the (i_b, i_q) plane in Fig. 4.4(b), where Eq. (4.64) manifests in the circular shape of the projected trajectories.

Employing the definition of i_α, the EOM is rewritten,

$$\partial_t \vec{i} = -b i_\times \vec{n}_q + (b i_q - 4q i_q i_b)\vec{n}_\times + 4q i_q i_\times \vec{n}_b \, . \tag{4.65}$$

The projection onto the $\vec{n}_q$ axis yields $\partial_t i_q = -b i_\times$. To decouple the EOM for the three components, we can express $i_\times$ as a function of i_q using the conserved quantities,

$$i_\times^2 = I^2 - i_q^2 - \left(\frac{E}{b} - \frac{2q}{b} i_q^2\right)^2 \, . \tag{4.66}$$

Finally, we arrive at the EOM

$$(\partial_t i_q)^2 = \left(b^2 I^2 - b^2 r^2\right) + \left(-b^2 + 4rqb\right) i_q^2 - 4q^2 i_q^4 \, . \tag{4.67}$$

Equation (4.67) is closely related to the differential equation of the cosine amplitudinis $\mathrm{cn}(t, k)$, an elliptical generalization of the cosine function. The cosine amplitudinis $\mathrm{cn}(t, k)$ solves the differential equation for the function $f_k(t)$ with a real parameter $k \in [0; 1]$,

$$(\partial_t f_k)^2 = 1 - k^2 - (1 - k^2) f_k^2 - k^2 f_k^4 \, . \tag{4.68}$$

Moreover, the ansatz

$$g = A \, \mathrm{cn}(\omega t + \varphi, k) \tag{4.69}$$

is a solution to the ordinary differential equation

$$(\partial_t g)^2 = A^2 \omega^2 (1 - k^2) - \omega^2 (1 - k^2) g^2 - \frac{\omega^2}{A^2} k^2 g^4 \, . \tag{4.70}$$

A coefficient comparison between Eq. (4.67) and (4.70) reveals the parameters

$$A^2 = \frac{b^2 I^2 - E^2}{b^2 - 4Eq} \tag{4.71a}$$

$$\omega^2 = b^2 - 4Eq + 4q^2 A^2 \tag{4.71b}$$

$$k^2 = \frac{4q^2 A^2}{\omega^2} \tag{4.71c}$$

for the final solution of i_q. Accordingly, the three components of the nuclear spin obey the time evolution,

$$i_q = A\,\mathrm{cn}(\omega t + \varphi, k)\ , \tag{4.72a}$$

$$i_x = \pm\sqrt{I^2 - i_q^2 - \left(\frac{E}{b} - \frac{2q}{b} i_q^2\right)^2}\ , \tag{4.72b}$$

$$i_b = \frac{2q}{b} i_q^2 - \frac{E}{b}\ . \tag{4.72c}$$

The remaining parameters E and φ are determined by the starting conditions. The additional nuclear-spin dynamics induced by the nuclear-electric quadrupolar interactions become relevant for the low-frequency spectrum of various correlation functions.

Chapter 5

Semiclassical approach for open quantum systems

In a closed spin system, the dynamics are reversible and the entropy is conserved. However, real systems are always coupled to an environment. Since a complete simulation of the environment is not possible, various approximations have been developed which allow for the description of the interaction between the system and its environment without explicitly treating the environmental degrees of freedom [182–188]. This approach leads to non-reversible quantum master equations in which the entropy is not a conserved quantity. The most general type of a Markovian master equation that describes the time evolution of a density operator ρ and preserves the rules of quantum mechanics, i.e., it is trace-conserving and ensures a positive-semidefinite density operator, is given by a Lindblad master equation,

$$\partial_t \rho = -\mathrm{i}[H, \rho] + \sum_m \left(L_m \rho L_m^\dagger - \frac{1}{2} \left\{ L_m^\dagger L_m, \rho \right\} \right) . \tag{5.1}$$

While the first part of the equation describes the unitary time evolution of the system, the second part captures the interaction between the system and the environment via the Lindblad operators (or jump operators) L_m. The Heisenberg form of the Lindblad equation,

$$\partial_t O = \mathrm{i}[H, O] + \sum_m \left(L_m^\dagger O L_m - \frac{1}{2} \left\{ L_m^\dagger L_m, O \right\} \right) , \tag{5.2}$$

governs the temporal evolution of a general observable O. In this thesis, we address two mechanisms that lead to an open quantum system. First, we include a spin-orbit coupling, which generates an interaction of the electron spin with the environmental charge carriers, resulting in spin-lattice relaxation. Second, we take into account the radiative recombination of an optically generated electron-hole pair. Both processes can be modeled by a Lindblad equation without explicit treatment of the environment.

We present two different approaches to integrate the coupling to the environment in this chapter. In the first approach, Secs. 5.1 and 5.2, we map the spin-coherent states to a density operator and derive modified equations of motion (MEOM). We develop a more elaborate approach based on quantum trajectory theory (QTT) [182, 189, 190] also known as the Monte-Carlo wave function approach or quantum jump theory. In Sec. 5.3, we review the QTT and introduce a quantum jump based semiclassical approach (QJ-SCA) the Secs. 5.4 and 5.5. The QJ-SCA allows for the exact description of the coupling to the environment by quantum jumps while the spin dynamics between the quantum jumps are approximated semiclassically. The advantages and disadvantages of both approaches are discussed in Sec. 5.6.

5.1 Spin-lattice relaxation

For a minimal isotropic model of spin-lattice relaxation, we introduce the three Lindblad jump operator $L_\alpha = \sqrt{\gamma} S_\alpha$, where γ is the decay rate and $\alpha \in \{x, y, z\}$ indicates the spin component. To demonstrate the effect of these jump operators, we evaluate the Lindblad master equation in Heisenberg form, Eq. (5.2), for the observable $O = S_\beta$,

$$\begin{aligned} \partial_t S_\beta &= \mathrm{i}[H, S_\beta] + \gamma \sum_\alpha \left(S_\alpha S_\beta S_\alpha - \frac{1}{2} \left\{ S_\alpha S_\alpha, S_\beta \right\} \right) \\ &= \mathrm{i}[H, S_\beta] - \gamma S_\beta \ . \end{aligned} \tag{5.3}$$

The term $-\gamma S_\beta$ generates an exponential relaxation of the spin component S_β with rate γ.

To include this relaxation mechanism in the SCA, we exploit the unique mapping between the (2×2)-dimensional density matrix $\rho_{1/2}$ and the expectation value $\langle \vec{S} \rangle$ for a spin 1/2,

$$\rho_{1/2} = \begin{pmatrix} \frac{1}{2} + \langle S_z \rangle & \langle S_x \rangle - \mathrm{i} \langle S_y \rangle \\ \langle S_x \rangle + \mathrm{i} \langle S_y \rangle & \frac{1}{2} - \langle S_z \rangle \end{pmatrix} \ . \tag{5.4}$$

While for a pure state $| \langle \vec{S} \rangle | = \frac{1}{2}$ holds, we obtain$| \langle \vec{S} \rangle | < \frac{1}{2}$ for a mixed state. For a single spin 1/2 in a classical time-dependent field $\vec{b}(t)$, Eq. (5.3) yields the EOM

$$\partial_t \langle \vec{S} \rangle = \vec{b}(t) \times \langle \vec{S} \rangle - \gamma \langle \vec{S} \rangle \ . \tag{5.5}$$

Identifying $\langle \vec{S} \rangle = \vec{s}^{(i)}$ and $\vec{b}(t) = \vec{b}^{(i)}_{\mathrm{eff}}$, we arrive at the modified equation of motion (MEOM),

$$\partial_t \vec{s}^{(i)} = \vec{b}^{(i)}_{\mathrm{eff}} \times \vec{s}^{(i)} - \gamma \vec{s}^{(i)} \ . \tag{5.6}$$

While each configuration in the SCA for a closed system can be assigned to a pure spin-coherent product state, the spin length is not conserved in Eq. (5.6). In the MEOM approach, each configuration already represents a mixed state. For this reason, fewer configurations are required to achieve the same accuracy. However, we note that the shortened spin length leads to an underestimation of the spin fluctuations. In Sec. 5.6, we demonstrate that this underestimation can produce unphysical artifacts.

5.2 Optical excitation and trion decay

Next, the optical excitation and the subsequent decay of the excited state will be included in the SCA. An electron-hole pair can be created in the QD by a circularly polarized laser pulse. The electron-hole pair together with the localized charge carrier result in a bound trion state $|T\rangle$ (see Sec. 3.4). A σ^+ polarized laser pulse induces the transition $|\uparrow\rangle \rightarrow |T\rangle$ while the state $|\downarrow\rangle$ is left unaffected.

The laser pulse can be described by the unitary matrix U_P, Eq. (3.12). To obtain the effect on a classical spin, we focus on a single electron spin and examine the (3×3)-dimensional density matrix including the states $|\uparrow\rangle$, $|\downarrow\rangle$, and $|T\rangle$. We assume that before a pulse the trion state is unoccupied, and the density matrix reads

$$\rho_{\mathrm{bp}} = \begin{pmatrix} \frac{1}{2} + s_{z,\mathrm{bp}} & s_{x,\mathrm{bp}} + \mathrm{i}s_{y,\mathrm{bp}} & 0 \\ s_{x,\mathrm{bp}} - \mathrm{i}s_{y,\mathrm{bp}} & \frac{1}{2} - s_{z,\mathrm{bp}} & 0 \\ 0 & 0 & 0 \end{pmatrix} . \tag{5.7}$$

Here, $s_{\alpha,\mathrm{bp}}$ is the spin component right before the pulse. The expectation values after the pulse for a general observable O are calculated according to

$$o_{\mathrm{ap}} = \mathrm{Tr}\left[U_P \rho_{\mathrm{bp}} U_P^\dagger O\right] . \tag{5.8}$$

The results for S_x, S_y, S_z, and $P_T = |T\rangle\langle T|$ are

$$s_{x,\mathrm{ap}} = |a|\left(s_{x,\mathrm{bp}}\cos(\varphi) + s_{y,\mathrm{bp}}\sin(\varphi)\right) , \tag{5.9a}$$

$$s_{y,\mathrm{ap}} = |a|\left(-s_{x,\mathrm{bp}}\sin(\varphi) + s_{y,\mathrm{bp}}\cos(\varphi)\right) , \tag{5.9b}$$

$$s_{z,\mathrm{ap}} = -\frac{1}{4}\left(1 - |a|^2\right) + \frac{s_{z,\mathrm{bp}}}{2}\left(1 + |a|^2\right) , \tag{5.9c}$$

$$p_{T,\mathrm{ap}} = \left(1 - |a|^2\right)\left(\frac{1}{2} + s_{z,\mathrm{bp}}\right) , \tag{5.9d}$$

where $|a|$ and φ are the absolute value and the argument of the complex pulse parameter a (see Sec. 3.4). To reconstruct the full (3×3)-dimensional density

matrix, the spin-trion off-diagonal elements $\rho_{\sigma,T} = \langle\sigma| U_P \rho_{\mathrm{bp}} U_P^\dagger |T\rangle$ and $\rho_{T,\sigma} = \langle T| U_P \rho_{\mathrm{bp}} U_P^\dagger |\sigma\rangle$ with $\sigma \in \{\uparrow, \downarrow\}$ would be required. Since the spin-trion off-diagonal elements decay to zero and decouple from the remaining dynamics, we refrain their calculation.

Finally, the trion decay has to be included in the SCA. In the Lindblad formalism, it is modeled by the jump operator $L_T = \sqrt{\gamma_T} |\uparrow\rangle \langle T|$ with the decay rate γ_T. We address the dynamics of the (3×3)-dimensional density matrix of the electron spin in a classical time-dependent magnetic field $\vec{b}(t)$ according to Eq. (5.2). We obtain the four closed EOMs for the spin elements and the trion occupation,

$$\partial_t \langle \vec{S} \rangle = \vec{b}(t) \times \langle \vec{S} \rangle + \frac{1}{2} \gamma_T \langle P_T \rangle \vec{e}_z \,, \tag{5.10a}$$

$$\partial_t \langle P_T \rangle = -\gamma_T \langle P_T \rangle \,. \tag{5.10b}$$

Furthermore, we obtain one equation for the trace conservation and four equations for the spin-trion correlator which decouple from the remaining elements and decay independently with the rate γ_T. The semiclassical EOM must be extended by an EOM for p_T,

$$\partial_t \vec{s}^{(i)} = \vec{b}_{\mathrm{eff}}^{(i)} \times \vec{s}^{(i)} + \frac{1}{2} \gamma_T p_T^{(i)} \vec{e}_z \,, \tag{5.11a}$$

$$\partial_t p_T^{(i)} = -\gamma_T p_T^{(i)} \,. \tag{5.11b}$$

The EOM for $p_T^{(i)}$ is trivially solved by the exponential $p_T^{(i)} = p_{T,0}^{(i)} \exp(-\gamma_T t)$. Therefore, the trion decay serves as a source term in the spin dynamics, Eq. (5.11a), which induces or reduces spin polarization.

5.3 Quantum trajectory theory

In the next step, we derive an approach that restores the direct mapping between the classical vectors and spin-coherent product states. For this purpose, we decompose the density operator $\rho = \sum_\mu p_\mu |\psi_\mu\rangle \langle\psi_\mu|$ and analyze the dynamics of the states $|\psi_\mu\rangle$ for a open quantum system. In contrast to a closed system, the dynamics are non-unitary due to the interaction with the environment. We first introduce the QTT for an arbitrary quantum mechanical system. Afterward, we identify the states $|\psi_\mu\rangle$ with the spin-coherent product state from the classical configuration μ to derive a hybrid approach.

We derive the time evolution of the state $|\psi_\mu\rangle$ starting from the Lindblad equation, Eq. (5.1), following the approach in Ref. [182]. First, we rewrite the Lindblad

equation by expanding the commutator and identifying complex conjugated pairs,

$$\partial_t \rho = -\mathrm{i}H\rho + (-\mathrm{i}H\rho)^\dagger + \sum_m \left(-\frac{1}{2}L_m^\dagger L_m \rho\right) + \left(-\frac{1}{2}L_m^\dagger L_m \rho\right)^\dagger + L_m \rho L_m^\dagger \,. \quad (5.12)$$

Two of the terms containing the Lindblad operators L_m can be written in the same form as the Hamiltonian H. This allows for rewriting the master equation to

$$\partial_t \rho = \underbrace{-\mathrm{i}H_B\rho + (-\mathrm{i}H_B\rho)^\dagger}_{\mathcal{L}_B\rho} + \sum_m \underbrace{L_m \rho L_m^\dagger}_{\mathcal{L}_{J,m}\rho} \,, \quad (5.13)$$

where we introduce the effective non-hermitian Hamiltonian H_B,

$$H_B = H + \frac{\mathrm{i}}{2}\sum_m L_m^\dagger L_m \,. \quad (5.14)$$

Since $L_m^\dagger L_m$ is a positive operator, the eigenvalues of H_B have a positive imaginary part. The superoperators $\mathcal{L}_B$ and $\mathcal{L}_{J,m}$ in Eq. (5.13) reduce the Lindblad equation to the comprehensive form

$$\partial_t \rho = \mathcal{L}_B \rho + \sum_m \mathcal{L}_{J,m}\rho \,. \quad (5.15)$$

The left part of the equation, $\partial_t \tilde{\rho} = \mathcal{L}_B \tilde{\rho}$, is a generalized form of the von Neumann equation. This von-Neumann equation is also applicable to non-hermitian Hamiltonians and its solution [182] is given by

$$\tilde{\rho}(t) = e^{\mathcal{L}_B t}\tilde{\rho}(0) = e^{-\mathrm{i}H_B t}\tilde{\rho}(0)\, e^{\mathrm{i}H_B^\dagger t} \quad (5.16)$$

with the non-unitary time-evolution operator $e^{-\mathrm{i}H_B t}$. As the eigenvalues of H_B have a positive imaginary part, $e^{-\mathrm{i}H_B t}$ describes not only the coherent dynamics induced by the Hamiltonian H but also an exponential decay induced by the Lindblad operators L_m. As a consequence, the trace of $\tilde{\rho}$ is not conserved. However, trace conservation is restored when taking into account the additional term $\sum_m \mathcal{L}_{J,m}\rho$.

Since the formal solution of the von Neumann part is known, we transform into an interaction picture with $\overline{\rho} = e^{-\mathcal{L}_B t}\rho$ and obtain a master equation with explicit time dependency,

$$\dot{\overline{\rho}} = \sum_m e^{-\mathcal{L}_B t}\mathcal{L}_{J,m} e^{\mathcal{L}_B t}\overline{\rho} \,. \quad (5.17)$$

This equation can be formally integrated

$$\overline{\rho}(t) = \overline{\rho}(0) + \sum_m \int_0^t dt_1 e^{-\mathcal{L}_B t_1}\mathcal{L}_{J,m} e^{\mathcal{L}_B t_1}\overline{\rho}(t_1) \,, \quad (5.18)$$

but the solution $\overline{\rho}(t)$ still depends on the history of $\overline{\rho}(t)$. Equation (5.18) can be understood as a recursive relation for $\overline{\rho}(t)$. By reinserting Eq. (5.18) into itself, one obtains the Dyson expansion,

$$\begin{aligned}\rho(t) =& e^{\mathcal{L}_B t}\rho(0) \\ &+ \sum_m \int_0^t dt_1 e^{\mathcal{L}_B(t-t_1)}\mathcal{L}_{J_m} e^{\mathcal{L}_B t_1}\rho(0) \\ &+ \sum_{m,m'} \int_0^t \int_0^{t_2} dt_1 dt_2 e^{\mathcal{L}_B(t-t_2)}\mathcal{L}_{J,m'} e^{\mathcal{L}_B(t_2-t_1)}\mathcal{L}_{J,m} e^{\mathcal{L}_B t_1}\rho(0) \\ &+ \dots ,\end{aligned} \tag{5.19}$$

where we replaced $\overline{\rho}$ by $e^{-\mathcal{L}_B t}\rho$. We note that Eq. (5.19) is a formal solution of the Lindblad equation and provides an intuitive way of understanding.

In the following, we interpret the terms of Eq. (5.19) line by line. In the first line, a time evolution from the density operator at time 0 to the time t is performed using the Hamiltonian H_B. In the second line, the density operator $\rho(0)$ is evolved to the time t_1, then the Liovillian $\mathcal{L}_{J,m}$ is applied, and finally the density operator is evolved from t_1 to t. The successive execution of these operators can be interpreted as a time evolution that is interrupted by a single quantum jump at time t_1, whereby we integrate over all possible times t_1 and sum over all possible Lindblad operators L_m. The third line can be interpreted the same way, however, the time evolution is interrupted at two times t_1 and t_2 at which a quantum jump with index m or m' is performed. The following lines which are not displayed in Eq. (5.19) follow the same scheme but include terms with three and more jump operations.

In Fig. 5.1, the structure of Eq. (5.19) schematically visualized. The different terms in the equation can be interpreted as the dynamics in different independent branches. These branches are distinguished by the number, the times, and the type of quantum jumps. The total solution $\rho(t)$ results from averaging the different branches at the end.

If we start with a general pure state $|\psi\rangle\langle\psi|$, the state stays pure for each branch since the time evolution $e^{\mathcal{L}_B t}$ and the quantum jump $\mathcal{L}_{J,m}$ do not affect the purity of a state:

$$e^{\mathcal{L}_B t}|\psi\rangle\langle\psi| = e^{-\mathrm{i}H_B t}|\psi\rangle\langle\psi| e^{\mathrm{i}H_B^\dagger t} =: |\psi(t)\rangle\langle\psi(t)| , \tag{5.20a}$$

$$\mathcal{L}_{J,m}|\psi\rangle\langle\psi| = L_m|\psi\rangle\langle\psi| L_m^\dagger =: |\psi'\rangle\langle\psi'| . \tag{5.20b}$$

The mixing of states only arises from averaging the different branches. As the number of branches is infinite, it is reasonable to employ a Monte-Carlo integration

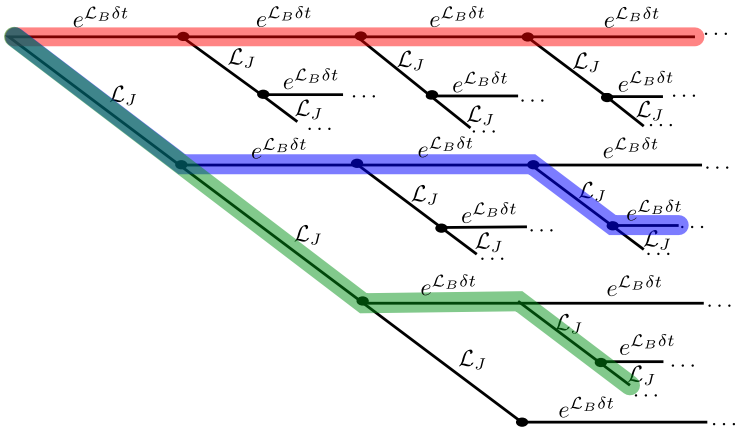

Figure 5.1: Schematic representation of the Dyson series, Eq. (5.19). The dynamics of the system can be interpreted as a combination of deterministic time evolution $e^{\mathcal{L}_B \delta t}$ with the infinitesimal time δt and random quantum jumps $\mathcal{L}_J$ in-between. The colored lines illustrate exemplary paths of a Monte-Carlo integration.

over different representative paths. This approach is visualized by the colored lines in Fig. 5.1.

Based on the previous findings, we introduce the following procedure which is called Monte Carlo wave function approach or quantum jump algorithm [189]: The time evolution without a quantum jump is given by the Schrödinger equation

$$\partial_t \left|\psi_\mu\right\rangle = -\mathrm{i} H_B \left|\psi_\mu\right\rangle \ , \tag{5.21}$$

with the modified Hamiltonian H_B. In addition, in each infinitesimal time step δt, there is an infinitesimal probability $\delta p_m = \delta t \left\langle\psi_\mu\right| L_m^\dagger L_m \left|\psi_\mu\right\rangle$ that a quantum jump,

$$\left|\psi_\mu(t+\delta t)\right\rangle = L_m \left|\psi_\mu(t)\right\rangle \ , \tag{5.22}$$

modifies the state. It can be rigorously shown that the combination of continuous non-hermitian dynamics and random quantum jumps asymptotically reproduces the Lindblad master equation for an infinite number of configurations [189]. We note that Eqs. (5.21) and (5.22) generate non-normalized states which have to be normalized before averaging. Alternatively, the normalized equations,

$$\partial_t \left|\psi'_\mu\right\rangle = -\mathrm{i} \left(H_B - \frac{\mathrm{i}}{2} \left\langle\psi'_\mu\right| \sum_m L_m^\dagger L_m \left|\psi'_\mu\right\rangle \right) \left|\psi'_\mu\right\rangle \tag{5.23}$$

and

$$|\psi'_\mu(t+\delta t)\rangle = \frac{L_m |\psi'_\mu(t)\rangle}{\langle\psi'_\mu(t)| L_m^\dagger L_m |\psi'_\mu(t)\rangle} , \tag{5.24}$$

can be used which guarantee normalization but lose the linearity in $|\psi'_\mu\rangle$ [182]. The quantum jump approach has the disadvantage that the Hilbert space dimension for the representation of the states $|\psi_\mu\rangle$ grows exponentially with the system size. In addition, several thousand realizations of the state have to be tracked for the Monte-Carlo integration. In the following, we use a hybrid approach where each state $|\psi_\mu\rangle$ is parameterized by classical vectors. This quantum jump based semiclassical approach (QJ-SCA) has the same computational effort as the SCA for closed systems. The state vectors in the SCA grow only linearly with the number of spins and, by construction of the SCA, several configurations of the system are in use. The non-hermitian dynamics will can modify the semiclassical EOMs and the quantum jumps can be included in the SCA exactly. In the following sections, we apply the QJ-SCA for both scenarios, the isotropic spin relaxation as well as the decay of the optically excited trion.

5.4 Quantum jump approach to the spin-lattice relaxation

In the following, we specify the QJ-SCA for spin-lattice relaxation. We employ the Lindblad operators $L_\alpha = \sqrt{\gamma} S_\alpha$, introduced in Sec. 5.1, to derive corrections to the SCA using QTT. We obtain the modified Hamiltonian for $S = 1/2$

$$H_B = H + \frac{\mathrm{i}}{2} \sum_\alpha \gamma S_\alpha S_\alpha = H + \gamma \frac{3}{8} \mathrm{i} . \tag{5.25}$$

This Hamiltonian is included in Eq. (5.23) which produces the differential equation

$$\partial_t |\psi_\mu\rangle = -\mathrm{i} \left[H_B - \frac{\mathrm{i}}{2} \langle\psi_\mu| \frac{3}{4} \gamma |\psi_\mu\rangle \right] |\psi_\mu\rangle = -\mathrm{i} H |\psi_\mu\rangle \ . \tag{5.26}$$

Even though the modified Hamiltonian H_B differs from H, the dynamics of a state $|\psi_\mu\rangle$ remain unchanged since the jump probability does not depend on the state. In addition to the continuous dynamics, a quantum jump occurs with the probability $\delta p = \frac{3}{4}\gamma\delta t$ any infinitesimal time step δt. For the practical implementation of the quantum jumps, we draw a random time τ, at which the next jump occurs, from an exponential distribution with the mean value $4/(3\gamma)$ rather than generating a random number in each time step for deciding whether a quantum jump takes place

or not. For the realization of a quantum jump, we first choose a random direction α and evaluate the impact on a spin-coherent state $|\vec{s}\rangle$,

$$|\vec{s}\rangle \to \frac{\sqrt{\gamma} S_\alpha |\vec{s}\rangle}{\sqrt{\langle \vec{s}| \gamma S_\alpha S_\alpha |\vec{s}\rangle}} = \sigma_\alpha |\vec{s}\rangle \ . \tag{5.27}$$

The Pauli matrix σ_α generates a π rotation around the α axis. This scheme can be easily integrated into the SCA. The EOMs remain unaltered. When the quantum jump occurs, we randomly choose one axis x, y, or z and perform a π rotation of the spin around this axis. As the amount of randomly drawn numbers, τ and α, is small in comparison to the number of steps in the numerical integration of the EOMs, the additional computational effort is negligible.

5.5 Quantum jump approach to the trion decay

We continue with the quantum jump approach for a more complex case and adapt the optical excitation and the trion decay to the QJ-SCA. For the sake of simplicity, we reduce the derivation to a single QD, however, the results can be easily generalized to a coupled QD ensemble. Again, we start from quantum mechanics and transfer the resulting scheme for the quantum jumps to the SCA afterward. As outlined in Sec. 5.2, we have to extend the Hilbert space of the electron spin by the trion state $|T\rangle$.

We assume that the trion state is unoccupied before a laser pulse. Hence, the electron spin system is in a Bloch state,

$$|\vec{s}\rangle = \sqrt{\frac{1}{2} + s_z} |\uparrow\rangle + e^{\mathrm{i}\varphi_{xy}} \sqrt{\frac{1}{2} - s_z} |\downarrow\rangle \ , \tag{5.28}$$

with the azimuth angle $\varphi_{xy} = \arctan(s_y, s_x)$. The σ^+ polarized laser pulse drives the transition between the $|\uparrow\rangle$ and the trion $|T\rangle$ state and is described by the unitary pulse operator

$$U_P = \begin{pmatrix} \sqrt{1-q^2} & 0 & * \\ 0 & e^{\mathrm{i}\varphi_2} & 0 \\ q e^{\mathrm{i}\varphi_1} & 0 & * \end{pmatrix} \tag{5.29}$$

with the pulse efficiency q, the relative phases φ_i, and two irrelevant matrix elements

marked by $*$. The state after the pulse is given by

$$\begin{aligned}|\psi_P\rangle &= U_P\,|\vec{s}\rangle \\ &= \sqrt{1-q^2}\sqrt{\frac{1}{2}+s_z}\,|\uparrow\rangle + e^{\mathrm{i}(\varphi_{xy}+\varphi_2)}\sqrt{\frac{1}{2}-s_z}\,|\downarrow\rangle + qe^{\mathrm{i}\varphi_1}\sqrt{\frac{1}{2}+s_z}\,|T\rangle \\ &= \sqrt{1-p_T}\,|\vec{s}_P\rangle + \sqrt{p_T}e^{\mathrm{i}\varphi_T}\,|T\rangle\ .\end{aligned} \tag{5.30}$$

In the last step, we identified the spin-coherent state after the pulse,

$$\vec{s}_P = \frac{1}{1-q^2(\frac{1}{2}+s_z)}\begin{pmatrix}\sqrt{1-q^2}\,(s_x\cos(\varphi_2)+s_y\sin(\varphi_2)) \\ \sqrt{1-q^2}\,(s_y\cos(\varphi_2)-s_x\sin(\varphi_2)) \\ s_z-\frac{1}{2}q^2(\frac{1}{2}+s_z)\end{pmatrix}\ , \tag{5.31}$$

as well as the trion occupation $p_T = q^2(1/2+s_z) \in [0,1]$ and the relative phase $\varphi_T = \varphi_1$ between the electron spin state and the trion state.

We continue with the characterization of the spin system after a laser pulse and include the nuclear spin states,

$$|\psi\rangle = \sqrt{1-p_T}\,|\vec{s}_P,\{\vec{i}_k\}\rangle + \sqrt{p_T}\exp(\mathrm{i}\varphi_T)\,|T,\{\vec{i}_k\}\rangle\,.$$

The trion decay is modeled by the jump operator $L_T = \sqrt{\gamma_T}\,|\uparrow\rangle\langle T|$, see Sec. 5.2. Equation (5.14) yields the modified Hamiltonian,

$$H_B = H + \frac{\mathrm{i}}{2}\gamma_T\,|T\rangle\langle T|\ . \tag{5.32}$$

Let us assume that H is time-independent and induces no coherent transitions between any electron spin state $|\vec{s}\rangle$ and the excited state $|T\rangle$, in particular, $\langle\vec{s}|\,H\,|T\rangle = 0$. Hence, the Hamiltonian H can be separated into the two parts, $H = H_s + H_T$ with $H_s\,|T\rangle = 0$ and $H_T\,|\vec{s}\rangle = 0$. Furthermore, $H_sH_T = H_TH_s = 0$ holds such that commutator $[H_s, H_T] = 0$ vanishes. For the Hamiltonian introduced in Eq. (3.15), we obtain the decomposition

$$\begin{aligned}H &= H_{\mathrm{HF}} + H_{\mathrm{SZ}} + H_{\mathrm{NZ}} + H_Q + \epsilon_T\,|T\rangle\langle T| \\ &= \underbrace{H_{\mathrm{HF}} + H_{\mathrm{SZ}} + \mathbb{E}_s(H_{\mathrm{NZ}} + H_Q)}_{H_s} + \underbrace{|T\rangle\langle T|\,(H_{\mathrm{NZ}} + H_Q) + \epsilon_T\,|T\rangle\langle T|}_{H_T}\end{aligned} \tag{5.33}$$

with $\mathbb{E}_s = |\uparrow\rangle\langle\uparrow| + |\downarrow\rangle\langle\downarrow|$. In the case of multiple coupled QDs, the inter-QD interaction is included in H_s as well. The Hamiltonian H_s governs the spin dynamics in the absence of a trion, and H_T captures the dynamics of the nuclear spins in the absence of an electron spin $\vec{S}$. The time-evolution operator of the Hamiltonian

$$H_B = H_s + H_T + \frac{\mathrm{i}}{2}\gamma_T\,|T\rangle\langle T| \tag{5.34}$$

is given by

$$\begin{aligned} U(t) &= \exp(-\mathrm{i}H_B t) \\ &= \exp(-\mathrm{i}H_s t)\exp(-\mathrm{i}H_T t)\exp\left(-\frac{\gamma_T t}{2}\left|T\right\rangle\left\langle T\right|\right) \\ &= \exp(-\mathrm{i}H_s t)\exp(-\mathrm{i}H_T t)\left(\mathbb{E}_s + \left|T\right\rangle\left\langle T\right|\exp\left(-\frac{\gamma_T t}{2}\right)\right) \ . \end{aligned} \tag{5.35}$$

Applied to the initial state $|\psi\rangle$, the time-evolution operator yields

$$\begin{aligned} |\psi(t)\rangle =& \sqrt{1-p_T}\exp(-\mathrm{i}H_s t)\left|\vec{s}_P, \{\vec{i}_k\}\right\rangle \\ &+ \sqrt{p_T}\exp(\mathrm{i}\varphi_T)\exp\left(-\frac{\gamma_T t}{2}\right)\exp(-\mathrm{i}H_T t)\left|T, \{\vec{i}_k\}\right\rangle \ . \end{aligned} \tag{5.36}$$

The time evolution is separated into two parts. The evolution in the absence of the trion is governed by the Hamiltonian H_s acting on all spins whereas the evolution in absence of a central spin is included in the Hamiltonian H_T acting on the nuclear spins only. If no quantum jump occurs, the latter contribution in Eq. (5.36) decays exponentially with rate γ_T and after a time $t \gg 1/\gamma_T$, we obtain

$$U(t)\left|\psi\right\rangle = \sqrt{1-p_T}\exp(-\mathrm{i}H_s t)\left|\vec{s}_P, \{\vec{i}_k\}\right\rangle \ , \tag{5.37}$$

which is not normalized. The normalized version of the above state reads $|\psi(t)'\rangle = \exp(-\mathrm{i}H_s t)\left|\vec{s}, \{\vec{i}_k\}\right\rangle$.

However, in every time step δt, there is the probability

$$\begin{aligned} \delta p &= \delta t \left\langle\psi(t)\right| L_T^\dagger L_T \left|\psi(t)\right\rangle \\ &= \delta t \gamma_T p_T \exp(-\gamma_T t) \end{aligned} \tag{5.38}$$

that a quantum jump occurs. Consequently, the total probability that a quantum jump occurs is given by the integral $\int_0^\infty \gamma_T p_T \exp(-\gamma_T t)dt = p_T$, and the probability for no quantum jump at all is $1 - p_T$. If a quantum jump occurs, the time τ follows an exponential distribution $p(\tau) = \gamma_T \exp(-\gamma_T \tau)$, and the state after the jump is given by

$$\begin{aligned} \left|\psi(\tau)\right\rangle_J &= \frac{L_T\left|\psi(t)\right\rangle}{\sqrt{\left\langle\psi(t)\right| L_T^\dagger L_T \left|\psi(t)\right\rangle}} \\ &= \exp(\mathrm{i}\varphi_T)\left|\uparrow\right\rangle\exp(-\mathrm{i}H_T t)\left|\{\vec{i}_k\}\right\rangle, \end{aligned} \tag{5.39}$$

where $\exp(\mathrm{i}\varphi_T)$ is a global phase that can be omitted. After the jump, the electron spin is aligned along the optical axis. The nuclear spins state is not modified by the jump operator.

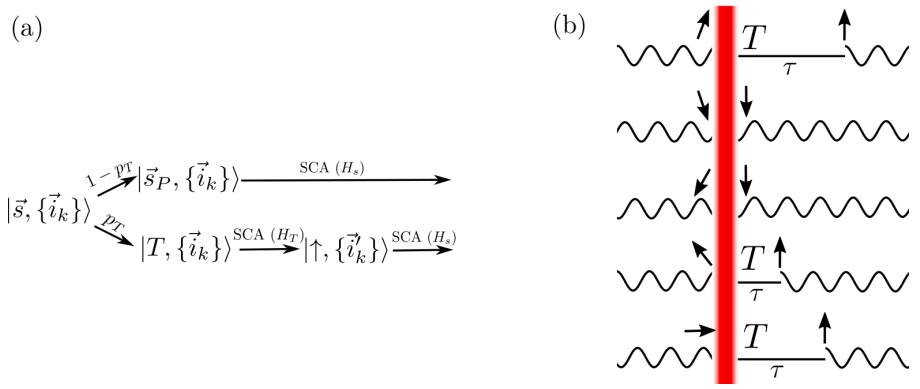

Figure 5.2: Schematics of the quantum jump algorithm for trion excitation and decay derived from the QTT and adapted to the SCA. (a) The dynamics after a laser pulse split into two branches: Either a quantum jump occurs or not. (b) Each semiclassical configuration evolves independently. While in some configurations the trion state is excited, other configurations remain unaffected by the laser pulse.

The previous considerations can be translated into the following algorithm for the QJ-SCA for the time evolution after we apply a laser pulse at the time $t = 0$:

1.) We start with a spin-coherent state $|\vec{s}, \{\vec{i}_k\}\rangle$ and predetermine whether a quantum jump will occur. With $1 - p_T$ there will be no quantum jump and we continue with branch 2.)(i). Otherwise, a quantum jump occurs, and we continue with branch 2.)(ii).

2.) (i) Since there is no quantum jump, we continue with the state $|\vec{s}_P, \{\vec{i}_k\}\rangle$ defined in Eq. (5.31) and evaluate the time evolution using the semiclassical EOM.

(ii) There will be a quantum jump. Hence, we continue with the state $|T, \{\vec{i}_k\}\rangle$.

1.) We predetermine the time τ of the quantum jump from the distribution $p(\tau) = \gamma_T \exp(-\gamma_T \tau)$ and perform a time evolution up to the time τ using the semiclassical EOM with $\vec{s} = \vec{0}$.

2.) The quantum jump occurs at the time τ. We set $\vec{s} = \frac{1}{2}\vec{e}_z$ and evaluate the further time evolution using the semiclassical EOM.

This algorithm is visualized in the two panels of Fig. 5.2. In Fig. 5.2(a), the two possible branches are shown schematically. In Fig. 5.2(b), various semiclassical configurations are depicted. All configurations choose their respective branch independently.

Let us now discuss some of the properties of the quantum jump algorithm. Compared to quantum mechanics, the only approximation made is the semiclassical treatment of the spin dynamics between the quantum jumps. Once the trion has decayed in all configurations, the direct mapping to spin-coherent product states is established, and the SCA for closed systems is restored. The additional numerical effort due to the laser pulse is negligible compared to the effort needed to solve the EOM (4.31) as only one or two random numbers have to be drawn per laser pulse.

5.6 Comparison of the approaches

Finally, the two approaches to treat open quantum systems in SCA, namely the MEOM approach and the QJ-SCA, are compared. We use the box-model approximation $A_k^{(i)} = A_0$ with $N_I = 100$ nuclear spins with $I = 3/2$ and neglect nuclear quadrupolar interactions. Depending on the scenario, we employ $N_{\mathrm{QD}} = 1$ or $N_{\mathrm{QD}} = 2$ QDs. For $N_{\mathrm{QD}} = 2$, we draw $J = J_{12}$ from an exponential distribution with the mean value $\overline{J} = 1/T^*$. In Fig. 5.3, two scenarios are presented in which spin fluctuations are irrelevant for the dynamics such that both approaches produce the same results. In 5.3(a), the dynamics of the z component of a single QD in absence of an external magnetic field is shown. The electron spin dynamics are governed by the hyperfine interaction with characteristic time scale T^* and the spin-lattice relaxation with the rate $\gamma = 0.001/T^*$. At time $t = 0$, the electron spin is initialized in z direction. On the time scale T^*, the spin z component relaxes to one third of the initial value due to the Overhauser field fluctuations, see Sec. 4.7. The spin-lattice coupling generates an additional exponential relaxation on the time scale $1/\gamma$. While the expectation value $\langle S_z^{(1)} \rangle$ matches for both approaches, the spin fluctuations $(\langle (\vec{S}^{(1)})^2 \rangle)^{1/2}$ differ. The spin fluctuations constantly produce the value 1/2 for the QJ-SCA but reduce exponentially to zero in the MEOM. In Fig. 5.3(b), the central spin dynamics of two interacting QDs are presented. We neglect the spin-lattice relaxation $\gamma = 0$ but include an external magnetic field of $\vec{b}_{\mathrm{ext}} = 50(T^*)^{-1}\vec{e}_x$. QD 1 is optically excited with a resonant π pulse at $t = 0$. The pulse polarizes the electron spin z component in QD 1 to approximately 1/2 of its maximum value and dephases on the time scale T^* with a Gaussian envelope. Due to the inter-QD interaction, QD 2 is driven by the electron spin of QD 1. Again, the electron spin dynamics are correctly described by both approaches, and the only difference lies in the spin length of QD 1. In the MEOM, the electron spin length remains roughly a quarter, whereas the QJ-SCA restores the spin length 1/2. The reduced spin length leads to an underestimation of the electron spin fluctuations. These fluctuations, however, are not relevant to the dynamics in the two precast scenarios.

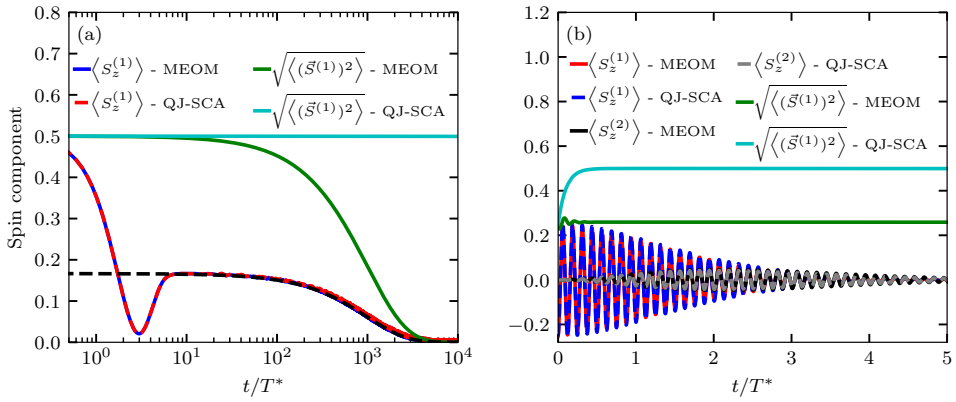

Figure 5.3: Comparison of the MEOM approach and QJ-SCA for two exemplary scenarios. (a) Electron spin relaxation in a single QD. The spin z component relaxes in a two-stage process with the time scales T^* and $1/\gamma$. The dashed black curve displays the exponential function $\exp(-\gamma t)/6$. (b) Optical excitation in a QD pair. QD 1 is excited at the time $t = 0$ and drives the second QD via the inter-QD interaction.

To illustrate the differences between the two approaches, we focus on two scenarios for which the fluctuations of the electron spin become relevant. In the first scenario, we study the equilibration of the Overhauser field of a single QD in the absence of an external magnetic field. For this purpose, we assume that the Overhauser field is initialized in a non-equilibrium state (e.g. induced by an optical pulse train). The Overhauser field distribution is initialized at time $t = 0$ to a Dirac comb,

$$p(b_{N,x}) = \alpha \sum_{n=-\infty}^{\infty} \delta\left(b_{N,x} - \frac{n}{2}\right) \exp\left(\frac{(b_{N,x}T^*)^2}{2}\right) , \tag{5.40}$$

with the Dirac delta $\delta(x)$ and the normalization constant α, see Fig. 5.4(a). The nuclear spins interact with the Knight field which thermally relaxes via spin-lattice relaxation with the rate $\gamma = 0.001/T^*$ to its high-temperature equilibrium. Figure 5.4(b) depicts the Overhauser field distribution for the MEOM and QJ-SCA approach after $t = 10^2 T^* < 1/\gamma$. On this time scale, the spin-lattice relaxation is not relevant, yet. The distribution of the Overhauser field is broadened by roughly $A_0 \propto 1/\sqrt{N_I}$ since the angular momentum of the electron spin transfers to the nuclear spins. For larger times $t = 10^4 T^* > 1/\gamma$, see Fig. 5.4(c), the spin-lattice relaxation becomes relevant. In the QJ-SCA, the Overhauser field equilibrates to the thermal equilibrium state indirectly via the hyperfine interaction and almost approaches a Gaussian distribution as expected in the high-temperature limit. In the MEOM, in contrast, the Knight field vanishes, induced by the reduction of the

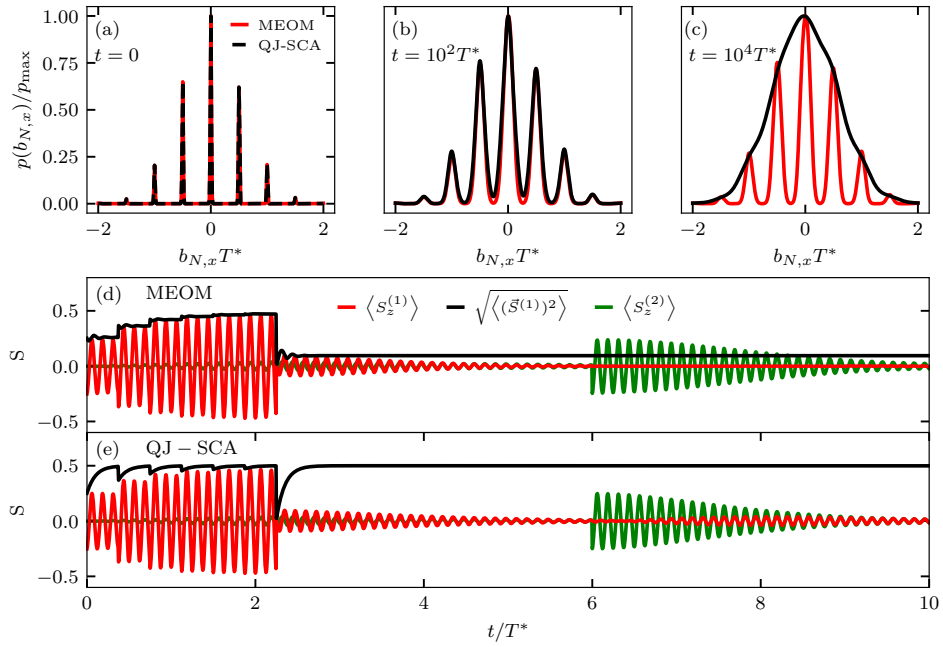

Figure 5.4: Comparison of the MEOM approach and the QJ-SCA for two scenarios in which electron spin fluctuations are relevant. (a)-(c) Equilibration of a non-equilibrium Overhauser field distribution at (a) time $t = 0$, (b) time $t = 10^2 T^*$, and (c) time $t = 10^4 T^*$. Panels (a)-(c) share the same legend. (d)-(e) Pulse protocol on two interacting QDs with six σ^+ polarized pulses on QD 1 at $t = n\Delta\tau$ with $\Delta\tau = 0.375 T^*$ and $n \in [0, 5]$, a σ^- polarized pulse on QD 1 at $t = 6\Delta\tau$ and a σ^+ polarized pulse on QD 2 at $t = 6T^*$ for (d) the MEOM approach and (e) the QJ-SCA. Panel (d) and (e) share the same legend.

electron spin length to 0. As the Knight field is the only field acting on the nuclear spins, the Overhauser field distribution remains unchanged even for large times $t = 10^4 T^*$, which is an artifact of the MEOM approach. We note that, due to the absence of the external magnetic field, the relaxation happens rather fast compared to experiments [47] where the Overhauser field distribution remains stable on the time scale of seconds to hours. By applying an external magnetic field, spin-flips are suppressed, and the equilibration time of the Overhauser field extends.

However, not only spin-lattice relaxation but also tailored pulse sequences can erase the Knight field, which we illustrate in Figs. 5.4(d)-(e). We neglect the spin-relaxation and address two QDs subject to a pulse sequence in the external magnetic field $\vec{b}_{\text{ext}} = 50(T^*)^{-1}\vec{e}_x$. We utilize the same pulse sequence in Fig. 5.4(d) for the MEOM approach and in Fig. 5.4(e) for the QJ-SCA. The pulse sequence starts with

six resonant σ^+ polarized π pulses at the times $t_n = n\Delta\tau$ acting on QD 1. We set $\Delta\tau = 0.375T^*$ and $n \in [0, 5]$. The temporal distance of the pulses is chosen in such a way that the pulse incidence corresponds to a minimum of $\langle S_z^{(1)} \rangle$. This increases the spin electron polarization of QD 1 after six pulses to almost $-1/2$. An additional σ^- polarized pulse is applied at $t = 6\Delta\tau$, which drives the transition $|\downarrow\rangle \rightarrow |T\rangle$, and the trion state is almost completely populated $p_T \approx 1$ (not displayed). As a consequence, the electron spin length in the MEOM is reduced almost to zero, while in the QJ-SCA the electron spin length is restored after the trion decay. Finally, at time $t = 6T^*$, QD 2 is excited, which can drive QD 1 via the inter-QD interaction. While the driven electron spin of QD 1 is clearly visible as a red curve in the time interval $t \in [6T^*, 10T^*]$ in the results of the QJ-SCA, QD 1 cannot respond due to the reduced spin length in the MEOM.

In conclusion, both approaches provide a description for the open quantum system in the SCA. The MEOM approach is simpler in its derivation but has the disadvantage of underestimating spin fluctuations. The QJ-SCA, on the other hand, offers the possibility to correctly represent spin fluctuations with the same computational effort. If spin fluctuation can be neglected, both approaches yield comparable results. In this thesis, the MEOM approach is used in Chapter 6 and 7. The QJ-SCA is applied in Chapter 9.

Chapter 6

Two-color pump-probe experiments

Ultrashort laser pulses on the time scale of picoseconds enable the coherent manipulation and control of the charge carrier spins in QDs. To study the interaction between different QDs, optical two-color experiments are particularly helpful. If the electron spin dynamics in a QD subensemble change when another disjoint subensemble is manipulated, a direct or indirect interaction between the QDs can be inferred. In this chapter, we focus on two-color pump-probe experiments [57, 58, 191] to propose a model of the inter-QD interaction based on the data available in the literature. The pulse protocols employed in pump-probe experiments as well as the central experimental results are discussed in Sec. 6.1. Depending on the constellation of the two pump pulses, phase shifts and dephasing times can be controlled. These experimental findings are consistent with an effective Heisenberg interaction between the resident electron spins in the different QDs. In Sec. 6.2, we introduce a toy model of two spins to qualitatively explain the basic mechanism of the inter-QD interaction. A quantitative analysis for a QD ensemble is presented in Sec. 6.3, where we compare the numerical simulation with the experimental data. We demonstrate an excellent agreement between experiment and theory when a wetting-layer mediated RKKY interaction is assumed. Parts of these results have been published in Ref. [59]. In Sec. 6.4, we discuss the influence of the electron g-factor variation on the ensemble spin dynamics. Moreover, in Sec. 6.5, we analyze the role of the electron spin component along the external magnetic field direction perpendicular to the optical axis.

6.1 Experimental results

We consider a pump-probe setup with two different laser frequencies. Depending on the laser frequency, different QDs in the ensemble are resonantly excited or read out. The QDs excited by a specific laser frequency form a subensemble of the total QD ensemble. In the experiment by Spatzek et al. [57], up to two subensembles are excited by the pump pulses. The spin dynamics of one of these subensemble are

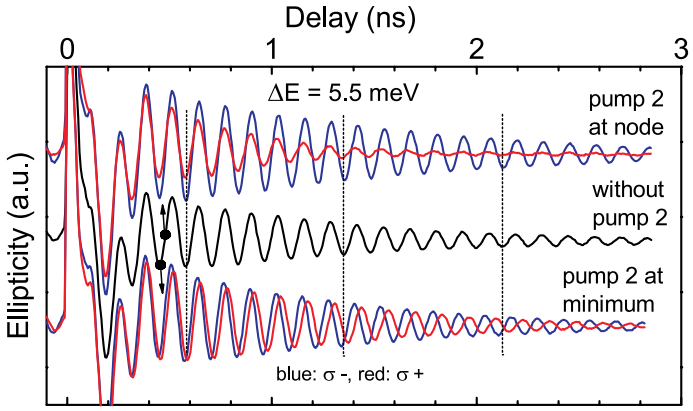

Figure 6.1: Time-dependent spin electron polarization of subensemble 1 for different pump configurations. For the reference curve (black), only subensemble 1 is excited. If the incidence time of pump pulse 2 is at a node of the reference curve (top), the dephasing time becomes shorter for σ^+ polarization of pump pulse 2 (red) and longer for σ^- polarization (blue). If the incidence time of pump pulse 2 is at a minimum of the reference curve (bottom), a positive phase shift relative to the reference curve is observed for σ^+ polarization of pump pulse 2 (red), and a negative phase shift is observed for σ^- polarization (blue). The incidence time of pump pulse 2 is indicated by the black dots. The figure is taken from Ref. [57].

read out by the probe pulse. Excitation and readout are repeated periodically with a repetition time $T_R = 13.2$ ns, and the measurements are averaged afterward.

In Fig. 6.1, the ellipticity signal, which is proportional to the electron spin polarization, is depicted as a function of time. Traces for different delays between the two pump pulses are displayed. The first pump pulse has σ^+ polarization and defines the time $t = 0$. Since the probe pulse has the same excitation energy, the time-dependent spin polarization of the subensemble excited by the first pump is depicted. The second pump pulse has either σ^+ or σ^- polarization or is turned off for a reference curve. In the reference curve (black curve), the electron spin precession of subensemble 1 in the external magnetic field is observed. The precession frequency is slightly different in the individual QDs due to g-factor variations and Overhauser field fluctuations. Therefore, the signal dephases yielding a decreasing envelope of the oscillations.

The red and blue curves show the situation when the second pump pulse is switched on. The second pump pulse is either σ^+ (red curves) or σ^- (blue curves) polarized and arrives either at a node (upper curves) or a minimum (lower curves) of the reference curve. Depending on the polarization and the incidence time, four different relative alignments of the electron spin polarization of the two subensembles are

realized. The different spin alignments produce a modification of the time-dependent spin polarization in subensemble 1. In comparison to the reference curve, either the dephasing time is shortened or extended (upper curves), or a positive or negative phase shift relative to the reference curve occurs (lower curves). We note that, without inter-QD interactions, all curves would match the reference curve since both subensembles would evolve independently. The overall behavior can be explained by a Heisenberg interaction between the electron spins of the different QDs. We address the dynamics in the coupled QDs by a simple toy model in the following section.

6.2 Two-spin model

To understand the phase shifts and the changing dephasing times, we focus on a minimal model. We represent each subensemble by a single electron spin and omit the nuclear spin baths. In addition, we employ the same electron g factor for both spins and model the spin alignment generated by the pump pulses by a proper choice of the starting condition.

We start with the Hamiltonian

$$H = J\vec{S}^{(1)}\vec{S}^{(2)} + \vec{b}\sum_i \vec{S}^{(i)} \,, \tag{6.1}$$

with the coupling strength J and external magnetic field $\vec{b}$. The semiclassical EOMs for the two spins $i \in \{1, 2\}$ read

$$\partial_t \vec{s}^{(i)} = \vec{b} \times \vec{s}^{(i)} + J\vec{s}^{(l)} \times \vec{s}^{(i)} \qquad (i \neq l) \,. \tag{6.2}$$

We make use of the equal g factors and transform into the rotating frame with the new coordinate system $\tilde{\vec{s}}^{(i)} = R\vec{s}^{(i)}$ and the rotation matrix $R = \exp([\,\vec{b}\,]_\times t)$ with the cross-product matrix $[\,\vec{b}\,]_\times$. The transformation yields the simplified EOM

$$\partial_t \tilde{\vec{s}}^{(i)} = J\tilde{\vec{s}}^{(l)} \times \tilde{\vec{s}}^{(i)} \qquad (i \neq l) \,. \tag{6.3}$$

Even though this system of ordinary differential equations is non-linear, it can be solved analytically due to its simple structure. We use the ansatz

$$\tilde{\vec{s}}^{(1,2)} = \vec{v}_1 \pm \vec{v}_2 \cos(\omega t) \pm \vec{v}_3 \sin(\omega t) \tag{6.4}$$

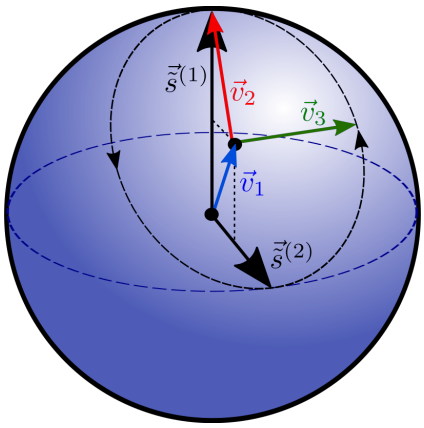

Figure 6.2: Dynamics of the electron spins $\vec{\tilde{s}}^{(1)}$ and $\vec{\tilde{s}}^{(2)}$ in the rotating coordinate system. The support vector $\vec{v}_1$ points to the center of the rotation. The support vectors $\vec{v}_2$ and $\vec{v}_3$ span the rotation trajectory.

with the support vectors

$$\vec{v}_1 = \frac{1}{2}\left(\vec{s}_0^{(1)} + \vec{s}_0^{(2)}\right) , \tag{6.5a}$$

$$\vec{v}_2 = \frac{1}{2}\left(\vec{s}_0^{(1)} - \vec{s}_0^{(2)}\right) , \tag{6.5b}$$

$$\vec{v}_3 = |\vec{v}_2|\left(\frac{\vec{v}_1}{|\vec{v}_1|} \times \frac{\vec{v}_2}{|\vec{v}_2|}\right) , \tag{6.5c}$$

and the non-linear angular frequency

$$\omega = 2Js\cos\left(\frac{\varphi}{2}\right) . \tag{6.6}$$

The frequency depends on the spin length $s = \left|\vec{\tilde{s}}^{(1)}\right| = \left|\vec{\tilde{s}}^{(2)}\right| = 1/2$ and the angle $\varphi = \measuredangle\left(\vec{\tilde{s}}^{(1)}, \vec{\tilde{s}}^{(2)}\right)$. As depicted in Fig. 6.2, the two spins rotate around each other on a common circular orbit. The rotation frequency becomes faster for smaller angles between the spins. The differential equations have two fixed points: If the spins are parallel, the circle degenerates to a single point, and if the spins are antiparallel, the angular frequency has the value $\omega = 0$.

In the stationary coordinate system, the motion of the spins is composed of two parts. The spins rotate around each other with the frequency ω and precess together about the external magnetic field axis with the frequency b. Employing the analytical solution, the four start configurations, that are generated with two pump lasers, can be analyzed for phase shifts and dephasing times. For this purpose, the first electron

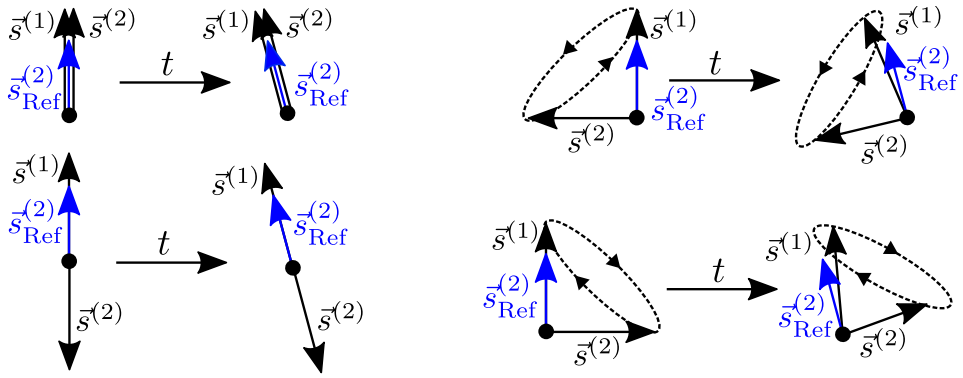

Figure 6.3: Schematic representation of the time evolution in the two-spin model ($\vec{s}^{(1)}$ and $\vec{s}^{(2)}$) compared to a single spin ($\vec{s}_{\mathrm{Ref}}$). The external magnetic field is perpendicular to the image plane. With an (anti-)parallel orientation, the time evolution of $\vec{s}^{(1)}$ and $\vec{s}_{\mathrm{Ref}}$ is identical. In the case of a perpendicular alignment of $\vec{s}^{(1)}$ and $\vec{s}^{(2)}$, however, there is a phase shift between $\vec{s}^{(1)}$ and $\vec{s}_{\mathrm{Ref}}$, which has a different sign depending on the constellation. In addition, $\vec{s}^{(1)}$ rotates out of the plane. By changing $J \to -J$, the phase shift remains unchanged, but the spin component in the magnetic field direction changes its sign.

is initially aligned in z-direction, $\vec{s}_0^{(1)} = \frac{1}{2}\vec{e}_z$, and the second electron spin $\vec{s}_0^{(2)}$ is either aligned collinear $\pm\frac{1}{2}\vec{e}_z$ or perpendicular $\pm\frac{1}{2}\vec{e}_y$ while the external magnetic field is aligned in x-direction.

In Fig. 6.3, the resulting time evolution is shown schematically. A single spin $\vec{s}_{\mathrm{Ref}}$, coupled only to the external magnetic field, serves as a reference value. Since the parallel and the antiparallel constellations represent a fixed point in the rotating coordinate system, the trajectories of $\vec{s}^{(1)}$ are identical to the reference $\vec{s}_{\mathrm{Ref}}$. Thus, no phase shift can be observed between $\vec{s}^{(1)}$ and $\vec{s}_{\mathrm{Ref}}$.

In contrast, for perpendicular starting conditions, the dynamics are more diverse. In this case, $\vec{s}^{(1)}$ and $\vec{s}^{(2)}$ rotate around each other in the rotating coordinate system, whereas $\vec{s}_{\mathrm{Ref}}$ is fixed in the rotating coordinate system. This leads to a phase shift between $\vec{s}^{(1)}$ and $\vec{s}_{\mathrm{Ref}}$. Thus, the phase shifts in the semiclassical picture can be attributed to the rotation of the spins around each other. We note that the direction of the phase shift does not depend on the sign of the coupling constant J. Employing the analytical solution of the EOMs, we evaluate the phase shift,

$$\phi(t) = \pm \arccos\left(\frac{1+\cos(\frac{J}{\sqrt{2}}t)}{\sqrt{2+2\cos^2(\frac{J}{\sqrt{2}}t)}}\right) = \frac{J^2t^2}{8} + O((Jt)^4)\,, \tag{6.7}$$

which is quadratic in J for short time scales [59].

In the simplified model, no dephasing occurs due to omitting the nuclear spins. Nevertheless, some statements about the dephasing behavior can be derived from the model. For this purpose, the two fixed points $\vec{s}^{(1)} = \vec{s}^{(2)}$ and $\vec{s}^{(1)} = -\vec{s}^{(2)}$ can be examined for their stability against small perturbations $\delta\vec{s}^{(1)}$ and $\delta\vec{s}^{(2)}$. The perturbations can occur, for example, due to the different Overhauser fields acting on the two electron spins. A linear stability analysis shows that the parallel case $\vec{s}^{(1)} = \vec{s}^{(2)}$ is marginally stable while the antiparallel case $\vec{s}^{(1)} = -\vec{s}^{(2)}$ is unstable. In the case of a nearly parallel alignment, both spins rotate around each other on a narrow trajectory, so the orbit hardly changes compared to the unperturbed case. Since the orbits hardly differ, no dephasing induced by the coupling J occurs. In the case of a nearly antiparallel alignment, the spins precess around each other approximately on an orthodrome of the Bloch sphere. Even a small change in the perturbation results in a significant modification of the orbit so that the coupling J produces a particularly strong dephasing in this case. The related dephasing time is independent of the sign of J.

Overall, the phase shifts and the changes in the dephasing time can be interpreted in a simple picture. If the spins are arranged perpendicularly, they rotate around each other, which manifests itself in the (oscillating) spin z component by a phase shift. If the spins are arranged parallel/antiparallel, they are on a stable/unstable trajectory. Hence, the dephasing time becomes longer/shorter.

6.3 Phase shift and distribution of the RKKY coupling constants

As a next step, the spin dynamics of the QD ensemble will be studied numerically. For this purpose, we assume that the ensemble consists of two subensembles, where subensemble A is excited by pump pulse 1 and subensemble B is excited by pump pulse 2. Based on the experiment [57], we assume that a ratio of the g factors of $g_e^{(B)}/g_e^{(A)} = 1.03$ holds. The external magnetic field is set to $\vec{b}_{\text{ext}} = 50(T^*)^{-1}\vec{e}_x$ which roughly corresponds to $B_{\text{ext}} = 1\,\text{T}$.

Apart from the g factors, we assume that all $N_{\text{QD}} = 10^4$ QDs are of the same type, where each QD contains $N_I = 10^4$ nuclear spins of length $I = 3/2$. Since the dynamics of the nuclear spins is negligible on the considered time scale, we omit the nuclear quadrupolar interactions and set all hyperfine coupling constants to the same value $A_k^{(i)} = A_0$. This constant is determined by the definition of the characteristic time scale $T^* = 1\,\text{ns}$. For the inter-QD interaction, we use the microscopic model based on a wetting layer mediated RKKY interaction described in Sec. 3.5. To generate the coupling constants J_{ij}, we draw the locations $\vec{R}_i$ of the QDs on a square

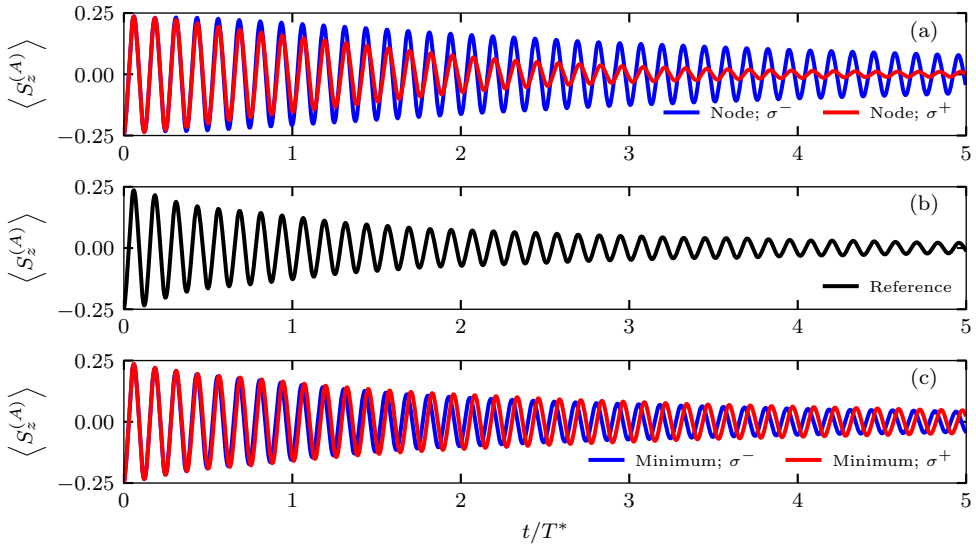

Figure 6.4: Reproduction of the experimental measurement results from Fig. 6.1. We simulate the dynamics of an ensemble with $N_{\mathrm{QD}} = 10^4$ QDs. For the reference curve in panel (b), only pump pulse 1 acts at the time $t = 0$. In panel (a), additionally, pump pulse 2 is applied at a minimum of the reference curve ($t = 1.11T^*$). Depending on the polarization of pump pulse 2, this leads to the extension (σ^+ polarization) or shortening (σ^- polarization) of the dephasing time. In panel (c), pump pulse 2 is applied at a node of the reference curve ($t = 1.15T^*$). This produces a positive (σ^+ polarization) or negative (σ^- polarization) phase shift relative to the reference curve.

as outlined in Sec. 4.6 and thereafter calculate the distance-dependent coupling constants $J_{ij} = J(|\vec{R}_i - \vec{R}_j|)$. For the distance dependency of the inter-QD coupling constants, we employ the NRG results illustrated in Fig. 3.5 and perform a linear interpolation between the data points extracted from the NRG.

In Fig. 6.4, the numerical results for the electron spin dynamics in two coupled QDs with the previously introduce parameter set are depicted. To allow a direct comparison with the experimental measurements in Fig. 6.1, the same choice of the colors and the arrangement of the curves is used. For the comparison with the experimental results, we define the observable for the averaged electron spin polarization of subensemble A,

$$\vec{S}^{(A)} = \frac{2}{N_{\mathrm{QD}}} \sum_{i \in A} \vec{S}^{(i)} \,, \tag{6.8}$$

which is proportional to the measured ellipticity. The expactation value of $\vec{S}^{(A)}$

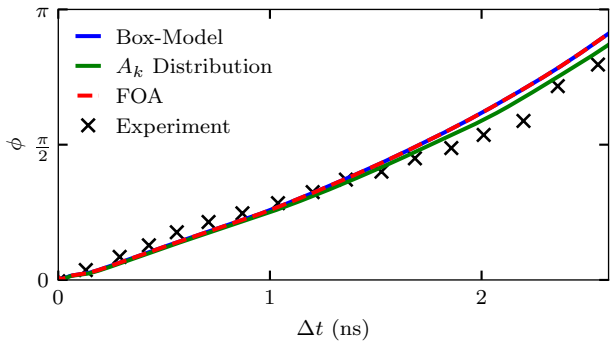

Figure 6.5: Phase shift ϕ between the reference curve and the curve for the incidence of pump pulse 2 at minimum (σ^+ polarized). We perform simulations for $A_k^{(i)} = A_0$ (box-model limit), a distribution of the coupling constants $A_k^{(i)}$, and a frozen Overhauser field approximation (FOA) respectively. The experimental data are taken from Ref. [57], and the numerical data are taken from Ref. [59]. ´

is evaluated according to Eq. (4.45) in the semiclassical MEOM. In Fig. 6.4(b), a reference curve is depicted in black. For the reference curve, we apply a π pulse with σ^+ polarization at $t = 0$. This pulse excites subensemble A, while subensemble B remains unaffected. A coherent oscillation in the external magnetic field with a dephasing on the time scale T^* can be observed. In Fig. 6.4(a), a second pump pulse is employed that resonantly excites subensemble B and has its incidence time at a node of the reference curve. The second pump pulse initially leads to a perpendicular alignment of the electron spins of the two subensembles. Depending on the polarization of pump pulse 2, it causes an extension or shortening of the dephasing time. However, the two-spin model in Sec. 6.2 predicts a phase shift for perpendicular alignment. The differing electron g factors as well as an additional phase shift induced by the trion decay generates a relative phase of $\frac{\pi}{2}$ between both subensembles which resolves this discrepancy. The effect of the varying electron g factor is studied in Sec. 6.4 in more detail. In Fig. 6.4(c), pump pulse 2 has its incidence time at a minimum of the reference curve, which produces a phase shift relative to the reference curve. The sign of the phase shift can be controlled by the polarization of pump pulse 2.

To investigate the situation more quantitatively, we examine the time dependency of the phase shift. In Fig. 6.5, the phase shift is shown for the excitation with the σ^+ polarized pump pulse 2 at a minimum of the reference curve. The x markers depict the experimental measurements. Interestingly, the phase shift grows almost linearly in time, although the two-spin model with a fixed coupling constant J predicts a quadratic increase, see Eq. (6.7). This mismatch is resolved by the fact that in a QD

ensemble a variation of the coupling constants occurs. While the slope of the phase shift provides information about the overall magnitude, the shape of the phase shift as a function of time is sensitive to the distribution of the coupling constants and thus provides a good benchmark for the agreement of a microscopic model with the experimental results.

The blue curve in Fig. 6.5 presents the phase shift $\phi(t)$ for the simulation from Fig. 6.4(c) and complies with an approximately linear behavior as observed in the experiment. While the shape of $\phi(t)$ is determined by the distribution of the inter-QD coupling constant, the hybridization $\Gamma_0 = 140\,\mu\text{eV}$ (see Sec. 3.5) has been adjusted to match the slope of the experiment. To demonstrate that the box model does not affect the dynamics, two additional simulations are displayed as green and red curves, for which a distribution of the hyperfine couplings $A_k^{(i)}$ was employed. In both cases, we use an exponential distribution and fix the mean value via the condition $T^* = 1\,\text{ns}$. To compensate for the considerably increased computational effort, we reduce the system size to $N_{\text{QD}} = N_I = 10^3$ for the green curve. In contrast, for the red curve, we keep the system size fixed at $N_{\text{QD}} = N_I = 10^4$, but freeze the dynamics of the nuclear spins. Both scenarios provide the same result as the box-model approximation. This illustrates that the nuclear spin dynamics can be neglected on the given time scale.

The sign of the phase shift can be reversed either by switching the polarization (σ^+ or σ^-) or by changing the incidence time (minimum or maximum) of pump pulse 2. However, switching the sign of all coupling constants, $J_{ij} \to -J_{ij}$, does not change the phase shift (not shown here). This becomes clear when considering the mechanism outlined in Sec. 6.2. To understand which information about the coupling constants J_{ij} can be obtained from the time-dependent phase shift, we focus on the effective field $\vec{b}_J^{(i)}$ generated by the inter-QD interaction, see Eq. (4.36). Since the electron spins are synchronized in the respective subensembles by the pump pulses, we employ the effective interaction strength,

$$J_i = \sum_{j \in B} J_{ij} \ , \tag{6.9}$$

introduced in Sec. 4.6. In Fig. 6.6(a), the distribution $p(J_i)$ for the coupling constants J_i calculated from the wetting layer induced RKKY interaction is shown. The effective interaction is predominantly ferromagnetic ($J_i < 0$) due to neighboring QDs with small distances, see Fig. 3.5. However, there is also a relevant probability for an antiferromagnetic interaction ($J_i > 0$). Since the sign of J_i does not enter the phase shift ϕ, we add distribution $p(|J_i|)$ as a red curve in Fig. 6.6(a). The distribution $p(|J_i|)$ is well approximated by an exponential distribution.

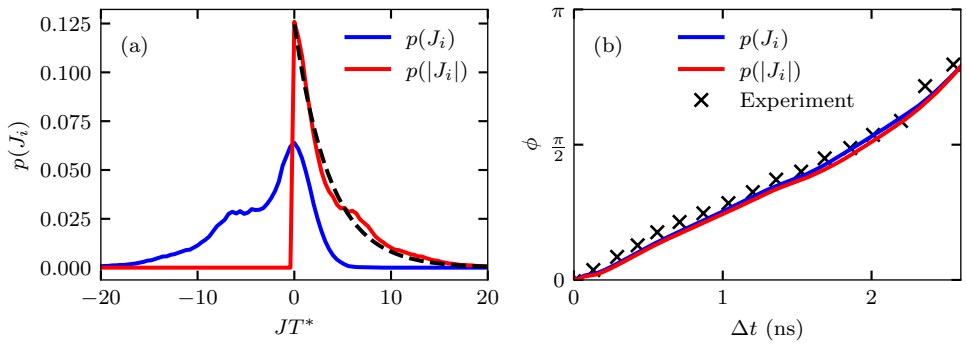

Figure 6.6: Results for the reduced two-QD model. (a) Distribution of the reduced coupling strength, $p(J_i)$, and its absolute value ,$p(|J_i|)$. The dashed line is an exponential distribution and serves as a guide to the eye. (b) Simulation of the reduced two-QD model, in which the coupling constant J follows the distribution $p(J_i)$ or $p(|J_i|)$. The experimental data (x markers) are taken from Ref. [57].

To demonstrate that the effective coupling constants J_i are relevant for the overall electron spin dynamics, we resort to the reduced model with only two QDs, see Sec. 4.6. Such a two-QD model includes only one coupling constant, $J = J_{12}$. This coupling constant is drawn randomly for each classical configuration from the distribution $p(J_i)$ or $p(|J_i|)$, respectively. The phase shifts resulting in the reduced model are shown in Fig. 6.6(b) as red and blue curves. There is an excellent agreement with the experiment as well as the elaborate numerical ensemble calculation. From this observation, we conclude that the dynamics predominantly depend on the distribution of the effective couplings J_i rather than on the details of the real couplings J_{ij}. Therefore, a reduced two-QD model with a significantly reduced numerical effort can be used as a replacement for a full ensemble calculation.

6.4 Variation of the electron g factor

Since the excitation energy is correlated with the electron g factor in the QDs, the subensembles in two-color pump-probe experiments have different mean electron g factors. The differing precession frequencies of the subensembles modify the relative alignment of the electron spins over time. By tuning the pump energy, the g factor of the subensemble can be adjusted due to the linear relation between excitation energy and mean g factor.

We investigate the influence of the electron g factors based on the experimental

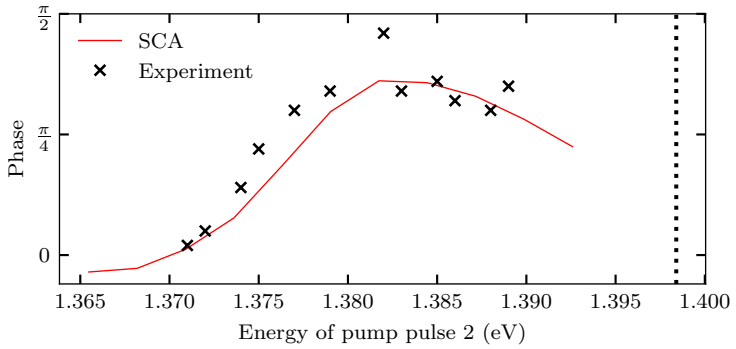

Figure 6.7: Influence of the energy of pump pulse 2 on the spin dynamics. Pump pulse 1 is set to the fixed energy 1.3984 eV (vertical dotted line) while the energy of pump pulse 2 is varied. Pump pump 2 with σ^+ polarization is applied at a minimum of the reference curve, and the phase shift ϕ is evaluated after 3 ns. For the simulation (red curve), we choose the system size $N_{\mathrm{QD}} = 2$ and $N_I = 100$. The electron g factors are determined by the pump energies using Eq. (6.10). The inter-QD couplings J are drawn from an exponential distribution with mean value $\overline{J} = 1/T^*$, and the box-model limit is employed for the hyperfine couplings $A_k^{(i)}$. The experimental data (x markers) are taken from Ref. [191].

data from Ref. [191]. In the experiment, the photon energy of pump pulse 1 is fixed at 1.3984 eV and the energy of pump pulse 2 is varied. For each pump energy, the phase shift relative to the reference curve is measured after 3 ns. We reproduce this result in our simulation by determining the g factor from the energy relation

$$g^{(i)} = \frac{g_2 - g_1}{\epsilon_2 - \epsilon_1}(\epsilon^{(i)} - \epsilon_1) + g_1 \ , \tag{6.10}$$

using the two points $(g_1, \epsilon_1) = (0.545, 1.38\,\mathrm{eV})$ and $(g_2, \epsilon_2) = (0.56, 1.395\,\mathrm{eV})$ extracted from Ref. [191]. The results of the numerical simulation as well as the experimental data are depicted in Fig. 6.7. For the simulation, we employ a reduced two-QD model and draw J from an exponential distribution with mean value $\overline{J} = 1/T^*$. Since the nuclear spin dynamics are irrelevant, we model each QD with $N_I = 100$ nuclear spins in the box-model approximation with length $I = 3/2$. Pump pulse 2 acts at a minimum of the reference curve, which initially produces a parallel alignment of the two electron spins. Thus, for equal g factors, no phase shift ϕ would occur. For differing g factors of the two subensembles, a phase shift ϕ relative to the reference curve may arise. The phase shift has the maximum at a pump energy of about 1.383 eV, which corresponds to the choice in Ref. [57]. For larger g factor differences, the phase shift decreases again. At 1.37 eV, for example, the electron spin in both subensembles are initially aligned in parallel. Averaged over

time, they behave as if they were antiparallel due to the different g factors. Thus, no phase shift is expected, which agrees with both, the experiment and the numerical calculation.

6.5 Spin tomography

An extension of the two-color pump-probe experiment was performed by Varwig et al. [58]. In addition to the π pump pulses with a pulse area of π, a detuned pulse with a pulse area of 2π was applied. The third pulse does not excite a trion due to its pulse area. However, when it is detuned with respect to pump pulses 1 and 2, a relative phase in the superposition of the electron spin states $|\uparrow\rangle$ and $|\downarrow\rangle$ is generated. This relative phase produces a rotation around the optical axis [51, 52] and, therefore, the third pulse is called rotational pulse (RP). The RP is slightly detuned to the excitation energy of subensemble A and strongly detuned to subensemble B. While the detuning of the RP to subensemble B is so large that the effect of the RP on this subensemble is negligible, the RP pulse leads to a rotation of the electron spins in subensemble A. This rotation is realized for the pulse parameter $a = 1$ and $\varphi \neq 0$, see Sec. 5.2. The parameter φ is determined by the degree of detuning and is tuned to $\pi/2$ in Ref. [58]. This choice rotates the spin x component along the magnetic field axis into the (yz) plane and enables the measurement of the spin component along the magnetic field axis.

In Fig. 6.8, the experimental data are shown as x markers. Due to the induced perpendicular spin alignment in combination with the inter-QD interaction, the subensembles rotate around each other out of the (yz) plane, see Fig. 6.6, and acquire a spin component along the x direction. The component increases on the time scale of the first 2 ns after pump pulse 2 and afterward remains almost constant at a plateau. We note that the experimental data are displayed with arbitrary units, so amplitude and sign are not specified. The blue curve in Fig. 6.8 depicts the results of the numerical simulation of a two-QD model, using an exponential distribution $p(J)$ with the same parameters as in 6.4. Similar to the experimental data, the spin x component initially increases and remains on a plateau. Interestingly, the spin x component is sensitive to a sign change $J \to -J$. To demonstrate this dependency, we changed the sign from an antiferromagnetic to ferromagnetic coupling and add the result as a red line in Fig. 6.6. Ferromagnetic and antiferromagnetic coupling produce exactly the same behavior with opposite sign. If J has a positive and a negative sign with equal probability, the spin x component disappears completely, see the green curve. In addition, we plotted the x component resulting from a full ensemble simulation, for which we use the inter-QD coupling constants obtained from NRG calculations as in Sec. 6.3. These coupling constants J_i are a mixture

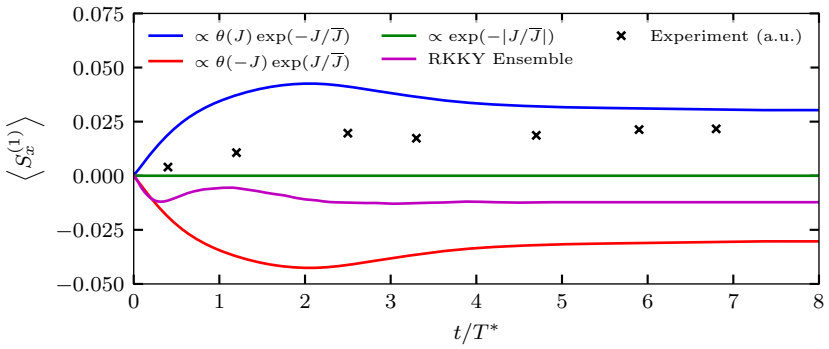

Figure 6.8: Spin component along the external magnetic field axis in a three-color pump-probe setup measured after the incidence of pump pulse 2. Pump pulse 2 excites subensemble B with σ^+ polarization at a minimum of the reference curve. The blue, red, and green curves depict the results for a two-QD model with an exponential distribution of the coupling constant J with only positive values of J (blue), only negative values of J (orange), or a mixture of positive and negative values of J (green). The magenta curve displays the result of a full ensemble calculation. The experimental data (x markers) are taken from Ref. [58].

of antiferromagnetic and ferromagnetic couplings with ferromagnetic couplings dominating. Due to the mixing of both signs, the polarization of the spin x component is reduced.

In conclusion, the spin x component is sensitive to the sign of the inter-QD coupling J_i and, in principle, allows for determining whether the inter-QD interaction is predominantly ferromagnetic or antiferromagnetic. However, since the experiments in Ref. [58] did not determine the absolute sign of the spin x component, the sign of the couplings cannot be inferred.

Chapter 7

Variation of the spectral width of the optical excitation

For the implementation of quantum functionality, decoherence is a significant challenge. In QDs, where the electron spin serves as a potential carrier of quantum information, the hyperfine interaction provides an essential contribution to the dephasing. In addition to the hyperfine interaction, the inhomogeneity of the electron g factors produces a significant dephasing in the ensemble at large magnetic fields. In this chapter, we demonstrate that inter-QD interactions, which are in the order of μeV, provide a relevant source of dephasing as well. However, the dephasing time arising from the inter-QD interactions can be tuned by tailored laser pulses. As a motivation for the investigations in this chapter, we present a pump-probe experiment with variable pulse spectra in Sec. 7.1. The model, which is employed to describe the experimental results, is introduced in Sec. 7.2. In Secs. 7.3, 7.4, and 7.5, we examine the dephasing effects arising from the hyperfine interaction, the electron g-factor inhomogeneity, and the inter-QD interactions, respectively. Finally, in Sec. 7.6, we combine all dephasing effects and summarize the outcome in Sec. 7.7. The results of this chapter have been published in Ref. [69]. The experimental measurements were performed by the Bayer group at TU Dortmund University [69].

7.1 Experimental results

We study pump-probe experiments that were performed on an InGaAs QD ensemble with tailored pump and probe pulses. The investigated sample contains 20 layers of self-assembled (In,Ga)As QDs [111] with a dot density per layer of $10^{10}\,\mathrm{cm}^{-2}$. To charge the QDs with electrons, a Si-δ-doping sheet beneath each QD layer provides approximately one electron per QD. However, detailed examinations show that at least 50% of the QDs are singly charged while the other QDs are neutral or doubly charged [57]. In Fig. 7.1(a), the PL spectrum of the QD ensemble is displayed as a filled grey curve. For the given sample, it has a full width at half maximum

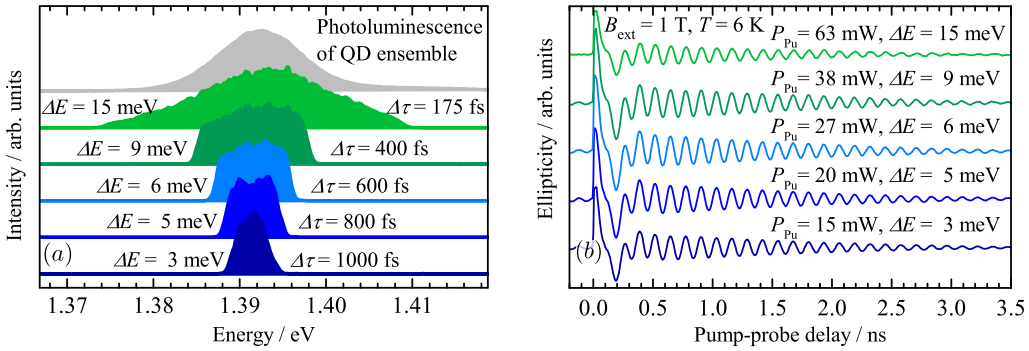

Figure 7.1: (a) Laser pulse spectra with varying spectral widths ΔE and the related pulse duration $\Delta\tau$. The uppermost spectrum is the photoluminescence (PL) emission of the QD ensemble. (b) Time-resolved ellipticity traces showing the electron spin precession and the dephasing of the QD ensemble at $B_{\mathrm{ext}} = 1\,\mathrm{T}$ and $T = 6\,\mathrm{K}$ for the different pulse widths. The figures are taken from Ref. [69]

(FWHM) of roughly 13 meV which is much broader than the typical homogeneous line width of a single QD [77]. The PL emission is centered around 1.393 eV. The tailored laser spectra are depicted as filled colored curves in Fig. 7.1(a) as well. Their central photon energy is tuned to the maximum of the PL emission. By tailoring the energy spectrum of the pump pulse, the number and the spectral composition of the excited QDs are adjusted. As the electron g factor depends nearly linearly on the excitation energy of the QD (see Sec. 3.2), the g-factor composition in the excited QD ensemble is tuned as well. For a broader laser spectrum, the variation of the g factors contributing to the signal increases. In addition, more QDs are excited such that the effective distance between the excited QDs reduces. Therefore, the effective inter-QD interaction strength is adjusted. As a consequence, the measurements are sensitive to inter-QD interactions as well.

The tailored laser pulses are generated by a Ti:Sapphire laser originally emitting pulses with a duration of 180 fs at a repetition rate of 76 MHz. The pulse duration is connected to the spectral width via Fourier transformation, so the duration of 180 fs corresponds to a spectral width of 15 meV. To tune the laser spectrum, the pulses are diffracted at a grating, which spatially widens the pulse. Placing a slit into the widened beam, the spectral width can be reduced to the desired degree. The resulting pulse spectra are depicted in Fig. 7.1(a) as colored filled curves. The spectrally tuned beam is split into a pump and a probe beam, such that the pump and the probe beam have the same energy spectrum and only differ in polarization and intensity. The circularly polarized pump pulses excite the electron spins which precess around the external magnetic field in Voigt geometry. The weaker probe beam is employed for readout of the electron spin polarization along the optical

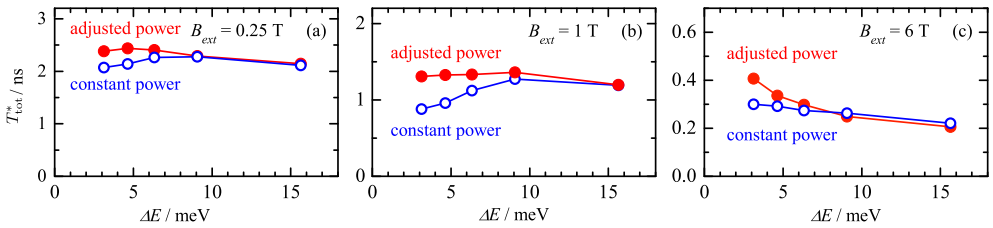

Figure 7.2: Dephasing times T^*_{tot} depending on the spectral pulse width. The data are extracted from fitting the traces of the ellipticity signal at (a) $B_{\mathrm{ext}} = 0.25\,\mathrm{T}$, (b) $B_{\mathrm{ext}} = 1\,\mathrm{T}$, and (c) $B_{\mathrm{ext}} = 6\,\mathrm{T}$. The laser power is either constant (blue) or adjusted (red). The figure is taken from Ref. [69].

axis.

Figure 7.1(b) shows the time-resolved ellipticity traces for the different laser spectra depicted in Fig. 7.1(a) at an external magnetic field strength of 1T. After roughly 0.5 ns, fast decaying excitations have vanished and solely the dynamics of the resident electron spins persist. The photo-generated spin polarization precesses with the average Larmor frequency of the ensemble which is the same for all traces since the central photon energy of the laser pulse is kept to the same value. The signal dephases on the time scale of a few ns. The Overhauser field fluctuations contribute only weakly to the dephasing as they have a strength of only 7.5 mT in the given sample. More relevant is the effect of the g-factor variation, which is proportional to the spread of the Larmor frequencies $\Delta\omega_L = \Delta g_e \mu_B B_{\mathrm{ext}}$. Since the g-factor variation in first approximation is proportional to the spectral width of the laser pulse, $\Delta g_e \propto \Delta E$, it is surprising that the traces in Fig. 7.1(b) have almost the same dephasing time, although spectral width varies by a factor of 6.

To examine the dephasing times in more detail, the fit function

$$S_z(t) = A\cos(\omega_L t)\exp\left(-\frac{t^2}{2{T^*_{\mathrm{tot}}}^2}\right) \tag{7.1}$$

is employed with the total dephasing time T^*_{tot}: The dephasing times determined from fitting are plotted for three different magnetic field strengths in Fig. 7.2. For the blue curves, the laser power is kept constant, such that the light intensity is lower after the slit especially for narrow slits. For the red curves, the laser power is adjusted such that the light intensity at the sample is constant. The red data points in panel (b) belong to the traces in Fig. 7.1(b). Regardless of the specific excitation conditions, no significant influence of the spectral laser width on the dephasing time can be detected within the limits of measurement accuracy. Only at a relatively strong magnetic field of 6 T, the dephasing time decreases with increasing spectral

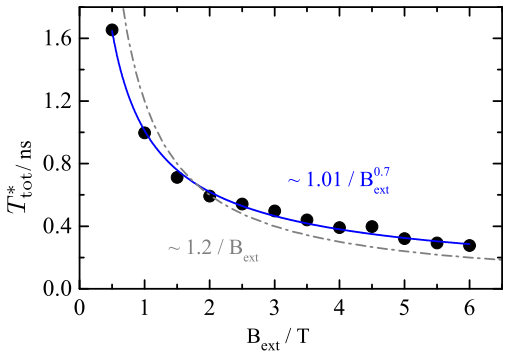

Figure 7.3: Dephasing time T^*_{tot} for a fixed pulse duration of 2 ps as a function of the external magnetic field B_{ext}. A fit $\sim B_{\mathrm{ext}}^{-1}$ is added as a dash-dotted gray line. A fit $\sim B_{\mathrm{ext}}^{-\alpha}$ with $\alpha > 0$ is indicated by the blue line. The plot is taken from Ref. [69].

width. At large magnetic fields, the variation of the electron g factor significantly reduces the dephasing time.

Figure 7.3 depicts the dephasing time for a fixed pulse duration of 2 ps as a function of the external magnetic field. The dephasing time decreases from 1.6 ns at 0.5 T to almost 0.2 ns at 6 T. We find that the data cannot be described by a $1/B_{\mathrm{ext}}$ fit (gray line). Fitting the exponent, $1/B_{\mathrm{ext}}^{\alpha}$, a good agreement with the experimental data is achieved for $\alpha = 0.7$.

To understand the experimental results, we take into account the combined effect of the nuclear spin fluctuations, the electron g-factor variation, and the inter-QD interactions. In the following, we implement a model that reproduces and explains the experimental findings.

7.2 Model and methods

To study the effect of inter-QD interactions on the dephasing time, we employ the model introduced in Chapter 3. We restrict ourselves to the interactions that are relevant on the time scale of a few nanoseconds. Accordingly, we omit the nuclear-electric quadrupolar interactions. To maintain the connection to the experiments, we address isotropic hyperfine interactions relevant for electron spins.

The Hamiltonian for a single QD is given by Eq. (3.15), and the Hamiltonian for the QD ensemble results from Eq. (3.14) with an effective Heisenberg interaction between electron spins of different QDs. We discuss the dephasing effect of the

different interactions separately, so the parameters for this study are introduced progressively in the upcoming sections. The laser spot typically comprises 10^6 QDs and hence a complete simulation of the ensemble is not possible. Instead, we focus on a reduced cluster that mimics the ensemble. A reduction to two QDs, as introduced in Sec. 4.6, is not adequate here, as the spectral width of the laser is continuously adjusted, and therefore the number of excited QDs is flexible. For our simulations, we employ a cluster of representative QDs which are drawn with random properties for the individual classical configurations. A cluster size of 10 QDs has proven to be useful. For the SCA outlined in Chapter 4, typically 10^5 independent configurations are evaluated and averaged. To obtain a continuous spectrum, a different set of random variables such as excitation energy, g factor, and coupling constants is used for each configuration. In total, we decompose the ensemble with 10^6 QDs to 10^5 representative clusters comprising 10 QDs each.

To account for the optical excitation, we employ the approach introduced in Sec. 5.2. We determine the complex pulse parameter a from the integration of Gaussian pulses with the envelope function,

$$\Omega(t) = \frac{\Theta}{2\pi\sigma_t^2} \exp\left(-\frac{t^2}{2\sigma_t^2}\right) , \tag{7.2}$$

and the area $\Theta = \pi$. The temporal pulse width σ_t is obtained from the spectral FWHM,

$$\Delta E = 2\sqrt{2\ln 2}\sigma_E = \frac{2\sqrt{2\ln 2}}{\sigma_t} , \tag{7.3}$$

with the spectral standard deviation σ_E. As the trion excitation energy $\epsilon_T^{(i)}$ is assigned individually for each QD, the pulse parameter $a \to a^{(i)}$ varies within the ensemble. In the experiment, the spin polarization is measured using the Faraday ellipticity, which is proportional to the trion excitation probability. We reproduce this behavior in our model by weighting the spin z component of each QD with the factor $(1 - |a^{(i)}|^2)$ so that resonant QDs contribute more to the signal than detuned QDs. For the implementation of the optical excitation and radiative decay we employ the MEOM approach, see Sec. 5.2.

Additional contributions to the dephasing that are not included in our model cannot be completely ruled out. Since the QDs are charged by donors, the effect of charge fluctuations near the QDs has to be discussed. A pure capacitive coupling shifts the energy, and therefore influences the excitation energy. However, this effect is already reflected in the PL emission of the QD ensemble shown in Fig. 7.1(a). In our cluster approach, this effect is incorporated by a correct choice of the distribution of the excitation energies $\epsilon_T^{(i)}$. However, we disregard charge fluctuations in and out

of a singly charged QD. Since spin coherence can be observed on time scales much longer than the dephasing time [111], this mechanism does not affect the short-time dephasing time. Moreover, a potential deformation of the electron wave function as a function of the external field can be discussed. The hyperfine couplings $A_k^{(i)}$ depend on the electron wave function at the position of the nucleus. The shape of the wave function is mainly determined by the diverging Coulomb interaction at the nucleus, which exceeds the Zeeman energy at magnetic fields $< 10\,\mathrm{T}$ by several orders of magnitude. Therefore, this effect can also be neglected.

7.3 Dephasing due to the hyperfine interaction

First, we investigate the influence of the nuclear spin fluctuations on the dephasing time in a single QD. The Overhauser field fluctuations can differ by an order of magnitude for different samples and depend significantly on the material and growth conditions. For the sample investigated here, the Overhauser field fluctuations are approximately 7.5 mT [104]. On the time scale of the electron spin dephasing, the nuclear spin dynamics can be neglected, justifying the assumption of a frozen Overhauser field. According to Sec. 4.7, the envelope function of the signal is Gaussian [37],

$$S_{\mathrm{env}}(t) = \pm S_0 \exp\left(-\frac{t^2}{2T_N^{*2}}\right) . \tag{7.4}$$

The standard deviation T_N^* is given by the fluctuations of the Overhauser field along the magnetic field axis

$$T_N^* = \sqrt{\frac{3}{\sum_k A_k^2 \langle I_k^2 \rangle}} . \tag{7.5}$$

The factor $\sqrt{3}$ in comparison to Sec. 4.7 is chosen such that T_N^* becomes the standard deviation of the Gaussian, Eq. (7.4), which allows for a better comparison to other dephasing contributions. The central limit theorem guarantees that the Overhauser field, in the case of many nuclear spins, is Gaussian distributed independently of the distribution of the hyperfine constant $p(A_k)$. Hence, the generic behavior of dephasing is encoded in T_N^*. Only on longer time scales, where the dynamics of the nuclear spins cannot be neglected, details of the distribution $p(A_k)$ become relevant [62, 118]. In the following, we employ exponentially distributed hyperfine coupling constants,

$$p(A_k) = \frac{1}{\overline{A}} \exp\left(-\frac{A_k}{\overline{A}}\right) , \tag{7.6}$$

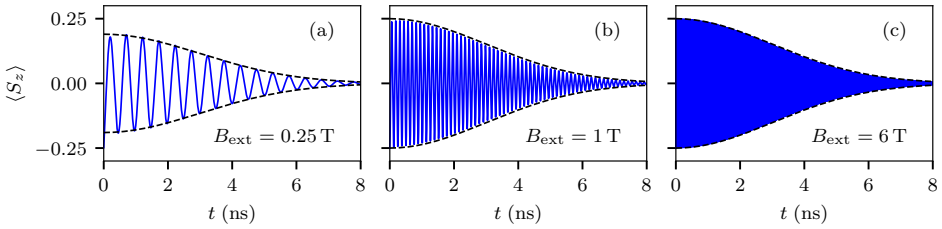

Figure 7.4: Dephasing due to the nuclear spin fluctuations after a single π-pulse for three different external magnetic fields. The parameters $T_N^* = 3\,\mathrm{ns}$, $g_e = 0.555$, and $J_{ij} = 0$ are used. The dashed lines mark the analytical envelope functions according to Eq. (7.4). The plot is taken from Ref. [69].

with the mean value $\overline{A}$. Figure 7.4 shows the electron spin dynamics for three different external magnetic field strengths after a resonant π pulse at $t = 0$, where the electron g factor is set to the fixed value 0.555 and the inter-QD interaction is neglected ($J_{ij} = 0$). Thus, the dephasing arises solely from the nuclear spin fluctuations. We include $N_I = 100$ nuclear spins of the length $I = 3/2$ in the QD and assume an averaged value $g_N\mu_N/g_e\mu_B = 1/800$ [61, 62, 136]. Based on the experimental data, we set $T_N^* = 3\,\mathrm{ns}$ [46, 47]. The envelope function of all curves in Fig. 7.4 is given by Eq. (7.4). Thus, the dephasing time is independent of the strength of the external magnetic field. Furthermore, we assume that T_N^* is equal for all QDs, such that this dephasing is not affected by the spectral width of the laser pulse.

7.4 Dephasing due to the electron g-factor dispersion

As a second contribution, we study the dephasing induced by the inhomogeneity of the electron g factors in the QD ensemble. Self-assembled QDs have random positions on the sample as well as individual properties of each QD. In this case, we are interested in the variation of the electron g factors $g_e^{(i)}$ and the excitation energies $\epsilon_T^{(i)}$ since they related to the dephasing behavior. The effective g factor in the solid is directly connected to the excitation energy via the Roth-Lax-Zwergling relation [69, 104, 109], so $g_e^{(i)}$ and $\epsilon_T^{(i)}$ follow a correlated probability distribution. We derive this distribution from the experimentally accessible data and employ the result to determine the dependence of the dephasing time on the magnetic field and the laser bandwidth. From the PL in Fig. 7.1(a), the distribution of excitation

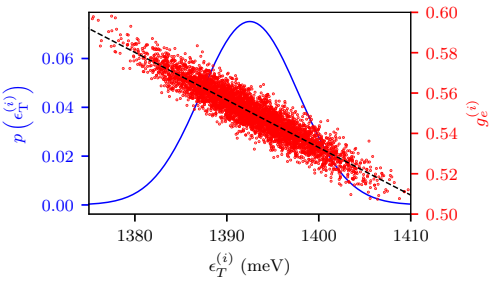

Figure 7.5: Combined distribution of the trion excitation energy $\epsilon_T^{(i)}$ and the electron g factor $g_e^{(i)}$. The excitation energy is Gaussian distributed $\epsilon_T^{(i)} \sim \mathcal{N}(\epsilon_{T,0}, \sigma_{\epsilon_T})$ (solid blue line) based on the experimental photoluminescence spectrum (cf. Fig. 7.1(a)). The linear relation between the average g factor $\overline{g}_e^{(i)}$ and the trion excitation energy $\epsilon_T^{(i)}$ is depicted as a black dashed line, see Eq. (7.8). The red dots depict 5000 pairs $(\epsilon_T^{(i)}, g_e^{(i)})$ with $g_e^{(i)} \sim \mathcal{N}(\overline{g}_e^{(i)}, \sigma_{g,0})$ generated randomly. The plot is taken from Ref. [69].

energies $\epsilon_T^{(i)}$ can be obtained. It is approximately Gaussian,

$$p(\epsilon_T^{(i)}) = \frac{1}{\sqrt{2\pi\sigma_{\epsilon_T}^2}} \exp\left(-\frac{(\epsilon_T^{(i)} - \epsilon_{T,0})^2}{2\sigma_{\epsilon_T}^2}\right) , \tag{7.7}$$

with a mean value $\epsilon_{T,0} = 1392.5\,\text{meV}$ and a standard deviation $\sigma_{\epsilon_T} = 5.3\,\text{meV}$. For spectrally narrow laser pulses, the average g factor can be determined for a fixed excitation energy [104, 109]. This relation is approximately linear,

$$\overline{g}(\epsilon_T^{(i)}) = m\epsilon_T^{(i)} + b , \tag{7.8}$$

and is estimated below with the parameters $m = -2.35\,\text{eV}^{-1}$ and $b = 3.83$ [192]. Furthermore, we assume that the electron g factor $g_e^{(i)}$ follows a Gaussian distribution even at a fixed excitation energy,

$$p(g_e^{(i)}) = \frac{1}{\sqrt{2\pi\sigma_{g,0}^2}} \exp\left(-\frac{(g_e^{(i)} - \overline{g}(\epsilon_T^{(i)}))^2}{2\sigma_{g,0}^2}\right) , \tag{7.9}$$

with the excitation-dependent mean value $\overline{g}(\epsilon_T^{(i)})$ and the intrinsic standard deviation $\sigma_{g,0} = 0.005$. Assuming that, for strong magnetic fields, the dephasing time is dominated by the variation of the g factors, the parameter $\sigma_{g,0} = 0.005$ is obtained from the measurements in Fig. 7.2 for 6 T. In Fig. 7.5, the distribution of $\epsilon_T^{(i)}$ and

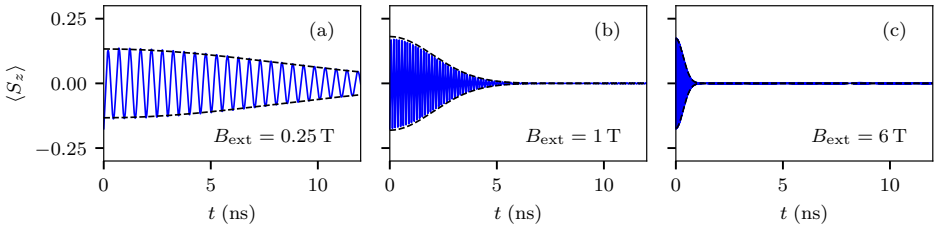

Figure 7.6: Dephasing due to the electron g-factor dispersion with $A_k^{(i)} = 0$, $J_{ij} = 0$, $\Delta E = 5\,\mathrm{meV}$. The spin dynamics is depicted for three different external magnetic fields. The dashed lines mark the Gaussian envelope functions with standard deviation T_g^* according to Eq. (7.10). The plot is taken from Ref. [69].

$g_e^{(i)}$ is shown. By construction, the parameters $\epsilon_T^{(i)}$ and $g_e^{(i)}$ follow a two-dimensional Gaussian distribution, where $\epsilon_T^{(i)}$ and $g_e^{(i)}$ are strongly correlated. In the numerical calculations, $N_C N_{\mathrm{QD}} = 10^6$ pairs $(\epsilon_T^{(i)},\ g_{\mathrm{e}}^{(i)})$ are generated and employed in the simulation.

The dephasing of the electron spin after a pulse due to the g-factor variation is shown in Fig. 7.6 for three different external magnetic fields. To isolate the effect of the g factors, the hyperfine interaction and the inter-QD interactions are switched off ($A_k^{(i)} = J_{ij} = 0$). The dephasing time decreases substantially for strong magnetic fields. Since we neglect the interactions with other spins, the dephasing time can be determined analytically. For a Gaussian distribution of the g factors, the dephasing time,

$$T_g^* = \frac{1}{\sigma_\omega} = \frac{1}{\sigma_g \mu_B B_{\mathrm{ext}}}\,, \tag{7.10}$$

is the inverse of the frequency deviation σ_ω and is directly related to the standard deviation σ_g of the g factors. In particular, the dephasing time $T_g^* \propto B_{\mathrm{ext}}^{-1}$ is inversely proportional to the magnetic field strength. Fig. 7.7(a) shows a comparison of the analytical expression, Eq. (7.10), to the numerical calculations, providing exact agreement.

The dependence of the dephasing time on the laser bandwidth ΔE can be estimated analytically as well, however, it follows a more complicated relation. A broadening of the spectral width of the laser leads to a broadening of the contributing g factors and thus to a reduction of the dephasing time. In Fig. 7.7(b), T_g^* is shown as a function of ΔE. For very large and very small bandwidths, the dephasing time T_g^* converges to two constant values. When ΔE is larger than the width of the PL, all

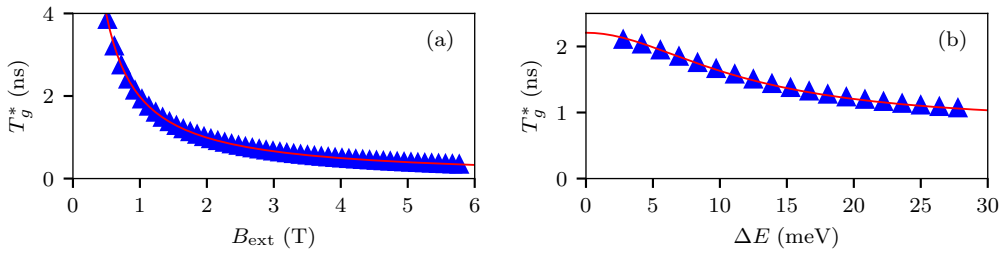

Figure 7.7: Dependence of the electron g-factor induced dephasing time T_g^* on (a) the external magnetic field B_{ext} and (b) the laser bandwidth ΔE. The data points (blue triangles) are extracted from numerical calculations with the parameters $A_k^{(i)} = 0$, $J_{ij} = 0$, $\Delta E = 5\,\text{meV}$. The red line depicts the dependence according to Eq. 7.16. The plots are taken from Ref. [69].

QDs contribute to the signal and T_g^* is minimal. A further broadening of the pulse spectrum has no additional effect since all QDs are excited already. If ΔE is very narrow, the intrinsic broadening $\sigma_{g,0}$ produces the upper bound of T_g^*. Between these limiting cases T_g^* depends on the bandwidth $\Delta E = 2\sqrt{2\ln 2}\,\sigma_E$, as well as on the parameters m, σ_{ϵ_T}, and $\sigma_{g,0}$. The variance of the contributing g factors,

$$\sigma_g^2 = \sigma_{g,0}^2 + \sigma_{g\Delta}^2 \,, \tag{7.11}$$

is composed of two contributions: the intrinsic broadening $\sigma_{g,0}$ and the broadening $\sigma_{g\Delta}$ due to the correlation between the excitation energy $\epsilon_T^{(i)}$ and the associated g factor $g_e^{(i)}$. The broadening of the g factors,

$$\sigma_{g\Delta} = |m|\sigma_{\epsilon_{T\Delta}} \,, \tag{7.12}$$

is related to the broadening of the excitation energies $\sigma_{\epsilon_{T\Delta}}$ contributing to the signal via the slope m, cf. Eq. (7.8). To determine the standard deviation $\sigma_{\epsilon_{T\Delta}}$, we introduce the weight $w(\epsilon_T^{(i)})$. This weight captures the fraction that a certain excitation energy $\epsilon_T^{(i)}$ contributes to the signal and consists of three components: (i) the probability of finding a QD with the excitation energy $\epsilon_T^{(i)}$, (ii) the efficiency of the pump pulse that excites the QD, and (iii) the efficiency of the probe pulse that reads out the QD. Thus, the weight has the form

$$w(\epsilon_T^{(i)}) \propto p(\epsilon_T^{(i)})\tilde{\Omega}^2(\epsilon_T^{(i)})\tilde{\Omega}^2(\epsilon_T^{(i)}) \,, \tag{7.13}$$

where $p(\epsilon_T^{(i)})$ is the distribution of excitation energies, and the efficiency of the pump pulse and the probe pulse is given by $\tilde{\Omega}^2(\epsilon_T^{(i)})$. Formally, $\tilde{\Omega}(\epsilon_T^{(i)})$ can be determined

by the Fourier transform of the envelope function of the laser pulse $\Omega(t)$. Equation (7.13) yields

$$w(\epsilon_T^{(i)}) \propto \exp\left(-\frac{(\epsilon_T^{(i)}-\epsilon_{T,0})^2}{2\sigma_{\epsilon_T}^2}\right)\exp\left(-\frac{(\epsilon_T^{(i)}-\epsilon_{T,0})^2}{2\sigma_E^2}\right)^4$$
$$= \exp\left(-\frac{(\epsilon_T^{(i)}-\epsilon_{T,0})^2}{2\sigma_{\epsilon_{T\Delta}}^2}\right) , \tag{7.14}$$

with the total broadening

$$\sigma_{\epsilon_{T\Delta}}^{-2} = \sigma_{\epsilon_T}^{-2} + \left(\frac{\sigma_E}{2}\right)^{-2} . \tag{7.15}$$

From the combination of Eqs. (7.10), (7.11),(7.12), and (7.15), we obtain

$$T_g^* = \frac{1}{\mu_B B_{\text{ext}}\sqrt{\sigma_{g,0}^2 + m^2(\sigma_{\epsilon_T}^{-2} + (\frac{\sigma_E}{2})^{-2})^{-1}}} , \tag{7.16}$$

which is added as a red line in Fig. 7.7(b). The analytical expression, Eq. (7.16), shows an excellent agreement with the numerical results. The dephasing time T_g^* is inverse proportional to the magnetic field. For the bandwidth, we find an inverse proportionality only in the limiting case $\sigma_{\epsilon_T} \gg \sigma_E \gg \sigma_{g,0}$. The dephasing produced by the nuclear spin fluctuations and the g-factor dispersion are independent of each other and additive in frequency space. Hence, the combined dephasing time can be directly calculated,

$$(T_{\text{tot}}^*)^{-2} = (T_{\text{N}}^*)^{-2} + \left(T_g^*\right)^{-2} . \tag{7.17}$$

7.5 Dephasing due to the inter quantum-dot interactions

Finally, the influence of the inter-QD interactions on the dephasing will be investigated. Including the electron spin-spin interaction, we obtain a complex many-body problem, which makes an analytical approach more difficult. To understand the generic behavior, we investigate the limiting cases of a large spectral width and a low spectral width of the laser pulse in the following. While in the former case almost all QDs are optically aligned, electron spins in most QDs are unpolarized in the latter case. This difference has a significant impact on the dephasing time and generates opposite effects as revealed in the following analysis.

Spectrally narrow laser pulse

In the case of a laser pulse with a small bandwidth, only a few QDs are polarized after the pulse. In particular, we assume that most QDs in the vicinity of a polarized QD are unpolarized and contribute to the dynamics with a random noise term. In Fig. 7.8(a), the dynamics of one of $N_{\mathrm{QD}} = 10$ QDs is shown, which is optically resonantly excited at the time $t = 0$, while the other QDs remain unaffected by the laser pulse. To illustrate the effect of the inter-QD interaction, nuclear spin fluctuations and electron g-factor variations are neglected. We employ a generic exponential distribution for J_{ij},

$$p(J_{ij}) = \frac{1}{\overline{J}} \exp\left(-\frac{J_{ij}}{\overline{J}}\right) , \tag{7.18}$$

with a mean value $\overline{J}$. In this scenario, each electron spin experiences a randomly fluctuating magnetic field $\vec{b}_J^{(i)} = \sum_j J_{ij} \vec{s}^{(j)}$ similarly to the Overhauser field. However, $\vec{b}_J^{(i)}$ is qualitatively different from the Overhauser field due to the external magnetic field. Under the simplification that all electron spins have the same g factor, we perform a transformation to a co-rotating coordinate system in which neither $\vec{b}_J^{(i)}$ nor the electron spins precess. Thus, in the co-rotating coordinate system, the analytic solution is

$$\langle S_z(t) \rangle = \frac{S_0}{3} \left(1 + 2\left[1 - 2\,\frac{t^2}{2\,T_J^{*2}}\right] \exp\left[-\frac{t^2}{2\,T_J^{*2}}\right]\right) \tag{7.19}$$

with the dephasing time

$$T_J^* = \sqrt{\frac{6}{\sum_j J_{ij}^2 S_j^2}} , \tag{7.20}$$

where j is an index for the unpolarized QDs. Equation (7.19) describes the dynamics in the co-rotating coordinate system and the envelope function of the dynamics in the laboratory system (see Fig. 7.8(a)). The envelope function first drops to almost zero on the time scale T_J^* and then grows again to one-third of the initial value. However, we expect that the regrowth is suppressed when additional dephasing effects are taken into account. In Fig. 7.8(a), we display a Gaussian with the standard deviation T_J^*, which captures the initial decay in good approximation. The factor $\sqrt{2}$ between the definitions of T_N^* in Eq. (7.5) and T_J^* in Eq. (7.20) arises from the fact that the Overhauser field is almost frozen in the laboratory system while $\vec{b}_J^{(i)}$ precesses around the external magnetic field. Thus, in the case of T_N^*, only the nuclear fluctuations along the x axis contribute to the dephasing while, in the case of T_J^*, the fluctuations of the electron spins in x and y direction are relevant.

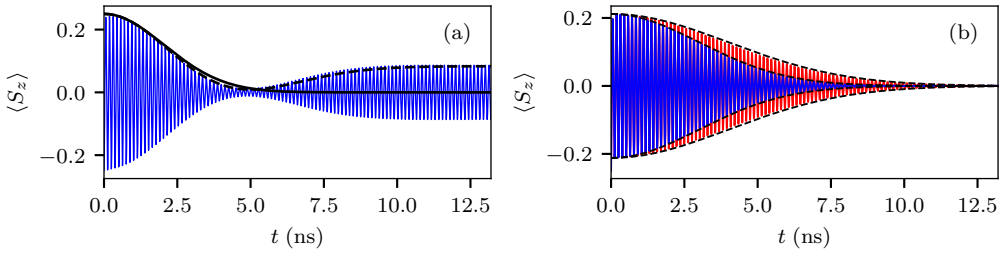

Figure 7.8: Dephasing due to the inter-QD interactions. (a) Numerical results for the spin z component after a resonant π pulse at $t = 0$ with the parameters $A_k^{(i)} = 0$, $g_e^{(i)} = 0.555$, $\overline{J} = 0.4\,\mathrm{ns}^{-1}$, and $B_{\mathrm{ext}} = 1\,\mathrm{T}$. The envelope function (black dashed line) is given by Eq. (7.19). The initial dephasing can be approximated by a Gaussian envelope function (black solid line) with standard deviation T_j^*. (b) Toy model for strongly interacting QDs. Two QDs are excited by a resonant π pulse at $t = 0$ with the parameters $T_N^* = 3\,\mathrm{ns}$, $g_e^{(i)} = 0.555$, and $B_{\mathrm{ext}} = 1\,\mathrm{T}$. The dephasing time with a strong inter-QD interaction ($\overline{J} = 200\,\mathrm{ns}^{-1}$, red curve) is a factor of $\sqrt{2}$ longer than the dephasing time without inter-QD interaction ($\overline{J} = 0$, blue curve).

Spectrally broad laser pulse

The second limit addressed analytically are laser pulses with large bandwidth. In this situation, all QDs are resonantly excited by the π pulse and, thus, initially oriented in the same direction. With respect to the semiclassical EOM, Eq. (4.32a), this means that $\vec{s}^{(i)}$ and $\vec{b}_J^{(i)}$ are parallel to each other, and the cross product vanishes. Thus, one might assume that these QDs do not contribute to the dephasing time. However, this does not imply that the inter-QD interaction does not affect the dephasing time in this scenario. To demonstrate the effect, we focus on a minimal model that consists of only two electron spins that are initially aligned in parallel and strongly coupled to each other. This model is described by the Hamiltonian

$$H = J\,\vec{S}^{(1)}\vec{S}^{(2)} + \vec{b}^{(1)}\vec{S}^{(1)} + \vec{b}^{(2)}\vec{S}^{(2)}\ , \tag{7.21}$$

where $\vec{b}^{(i)}$ is the frozen magnetic field,

$$\vec{b}^{(i)} = \vec{b}_{\mathrm{ext}}^{(i)} + \vec{b}_N^{(i)}\ . \tag{7.22}$$

In the following, we show that, in the limiting case of a strong interaction J, the spins jointly precess around the average magnetic field $\vec{b}_+$. This average field has lower fluctuations than the individual fields so the dephasing time is extended.

Transforming to the rotated coordinate system of the average field, $\vec{b}_+ = (\vec{b}^{(1)} + \vec{b}^{(2)})/2$, we obtain the new Hamiltonian,

$$H' = J_{12}\vec{\tilde{S}}^{(1)}\vec{\tilde{S}}^{(2)} + \vec{b}_-(\vec{\tilde{S}}^{(1)} - \vec{\tilde{S}}^{(2)}) \tag{7.23}$$

with the transformed spin operators $\vec{\tilde{S}}^{(i)}$ and the deviating field $\vec{b}_- = (\vec{b}^{(1)} - \vec{b}^{(2)})/2$. The classical equations of motion yield

$$\partial_t \vec{\tilde{s}}^{(1)} = \left(\vec{b}_- + J\vec{\tilde{s}}^{(2)}\right) \times \vec{\tilde{s}}^{(1)} \,, \tag{7.24a}$$

$$\partial_t \vec{\tilde{s}}^{(2)} = \left(-\vec{b}_- + J\vec{\tilde{s}}^{(1)}\right) \times \vec{\tilde{s}}^{(2)} \,. \tag{7.24b}$$

We assume that the spins initially are aligned in parallel, except for a small deviation $\vec{\beta}$ ($|\vec{\beta}| \ll 1$)

$$\vec{\tilde{s}}^{(1)}(0) = \frac{1}{2}\left(\vec{e}_z + \vec{\beta}\right) \,, \tag{7.25a}$$

$$\vec{\tilde{s}}^{(2)}(0) = \frac{1}{2}\left(\vec{e}_z - \vec{\beta}\right) \,. \tag{7.25b}$$

These relations are used as an initial condition in the EOM,

$$\partial_t \vec{\tilde{s}}^{(1)}(0) = \frac{1}{2}\left(\vec{b}_- \times \vec{e}_z + \vec{b}_- \times \vec{\beta} + J\vec{e}_z \times \vec{\beta}\right) \,, \tag{7.26a}$$

$$\partial_t \vec{\tilde{s}}^{(2)}(0) = \frac{1}{2}\left(\vec{e}_z \times \vec{b}_- + \vec{b}_- \times \vec{\beta} + J\vec{\beta} \times \vec{e}_z\right) \,, \tag{7.26b}$$

to determine the time derivative. For the choice $\vec{\beta} = \frac{\vec{b}_-}{J}$, the time derivative $\partial_t \vec{\tilde{s}}^{(i)}(0)$ disappears. Therefore, there is no dynamics in the rotated coordinate system while the spins in the laboratory system precess about the averaged field $\vec{b}_+$. In the limiting case $J \gg |\vec{b}_-|, |\vec{\beta}|$ vanishes. Consequently, the coupled parallel spins precess jointly around the averaged field $\vec{b}_+$. The fields $\vec{b}^{(i)}$ contributing to the average $\vec{b}_+$ are composed of different components and follow a probability distribution whose fluctuations are summarized by $\sigma_b = \sigma_{b^{(1)}} = \sigma_{b^{(2)}}$. To determine the variance $\sigma^2_{b_+}$ of the average field $\vec{b}_+$, we apply the calculation rules for cumulants of a distribution,

$$\begin{aligned} \sigma^2_{b_+} &= \frac{1}{4}\left(\sigma^2_{b^{(1)}} + \sigma^2_{b^{(2)}}\right) = \frac{1}{2}\sigma^2_b \\ \Rightarrow \sigma_{b_+} &= \frac{1}{\sqrt{2}}\sigma_b \,. \end{aligned} \tag{7.27}$$

The fluctuation scale σ_{b_+} of the averaged field $\vec{b}_+$ is thus by a factor of $\sqrt{2}$ smaller than the fluctuation scale of the original fields $\vec{b}^{(i)}$. When N_{QD} QDs interact, this

factor increases to $\sqrt{N_{\mathrm{QD}}}$. Hence, the dephasing time can be significantly increased by the inter-QD interactions. The electron spin dynamics of the minimal model are shown in Fig. 7.8(b).

Summarizing the results of both limiting cases, the inter-QD interactions have a significant effect on the dephasing time. While unpolarized QDs constitute an additional source of noise and produce a faster dephasing, optically aligned electron spins stabilize each other. The number of polarized/unpolarized QDs is controlled by the spectrum of the laser pulse. Interestingly, the effect of the inter-QD interactions behaves exactly oppositely to the g-factor dispersion: While the g-factor dispersion leads to a decreasing dephasing time when more QDs are excited, the inter-QD interactions generate a stabilization of the electron spin polarization and increase the dephasing time. In the following section, all effects on the dephasing are combined to explain the nearly bandwidth-independent dephasing time in the experiment.

7.6 Total dephasing time

In the last three sections, we have investigated the three basic dephasing mechanisms for electron spins in QDs as well as their dependence on the external magnetic field and the spectral laser width. The Overhauser field fluctuations produce an approximately constant dephasing time, which is independent of the external magnetic field and the spectral width of the laser. In contrast, the dispersion of the electron g factor leads to a dephasing time that significantly depends on the magnetic field strength as well as the laser bandwidth. The inter-QD interactions can generate both, a prolongation or shortening of the dephasing time, essentially depending on the number of excited QDs and therefore the laser bandwidth. However, the dependency is reversed in comparison to the dephasing induced by the g-factor dispersion. In this section, we show that only the combination of all these effects explains the experimental results. We employ the numerical cluster approach to simulate the interacting QDs. Most model parameters can be extracted from the literature and are referenced in the previous three sections. Only the interaction strength of the inter-QD interactions remains an undetermined parameter which is estimated to be in the order of µeV by Spatzek et al. [57].

In Fig. 7.9, the dephasing time is shown as a function of the laser bandwidth for three different magnetic fields and different inter-QD interaction strengths. For very small magnetic fields, Fig. 7.9(a), the dephasing time T^*_{tot} is almost independent of ΔE for $\overline{J} = 0$ (dark blue curve). However, the g-factor dispersion leads to a negative slope which is weak due to the small magnetic field. When adding the inter-QD interactions, the slope of the curves changes from predominantly

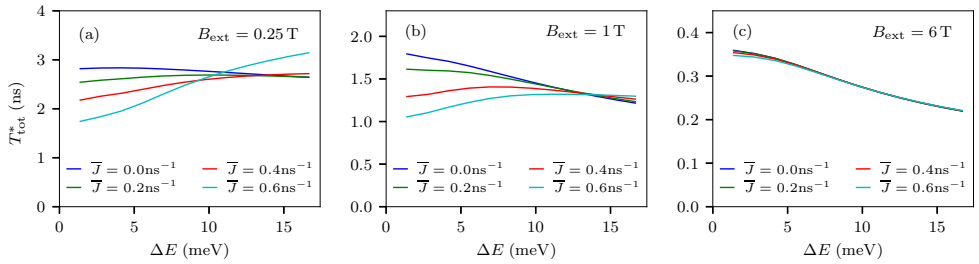

Figure 7.9: Dephasing time T^*_{tot} as a function of the spectral width of the laser for three different magnetic fields (a) 0.25 T, (b) 1 T, and (c) 6 T. All three dephasing effects are included in the numerical calculation. The plot is taken from Ref. [69].

negative to predominantly positive, since the electron spins disturb each other at low bandwidths and stabilize each other at large bandwidths. At 1 T, Fig. 7.9(b), the g-factor variation becomes much more relevant. Without inter-QD interactions $\overline{J} = 0$, a negative slope is observed. When more spins excited are by the laser, more different g factors contribute to the signal and produce a faster dephasing. Again, the inter-QD interactions lead to a reversed trend in the ΔE dependence. For a strong magnetic field of 6 T, the g-factor dispersion dominates clearly, see Fig. 7.9(c). No significant effect is observed for interaction strengths up to $\overline{J} = 0.6\,\mathrm{ns}^{-1}$, and the curves coincide. Over the full magnetic field range, a good agreement with the experimental data in Fig. 7.2 is obtained for $\overline{J} = 0.4\,\mathrm{ns}^{-1}$.

In Fig. 7.10(a), the experimental data (x markers) are compared to the numerical results for $\overline{J} = 0.4\,\mathrm{ns}^{-1}$ (solid lines). The numerical and experimental results are in good agreement. The discrepancy between the value $\overline{J} = 0.4\,\mathrm{ns}^{-1}$ corresponding to 0.27 µeV determined here and the 1 µeV estimated in the experiment of Spatzek et al. [57] can be easily understood. In our cluster model, we include 10 interacting QDs, while Spatzek et al. employ an effective model with two spins. A rescaling of $\sqrt{10} \times 0.27\,\mu\mathrm{eV} \approx 0.85\,\mu\mathrm{eV}$ provides a good agreement within the measurement accuracy.

As a further aspect, the magnetic field dependence is investigated in more detail. For this purpose, the experimental results (x markers) and the numerical data (triangles) for $\overline{J} = 0.4\,\mathrm{ns}^{-1}$ are presented in Fig. 7.10(b). The dephasing time reduces in both cases with increasing magnetic field, and the numerical and experimental curves exhibit a similar curvature. The numerical values are, however, slightly larger. It should be noted that the experimental data from Fig. 7.2 and Fig. 7.3 are not completely compatible. A possible explanation could be measurement series at different positions of the sample. The numerical data deviates from a B_{ext}^{-1} dependence (grey curve), and similar to the experiments a fit proportional

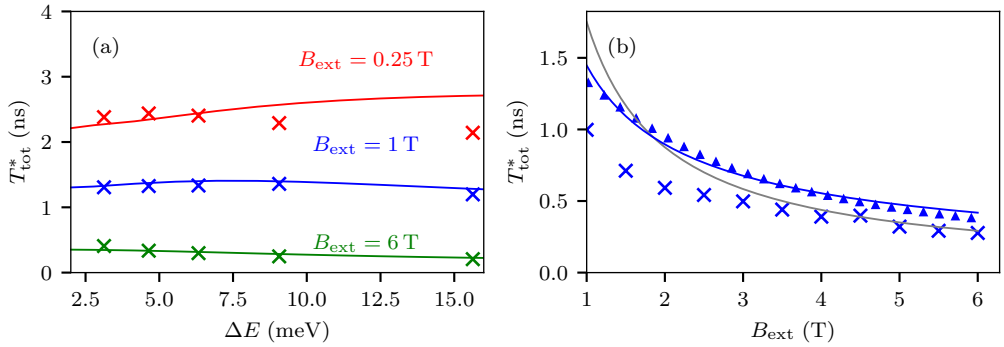

Figure 7.10: Comparison of the numerical results for $\overline{J} = 0.4\,\mathrm{ns}^{-1}$ with the experimental measurements with adjusted power from Sec. 7.1 (x markers). (a) Dephasing time T^*_{tot} as a function of the spectral laser width ΔE. Results for various external magnetic fields are depicted in different colors. (b) Dephasing time as a function of the magnetic field B_{ext} for a fixed bandwidth $\Delta E = 1.5\,\mathrm{meV}$. The data points of the numerical calculation (blue triangles) are compared to a dependence $\propto B_{\mathrm{ext}}^{-1}$ (grey curve) and a dependence $\propto B_{\mathrm{ext}}^{-\alpha}$ with $\alpha = 0.7$ (blue curve). The plots are taken from Ref. [69].

to $B_{\mathrm{ext}}^{-\alpha}$ provides the best agreement for $\alpha = 0.7$. The deviation to a dependence proportional to B_{ext}^{-1} arises from the interplay of all three dephasing contributions. While the g-factor dispersion alone would produce a B_{ext}^{-1} behavior, the nuclear spin fluctuations and the inter-QD interactions generate deviations.

7.7 Chapter conclusion

In this chapter, we have studied the influence of the inter-QD interactions on the dephasing time. The investigation is based on pump-probe experiments, in which the spectral width ΔE of the laser pulse is tailored. Naively, one would expect a dependence of the dephasing time $T^*_{\mathrm{tot}} \propto \Delta E^{-1}$ due to the electron g-factor dispersion, but this was observed only for large magnetic fields. In contrast, for small magnetic fields, the dephasing time is almost independent of the laser bandwidth. We explain this phenomenon by a counterbalancing effect caused by the inter-QD interactions. While the inter-QD interactions lead to additional noise at small spectral widths, the spins stabilize each other for large spectral widths. We verify this simplified picture, using a numerical cluster approach. In our simulation, we include all relevant dephasing mechanisms that play a role on the time scale of a few ns: the nuclear spin fluctuations, the g-factor inhomogeneity, and the inter-QD

interactions. Both, the experimental magnetic field dependence and the spectral width dependence, can be reproduced with good accuracy.

Chapter 8

Cross-correlation spin-noise spectroscopy in equilibrium

In the Chapters 6 and 7, the inter-QD interactions were investigated in pump-probe experiments. In these experiments, the system is brought out of equilibrium by pump pulses and is investigated with time resolution. Selecting different QD subsets of the ensemble either by multi-color experiments or tailored pulse shapes, the results are sensitive to inter-QD interactions. In the following, we address a different class of experiments, namely spin-noise spectroscopy (see Sec. 2.3), where the system remains in thermal equilibrium. The spin-noise spectrum provides detailed information about the spin dynamics in QD ensembles and serves as a useful tool to identify the relevant time and energy scales in QD ensembles due to their strong optical response [60]. In addition to the conventional spin-noise spectroscopy, higher-order correlation spectra gain interest recently due to the sensitivity to quantum effects [84]. In this chapter, we focus on two-color spin-noise experiments, which were first implemented on heterogeneous spin vapor [77] and provide a cross-correlation spectrum that is sensitive to interactions between different spin species. The spin cross-correlation spectrum has not been studied experimentally in QD ensembles yet, though two-color spin-noise experiments were performed on QD ensembles to investigate the homogeneous line width [120].

We introduce the autocorrelation and cross-correlation spectra in Secs. 8.1, 8.2, and 8.3. To benchmark the approach, we begin with the box-model approximation in Secs. 8.4 and 8.5. We implement a two-QD reduction and compare the SCA to an exact quantum mechanical calculation. To understand the generic behavior, we investigate a toy model containing only two spins in Sec. 8.6. In Secs. 8.7 to 8.10, we employ a realistic set of parameters and study various impacts on the cross-correlation spectrum, such as the hyperfine distribution, the quadrupolar interactions, the external magnetic field, and the electron g-factor distribution. Finally, in Sec. 8.11, we connect these results to recent experiments.

The results of this chapter have been published in Ref. [193]. The quantum mechanical calculations in Sec. 8.5 were provided by Iris Kleinjohann.

8.1 Autocorrelation function

In thermal equilibrium, the expectation values of observables without explicit time-dependency are time-independent. To obtain information about the dynamics of the spin system, it is necessary to either move the system out of equilibrium or to examine temporal correlation functions. The former approach is pursued in pump-probe setups, while the latter is exploited in spin-noise spectroscopy. We start with the autocorrelation function of the electron spin z component,

$$C_2(t) = \langle S_z(0) S_z(t) \rangle \ . \tag{8.1}$$

For a spin 1/2, quantum mechanics yields $C_2(0) = 1/4$ independent of the density operator due to the relation $S_z^2 = (1/4)\mathbb{E}$. The naive approach for a semiclassical evaluation would be the replacement of the spin operator S_z by its classical counterpart s_z and an additional average over several configurations, specifically $\langle S_z^2 \rangle = \langle\langle s_z^2 \rangle\rangle$, with $\langle\langle ... \rangle\rangle$ denoting the configuration average. For a spin aligned in x direction, we obtain $s_z^2 = 0$ while a spin in z direction yields $s_z^2 = 1/4$. Spins uniformly distributed on the Bloch sphere produce the expectation value $\langle\langle s_z^2 \rangle\rangle = 1/12$, which differs from the quantum mechanical result. Furthermore, the correlator defined in Eq. (8.1) can be complex in general while a purely classical evaluation is always real.

Alternative formulations of the SCA, based on a truncated Wigner approximation [194], use spin vectors of the squared length $s(s+1)$ instead of s^2. In this way, the expectation value of $1/4$ at $t = 0$ is restored. However, an imaginary part for $t \neq 0$ cannot be covered by a purely classical treatment. We take a different route and explicitly evaluate the correlation function employing spin-coherent states in combination with basic spin algebra. We obtain an evaluation rule which exactly preserves the quantum mechanical properties at the level of a single spin.

We first calculate C_2 for a single spin 1/2 and generalize the results later on for general spin systems. The most general time-dependent hermitian Hamiltonian for a single spin 1/2 has 4 degrees of freedom and can be parameterized by $H(t) = \vec{B}(t)\vec{S} + E_0(t)$ with a classical time-dependent field $\vec{B}(t)$. The time-dependent energy offset $E_0(t)$ only generates a global phase that is physically irrelevant. The time-evolution operator is given by

$$\begin{aligned} U(t) &= \mathcal{T} \exp\left(-\mathrm{i} \int_0^t H(t')dt' \right) \\ &= e^{\mathrm{i}\varphi(t)} \exp\left(-\mathrm{i}\, \vec{\alpha}(t)\vec{S} \right) = e^{\mathrm{i}\varphi(t)} R_{\vec{\alpha}(t)} \end{aligned} \tag{8.2}$$

with the time-ordering operator $\mathcal{T}$ and the global phase $\varphi(t)$. The time-evolution operator $U(t)$ is an element of the SU(2) and, therefore, characterizes a rotation around an axis $\vec{\alpha} \in \mathbb{R}^3$ with the angle $|\vec{\alpha}| = \alpha$. The vector $\vec{\alpha}$ can be extracted by solving the time-ordered exponential function. We postpone the explicit calculation of $\vec{\alpha}(t)$ for the moment and use the rotation representation of the time-evolution operator to evaluate the correlator C_2 in respect to an initial spin-coherent state $|\vec{s}_0\rangle$,

$$\begin{aligned} \langle \vec{s}_0 | \, S_z(0) S_z(t) \, | \vec{s}_0 \rangle &= \langle \vec{s}_0 | \, S_z R_{-\vec{\alpha}(t)} S_z R_{\vec{\alpha}(t)} \, | \vec{s}_0 \rangle \\ &= \langle \vec{s}_0 | \, (\vec{e}_z \vec{S}) R_{-\vec{\alpha}(t)} (\vec{e}_z \vec{S}) R_{\vec{\alpha}(t)} \, | \vec{s}_0 \rangle \ . \end{aligned} \tag{8.3}$$

In the next step, we exploit the relation,

$$\begin{aligned} R_{-\vec{\alpha}}(\vec{n}\vec{S}) R_{\vec{\alpha}} &= \exp(-\mathrm{i}\, \vec{\alpha}\vec{S})(\vec{n}\vec{S}) \exp(\mathrm{i}\, \vec{\alpha}\vec{S}) \\ &= \exp(-\left[\vec{\alpha}\right]_\times) \vec{n}\vec{S} \\ &= (\tilde{R}_{\vec{\alpha}} \vec{n}) \vec{S} \end{aligned} \tag{8.4}$$

with the cross-product matrix $[...]_\times$, that translates a rotation $R_{\vec{\alpha}}$ of the SU(2) to a rotation $\tilde{R}_{\vec{\alpha}}$ of the SO(3). This yields

$$\langle \vec{s}_0 | \, S_z(0) S_z(t) \, | \vec{s}_0 \rangle = \langle \vec{s}_0 | \, (\vec{e}_z \vec{S}) (\tilde{R}_{\alpha(t)} \vec{e}_z \vec{S}) \, | \vec{s}_0 \rangle \ . \tag{8.5}$$

By means of the basic relation $S_\alpha S_\beta = (1/4)\delta_{\alpha\beta} + (\mathrm{i}/2) \sum_\gamma \epsilon_{\alpha\beta\gamma} S_\gamma$ for spin 1/2, we obtain

$$(\vec{n}_1 \vec{S})(\vec{n}_2 \vec{S}) = \frac{1}{4}(\vec{n}_1 \vec{n}_2) + \frac{\mathrm{i}}{2}(\vec{n}_1 \times \vec{n}_2) \vec{S} \, . \tag{8.6}$$

Thus, the correlator is rewritten as

$$\begin{aligned} \langle \vec{s}_0 | \, S_z(0) S_z(t) \, | \vec{s}_0 \rangle &= \langle \vec{s}_0 | \, \frac{1}{4}(\vec{e}_z \tilde{R}_{\alpha(t)} \vec{e}_z) + \frac{\mathrm{i}}{2}(\vec{e}_z \times \tilde{R}_{\alpha(t)} \vec{e}_z) \vec{S} \, | \vec{s}_0 \rangle \\ &= \frac{1}{4} \vec{e}_z \tilde{R}_{\alpha(t)} \vec{e}_z + \frac{\mathrm{i}}{2}(\vec{e}_z \times \tilde{R}_{\alpha(t)} \vec{e}_z) \vec{s}_0 \\ &= \frac{1}{4} \vec{n}_z(0) \vec{n}_z(t) + \frac{\mathrm{i}}{2} \, (\vec{n}_z(0), \vec{n}_z(t), \vec{s}_0) \end{aligned} \tag{8.7}$$

with the triple product $(\vec{a}, \vec{b}, \vec{c}) = (\vec{a} \times \vec{b})\vec{c}$ and the time-dependent vector $\vec{n}_z(t) = \tilde{R}_{\alpha(t)} \vec{e}_z$. Equation (8.7) can be interpreted as an alternative way to evaluate the correlation function C_2. In contrast to the naive approach, Eq. (8.7) yields $C_2(0) = 1/4$ and allows for an imaginary part. We include this finding into the SCA by identifying $\vec{B}(t)$ with the effective magnetic field $\vec{b}_{\mathrm{eff}}(t) = \frac{\partial \tilde{H}(\vec{s})}{\partial \vec{s}}$ that acts on the

spin $\vec{S}$. Interestingly, we have to evaluate the effect of the magnetic field $\vec{b}_{\text{eff}}(t)$ on the vector $\vec{n}_z(t)$ rather than the initial state $\vec{s}_0$.

Finally, the rotation axis $\vec{\alpha}$ has to be determined. Instead of calculating the rotation matrix directly, we employ a more compact quaternionic representation. The Pauli matrices $\{\sigma_0, \mathrm{i}\sigma_x, \mathrm{i}\sigma_y, \mathrm{i}\sigma_z\}$ and the basic quaternions $\{1, \mathrm{i}, \mathrm{k}, \mathrm{l}\}$ share the same algebra, namely $\mathrm{i}^2 = \mathrm{l}^2 = \mathrm{k}^2 = -1$ and $\mathrm{ik} = \mathrm{l}$, $\mathrm{kl} = \mathrm{i}$, $\mathrm{li} = \mathrm{k}$. Thus, unit quaternions are isomorphic to the group SU(2). Due to the two-to-one homomorphism of the SU(2) onto the SO(3), unit quaternions can be used to represent the SO(3) rotation group. Summarizing the basic quaternions $\vec{\mathrm{j}} = (\mathrm{i}, \mathrm{k}, \mathrm{l})^T$, any quaternion number $r = s + \vec{v}\vec{\mathrm{j}}$ can be separated into a scalar part $s \in \mathbb{R}$ and a vector part $\vec{v} \in \mathbb{R}^3$. Employing the quaternion algebra, the multiplication of two quaternions r_1 and r_2 yields

$$\begin{aligned} r_1 r_2 &= (s_1 + \vec{\mathrm{j}}\vec{v}_1)(s_2 + \vec{\mathrm{j}}\vec{v}_2) \\ &= s_1 s_2 - \vec{v}_1\vec{v}_2 + \vec{\mathrm{j}}(s_1\vec{v}_2 + s_2\vec{v}_1 - \vec{v}_1 \times \vec{v}_2) \,. \end{aligned} \tag{8.8}$$

A SO(3) rotation $\tilde{R}_\alpha$ is represented by the unit quaternion

$$r_{\vec{\alpha}} = \cos(\alpha/2) + \frac{\vec{\alpha}}{\alpha}\vec{\mathrm{j}}\sin(\alpha/2) \,. \tag{8.9}$$

Since the SO(3) is covered twice in the SU(2), the quaternions $r_{\vec{\alpha}}$ and $-r_{\vec{\alpha}}$ represent the same rotation. In the quaternionic representation, the rotated vector $\vec{n}' = \tilde{R}_\alpha \vec{n}$ is obtained by the rule

$$\vec{\mathrm{j}}\vec{n}' = r_{\vec{\alpha}}(\vec{\mathrm{j}}\vec{n})r_{\vec{\alpha}}^{-1} \tag{8.10}$$

with the inverse $r_{\vec{\alpha}}^{-1} = r_{\vec{\alpha}}^*/(r_{\vec{\alpha}}^* r_{\vec{\alpha}})$. Consequently, two consecutive rotations r_1 and r_2 are combined by a quaternion multiplication $r = r_1 r_2$.

To calculate the time evolution of the rotation r, we first apply an infinitesimal rotation $r' \approx 1 + \vec{b}_{\text{eff}}\vec{\mathrm{j}}dt$ to r by a quaternion multiplication,

$$\begin{aligned} r'r &= (1 + \vec{b}_{\text{eff}}\,\vec{\mathrm{j}}\,dt)(s + \vec{v}\,\vec{\mathrm{j}}) \\ &= s - \vec{b}_{\text{eff}}\,\vec{v}\,dt + (\vec{v} + s\,\vec{b}_{\text{eff}}\,dt + \vec{b} \times \vec{v}\,dt)\vec{\mathrm{j}}, \end{aligned} \tag{8.11}$$

which can be rewritten to the differential quotient

$$\Rightarrow \frac{r'r - r}{dt} = -\vec{b}_{\text{eff}}\,\vec{v} + (s\vec{b}_{\text{eff}} + \vec{b}_{\text{eff}} \times \vec{v})\vec{\mathrm{j}} \,. \tag{8.12}$$

For the scalar part s and the vector part $\vec{v}$, we obtain the simple EOM,

$$\partial_t s = -\vec{b}_{\text{eff}} \times \vec{v} \,, \tag{8.13a}$$

$$\partial_t \vec{v} = s\vec{b}_{\text{eff}} + \vec{b}_{\text{eff}} \times \vec{v} \,, \tag{8.13b}$$

which have to be evaluated alongside the semiclassical EOM (4.32a) and (4.32b) for the evaluation of the autocorrelation function.

8.2 Cross-correlation function

In addition to the autocorrelation function, the cross-correlation function is of particular interest for studying interacting QDs. Both are temporal correlation functions of the second order. We demonstrate that only the cross-correlation function is suitable to obtain information about the inter-QD interactions. Cross-correlation functions can be obtained in setups with two probe lasers with disjoint spectra [77, 120]. Each probe laser yields a separate autocorrelation function,

$$C_2^{(1)}(t) = \langle S_z^{(1)}(0) S_z^{(1)}(t) \rangle \ , \tag{8.14a}$$

$$C_2^{(2)}(t) = \langle S_z^{(2)}(0) S_z^{(2)}(t) \rangle \ , \tag{8.14b}$$

whereby we consider a single representative QD per subensemble. A combined measurement with both lasers provides the combined auto-correlation function,

$$\begin{aligned} C_2^{(1+2)}(t) &= \left\langle \left(S_z^{(1)}(0) + S_z^{(2)}(0) \right) \left(S_z^{(1)}(t) + S_z^{(2)}(t) \right) \right\rangle \\ &= C_2^{(1)}(t) + C_2^{(2)}(t) + C_2^{(\times)}(t), \end{aligned} \tag{8.15}$$

which consists of the sum of the individual autocorrelation functions and another contribution $C_2^{(\times)}(t)$. This additional contribution is identified as the cross-correlation function,

$$C_2^{(\times)}(t) = \langle S_z^{(1)}(0) S_z^{(2)}(t) \rangle + \langle S_z^{(2)}(0) S_z^{(1)}(t) \rangle \, . \tag{8.16}$$

In the case of uncorrelated QDs, the correlator $\langle S_z^{(i)}(0) S_z^{(j)}(t) \rangle = \langle S_z^{(i)}(0) \rangle \langle S_z^{(j)}(t) \rangle$ factorizes. Since we obtain $\langle S_z^{(i)}(t) \rangle = 0$ in the high-temperature limit, the cross-correlation function yields a finite value only if there is an interaction between the QDs. To generalize this property for finite temperatures and non-equilibrium situations, it is instructive to introduce the cross-correlation cumulant,

$$\begin{aligned} K_2^{(\times)}(t) = &\langle S_z^{(1)}(0) S_z^{(2)}(t) \rangle + \langle S_z^{(2)}(0) S_z^{(1)}(t) \rangle \\ &- \langle S_z^{(1)}(0) \rangle \langle S_z^{(2)}(t) \rangle - \langle S_z^{(2)}(0) \rangle \langle S_z^{(1)}(t) \rangle \, . \end{aligned} \tag{8.17}$$

However, in this chapter, we restrict ourselves to the high-temperature limit, and $C_2^{(\times)}(t) = K_2^{(\times)}(t)$ holds.

In the SCA, only spin-coherent product states without entanglement are realized. Accordingly, the correlator yields

$$\langle \vec{s}^{(i)} | \langle \vec{s}^{(j)} | \vec{S}^{(i)} \vec{S}^{(j)} | \vec{s}^{(i)} \rangle | \vec{s}^{(j)} \rangle = \langle \vec{s}^{(i)} | \vec{S}^{(i)} | \vec{s}^{(i)} \rangle \langle \vec{s}^{(j)} | \vec{S}^{(j)} | \vec{s}^{(j)} \rangle \ . \tag{8.18}$$

Thus, the cross-correlation function,

$$C_2^{(\times)}(t) = \frac{1}{N_C} \sum_{\mu} s_{z,\mu}^{(1)}(0) s_{z,\mu}^{(2)}(t) + s_{z,\mu}^{(2)}(0) s_{z,\mu}^{(1)}(t) \ , \tag{8.19}$$

can be trivially evaluated by an average over the classical configurations. While the combined correlation function has already been studied by Smirnov et al. [195], spin cross-correlations have not been investigated for QDs yet.

8.3 Correlation spectra

In the previous sections, the autocorrelation and cross-correlation functions were introduced as temporal expectation values. In experiments, however, it is convenient to study correlation functions in frequency space. We define the correlation spectra,

$$\tilde{C}_2^{(\alpha)}(\omega) = \frac{1}{2\pi} \int_{-\infty}^{\infty} C_2^{(\alpha)}(t) e^{-\mathrm{i}\omega t} dt, \tag{8.20}$$

as the Fourier transform of the temporal correlation functions. With this definition, the inverse transformation is given by

$$C_2^{(\alpha)}(t) = \int_{-\infty}^{\infty} \tilde{C}_2^{(\alpha)}(\omega) e^{\mathrm{i}\omega t} d\omega. \tag{8.21}$$

For numerical calculations, as well as in experiments, only a finite measurement time T_m can be covered, which determines the resolution in frequency space. However, our calculations reach long measurement times of $T_m = 10^4 T^*$ so that all relevant effects are resolved.

The evaluation of Eq. (8.21) at $t = 0$ provides important properties of the correlation spectra. Since trivially $C_2^{(1)}(0) = C_2^{(2)}(0) = 1/4$ and $C_2^{(\times)}(0) = 0$ hold in the high-temperature regime, the sum rules [77],

$$\int_{-\infty}^{\infty} \tilde{C}_2^{(1)}(\omega) d\omega = \frac{1}{4} \ , \tag{8.22a}$$

$$\int_{-\infty}^{\infty} \tilde{C}_2^{(2)}(\omega) d\omega = \frac{1}{4} \ , \tag{8.22b}$$

$$\int_{-\infty}^{\infty} \tilde{C}_2^{(\times)}(\omega) d\omega = 0 \ , \tag{8.22c}$$

follow directly. The autocorrelation spectrum is non-negative and has a spectral weight of 1/4. The cross-correlation spectrum has only non-zero contributions

when the QDs interact. The sum rule, Eq. (8.22c), yields a total spectral weight of zero. Therefore, for every positive contribution in the spectrum, there is a negative counterpart. The sum rules provide important properties of the correlation spectra, which are useful for the interpretation of the results in the following sections.

8.4 Reduction to an effective two quantum-dot system

To model a QD ensemble, we employ the Hamiltonian introduced in Eq. (3.14). In the general form, the Hamiltonian accounts not only for a self-assembled QD ensemble, but is also applicable to QD molecules [196], QD chains [197], and QD super-lattices [198]. Here, the respective geometry of the problem is encoded in the couplings J_{ij}. To reduce the computational effort, we apply the two-QD reduction introduced in Sec. 4.6. This system corresponds to the minimum number of QDs required to study the basic properties of the cross-correlation function. To maintain the correct physical results, we use the effective interaction strength J_{fluc}, Eq. (4.50). In general, the results we obtained for the two-QD reduction are also valid for QD molecules with two QDs.

To validate the quality of the effective two-QD model, we address the original problem of a large QD ensemble to define the appropriate reference. We randomly place N_{QD} QDs on a square with periodic boundary conditions and edge length $L = \sqrt{N_{\mathrm{QD}}} \times 100\,\mathrm{nm}$, see Sec. 4.6. This procedure reproduces the QD density of $n = (100\,\mathrm{nm})^{-2}$ [57]. From the random positions $\vec{R}_i$, we determine the interaction strengths $J_{ij} = J(R_{ij})$ with $R_{ij} = |\vec{R}_i - \vec{R}_j|$. For the sake of simplicity, we choose an exponential distance dependency,

$$J(R_{ij}) = \alpha \exp\left(-\frac{R_{ij}}{\rho_0}\right), \tag{8.23}$$

with the characteristic length scale $\rho_0 = 20\,\mathrm{nm}$ of the interaction and the prefactor α, which parameterizes the interaction strength.

For the simulation of a larger ensemble, we employ the box model limit $A_k^{(i)} = A_0$, restricting ourselves to $N_I = 100$ nuclear spins of the length $I = 1/2$. Hence, we neglect quadrupolar interactions. Based on the experimental results [57, 69], we set the overall interaction strength to

$$\bar{J} \;=\; \frac{1}{N_{\mathrm{QD}}} \sum_{i=1}^{N_{\mathrm{QD}}} \overline{J}_{\mathrm{fluc}}^{(i)} = \frac{1}{T^*}\,. \tag{8.24}$$

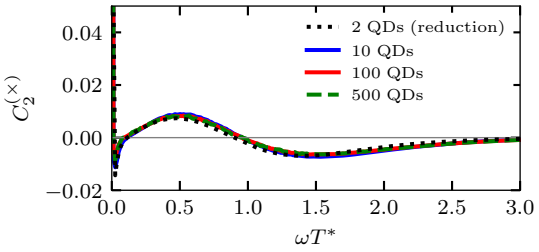

Figure 8.1: Validation of an effective two-QD model. The cross-correlation spectrum $\tilde{C}_2^{(\times)}$ of an effective two-QD model coincides with the cross-correlation spectrum for different ensemble sizes. The figure is taken from Ref. [193].

Accordingly, the inter-QD interactions have the same order of magnitude as the Overhauser field fluctuations.

In Fig. 8.1, the cross-correlation spectra for different numbers of QDs from $N_{\mathrm{QD}} = 10$ to $N_{\mathrm{QD}} = 500$ are presented as colored lines. To measure the cross-correlation function in the ensemble, we divide the QDs into two subensembles and replace $S_z^{(i)}$ in Eq. (8.19) by the averaged spin of the respective subensemble. We compare the cross-correlation spectra for ensembles of different size in the absence of an external magnetic field. In addition, the two-QD reduction is shown as a black dotted line, for which we use exponentially distributed $p(J)$, see Sec. 4.6. We postpone the physical discussion of the curves to the following sections and notice, first of all, that all curves agree very well. However, when the inter-QD interactions become larger than the Overhauser field, deviations in the low-frequency spectrum are expected, and a larger QD cluster has to be considered [195]. For the following investigations in this chapter we stick to $N_{\mathrm{QD}} = 2$ QDs.

8.5 Correlation spectra in the box-model limit

First, we investigate the correlation spectra in a simplified parameter regime. This allows for studying the generic behavior of the system, and at the same time enables the comparison to an exact quantum mechanical approach (QMA). We employ $N_{\mathrm{QD}} = 2$ QDs and switch off the external magnetic field. We retain the box-model approximation, $A_k^{(i)} = A_0$, with $N_I = 100$ nuclear spins of the length $I = 1/2$. As a result of the box-model approximation, the commutator relation $[(I_{\mathrm{tot}}^{(i)})^2, H] = 0$ with the total nuclear spin $\vec{I}_{\mathrm{tot}}^{(i)} = \sum_k \vec{I}_k^{(i)}$ holds and the Hamiltonian splits into blocks of fixed quantum numbers $I_{\mathrm{tot}}^{(i)}$. These blocks are strongly degenerate. Thus,

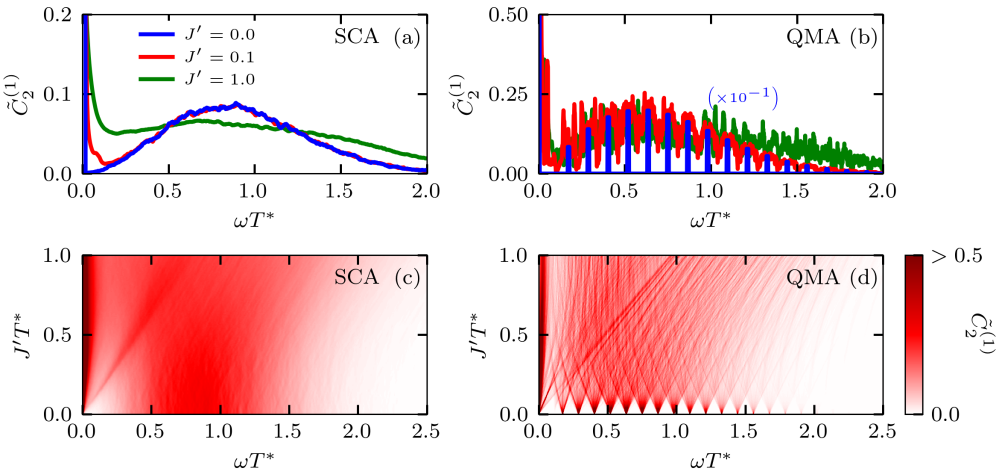

Figure 8.2: Comparison of the autocorrelation spectrum of the SCA (left panels) and the QMA (right panels). The upper panels, (a) and (b), depict the autocorrelation spectrum for a fixed J' measured in units of $1/T^*$. The legend in panel (a) applies to panel (b) as well. For a better presentation, the amplitude of the blue curve in panel (b) is reduced by the factor 10^{-1}. The lower panels, (c) and (d), depict the autocorrelation spectrum as a function of the frequency ω and the interaction strength J'. The magnitude of the correlation function is color-coded according to the legend on the right-hand side. The plots are taken from Ref. [193].

the number of states to be considered grows only quadratically and not exponentially with N_I [199]. As a consequence, the complexity of the problem reduces significantly. The quality of the SCA can be benchmarked to the QMA in a regime with many nuclear spins. To allow for a direct comparison between the SCA and the QMA, we introduce the rescaled coupling constant $J' = \sqrt{3/(4\langle S^2\rangle)}J$. Here, $\langle S^2\rangle = 1/4$ holds in the SCA, and $\langle S^2\rangle = 3/4$ holds in the QMA.

In Figs. 8.2(a) and 8.2(b), the autocorrelation spectra for three different interaction strengths J' are shown for the SCA and the QMA, respectively. Without interaction between the QDs, $J' = 0$, the QDs evolve independently of each other, and the solution factorizes to a single QD problem. In the semiclassical case, see the blue curve in Fig. 8.2(a), the result agrees with the FOA [37], see Sec. 4.7. The spectrum exhibits two peaks. A delta peak is positioned at $\omega = 0$, and a broader peak with the width $1/T^*$ is placed at $1/T^*$. The delta peak corresponds to the non-decaying component $C_2(t \to \infty)$, whereas the broader peak arises from the precession of the electron spin around a normally distributed Overhauser field. While the spectrum in the SCA is continuous, the QMA produces a Dirac comb whose envelope coincides with the SCA. The peaks arise from the transitions between a finite number of

states in quantum mechanics. In the box-model approximation, the energy levels are strongly degenerate and have a separation of $A_0 \propto 1/\sqrt{N_I}$, which approaches a continuous spectrum for large N_I. While for $J' = 0$ the total angular momentum $\vec{F}^{(i)} = \sum_k \vec{I}_k^{(i)} + \vec{S}^{(i)}$ of each individual QD is conserved, in the case of interacting QDs ($J' \neq 0$) only the total angular momentum of the QD ensemble $\vec{F}_{\mathrm{tot}} = \sum_i \vec{F}^{(i)}$ is conserved. As a consequence, the degeneracy of the sharp peaks is lifted, and the peaks fan out. The discrete spectrum in the QMA approaches the continuous classical spectrum except for some noise.

For a better illustration, in Figs. 8.2(c) and 8.2(d) the autocorrelation spectrum $\tilde{C}_2^{(1)}$ as a function of ω and J' is shown as a color map. The curves from panels (a) and (b) can be taken as horizontal cuts. While the generic behavior is essentially the same in the SCA and the QMA, the major difference comes from the discretized spectrum in the QMA. In both approaches, three qualitative effects can be recognized, which are induced by the inter-QD interactions. First, the zero-frequency peak is broadened when increasing J', since $\vec{F}^{(i)}$ and, thus, the Overhauser field is no longer conserved. Furthermore, there is an additional peak due to the inter-QD interactions at $\omega = J'$, which splits off from the zero-frequency peak. In the color plot, this peak produces a straight line starting in the origin. The third feature is a broadening of the Overhauser field peak around $1/T^*$. The additional broadening arises from the fact that the second electron spin serves as an additional noise source. In a simplified picture, the coupled electron spin adds to the Overhauser field fluctuations as another spin with the coupling constant J'.

In Fig. 8.3, the cross-correlation spectrum $\tilde{C}_2^{(\times)}$ is depicted for three fixed values of J' in panels (a) and (b). Moreover, the cross-correlations as a function of J' and ω are presented in panel (c) for the SCA and in panel (d) for the QMA as a color plot. In the color plots, strong correlations are shown in red, and anticorrelations are indicated in blue. Without interactions between the QDs, the QDs are uncorrelated, and the cross-correlations vanish. For non-zero interaction strengths, cross-correlations emerge. According to the sum rule, Eq. (8.22c), the spectrum has positive and negative contributions with equal integral weight. Except for some noise due to the discrete nature of the spectrum, the QMA essentially agrees with the SCA. The impact of the inter-QD interactions is best observed in the color plots and can be summarized by the following effects. Due to the inter-QD interactions, the zero-frequency peak splits into three parts: a positive delta peak at $\omega = 0$, anticorrelations near $\omega = 0$, and a negative peak at $\omega = J'$. The latter contribution is again reflected by a straight line in the color plot. Furthermore, the Overhauser field fluctuations are represented by two broad peaks around $1/T^*$: Positive correlations arise for smaller frequencies, and anticorrelations are observed for larger frequencies. However, the features can overlap and cancel each other.

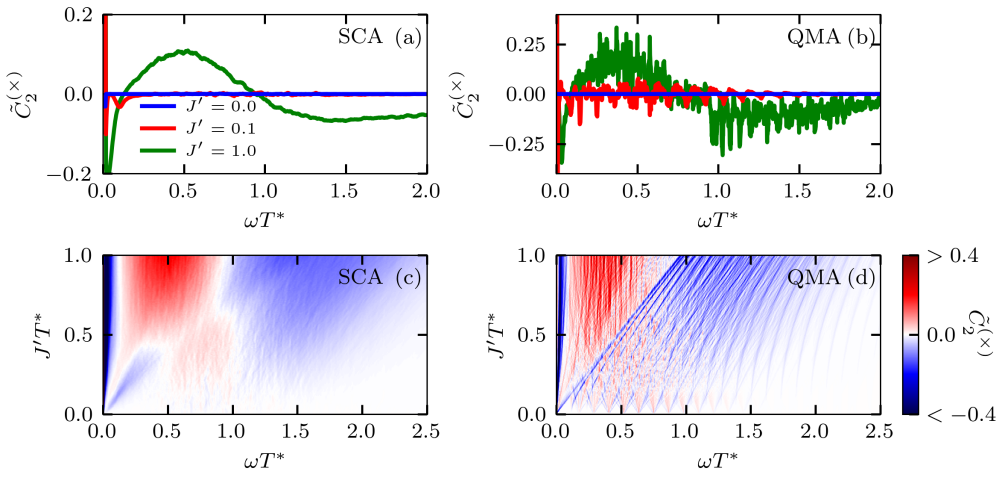

Figure 8.3: Comparison of the cross-correlation spectrum of the SCA (left panels) and the QMA (right panels). The upper panels, (a) and (b), depict the cross-correlation spectrum for a fixed coupling strength J' measured in units of $1/T^*$. The legend in panel (a) applies to panel (b) as well. The lower panels, (c) and (d), depict the cross-correlation spectrum as a function of the frequency ω and the interaction strength J'. The magnitude of the correlation function is color-coded according to the legend on the right-hand side. The plots are taken from Ref. [193].

8.6 Correlation functions in the frozen Overhauser field approximation

To explain the features of the cross-correlation spectrum in the previous section, we exploit the separation of the electronic and nuclear time scales. On the time scale of a few ns, the dynamics of the nuclear spins can be neglected, and the electron spins precess around static Overhauser fields. We address the Hamiltonian

$$H_e = \vec{S}^{(1)}\vec{b}^{(1)} + \vec{S}^{(2)}\vec{b}^{(2)} + J\vec{S}^{(1)}\vec{S}^{(2)} \tag{8.25}$$

with the static fields $\vec{b}^{(i)} = \vec{b}^{(i)}_{\text{ext}} + \vec{b}^{(i)}_N$. It is useful to introduce the average field $\vec{b}_+ = (\vec{b}^{(1)} + \vec{b}^{(2)})/2$ and the deviation field $\vec{b}_- = (\vec{b}^{(1)} - \vec{b}^{(2)})/2$. Inserting these definitions, the Hamiltonian reads

$$H_e = b_+(S_z^{(1)} + S_z^{(2)}) + \vec{b}_-(\vec{S}^{(1)} - \vec{S}^{(2)}) + J\vec{S}^{(1)}\vec{S}^{(2)} \ , \tag{8.26}$$

where we chose the quantization axis z along the direction of the average field. The transformation $U = \exp(-\mathrm{i}b_+(S_z^{(1)} + S_z^{(2)})t)$ into the rotated coordinate system of

the average field $\vec{b}_+$ yields

$$\begin{aligned} H' &= \vec{b}_-(t)(\vec{S}^{(1)} - \vec{S}^{(2)}) + J\vec{S}^{(1)}\vec{S}^{(2)} \\ &\approx b_{z,-}(S_z^{(1)} - S_z^{(2)}) + J\vec{S}^{(1)}\vec{S}^{(2)} \ , \end{aligned} \tag{8.27}$$

where b_+ vanishes and $\vec{b}_-(t)$ becomes time dependent. We can split $\vec{b}_-(t) = b_{z,-}\vec{e}_z + \vec{b}_{\perp,-}(t)$ into two parts: a time-independent part along the z axis and a fast oscillating part $\vec{b}_{\perp,-}(t)$ that we neglect. After transforming back, we obtain

$$H_e \approx b_+(S_z^{(1)} + S_z^{(2)}) + b_{z,-}(S_z^{(1)} - S_z^{(2)}) + J\vec{S}^{(1)}\vec{S}^{(2)}. \tag{8.28}$$

This Hamiltonian commutes with $S_z = S_z^{(1)} + S_z^{(2)}$, and all eigenenergies and eigenstates can be determined algebraically. The eigenenergies read

$$\epsilon_{1,2} = \frac{J}{4} \pm b_+ \ , \qquad \epsilon_{3,4} = -\frac{J}{4} \pm \sqrt{\frac{J^2}{4} + (b_{z,-})^2} \ , \tag{8.29}$$

and the corresponding eigenstates are

$$|\epsilon_{1,2}\rangle = \left|\pm\frac{1}{2}, \pm\frac{1}{2}\right\rangle \ , \tag{8.30a}$$

$$|\epsilon_{3,4}\rangle = \alpha \left|\pm\frac{1}{2}, \mp\frac{1}{2}\right\rangle \pm \sqrt{1-\alpha^2} \left|\mp\frac{1}{2}, \pm\frac{1}{2}\right\rangle \tag{8.30b}$$

with the abbreviation

$$\alpha = \frac{1}{\sqrt{2}} \frac{x}{\sqrt{1 + x^2 - \sqrt{1+x^2}}} \quad \text{and} \quad x = \frac{J}{2b_{z,-}}. \tag{8.31}$$

We note that the limit of a vanishing inter-QD interactions yields $\lim_{x\to 0} \alpha = 1$, and a strong inter-QD interaction produces $\lim_{x\to\infty} \alpha = \frac{1}{\sqrt{2}}$.

We employ the analytic eigendecomposition to determine the correlation spectra in the simplified model. The longitudinal correlation functions have the form,

$$\langle S_z^{(1)}(t) S_z^{(1)} \rangle = \frac{1}{4} + \frac{\alpha^2(1-\alpha^2)}{2}(\cos(\omega_\parallel t) - 1) \ , \tag{8.32a}$$

$$\langle S_z^{(1)}(t) S_z^{(2)} \rangle = \frac{\alpha^2(1-\alpha^2)}{2}(1 - \cos(\omega_\parallel t)) \ , \tag{8.32b}$$

with the longitudinal frequency

$$\omega_\parallel = \sqrt{J^2 + 4b_{z,-}^2} \ . \tag{8.33}$$

Both, the autocorrelation function and the cross-correlation function, consist of a constant part and an oscillating part. Consistent with the sum rules, Eq. (8.22a), (8.22b) and (8.22c), both parts have a positive sign for the autocorrelation function and an alternating sign for the cross-correlation function. Accordingly, the frequency spectrum consists of two delta peaks at $\omega = 0$ and $\omega = \omega_{\parallel}$. For the transverse components, we obtain

$$\begin{aligned}\langle S_x^{(1)}(t) S_x^{(1)} \rangle =& \frac{\alpha^2}{8} \left(\cos(\omega_\perp^{++} t) + \cos(\omega_\perp^{-+} t) \right) \\ &+ \frac{1-\alpha^2}{8} \left(\cos(\omega_\perp^{+-} t) + \cos(\omega_\perp^{--} t) \right) \ , \end{aligned} \tag{8.34a}$$

$$\begin{aligned}\langle S_x^{(1)}(t) S_x^{(2)} \rangle =& \frac{\sqrt{\alpha^2(1-\alpha^2)}}{8} (-\cos(\omega_\perp^{++} t) - \cos(\omega_\perp^{-+} t) \\ &+ \cos(\omega_\perp^{+-} t) + \cos(\omega_\perp^{--} t)), \end{aligned} \tag{8.34b}$$

with the four frequencies

$$\omega_\perp^{\pm+} = b_+ \pm \left(\frac{J}{2} + \sqrt{\frac{J^2}{4} + b_{z,-}^2} \right) \ , \tag{8.35a}$$

$$\omega_\perp^{\pm-} = b_+ \pm \left(\frac{J}{2} - \sqrt{\frac{J^2}{4} + b_{z,-}^2} \right) \ . \tag{8.35b}$$

Due to the rotational symmetry around the z axis, the same result is obtained for the y direction. For the limiting case $J \to 0$, the cross-correlation functions are consistently zero. For a better interpretation of the results, we have to bear in mind that the longitudinal correlation function and transversal correlation functions are chosen with respect to the average field $\vec{b}_+$ and not with respect to the external magnetic field $\vec{b}_{\text{ext}}$. This distinction becomes negligible in the case of a strong external magnetic field. For zero external magnetic field, the field $\vec{b}_+$ corresponds to the Overhauser field and is isotropically distributed in the high-temperature limit. Accordingly, the contributions along x, y, and z axis mix with equal ratios. The classical configuration average over the randomly distributed Overhauser field finally yields a continuous spectrum.

For the calculation of the cross-correlation spectrum in Fig. 8.3, the external magnetic field is absent. As a result, the spectrum consists equally of longitudinal and transverse components. The longitudinal components produce the zero frequency peak and the peak at $\omega_{\parallel} \approx J'$. The transverse components generate the positive and negative components around $1/T^*$. The negative components close to zero, which correspond to very slow dynamics, are not included in the minimal model employed here since the dynamics of the nuclear spins are neglected.

8.7 Distribution of the coupling constants

We introduce the randomness of the coupling constants in the QD ensemble to study the influence of hyperfine coupling constants, the nuclear-electric quadrupolar interactions, the external magnetic field, and the distribution of the electron g factors in the upcoming sections. We examine a system of $N_{\mathrm{QD}} = 2$ QDs with $N_I = 100$ nuclear spins each. This system represents either a QD ensemble in the two-QD reduction or a QD molecule. The nuclear spins are assigned the length $I = 3/2$ which coincides with Ga and As. For the hyperfine coupling distribution, we assume a typical wave function of the electron spin and exploit that $A_k \propto |\psi(\vec{r}_k)|^2$ holds. For a Gaussian wave function, $\psi(\vec{r}) \propto \exp(-r^2/(2L^2))$, and a flat 2D QD with the characteristic length L, we obtain the probability distribution [118]

$$p(A_k) = \frac{L^2}{R^2}\frac{1}{A_k}. \tag{8.36}$$

Here, $R > L$ is the cutoff radius and defines the smallest hyperfine constant A_{min}. We use $R = 2L$ and determine the maximum hyperfine constant A_{max} by the condition, Eq. (3.4).

For the inter-QD interaction, we employ an exponential distribution with the mean value $\overline{J} = 1/T^*$ (see Sec. 4.6). Finally, the effect of the quadrupolar interactions is investigated. For this purpose, we adhere to the parameters introduced in Ref. [74]. We use uniformly distributed coupling constants $q_k^{(i)} \in [0, 2\overline{q}]$ with the mean value $\overline{q} = 0.015(T^*)^{-1}$, and the easy axes $\vec{n}_{Q,k}^{(i)}$ are uniformly distributed in a cone around the growth axis $\vec{e}_z$ with the apex angel $\theta_{\mathrm{max}} = 1.19$. The biaxiality is set to $\eta = 0.5$.

8.8 Effect of the nuclear-electric quadrupolar interactions

In this section, we investigate the low-frequency spectrum, which is not correctly accounted for in the FOA. For this part of the spectrum, the slow dynamics of the nuclear spins are crucial, so that the distribution of the hyperfine coupling constants and the nuclear quadrupolar interactions are relevant. In Fig. 8.4, various correlation spectra are shown in the absence of an external magnetic field. As a reference, in Fig. 8.4(a), the results for the box-model limit, $A_k^{(i)} = A_0$, are shown. Figures. 8.4(b) and 8.4(c) take into account the distribution of $A_k^{(i)}$. Moreover, in Fig. 8.4(c), the quadrupolar interactions are added as well. The autocorrelation

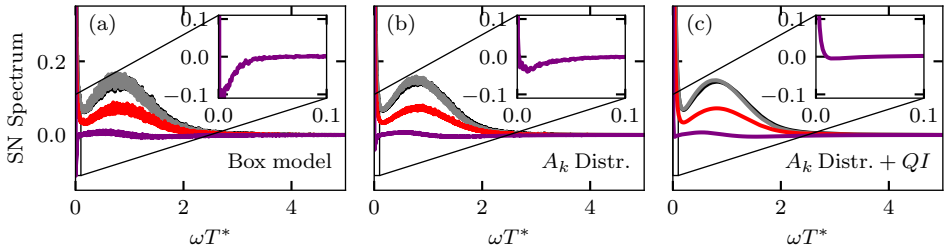

Figure 8.4: Comparison of the correlation spectra $\tilde{C}_2^{(1)}$ (red), $\tilde{C}_2^{(1+2)}$ (gray), $\tilde{C}_2^{(1)} + C_2^{(2)}$ (black), and $\tilde{C}_2^{(\times)}$ (violet) at $B_{\text{ext}} = 0$. Panel (a) uses the box-model approximation. In panels (b) and (c), the distribution in Eq. (8.36) is included. The quadrupolar interactions are only included in panel (c). The cross-correlation spectra $\tilde{C}_2^{(\times)}$ at low frequencies are enlarged in the insets. The plot is taken from Ref. [193]

spectrum $\tilde{C}_2^{(1)}$ is always indicated in red, the combined spectrum $\tilde{C}_2^{(1+2)}$ in gray, the summed spectrum $\tilde{C}_2^{(1)} + \tilde{C}_2^{(2)}$ in black, and the cross-correlation spectrum $\tilde{C}_2^{(\times)}$ in violet. Since both QDs are modeled with the same properties, $\tilde{C}_2^{(1)} = \tilde{C}_2^{(2)}$ holds.

The autocorrelation function consists of two peaks at $\omega = 0$ and $\omega = 1/T^*$. An additional peak at $\omega = J$ as proposed in Sec. 8.5 is not visible, because the couplings J are drawn from an exponential distribution, such that the associated peak is washed out. The inter-QD interactions only generate a broadening of the spectrum. Consequently, the autocorrelation spectrum does not provide any indication of inter-QD interactions, since a broadening of the peaks can also be achieved result from adjusted single QD parameters like T^*. The distribution of the hyperfine coupling constants is only relevant in the low-frequency spectrum and leads to a slight broadening of the zero-frequency peak, see Fig. 8.4(b). The quadrupolar interactions amplify this effect, see Fig. 8.4(c).

The summed and combined autocorrelation spectra exhibit the same features as the autocorrelation function and differ only slightly. Their difference defines the cross-correlation spectrum that is depicted as a violet curve. For the box-model limit in Fig. 8.4(a), the low-frequency cross-correlation spectrum has a positive delta peak at $\omega = 0$ and strong anticorrelations for small ω. We assign the latter feature to the slow dynamics of the nuclear spins. Again, the peak at $\omega = J$ is not visible, due to the randomness of the coupling constants. The high-frequency spectrum around $\omega T^* = 1$ comprises positive correlations for $\omega T^* < 1$ and anticorrelations for $\omega T^* > 1$. Again the distribution of hyperfine coupling constants, see Fig. 8.4(b), only modifies the low-frequency spectrum. The zero-frequency peak is broadened in

the cross-correlation spectrum, leading to a partial cancellation with the adjacent anticorrelations, which are significantly attenuated. The quadrupolar interactions further amplify this effect, so that the anticorrelations almost disappear at small frequencies, see Fig. 8.4(c).

8.9 Effect of the electron g-factor variation

When a transverse magnetic field is applied, the electron spin starts to precess with the Larmor frequency $\omega_L = \mu_B g_0 B_{\text{ext}}$ around the external magnetic field axis. The effective g factor of electrons in InGaAs QDs is about $g_0 = 0.55$. The nuclear spins are much less affected by the magnetic field due to the larger mass. For the ratio of between the strengths of the nuclear and electron Zeeman term, we obtain the average value $g_{N,k}^{(i)}\mu_N / g_0\mu_B \approx 1/800$ considering the different isotopes in InGaAs [136]. For a sufficiently large magnetic field, the Larmor precession of the electron spin becomes the dominant energy scale, leading to a shift of the correlation spectra to larger frequencies. This shift can be already observed in the FOA, see Sec. 8.6. For large magnetic fields, the dynamics induced by hyperfine interactions and the quadrupolar interactions are suppressed. Instead, the distribution of the electron g factors becomes relevant. The g factor of the electron spin correlates with the excitation energy [69, 104, 109] following a nearly linear relation. In addition, the g factors for a fixed excitation energy vary due to inhomogeneous growth conditions.

To illustrate both effects, we employ two g-factor distributions in the following. In distribution I,

$$\begin{aligned} g_e^{(1)} &= g_0 \ , \\ g_e^{(2)} &= 1.015 g_0 \ , \end{aligned} \tag{8.37}$$

both QDs have different but fixed g factors. In distribution II,

$$\begin{aligned} g_e^{(1)} &\sim \mathcal{N}(g_0, 0.005) \ , \\ g_e^{(2)} &\sim \mathcal{N}(1.015 g_0, 0.005) \ , \end{aligned} \tag{8.38}$$

the g factors are additionally drawn from a normal distribution whose parameters are based on experimental data [69, 104]. Figure 8.5 shows various correlation spectra for the two distributions I and II at different external magnetic fields. For distinguishing the correlation spectra, we stick to the same color coding as in Fig. 8.4.

In Figs. 8.5(a) and 8.5(b) the spectra for a weak magnetic field corresponding to the electron Larmor frequency $\omega_L = 5/T^*$ ($B_{\text{ext}} = 100\,\text{mT}$) are depicted. The

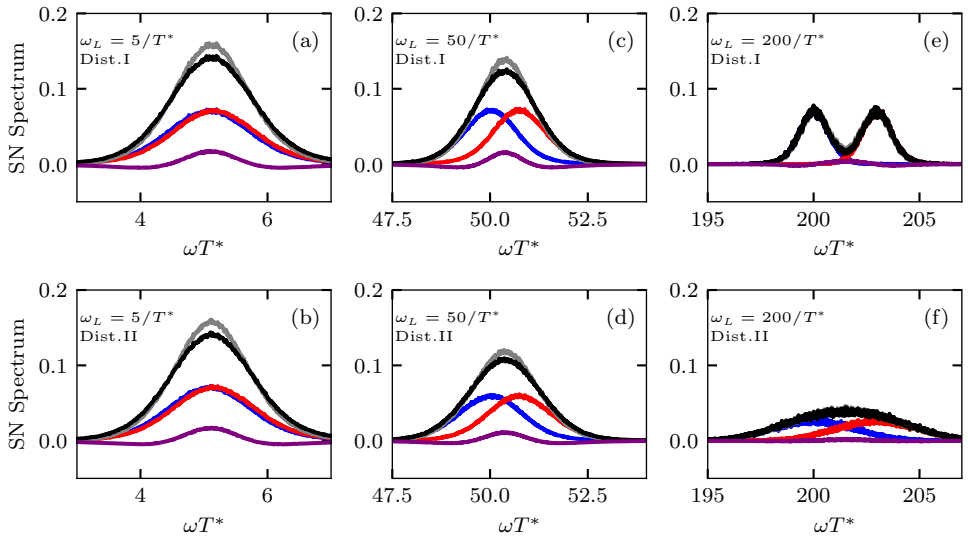

Figure 8.5: Comparison of the transversal correlation spectra $\tilde{C}_2^{(1)}$ (red), $\tilde{C}_2^{(2)}$ (blue), $\tilde{C}_2^{(1+2)}$ (gray), $\tilde{C}_2^{(1)} + \tilde{C}_2^{(2)}$ (black) and $\tilde{C}_2^{(\times)}$ (violet) for various external magnetic fields as well as electron g-factor distributions. The upper panels employ the distribution I, Eq. (8.37); the lower panels relate to the distribution II, Eq. (8.38). The external magnetic fields correspond to $\omega_L = 5/T^*$ ($B_{\text{ext}} = 100\,\text{mT}$) in panels (a) & (b), $\omega_L = 50/T^*$ ($B_{\text{ext}} = 2\,\text{T}$) in panels (c) & (d), and $\omega_L = 200/T^*$ ($B_{\text{ext}} = 4\,\text{T}$) in panels (e) & (f). The plot is taken from Ref. [193].

autocorrelation spectra $\tilde{C}_2^{(i)}$ have a Gaussian shape and are centered around the Larmor frequency. The width is given by the fluctuation scale $1/T^*$. Due to the weak magnetic field, the g-factor distribution is almost irrelevant, since the energy scale $\Delta\omega = B_{\text{ext}}\mu_B(g_e^{(1)} - g_e^{(2)})$ is small compared to other energy scales of the system. The cross-correlation spectrum is centered around ω_L as well. It has positive and negative components which can be understood by the results of the FOA. For the transverse case, the four frequencies in Eqs. (8.35a) and (8.35b) are relevant. The two inner frequencies $\omega_\perp^{\pm-}$ have a positive weight and are responsible for the positive correlations at ω_L, whereas the two outer frequencies $\omega_\perp^{\pm+}$ produce the anticorrelated wings.

For a larger magnetic field of $\omega_L = 50/T^*$ ($B_{\text{ext}} = 1\,\text{T}$) the g-factor distribution becomes relevant. For distribution I, see Fig. 8.5(c), the autocorrelation functions are centered around the Larmor frequency $\omega_L^{(i)} = \mu_B g_e^{(i)} B_{\text{ext}}$ of the respective QD. For distribution II, see Fig. 8.5(d), the centers remain the same, but there is an additional broadening due to the g-factor variation. The shape of the cross-correlation function

is similar to the result for weaker magnetic fields: It is centered around the mean Larmor frequency. Only the amplitude of the cross-correlation function decreases due to the additional g-factor variation.

For very large magnetic fields, $\omega_L = 200/T^*$ ($B_{\text{ext}} = 4\,\text{T}$), see Figs. 8.5(e) and 8.5(f), the autocorrelation functions separate, since the energy scale $\Delta\omega_L$ exceeds the fluctuation scale $1/T^*$. This leads to a significant reduction of the amplitude of the cross-correlation spectrum, since the prefactor α in Eq. (8.31) decreases. For distribution II, there is an additional cancellation of the positive and negative components. Hence, the cross-correlations almost completely vanish.

8.10 Correlation spectra in a longitudinal magnetic field

Finally, the cross-correlation spectrum in the longitudinal magnetic field is examined. According to the FOA, see Eq. (8.32b), contributions essentially appear at two frequencies, $\omega = 0$ and $\omega = \omega_\parallel$. These contributions are not shifted to higher frequencies by the external magnetic field. Thus, long-time effects, such as the quadrupolar interactions, are relevant in a longitudinal field in contrast to the transversal field. Furthermore, the electron g-factor distribution contributes to the spectrum due to the non-zero magnetic field. In Fig. 8.6(a), the correlation spectra for a weak magnetic field, $\omega_L = 5/T^*$, are shown using the same color coding as in the previous figures. The distribution of the hyperfine coupling constants, the quadrupolar interactions, and the g-factor distribution II are included in the dynamics. The autocorrelation spectra, red and blue, consist of a zero-frequency peak broadened by the quadrupolar interactions and contributions at the Larmor frequency due to the mixing with the transverse component at a weak magnetic field, cf. Sec. 8.6. The cross-correlation spectrum consists of a positive delta peak at $\omega = 0$ (not visible), and two negative peaks close to $\omega = 0$ and at $\omega = \overline{J} = 1/T^*$. We can assign the positive peak at $\omega = 0$ and the broad negative peak at $\omega = \overline{J}$ to the two frequencies in the solution of the FOA, Eq. (8.32b). The negative peak close to zero is attributed to the slow nuclear spin dynamics. For strong inter-QD interactions, the frequency $\omega_\parallel$ approximately coincides with the interaction strength of the inter-QD interaction, $\omega_\parallel \approx J$. Therefore, the related peak in the cross-correlation spectrum enables the study of the distribution $p(J)$

To reveal the effect of the quadrupolar interactions and the electron g factors, the cross-correlation spectrum for larger magnetic fields is shown in Fig. 8.6(b), $\omega_L = 50/T^*$, and Fig. 8.6(c), $\omega_L = 200/T^*$. We separate the individual effects by examining the four possibilities of (i) quadrupolar interactions on or off and (ii)

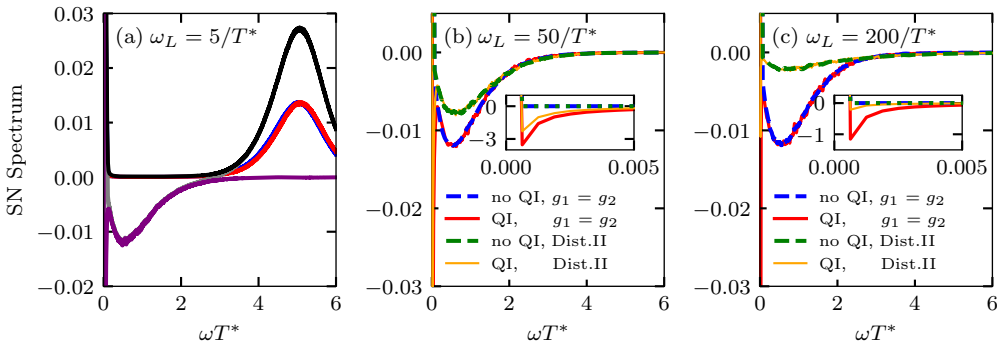

Figure 8.6: (a) Correlation spectra $\tilde{C}_2^{(1)}$ (blue), $\tilde{C}_2^{(2)}$ (red), $\tilde{C}_2^{(1+2)}$ (gray), $\tilde{C}_2^{(1)} + \tilde{C}_2^{(2)}$ (black), and $\tilde{C}_2^{(\times)}$ (violet) in a longitudinal magnetic field corresponding to $\omega_L = 5/T^*$. (b) and (c) Cross-correlation spectrum $\tilde{C}_2^{(\times)}$ for the four combinations of: (i) quadrupolar interactions switched on and off and (ii) equal electron g factors or g-factor distribution II (see Eq. (8.38)). The external magnetic field corresponds to (b) $\omega_L = 50/T^*$ and (c) $\omega_L = 200/T^*$. The plot is taken from Ref. [193].

equal g factors or g-factor distribution II. The quadrupolar interactions are only relevant for the low-frequencies. The additional nuclear spin dynamics induced by quadrupolar interactions produce negative cross-correlations close to $\omega = 0$ that are absent without quadrupolar interactions. However, the quadrupolar interactions are suppressed by the nuclear Zeeman effect [73], so that the peak is attenuated at large magnetic fields. The distribution of the electron g factors does not affect the shape of the cross-correlation spectrum but leads to a substantial reduction of the amplitude, especially for large magnetic fields.

8.11 Connection to experiments

The autocorrelation spectrum or power spectrum has been experimentally extensively studied [73]. It reveals the spin dynamics in equilibrium and provides information about various interactions. However, our investigation shows that the autocorrelation spectrum is not sensitive to inter-QD interactions. Accordingly, theoretical descriptions with independent QDs are sufficient [74, 118]. The inter-QD interactions only produce a modification of the peak widths but do not change the autocorrelation spectrum qualitatively. The modification of the peak widths can be absorbed in a renormalized single-QD dephasing time $\tilde{T}^*$, so all previous studies are compatible with an extension to interacting QDs. In contrast, the cross-correlation spectrum has not been experimentally studied for QDs. There have been spin-noise

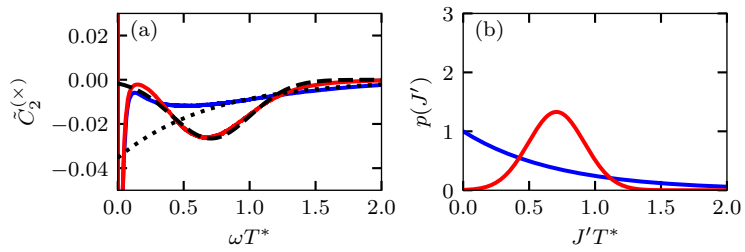

Figure 8.7: Effect of the distribution $p(J')$ on the cross-correlation spectrum in a longitudinal magnetic field corresponding to $\omega_L = 5/T^*$. (a) Cross-correlation spectrum. The black dashed and dotted lines are exponential and Gaussian fits to the cross-correlation spectrum. (b) Associated distributions $p(J')$. The red curves belong to a Gaussian distribution with the mean value $\overline{J} = 1/T^*$ and the standard deviation $\sigma = 0.3/T^*$. The blue curves belong to an exponential distribution with the mean value $\overline{J} = 1/T^*$. The plot is taken from Ref. [193].

measurements, which measured $\tilde{C}_2^{(1)}$, $\tilde{C}_2^{(2)}$, and $\tilde{C}_2^{(1+2)}$ for a QD ensemble in the absence of an external magnetic field to determine the homogeneous linewidth of a QD [120]. From these quantities, in principle, the cross-correlation spectrum $\tilde{C}_2^{(\times)}$ could be determined. In the investigated frequency range, $\tilde{C}_2^{(\times)}$ vanishes within the measurement accuracy. This result agrees with our predictions since the experiment focused on small frequencies at which the quadrupolar interactions lead to substantial suppression of the spectrum.

Our studies suggest that there is a window at weak magnetic fields at which the cross-correlation spectrum can be studied particularly well. In the absence of an external magnetic field, the quadrupolar interactions suppress cross-correlations, while in the presence of a very strong magnetic field, the electron g-factor variation leads to the attenuation of cross-correlations. The cross-correlation spectrum is of special interest in the presence of a longitudinal magnetic field since it provides insight into the distribution of the inter-QD coupling constants in the QD ensemble. In Fig. 8.7, the cross-correlation spectrum in a longitudinal magnetic field for two different distributions $p(J')$ is shown as an example. The cross-correlation spectrum is depicted in Fig. 8.7(a) and the corresponding distributions $p(J')$ are presented in Fig. 8.7(b). For large frequencies, the cross-correlation spectrum and the distribution $p(J')$ coincide. This finding allows for obtaining additional information about the microscopic interaction mechanism.

Chapter 9

Higher-order cross-correlation spectra in non-equilibrium

For potential applications in spintronics and quantum information processing, a coherent manipulation of the qubits in the system is desired. For this purpose, we investigate non-equilibrium spin states that arise from periodic laser pulse trains. In pump-probe experiments, it was observed that the Overhauser field distribution can be coherently manipulated [111]. Under periodic optical excitation, the spin system synchronizes with the repetition rate of the pulses. The optically induced non-equilibrium spin state remains stable for several minutes to hours, even if the periodic excitation is switched off [47, 200]. This spin mode-locking effect is the basis of many theoretical investigations [48, 62–64, 109, 176, 194, 200–202], that consistently assume non-interacting QDs. In this chapter, we examine the effect of periodic pulse sequences on interacting QDs. We show that the pulse train imposes a strong correlation between the Overhauser fields of different QDs, which is an interesting aspect in the generation of tailored non-equilibrium states. Since only the electron spin dynamics are measurable in pump-probe experiments, the Overhauser field correlations remain hidden in single-color pump-probe experiments. We illustrate that the Overhauser field correlations can be measured indirectly via cross-correlation functions, where the fourth-order cross bi-spectrum proves to be particularly useful.

After establishing the model in Sec. 9.1, we address the mode-locking effect in a single QD in Sec. 9.2 to provide a reference for the following investigations. Afterward, we focus on interacting QDs and study the effect of the pulse sequence on second-order correlation functions in Sec. 9.3. In Secs. 9.4 to 9.6, we examine the effect of the pulse sequence on the Overhauser field distribution, and finally, in Sec. 9.7, we investigate the cross-correlation bi-spectrum.

9.1 Model and methods

We investigate the influence of periodic pulse trains on interacting QDs. While the electron spins precess in the external magnetic field of $B_{\text{ext}} = 1\,\text{T}$ on the time scale of 100 ps, the spin mode-locking effect emerges on the time scale of seconds [47]. Accordingly, about ten orders of magnitude in time must be bridged in the numerical simulation. Therefore, we restrict ourselves to the essential effects to reach the periodically driven quasi-equilibrium state as close as possible.

We employ the Hamiltonian, Eq. (3.14), and take into account the external magnetic field, the hyperfine interaction between the electron spin and the nuclear spins, as well as the interaction between the QDs. Less relevant effects like nuclear-electric quadrupolar or dipole-dipole interactions are neglected. We restrict ourselves to $N_{\text{QD}} = 2$ QDs, as the reduction to an effective two-QD model has proven to be adequate in the previous chapters. The model either describes a QD molecule consisting of two QDs or a QD ensemble for the case of weak inter-QD interactions. We include $N_I = 100$ nuclear spins with the length $I = 3/2$ in box-model approximation, which has the numerical advantage that all nuclear spins in the QD remain synchronized and can be combined in a single vector $\vec{i}^{(i)} = \sum_k \vec{i}_k^{(i)}$ per QD. The spins are subject to an external magnetic field in Voigt geometry with $b_{\text{ext}} = 50/T^*$. This field is equal for both QDs and corresponds to roughly 1 T. For the evaluation of the correlation functions, we employ the quaternion based approach, see Sec. 8.1. The periodic optical excitation is modeled by instantaneous π pulses, and the trion decay is captured by the quantum jump approach outlined in Sec. 5.5.

9.2 Nuclear-induced frequency-focusing for a single quantum dot

The repetition time T_R of a periodic pulse train is imprinted on the spin dynamics of the driven system. In the case of a periodically pulsed QD, the synchronization emerges in a two-stage process. The electron spin approaches its quasi-equilibrium state on a time scale on which the dynamics of the nuclear spins can be considered frozen. On a much longer time scale, the repetition rate of the laser pulses is transferred to the nuclear spins via the hyperfine interaction. In this process, the Overhauser field adjusts in such a way that the electron spin performs a (half-)integer number of revolutions within a repetition period T_R. This effect is called nuclear-induced frequency-focusing (NIFF).

An analytical mechanism that explains the NIFF was presented by Glazov et al. [48]. The authors demonstrate that the averaged Knight field has a component in the

magnetic field direction that oscillates with the nuclear Larmor frequency. This component in turn drives the nuclear spins resonantly similar to the nuclear magnetic resonance (NMR). Once the nuclear spins are aligned so that the electron spin performs an integer number of revolutions during T_R, the driving ends, and the nuclear spins have reached their non-equilibrium steady state. This process generates a comb-like structure of the Overhauser field distribution. In further numerical investigations, half-integer modes of the electron spins have been found [61–63, 136]. In the following, we present a calculation inspired by Ref. [48] where we include the relevant term that allows for half-integer spin precession modes as well.

First, we focus on a short time scale, on which the nuclear spins are considered frozen, and determine the electronic steady state. After a pulse, the electron spin $\vec{S}$ is subject to the sum $\vec{b} = b\vec{n} = \vec{b}_{\text{ext}} + \vec{b}_N$ of the external magnetic field $\vec{b}_{\text{ext}} = b_{\text{ext}}\vec{e}_x$ and the Overhauser field $\vec{b}_N$ while the trion decays into the spin up state

$$\partial_t \vec{S} = \vec{b} \times \vec{S} + \frac{P_T}{2}\vec{e_z} \,, \tag{9.1a}$$

$$\partial_t P_T = -\gamma P_T \,. \tag{9.1b}$$

The repopulation of the spin-up state governed by the trion term $P_T\vec{e_z}/2$ was neglected in Ref. [48], which prevents the half-integer modes.

We apply a resonant π pulse whose effect is given by

$$\vec{S}^+ = \left(\frac{S_z^-}{2} - \frac{1}{4}\right)\vec{e}_z \,, \tag{9.2a}$$

$$P_T^+ = S_z^- + \frac{1}{2} \,, \tag{9.2b}$$

where $\vec{S}^\pm$ and $P_T^\pm$ are the spin and trion components before (-) and after (+) the pulse, and P_T^- is assumed to be zero. The trion population and the spin components before the next pulse are given by the time evolution,

$$\vec{S}^- = (\vec{n}\vec{c}_1)\vec{n} + (\vec{c}_1 - (\vec{n}\vec{c}_1)\vec{n})\cos(bT_R) + (\vec{n} \times \vec{c}_1)\sin(bT_R) + \vec{c}_2 \exp(-\gamma T_R) \tag{9.3}$$

with the constants

$$\vec{c}_1 = \vec{S}^+ - \vec{c}_2 \,, \tag{9.4a}$$

$$\vec{c}_2 = -\frac{P_T^+}{2}\frac{1}{\gamma^2 + b^2}(b_z\vec{b} + \gamma^2\vec{e}_z + \gamma\vec{b} \times \vec{e}_z). \tag{9.4b}$$

The electronic steady state are determined from a self-consistency equation obtained by combining Eqs. (9.2a) to (9.4b). In the limit of a strong external field, $\gamma \ll b_{\text{ext}}$

and $b_N \ll b_{\text{ext}}$, Eq. (9.3) reduces to $S_z^- = S_z^+ \cos(bT_R)$ revealing the electronic steady state,

$$S_z^+ = \frac{1}{2\cos(bT_R) - 4}\,, \tag{9.5a}$$

$$P_T^+ = \frac{\cos(bT_R) - 1}{\cos(bT_R) - 2}\,. \tag{9.5b}$$

The nuclear spins cannot follow the fast electron spin dynamics and are essentially exposed to the Knight field averaged over one repetition period,

$$\begin{aligned}\vec{\overline{S}} &= \frac{1}{T_R}\int_0^{T_R} \vec{S} dt \\ &= (\vec{n}\vec{c}_1)\vec{n} + \frac{\vec{c}_1 - (\vec{n}\vec{c}_1)\vec{n}}{bT_R}\sin(bT_R) + \frac{\vec{n}\times\vec{c}_1}{bT_R}(1-\cos(bT_R)) \\ &+ \frac{\vec{c}_2}{\gamma T_R}(1-\exp(-\gamma T_R))\,.\end{aligned} \tag{9.6}$$

We determine the averaged electron spin $\vec{\overline{S}}$ in the leading order of $b_{\text{ext}} \gg b_N$,

$$\vec{\overline{S}} = \begin{pmatrix} S_z^+ \frac{b_{N,z}}{b} \\ -\frac{S_z^+}{bT_R}\frac{\gamma}{b}(\cos(bT_R)-1)\left(\sin(bT_R) + \frac{\gamma}{b}(1-\cos(bT_R))\right) \\ \frac{S_z^+}{bT_R}\left(\sin(bT_R) + \frac{\gamma}{b}(\cos(bT_R)-1)\left(\frac{\gamma}{b}\sin(bT_R) + \cos(bT_R)\right)\right) \end{pmatrix}\,. \tag{9.7}$$

While $\overline{S}_y$ and $\overline{S}_z$ are approximately constant, $\overline{S}_x$ is proportional to

$$b_{N,z} \approx A_0 I_\perp \cos(z b_{\text{ext}} t + \varphi) \tag{9.8}$$

with $I_\perp = \sqrt{I^2 - I_x^2}$ and, thus, oscillates with the nuclear Larmor frequency $z b_{\text{ext}}$. For the nuclear spins, we have the situation typical for NMR [48] with the constant field

$$\vec{b}_{\text{const}} = \begin{pmatrix} z b_{\text{ext}} \\ A_0 \overline{S}_y \\ A_0 \overline{S}_z \end{pmatrix} \tag{9.9}$$

and the driving field

$$\vec{b}_{\text{NMR}} = \begin{pmatrix} A_0 S_z^+ \frac{b_{N,z}}{b} \\ 0 \\ 0 \end{pmatrix}\,. \tag{9.10}$$

As the averaged Knight field $A_0\overline{S}$ is much weaker than the external magnetic field zb_{ext}, the constant field $\vec{b}_{\text{const}}$ and the driving field $\vec{b}_{\text{NMR}}$ are almost parallel. However, for the dynamical formation of a nuclear spin polarization in x direction, only the driving field perpendicular to the constant field contributes. As the driving field is aligned in the x direction, it is crucial that the constant field is tilted off the x axis.

To calculate the driving rate of the Overhauser field $b_{N,x}$, we follow the general theory of NMR [48]. The driving NMR field $A_0\overline{S}_x(t)$ produces a shift of the averaged component $\overline{I}_z$. In the leading order of A_0, we obtain [48]

$$\overline{I}_z \approx -\frac{A_0^2 I_\perp^2 S_z^+}{2zb^2} \,, \tag{9.11}$$

while $\overline{I}_y = 0$ vanishes caused by $\overline{S}_x(t) \propto b_{N,z}$. For the rate of the dynamic nuclear polarization, we employ the established NMR expression [48],

$$\begin{aligned} \partial_t I_x &= A_0\overline{S}_y\overline{I}_z - A_0\overline{S}_z\overline{I}_y \\ &= -\frac{A_0^3 I_\perp^2 S_z^+ \overline{S}_y}{2zb^2} \,, \end{aligned} \tag{9.12}$$

and, therefore, the Overhauser field obeys

$$\begin{aligned} \partial_t b_{N,x} &= A_0 \partial_t I_x \\ &= -\frac{A_0^4 I_\perp^2 S_z^+ \overline{S}_y}{2zb^2} \,. \end{aligned} \tag{9.13}$$

The rate, Eq. (9.13), determines how fast the Overhauser field is driven. First, the rate exhibits a dependence $\propto b^{-2}$, which agrees with the results of Refs. [63, 136]. Second, assuming that $I_\perp \propto \sqrt{N_I}$, the rate scales with $A_0^4 N_I = A_0^2 (T^*)^{-2}$, which matches the observation of Ref. [62]. Whenever $\overline{S}_y$ vanishes, the dynamics of I_x freeze. The condition $\overline{S}_y = 0$ yields

$$bT_R = 2n\pi \vee bT_R = 2n\pi + 2\tan^{-1}\left(\frac{b}{\gamma}\right) \tag{9.14}$$

$$\overset{b\gg\gamma}{\Rightarrow} bT_R = n\pi \tag{9.15}$$

with $n \in \mathbb{Z}$ in agreement with Ref. [62]. The resonance condition contains both, integer and half-integer numbers of revolutions of the electron spin in the interval T_R. If the resonance condition, Eq. (9.14), is fulfilled, the driving field $\vec{b}_{\text{NMR}}$ does not vanish, but becomes parallel to $\vec{b}_{\text{const}}$.

In Fig. 9.1, numerical results of the electron and nuclear spin dynamics during a periodic pulse train are presented. We focus on a single QD $N_{\text{QD}} = 1$, and all

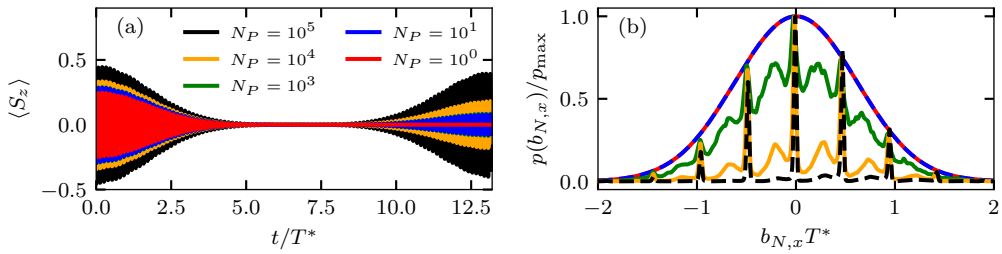

Figure 9.1: Spin dynamics induced by a periodic pulse train. (a) Electron spin dynamics after the incidence of N_P laser pulses. (b) Overhauser field distribution (OHD) after N_P pulses. For illustration, the OHD $p(b_{N,x})$ is divided by its maximum value $p_{\max}$. Both panels employ the same color code.

other parameters comply with Sec. 9.1. The pulse train consists of σ^+ polarized pulses with the repetition time $T_R = 13.2T^*$. Figure 9.1(a) depicts the electron spin dynamics between two consecutive pulses. While the spin polarization dephases on the time scale T^* after the first pulse, the electronic steady state leads to a revival of the spin polarization directly before the next pulse already after $N_P = 10$ pulses.

To study the effect of optical excitation on the nuclear spins, we examine the Overhauser field distribution (OHD) $p(b_{N,x})$, which we obtain by processing the Overhauser fields $b^{\mu}_{N,x}$ of each classical configuration μ in a histogram. The results are depicted in Fig. 9.1(b). The OHD is initially Gaussian distributed due to the central limit theorem and retains this shape after $N_P = 10$ pulses due to the slow nuclear dynamics. After about $N_P = 10^3$ pulses, peaks are formed in the OHD due to the resonance condition, Eq. (9.14). The sharp peaks correspond to an integer number of electron spin revolutions, and the broader peaks are related to a half-integer number of electron spin revolutions. In the regime investigated here, the integer modes become more pronounced during the pulse sequence, while the half-integer modes deplete. For $N_P = 10^5$, almost only integer modes are favored. The comb-like OHD leads to commensurate electron spin precession frequencies, which strongly amplify the electron spin revival.

9.3 Breaking time-translation invariance

We continue with the dynamics of two interacting QDs. Both QDs are excited with σ^+ polarized pulses at the times nT_R with $n \in \mathbb{N}_0$ and $T_R = 13.2T^*$. This corresponds to a situation where the spectral width of the laser is large enough to

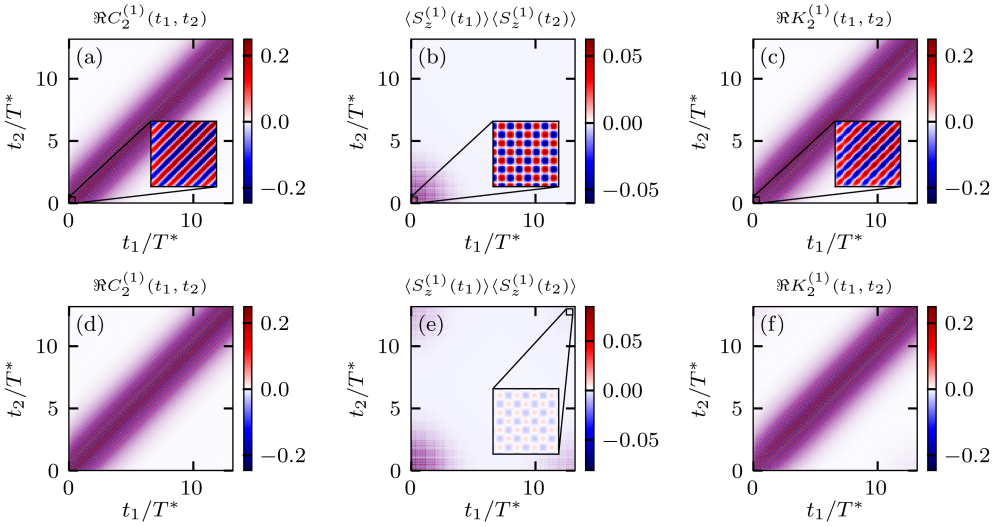

Figure 9.2: Real part of the autocorrelation function between two consecutive pulses as a function of the times t_1 and t_2. The upper panels display the results after the first pulse, and the lower panels are obtained after a pulse sequence of $N_P = 10^5$ pulses. The panels (a) and (d) depict the autocorrelation function $\Re C_2^{(1)}(t_1, t_2)$, the panels (b) and (e) the factorization $\langle S_z^{(1)}(t_1)\rangle \langle S_z^{(1)}(t_2)\rangle$ and the panels (c) and (f) the cumulant $\Re K_2^{(1)}(t_1, t_2)$.

resonantly excite both QDs simultaneously. The mean interaction strength $\overline{J} = T^*$ is chosen in the order of magnitude of the Overhauser field fluctuations.

We study second-order correlation functions of the type $\langle S_z^{(i)}(t_1) S_z^{(j)}(t_2)\rangle$ as they can be extracted from spin-noise spectroscopy. For $i = j$, we recover the conventional second-order autocorrelation function $C_2^{(i)}$. For $i \neq j$, we obtain the second-order cross-correlation function $C_2^{(\times)}$. In equilibrium, these correlation functions depend only on the time difference $\Delta t = t_2 - t_1$ due to the time-translation invariance. However, optical excitation breaks the time-translation invariance, and the correlator may depend non-trivially on both times. Since the autocorrelation function $C_2^{(i)}$ is complex in general, we first address the experimentally accessible real part,

$$\Re C_2^{(1)} = \frac{1}{2}\left[C_2^{(1)} + \left(C_2^{(1)}\right)^\dagger\right] . \tag{9.16}$$

In Fig. 9.2, the symmetrized correlator $\Re C_2^{(1)}$, the direct product $\langle S_z^{(1)}(t_1)\rangle \langle S_z^{(1)}(t_2)\rangle$, and the cumulant $\Re K_2^{(1)}$ are shown as a function of t_1 and t_2. The upper panels depict the dynamics after the first pulse, and the lower panels after a sequence

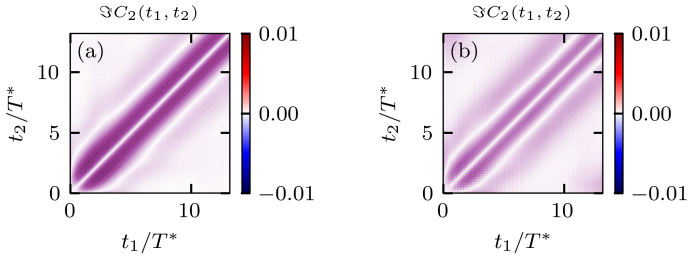

Figure 9.3: Imaginary part of the auto-correlation function $\Im C_2(t_1, t_2)$ as a function of the times t_1 and t_2, (a) after a single pulse at $t = 0$ and (b) after a pulse sequence of $N_P = 10^5$ pulses.

of $N_P = 10^5$ pulses. We note that the factorization $\langle S_z^{(1)}(t_1)\rangle \langle S_z^{(1)}(t_2)\rangle$ contains information, which can be extracted from regular pump-probe measurements.

The correlator $\Re C_2^{(1)}$ in Fig. 9.2(a) is pronounced around the diagonal $t_1 = t_2$. When the deviation Δt exceeds the dephasing time T^*, the amplitude of $\Re C_2^{(1)}$ decreases significantly. The fast oscillations, see the inset, arise from the electron Larmor precession in the external magnetic field. Independent of the pulse incidence, $\Re C_2$ depends solely on the difference Δt. In the factorization, see Fig. 9.2(b), the pulse at $t = 0$ is clearly visible. The signal reduces once the average time $\bar{t} = (t_1 - t_2)/2$ is large compared to T^*. In addition, the oscillation, see the inset, depend explicitly on t_1 and t_2, and not only on Δt. The cumulant $\Re K_2^{(1)}$, see Fig. 9.2(c), is translational invariant for large times $\bar{t}$ while the time-translation invariance is broken for times $\bar{t}$ close to the incidence time of the pulse.

During a long pulse sequence, $\Re C_2$ remains unchanged, see Fig. 9.2(d). In the factorization $\langle S_z^{(1)}(t_1)\rangle \langle S_z^{(1)}(t_2)\rangle$, however, additional revivals form for $t_1/T^* \approx 13.2$ or $t_2/T^* \approx 13.2$, see the corners of Fig. 9.2(e). The cumulant $\Re K_2^{(1)}$, see Fig. 9.2(f), essentially constitutes a combination of both the autocorrelator and the factorization.

From a theoretical perspective, it is also interesting to study the imaginary part of the correlator. Although it is not experimentally accessible, it acquires a non-zero value due to the broken spin-inversion symmetry. While the imaginary part would disappear in a conventional semiclassical evaluation of the autocorrelation function, the quaternion-based method, Eq. (8.7), enables access to the imaginary part. The imaginary part $\Im \langle S_z^{(i)}(t_i)\rangle$ is trivially zero, since $S_z^{(i)}$ is hermitian. Thus, the factorization $\Im[\langle S_z^{(i)}(t_1)\rangle \langle S_z^{(i)}(t_2)\rangle] = 0$ vanishes, and $\Im C_2^{(i)} = \Im K_2^{(i)}$ holds. Consequently, we restrict ourselves to the presentation of $\Im C_2^{(1)}$ in Fig. 9.3. In

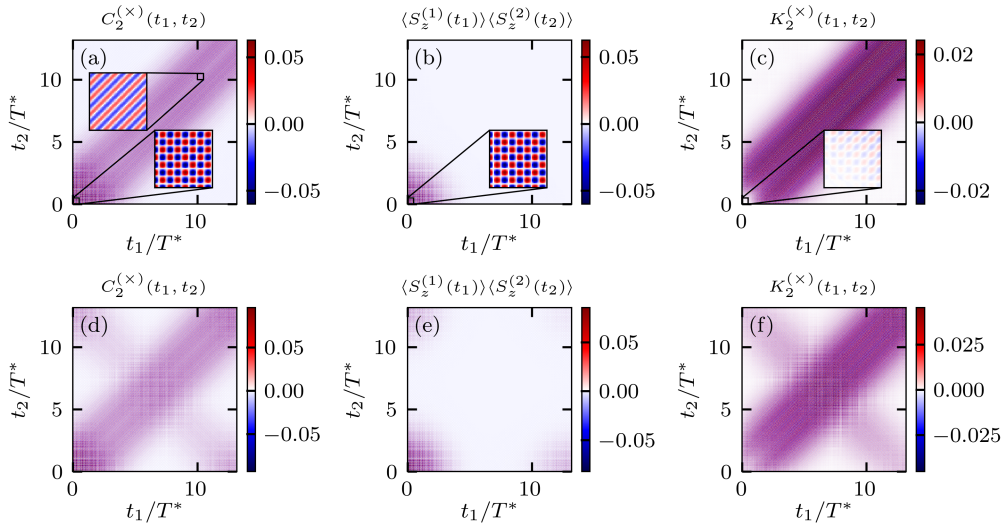

Figure 9.4: Cross-correlation function between two consecutive pump pulses as a function of the times t_1 and t_2. The upper panels display the result after a single pulse at $t = 0$, and the lower panels are obtained after a pulse sequence of $N_P = 10^5$ pulses. The panels (a) and (d) depict the cross-correlation function $C_2^{(\times)}(t_1, t_2)$, the panels (b) and (e) the factorization $\langle S_z^{(1)}(t_1)\rangle \langle S_z^{(2)}(t_2)\rangle$, and the panels (c) and (f) the cumulant $K_2^{(\times)}(t_1, t_2)$.

Fig. 9.3(a), the imaginary part of $C_2^{(i)}$ is shown after the first pulse. By definition, $\Im C_2^{(1)}$ vanishes for $t_1 = t_2$. Moreover, $\Im C_2^{(1)}$ vanishes if t_1 or t_2 equals zero since an imaginary part only builds up after the pulse when the spin-inversion symmetry is broken. After a long pulse sequence, see Fig. 9.3(b), revivals at $(t_1, t_2) = (0, 13.2T^*)$ and $(t_1, t_2) = (13.2T^*, 0)$ appear.

For the investigation of interacting QDs, the cross-correlation function is of special interest. The cross-correlator $C_2^{(\times)}$ is purely real within the SCA due to the neglection of quantum entanglement between different spins. Specifically, the evaluation of Eq. (8.19) with spin-coherent product states yields a zero imaginary part. Figure 9.4 shows the cross-correlator $C_2^{(\times)}$, the factorization $\langle S_z^{(1)}(t_1)\rangle \langle S_z^{(2)}(t_2)\rangle$, and the cumulant $K_2^{(\times)}$. The upper panels present the correlators after the first pulse, and the lower panels present the correlators after a pulse sequence of $N_P = 10^5$ pulses. In our simulations, there are at least two effects that generate cross-correlations. First, the inter-QD interactions produce cross-correlations, as discussed in Chapter 8. Second, cross-correlations are induced by the pulses. Since the pulses align both electron spins in parallel at the same time, cross-correlations are generated even

without inter-QD interactions.

We start with an analysis of the cross-correlations after a single laser pulse. Figure 9.4(a) depicts the cross-correlator $C_2^{(\times)}$ which mostly exhibits non-zero contributions on the diagonal, $t_1 \approx t_2$. The pulse breaks the time-translational invariance near $t_i \approx 0$ while the time-translational invariance is recovered for larger time scales, see the insets. Splitting $C_2^{(\times)}$ into the factorization and the cumulant allows separating the two origins for cross-correlations. The factorization, see Fig. 9.4(b), solely contains the cross-correlations generated by the pulses. These cross-correlations remain even if the inter-QD interaction is switched off, $J = 0$ (not shown here). In contrast, the cumulant $K_2^{(\times)}$, see Fig. 9.4(c), contains correlations that build up over time by the inter-QD interactions. These correlations vanish after the pulse incidence $t_1 = t_2 = 0$, $K_2^{(\times)}(0,0) = 0$, since the electron spins are realigned by the laser pulses. If the QDs are non-interacting, the cross-correlator $C_2^{(\times)}$ factorizes and $K_2^{(\times)} = 0$ vanishes at all times by construction.

A longer pulse train strongly modifies the cross-correlation functions. The factorization after the pulse train, see Fig. 9.4(e), exhibits additional revivals directly before the next pulse, i.e., at $t_1 = 13.2T^*$ and $t_2 = 13.2T^*$. Moreover, the cross-correlator and the cumulant, see Figs. 9.4(d) and 9.4(f), acquire additional antidiagonal contributions at times $t_1 + t_2 \approx 13.2T^*$. These cross-correlations arise from the imprint of the repetition time T_R on the dynamics of the spins. We attribute this effect to the emergence of correlations between the nuclear spins of different QDs induced by the long pulse sequence.

9.4 Emergence of correlated Overhauser fields

The periodic pulse sequence leads to a synchronization of the spin dynamics with the pumping periodicity. A comb-like structure of the OHD emerges, which is preserved in experiments for minutes to hours after the driving laser field is switched off. In this section, we investigate the influence of inter-QD interactions on the OHD. For this purpose, we examine the combined OHD $p(b_{N,x}^{(1)}, b_{N,x}^{(2)})$ obtained by processing the pairs $(b_{N,x}^{(1)}, b_{N,x}^{(2)})_\mu$ of all configurations μ into a two-dimensional histogram. The combined OHD is a probability density and is proportional to the probability that the system simultaneously adopts the Overhauser field $b_{N,x}^{(1)}$ in QD 1 and the Overhauser field $b_{N,x}^{(2)}$ in QD 2.

In Fig. 9.5, the combined OHD for pulse sequences with different numbers N_P of pulses is depicted. We choose a fixed inter-QD interaction strength $J = 0.1T^*$ that is

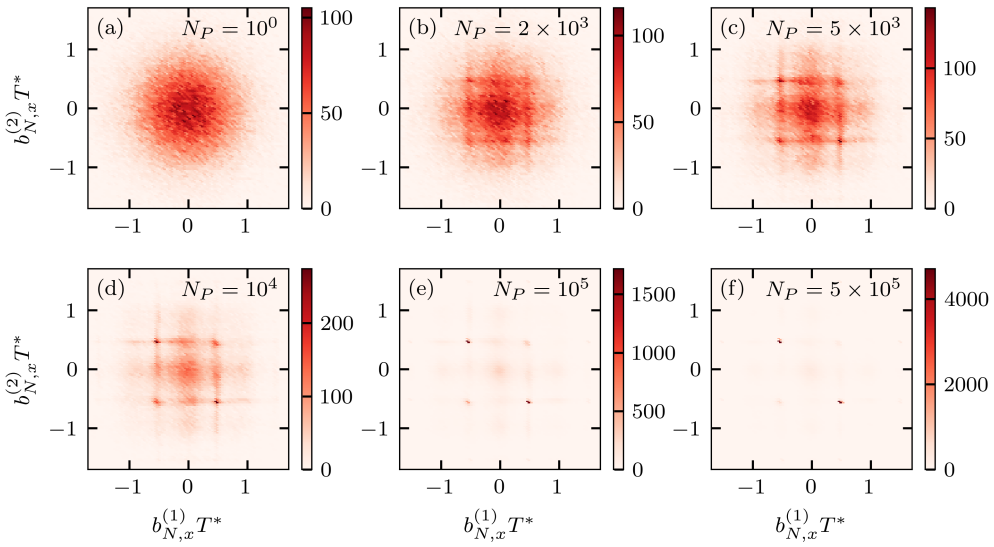

Figure 9.5: Combined OHD $p(b^{(1)}_{N,x}, b^{(2)}_{N,x})$ of two optically driven QDs ($N_{\mathrm{QD}} = 2$, $J = 0.1/T^*$, $b_{\mathrm{ext}} = 50.5/T^*$, $T_R = 2\pi T^*$) after various numbers of pulses in the range from (a) $N_P = 1$ to (f) $N_P = 5 \times 10^5$.

weaker than the fluctuation scale of the Overhauser field. The fixed value of J allows for a comprehensive study of the dependence on the inter-QD interaction strength in Sec. 9.6. We apply a pulse sequence with the repetition period $T_R = 2\pi T^*$, which corresponds to roughly 6 ns, and set the external magnetic field to $b_{\mathrm{ext}} = 50.5/T^*$. For this setting, two integer modes of the electron spin precession are covered by the initial Gaussian OHD depicted in Fig. 9.5(a). Both QDs are uncorrelated in a high-temperature regime and follow a Gaussian distribution independently. Synchronized by the effect of the pulse sequence, after $N_P = 2 \times 10^3$ pulses, a lattice structure evolves in the OHD, see Fig. 9.5(b). The integer modes are located at $b^{(i)}_{N,x} = (0.5 + n)/T^*$ and the half-integer modes at $b^{(i)}_{N,x} = n/T^*$ with $n \in \mathbb{Z}$. The integer peaks are much sharper than the half-integer peaks since there is no trion decay involved for integer resonances. When the combined OHD can be represented as a product of the individual OHDs, no relevant correlation between the Overhauser fields has formed. A longer simulation time with an increasing number of pulses results in two main effects: First, the half-integer resonances become less pronounced while the integer resonances sharpen. Second, the Overhauser fields of the two QDs begin to correlate. After $N_P = 5 \times 10^5$ pulses, each electron spin favors one of the two possible integer modes. However, the two electron spins do not favor the same precession mode. Thus, the OHDs of the two QDs are strongly anticorrelated.

9.5 Mode repulsion

In the previous section, the repetition time T_R was set to allow for two integer resonances within the Gaussian envelope of the OHD. A variation of T_R efficiently adjusts the number of possible modes. In Fig. 9.6, the combined OHD after $N_P = 5 \times 10^5$ pulses for different repetition times T_R is presented. Here, $T_R/T^* = 4\pi \approx 13$ roughly corresponds to the experimentally relevant repetition rate of 76 MHz. When increasing the repetition time, the peaks of the OHD move closer to each other. The combined OHD forms a lattice-like structure, where the peaks on the diagonal $b^{(1)}_{N,x} = b^{(2)}_{N,x}$ are vacated. Therefore, the electron spin precession obeys the resonance condition, Eq. (9.14), but the weights of the OHD redistribute in such a way that two electron spins do not precess with the same frequency.

To understand this mode repulsion, we recapitulate how resonances emerge in a single QD, see Sec. (9.2). The nuclear spins are subject to an averaged Knight field with two components: a resonant driving field in the external magnetic field direction and a constant field perpendicular to the external magnetic field. Whenever a resonance condition is met, the transversal constant field disappears, and the driving stops. In the following, we suggest that this mechanism is bypassed when both QDs share the same electron spin precession mode. If both electron spins precess with the same frequency, we can transform to a common rotated coordinate system in which the magnetic field $b_{\text{ext}} + b_{N,x}$, acting on both electron spins, vanishes. Therefore, we employ the analytical solution for the dynamics of two interacting electron spins, see Sec. 6.2. The inter-QD interaction causes an out-of-plane rotation of the electron spin which transfers the spin x component to the (yz) plane. This electron spin rotation generates a driving field perpendicular to the external magnetic field acting on the nuclear spins, which leads to a continuous driving that does not stop at the resonance condition. As a consequence, the nuclear spins are driven out of the shared

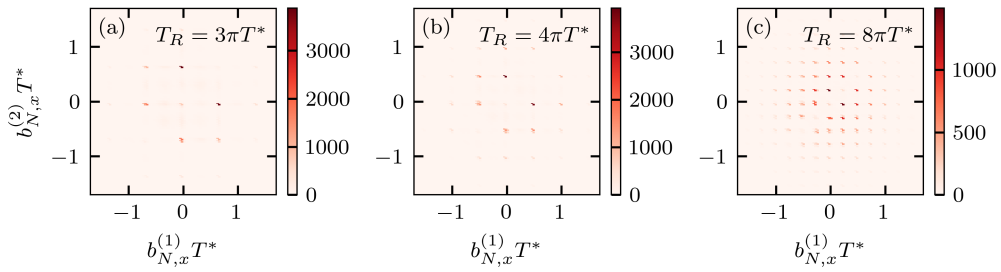

Figure 9.6: Combined OHD $p(b^{(1)}_{N,x}, b^{(2)}_{N,x})$ of two periodically driven QDs ($N_{\text{QD}} = 2$, $J = 0.1/T^*$, $b_{\text{ext}} = 50/T^*$, $N_P = 5 \times 10^5$) for various repetition times T_R.

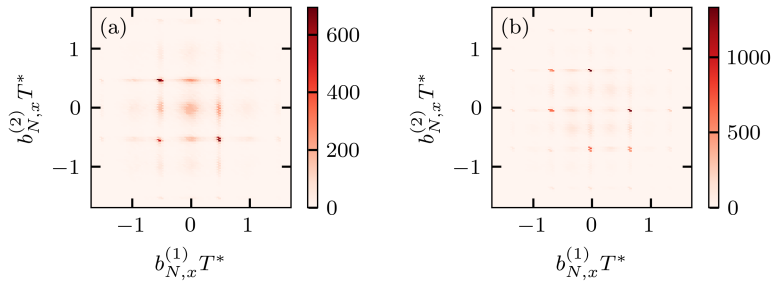

Figure 9.7: Combined OHD $p(b^{(1)}_{N,x}, b^{(2)}_{N,x})$ of three optically driven QDs ($N_{\mathrm{QD}} = 3$, $J = 0.1/T^*$, $N_P = 5 \times 10^5$) for two different combinations of the repetition time and the external magnetic field, (a) $T_R = 2\pi T^*$ and $b_{\mathrm{ext}} = 50.5/T^*$ as well as (b) $T_R = 3\pi T^*$ and $b_{\mathrm{ext}} = 50/T^*$.

mode. On the other hand, if the two QDs satisfy different resonance conditions, no common rotated coordinate system exists and the out-of-plane rotation is suppressed for $J \ll \Delta\omega$ with the mode distance $\Delta\omega$. This mechanism is independent of the sign of J. Accordingly, we would obtain the same results in Fig. 9.6 if we set $J \to -J$ (not shown here).

Investigating a QD ensemble, the question about a generalization for $N_{\mathrm{QD}} > 2$ arises. Due to computational constraints, we restrict ourselves to $N_{\mathrm{QD}} = 3$ QDs and set $J_{ij} = 0.1(T^*)^{-1}$ such that all three QDs are coupled to each other. All QDS are excited by the σ^+ polarized laser pulse at times nT_R. In Fig. 9.7(a), we present the combined OHD for a repetition period of $T_R = 2\pi T^*$ that produces two integer resonances within the initial Gaussian OHD. This choice of T_R generates a geometric frustration as the three electron spins have to share two integer modes. As a consequence, almost no correlation is formed in the combined OHD. Furthermore, the half-integer modes are favored more strongly in comparison to the case without frustration, see Fig. 9.5(f). In Fig. 9.7(b), the combined OHD is shown for a repetition period of $T_R = 3\pi T^*$ that enables three integer resonances. Hence, the number of coupled QDs and the number of integer modes coincide. Due to the finite number of pulses, the OHD has not yet reached the quasi-stationary steady state. However, the distribution reveals already that the occupation of a common mode is strongly suppressed. We expect that when the number of coupled QDs increases, the number of pulses required to reach the quasi-stationary steady state increases as well. For a large number of QDs, we predict that the mode repulsion enables the generation of dynamic spin phases. However, the study of this intricate situation is beyond the scope of this thesis. For the following investigations, we restrict ourselves to $N_{\mathrm{QD}} = 2$ QDs again.

9.6 Influence of the inter quantum-dot coupling strength

We continue with the investigation of the influence of the inter-QD interaction strength J. In Fig. 9.8, the combined OHD after $N_P = 5 \times 10^5$ pulses with the repetition period $T_R = 2\pi T^*$ is displayed. We identify three regimes depending on the interaction strength. For very weak inter-QD interactions, see Figs. 9.8(a) and 9.8(b), the QDs evolve almost independent of each other. Each QD forms its own OHD with the resonances determined by Eq. (9.14). The combined OHD thus factorizes into a product of the single-QD OHDs, $p(b^{(1)}_{N,x}, b^{(2)}_{N,x}) \approx p(b^{(1)}_{N,x})p(b^{(2)}_{N,x})$. For intermediate J, see Figs. 9.8(c) and 9.8(d), the peaks still satisfy the single-QD resonance condition, Eq. (9.14). However, the weights are redistributed in such a way that the Overhauser fields become correlated, and the electron spins do not precess with the same frequency. We note that the OHDs $p(b^{(i)}_{N,x})$ of a single QD would not reflect the correlations in this parameter regime of J. For strong J, see Figs. 9.8(e) and 9.8(f), the inter-QD interaction becomes predominant, and the OHD changes significantly. The two electron spins are parallelly aligned by the laser pulses. Afterward, the strongly coupled spins precess around the average Overhauser field,

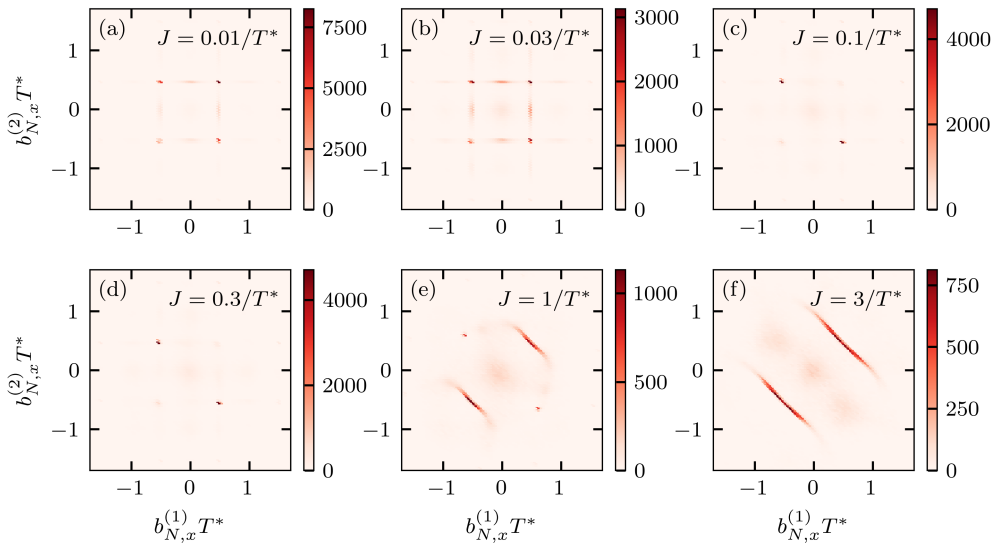

Figure 9.8: Combined OHD $p(b^{(1)}_{N,x}, b^{(2)}_{N,x})$ of two periodically driven QDs ($N_{\mathrm{QD}} = 2$, $b_{\mathrm{ext}} = 50.5/T^*$, $T_R = 2\pi T^*$, $N_P = 5 \times 10^5$) for various interaction strengths J. Both QDs are excited by σ^+ polarized pulses at times $t = nT_R$ with $n \in \mathbb{N}_0$.

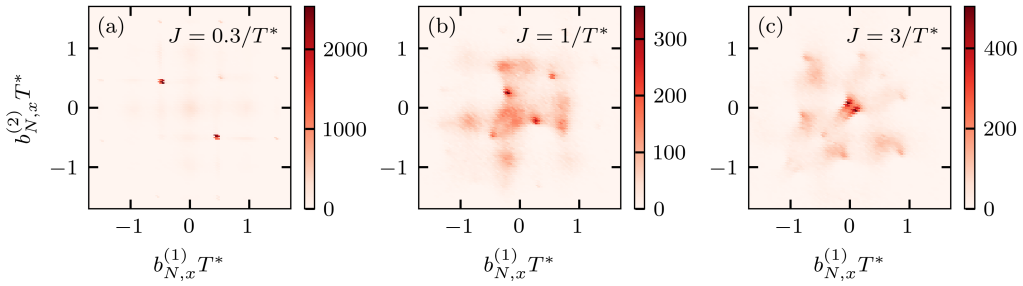

Figure 9.9: Combined OHD $p(b^{(1)}_{N,x}, b^{(2)}_{N,x})$ of two periodically driven QDs ($N_{\mathrm{QD}} = 2$, $b_{\mathrm{ext}} = 50.5/T^*$, $T_R = 2\pi T^*$, $N_P = 5 \times 10^5$) for various interaction strengths J. QD 1 is excited with σ^+ polarization and QD 2 with σ^- polarization at times $t = nT_R$ with $n \in \mathbb{N}_0$.

so that $(b^{(1)}_{N,x} + b^{(2)}_{N,x})/2$ has to fulfill the resonance condition, Eq. (9.14). Accordingly, the antidiagonal lines form in the combined OHD.

For further investigation, we employ an alternative pulse train, where QD 1 is exposed to σ^+ polarization and QD 2 to σ^- polarization. As a result, the electron spins are antiparallelly aligned at $t = nT_R$. In Fig. 9.9, the combined OHD for different inter-QD interaction strengths J is shown. In the weak interacting regime, the QDs are almost decoupled, and we trivially obtain the same results as in Fig. 9.8 (not shown). For the intermediate regime, see Fig. 9.9(a), we observe the same behavior as for the original pulse sequence. The inter-QD interactions are a small perturbation and prevent the emergence of the same mode due to the mechanism described in Sec. 9.5. For large J, see Figs. 9.9(b) and 9.9(c), an irregular pattern forms in the combined OHD. For an explanation, we refer to the analytical solution of the two-spin problem, discussed in Sec. 6.2. While parallel spins form a stable fixed point, antiparallel spins yield an unstable fixed point. This instability is transferred to the OHD via the hyperfine interaction.

9.7 Cross-correlation bi-spectrum

The inter-QD interactions generate a substantial modification of the OHD. However, since the OHD cannot be measured directly in experiments, we investigate a suitable electron spin correlation function in the following to make the optically induced manipulation of the system experimentally accessible. For this purpose, we first consider a single QD. Jäschke et al. [200] demonstrated that the autocorrelation spectrum $\tilde{C}_2(\omega)$ enables access to the OHD of a single QD: The QD is first driven

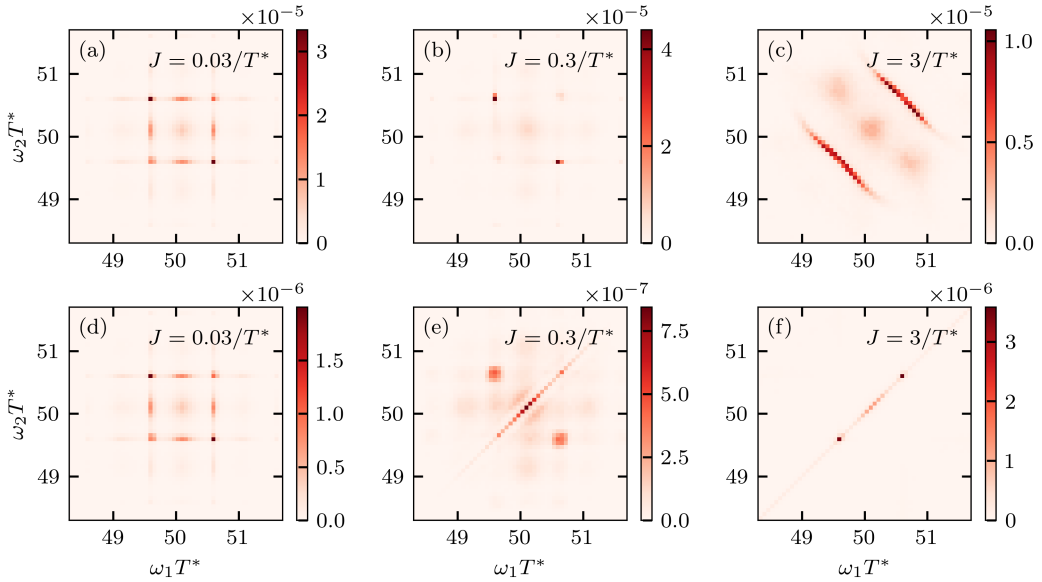

Figure 9.10: Cross-correlation bi-spectra measured in darkness after a periodic pulse train for two interacting QDs ($N_{\mathrm{QD}} = 2$, $b_{\mathrm{ext}} = 50.5/T^*$, $T_R = 2\pi T^*$, $N_P = 5 \times 10^5$). For the upper panels, the interaction J is switched off during the measurement while it is switched on for the lower panels.

by a periodic pulse sequence to form the non-equilibrium OHD. Once the non-equilibrium state is reached, the system is left in darkness. The electron spins revolve with the frequency $b_{\mathrm{ext}} + b_{N,x}$ while the nuclear spins are approximately frozen. Hence, the autocorrelation spectrum $\tilde{C}_2(\omega)$ is proportional to the OHD shifted by b_{ext}. By this procedure, the OHD can be read out indirectly via the electron spin dynamics.

In the following, we generalize the procedure for two interacting QDs. We introduce the fourth-order spin cross-correlation function,

$$C_4^{(\times)}(t_1, t_2, t_3, t_4) = \langle S_z^{(1)}(t_1) S_z^{(1)}(t_2) S_z^{(2)}(t_3) S_z^{(2)}(t_4) \rangle \ . \tag{9.17}$$

For uncorrelated spins, $C_4^{(\times)}(t_1, t_2, t_3, t_4)$ factorizes into the product $C_2^{(1)}(t_1, t_2) \times C_2^{(2)}(t_3, t_4)$. We define the cross bi-spectrum $\tilde{C}_4^{(\times)}(\omega_1, \omega_2)$ by a Fourier transformation of $t_2 - t_1$ and $t_4 - t_3$ while the remaining two times t_2 and t_1 are averaged out. The bi-spectrum $\tilde{C}_4^{(\times)}(\omega_1, \omega_2)$ connects the autocorrelation functions $\tilde{C}_2^{(i)}(\omega)$ of both QDs. Therefore, it is a measure for the simultaneous precession of the electron spin in QD 1 with the frequency ω_1 and the electron spin in QD 2 with the frequency ω_2.

To measure $\tilde{C}_4^{(\times)}$, we follow the scheme of Jäschke et al. [200]. First, the system is driven by a periodic pulse train, and afterward in darkness the cross-correlation bi-spectrum $\tilde{C}_4^{(\times)}$ is measured. In addition, we distinguish between two kinds of samples with either a fixed or a controllable inter-QD interaction. For a wetting-layer mediated RKKY interaction, the interaction strength might be controlled by applying a gate voltage to modify the chemical potential and, therefore, the wetting-layer filling. For a purely optical RKKY interaction, the interaction strength can be adjusted by controlling the power of the CW laser. In the case of a controllable interaction, we assume that the interaction is turned on during the optical excitation and is switched off in darkness to measure $\tilde{C}_4^{(\times)}$.

In the upper panels of Fig. 9.10, we present the cross-correlation bi-spectrum for QDs with controllable inter-QD interactions. As expected, the spectra agree well with the corresponding OHDs in Figs. 9.8(b), 9.8(d) and 9.8(f). In the lower panels of Fig. 9.10, we present the cross-correlation bi-spectrum for QDs with fixed interaction strength. In this case, the inter-QD interactions are still present while measuring $\tilde{C}_4^{(\times)}$. For a weak interaction strength, $J = 0.03T^*$, the spectra in Figs. 9.10(a) and 9.10(d) coincide as the inter-QD interaction is negligible. For $J = 0.3T^*$, see Fig. 9.10(e), substantial modifications arise when the inter-QD interactions persist during the measurement of $\tilde{C}_4^{(\times)}$: The two peaks in the combined OHD are imprinted on the correlation spectrum, but are broadened by the interaction strength of $0.3T^*$. In addition, there is a prominent diagonal contribution induced by the synchronization of the electron spins. For large J, see Fig. 9.10(f), the bi-spectrum exhibits only contributions for equal frequencies $\omega_1 = \omega_2$. The electron spins are synchronized and precess at the same frequency due to their strong coupling.

In summary, for weak and medium inter-QD interactions, the cross-correlation bi-spectrum is a suitable quantity for the indirect measurement of the combined OHD. For strong spin-spin interactions, however, the inter-QD interactions must be switched off during the measurement of $\tilde{C}_4^{(\times)}$ to obtain the combined OHD.

Chapter 10

Nuclear-spin polaron formation

In the following chapter, we investigate the intertwined dynamics between the electron spin and the nuclear spins in a single QD in the low-temperature regime. The electron spin is coupled via hyperfine interaction to nuclear spins located in the electron wave function. Assuming a positive hyperfine constant, the energy of the system is minimized by an antiparallel alignment of the electron and nuclear spins. This highly correlated state is termed nuclear-spin polaron and forms only at very low temperatures well below typical cryostatic temperatures. Such extreme conditions can only be reached by laser cooling techniques. While the nuclear spins can be cooled down to very low temperatures, the electron spin is strongly coupled to the environment and obtains the lattice temperature. This suggests a two-temperature treatment, where two thermal reservoirs are introduced. The electron spin interacts with the lattice at cryostatic temperature via spin-lattice interaction mediated by spin-orbit coupling while the nuclear spins are strongly isolated from the lattice and interact with adjacent optically cooled nuclear spins via dipole-dipole interactions. A mean-field solution of this approach was presented by Merkulov [44], and the spin-polaron formation was predicted for nuclear temperatures of $10^{-7}\,\mathrm{K}$ at cryostatic electron spin temperatures of 1 K. Direct experimental detection of a nuclear-spin polaron state has not been reported yet, however, the experiments are ongoing [45, 85]. The influence of nuclear-spin fluctuations has been investigated recently [86, 203]. In this chapter, we discuss a nuclear-spin polaron formation beyond the mean-field approach using kinetic rate equations where electron-spin fluctuations and nuclear-spin fluctuations are incorporated. The kinetic rate equation approach restores the exact thermodynamic solution in the single temperature regime. Major results of this chapter are published in Ref. [173] and have been obtained in equal parts by Iris Kleinjohann and the author. Kleinjohann et al. developed a generalization for arbitrary hyperfine interactions published in Ref. [204], which is briefly addressed in Sec. 10.10.

10.1 Two-temperature concept and kinetic rate equations

We consider a singly charged QD or donor/acceptor bound electron/hole and only take into account the hyperfine interaction, Eq. (3.3). Hence, quadrupolar interactions and an external magnetic field are neglected. However, we incorporate a coupling of the spins to their environment. For this purpose, we introduce fluctuating effective magnetic fields as a perturbation. They are related to interactions of the electron spin with the lattice or a dipole-dipole interaction between the nuclei. We represent them by the operators

$$V_n = b_0 \sum_{k,\alpha} b_k^\alpha I_k^\alpha \tag{10.1a}$$

for the nuclei and

$$V_e = B_0 \sum_{\alpha} B^\alpha S^\alpha \tag{10.1b}$$

for the electron spin, where b_0 and B_0 are dimensional constants describing the coupling strength to the environment, while the dimensionless operators b_k^α and B^α describe effective magnetic fields acting on the electron or nuclear spin. These operators fulfill the standard spin-commutation relations

$$[b_k^\alpha, b_{k'}^\beta] = \mathrm{i}\delta_{kk'}\epsilon_{\alpha\beta\gamma} b_k^\gamma, \tag{10.2a}$$

$$[B^\alpha, B^\beta] = \mathrm{i}\epsilon_{\alpha\beta\gamma} B^\gamma, \tag{10.2b}$$

$$[b_k^\alpha, B^\beta] = 0. \tag{10.2c}$$

with the Levy-Civita symbol $\epsilon_{\alpha\beta\gamma}$. The microscopic mechanism of the environmental coupling is hidden in the effective fields. However, we can assume that the lattice phonons relevant for field B^α incorporate different temperatures T_e than the optically cooled nuclear spins with temperature T_n.

We include the reservoir-system interactions in form of a quantum-master equation approach. We employ the eigenstates $|m\rangle$ with eigenenergies E_m of the system Hamiltonian (3.3) to introduce the distribution $f_m = \varrho_{mm}$, the diagonal part of the system's density matrix in energy eigenbasis. For weak perturbations V_n and V_e, the Pauli master equation for f_m reads [205]

$$\frac{\partial f_m}{\partial t} = \sum_{m'} (W_{mm'} f_{m'} - W_{m'm} f_m). \tag{10.3}$$

with the transition rate $W_{mm'}$ from the state $|m'\rangle$ to the state $|m\rangle$. The rates can be obtained from Fermi's golden rule under the assumption of a reservoir in thermal equilibrium,

$$W_{i,mm'} = \sum_{r_i,r_i'} \frac{2\pi}{Z_i} \delta_{\Delta\epsilon,-\Delta E} \exp\left(-\frac{\epsilon_{r_i'}}{k_B T_i}\right) |\langle r_i|\langle m|V_i|m'\rangle|r_i'\rangle|^2, \tag{10.4}$$

where the subscript $i \in \{n, e\}$ distinguishes the nuclear/electronic reservoir, ϵ_{r_i} is the energy of the reservoir eigenstate $|r_i\rangle$, $\Delta\epsilon = \epsilon_{r_i} - \epsilon_{r_i'}$ and $\Delta E = E_m - E_{m'}$ denote the energy differences, and Z_i is the partition function of the corresponding reservoir. Note, when treating off-diagonal elements of the density matrix, the Pauli master equation can be generalized to a Lindblad master equation [204]. The total transition rate incorporates both reservoirs

$$W_{mm'} = W_{n,mm'} + W_{e,mm'} \ . \tag{10.5}$$

Interfering contributions of the perturbations V_e and V_n are absent due to the commutation relations (10.2c).

Note, the partial rates of the process $m' \to m$ and its reverse $m \to m'$ are related by the Boltzmann factors

$$\frac{W_{n,mm'}}{W_{n,m'm}} = \exp\left(\frac{E_{m'} - E_m}{k_B T_n}\right), \tag{10.6a}$$

$$\frac{W_{e,mm'}}{W_{e,m'm}} = \exp\left(\frac{E_{m'} - E_m}{k_B T_e}\right), \tag{10.6b}$$

with the corresponding reservoir temperature T_i. For equal temperatures $T_n = T_e \equiv T$, also the total transition rates $W_{mm'}$ and $W_{m'm}$ fulfill the same relation as Eq. (10.6) and density matrix approaches the correct thermodynamic steady state

$$f_m = Z^{-1} \exp\left(-\frac{E_m}{k_B T}\right), \tag{10.7}$$

with partition function of the system Z, independent of the transition rate values.

10.2 Reduced rate equations

The rate Eq. (10.3) describes the transition rates between the energy eigenstates of the system mediated by interactions with the environment. As the number of states grows exponentially with the number of spins, a treatment without approximation

is not possible for large systems, e.g., for a QD with 10^5 to 10^6 nuclear spins. To this end, we employ a simplified model and exploit symmetries. We focus on the Hamiltonian

$$H = \sum_{k=1}^{N} A_k I_k^z S^z \tag{10.8}$$

in the Ising limit, which is physically realized by heavy-hole spins in III-V or II-VI semiconductor QDs. In addition, we set the spin length to 1/2 for all spins in the system. This assumption is exact for a bound hole state in a QD when the $I = 3/2$ spin multiplet is reduced to a Kramers degenerate pair due to symmetry reduction. For the nuclear spins, the large number of spins in the bath justifies the approximation of spin 1/2. As characteristic scale, we establish the nuclear fluctuation rate $\omega_h = (\sum_k A_k^2)^{1/2}$, which is directly related to the electron dephasing time $T^* = \sqrt{4/3}\omega_h^{-1}$ for spin 1/2. The dephasing time T^* has the typical order of 1 ns for QD systems [46] and can be up to two orders of magnitude smaller for donor-bound electrons [128, 206]. For sake of simplicity, we assume that only matrix elements, where just a single spin is flipped, are non-zero,

$$\begin{aligned}\frac{\partial f(\{I_k^z\}, S^z)}{\partial t} =& f(\{I_k^z\}, -S^z) W_e(\{I_k^z\}, -S_z) - f(\{I_k^z\}, S^z) W_e(\{I_k^z\}, S^z) \\ &+ \sum_{k'} [\, f(\{I_1^z, \ldots, -I_{k'}^z, \ldots, I_N^z\}, S^z) W_{k'}(-I_{k'}^z, S^z) \\ &\quad - f(\{I_k^z\}, S^z) W_{k'}(I_{k'}^z, S^z)\,] \,.\end{aligned} \tag{10.9}$$

For Hamiltonian (10.8) with the eigenenergy $E(\{I_k^z\}, S^z) = S^z \sum_k A_k I_k^z$, the electron spin-flip rate Eq. (10.4) simplifies to

$$W_e(\{I_k^z\}, S^z) = W_e^{(0)} \min\left(1, e^{-2\beta_e S^z \sum_k A_k I_k^z}\right) \,. \tag{10.10}$$

The flip process to a state of higher energy is suppressed exponentially with the Boltzmann factor using the inverse temperature $\beta_e = 1/(k_B T_e)$. In the same way, we establish the nuclear rate,

$$W_{k'}(I_{k'}^z, S^z) = W_n^{(0)} \min\left(1, \exp\left(-\beta_n |A_{k'} S^z|\right)\right) \tag{10.11}$$

with the phenomenological flip rate $W_n^{(0)}$ and the inverse nuclear temperature $\beta_n = 1/(k_B T_n)$. Note, in general, the prefactors $W_e^{(0)}$ and $W_n^{(0)}$ have an energy dependence, which varies slowly compared to the exponential function in the Boltzmann factor. Since we do not aim for a microscopic description of the flip rates, we assume $W_e^{(0)}$ and $W_n^{(0)}$ to be constant. In this way, the physical origin of the flip processes and the details of the environment remain unspecified.

10.3 Steady-state solution of the rate equations

To gain numerical and analytical access, we apply the box-model approximation $A_k = A_0$. In the box model, all states with the same total nuclear spin $I^z = \sum_k I_k^z$ are degenerate. This allows the introduction of the reduced distribution $g(I^z, S^z)$ which no longer depends on the individual nuclear spin configuration $\{I_k^z\}$ but on the total nuclear spin I^z. The resulting rate equation,

$$\begin{aligned}\frac{\partial g(I^z,S^z)}{\partial t} &= W_e(I^z,-S^z)\,g(I^z,-S^z) - W_e(I^z,S^z)\,g(I^z,S^z)\\ &\quad+\sum_{j=\pm1} W_n^{(j)}(I^z-j,S^z)\,g(I^z-j,S^z)\\ &\quad-\sum_{j=\pm1} W_n^{(j)}(I^z,S^z)\,g(I^z,S^z),\end{aligned} \tag{10.12}$$

becomes analytically solvable and incorporates the spin-flip rates

$$W_e(I^z,S^z) = W_e^{(0)}\min(1,\exp\left(-\beta_e A_0|I^z|\right)) \tag{10.13a}$$

$$W_n^{(\pm1)}(I^z,S^z) = W_n^{(0)} N_{\mp}(I^z)\min\left(1,\exp\left(-\frac{\beta_n A_0}{2}\right)\right)\ , \tag{10.13b}$$

where we distinguish the rates for nuclear spin flips in up and down directions. They differ by the number $N_{\mp}(I^z)$ of nuclear spins in the up and down directions. In addition, we assume a much faster electron spin-flip rate in comparison to the nuclear spin-flip rate ($W_e^{(0)} \gg W_n^{(0)}$). This assumption is well justified due to the much stronger coupling of the electron spin to the environment [105]. We exploit this separation of time scales and assume that the electron spin is always in thermal equilibrium with respect to the current nuclear spin polarization

$$\frac{g(I^z,\uparrow)}{g(I^z,\downarrow)} = \exp\left(-\beta_e A_0 I^z\right)\ , \tag{10.14}$$

which is given by the Boltzmann distribution. This allows the introduction of a nuclear spin distribution,

$$g(I^z) = g(I^z,\uparrow) + g(I^z,\downarrow)\ . \tag{10.15}$$

Knowing the nuclear spin distribution $g(I^z)$, we can reconstruct the full distribution $g(I^z, S^z)$ by using Eqs. (10.14) and (10.15). By calculating the time derivative of Eq. (10.15) and using Eqs. (10.12) and (10.14), we can derive a rate equation for the nuclear spin distribution

$$\frac{\partial g(I^z)}{\partial t} = \sum_{j=\pm1}\Gamma^{(j)}(I^z-j)g(I^z-j) - \Gamma^{(j)}(I^z)g(I^z). \tag{10.16}$$

with the effective nuclear spin-flip rates,

$$\Gamma^{(\pm 1)}(I^z) = W_n^{(0)} N_{\mp}(I^z) \frac{\cosh(\beta_e A_0 I^z/2 \pm \beta_n A_0/4)}{\cosh(\beta_e A_0 I^z/2)\exp(\beta_n A_0/4)} \,. \tag{10.17}$$

Note, since electron spin flips do not change the quantum number I^z their contributions cancel each other, and the $W_e^{(0)}$ dependency vanishes. The steady-state solution of the rate Eq. (10.16) is defined by the condition $\partial_t g(I^z) = 0$ and can be derived by using the detailed balance condition

$$g(I^z)\Gamma^{(+1)}(I^z) = g(I^z+1)\Gamma^{(-1)}(I^z+1). \tag{10.18}$$

The condition (10.18) yields the relative weights of two neighboring states I^z and I^z+1,

$$\begin{aligned} \frac{g(I^z+1)}{g(I^z)} =& \frac{N/2-I^z}{N/2+I^z+1} \times \frac{\cosh\left(\beta_e A_0 (I^z+1)/2\right)}{\cosh\left(\beta_e A_0 I^z/2\right)} \\ & \times \frac{\cosh\left(\beta_n A_0/4 + \beta_e A_0 I^z/2\right)}{\cosh\left(\beta_n A_0/4 - \beta_e A_0 (I^z+1)/2\right)} \end{aligned} \tag{10.19}$$

with $I^z = -N/2, \ldots, N/2$ and the normalization condition $\sum_{I^z} g(I^z) = 1$. To determine $g(I^z)$ numerically, one can first set $g(-N/2) = c$ with an arbitrary constant c. Starting from $g(-N/2)$ all further $g(I^z)$ can be determined successively using Eq. (10.19). Finally, the constant c can be determined from the normalization condition $\sum_{I^z} g(I^z) = 1$. The full distribution $g(I^z, S^z)$ can be reconstructed from $g(I^z)$ using the Boltzmann ratio (10.14) and enables the calculation of various observables in the steady state. Note, already for spin numbers of $N = 10^3$, the distribution $g(I^z)$ has entries that may vary by a factor $> 10^{1000}$ which cannot be stored in a double precision floating point format. For the numerical implementation, it is therefore necessary to store $\ln(g(I^z))$ instead of $g(I^z)$. Note, this procedure is stable and enables the direct calculation of the steady state with linear scaling, which enables an efficient evaluation even for $N > 10^6$. For finite temperatures, the steady state is unique. However, for the case of zero temperatures, Eq. (10.19) is not well defined and the ratio might be 0 or ∞, which allows the steady state to be degenerate.

10.4 Simplified analytical treatments

Before we analyze the nuclear-spin polaron formation numerically, we investigate simplified analytical treatments like the single temperature limit or a two-temperature mean-field approach.

Single temperature regime

For the case of a single temperature $\beta = \beta_e = \beta_n$, the system becomes analytically solvable. The density matrix of the system in thermal equilibrium has the form

$$\rho_{\text{th}} = \frac{1}{Z} e^{-\beta H} \tag{10.20}$$

with partition function $Z = \text{Tr}\left[e^{-\beta H}\right]$, independent of the rates $W_e^{(0)}$ and $W_n^{(0)}$. Since the Hamiltonian is already diagonal, the partition function can be explicitly calculated

$$Z = 2^{N+1} \left(\cosh(\beta A_0/4)\right)^N \ . \tag{10.21}$$

While $\langle S^z \rangle = \langle I^z \rangle = 0$ are trivially zero, we can calculate the expectation value of the electron-nuclear spin correlator in thermal equilibrium:

$$\langle S^z I^z \rangle = -\frac{N}{4} \tanh\left(\frac{\beta A_0}{4}\right) \ . \tag{10.22}$$

In the single temperature limit, the correlator changes continuously between the uncorrelated high temperature state $\langle S^z I^z_{\text{tot}} \rangle (\beta = 0) = 0$ to the maximally correlated spin polaron state at low temperatures $\langle S^z I^z \rangle (\beta \to \infty) = -N/4$. Hence, in the single temperature case, no phase transition takes place, and the cross-over scale for the spin polaron transition is given by A_0.

Mean-field approach

Another possibility to study the nuclear-spin polaron transition is offered by a mean-field approach [44], which is applicable for the Ising as well as the isotropic case. An extension to arbitrary hyperfine anisotropy is presented in Ref. [204]. For the sake of simplicity, we restrict ourselves to the Ising case here.

We assume that the electron spin is in contact with the lattice temperature β_e and is subject to a mean Overhauser field $A_0 \langle I^z \rangle$, which we assume here to be a classical field without fluctuations. The optically cooled nuclear spins are in contact with another temperature β_n and are subject to a mean Knight field $A_0 \langle S^z \rangle$. This assumption separates the problem into two subproblems that can be solved independently. This results in the expectation values

$$\langle S^z \rangle = -\frac{1}{2} \tanh\left(\frac{\beta_e A_0 \langle I^z \rangle}{2}\right) \tag{10.23a}$$

$$\langle I^z \rangle = -\frac{N}{2} \tanh\left(\frac{\beta_n A_0 \langle S^z \rangle}{2}\right) \ . \tag{10.23b}$$

To obtain the solution to the overall problem, the Eqs. (10.23) must be solved self-consistently. Depending on the chosen temperature pair (β_e, β_n), the number of solutions is different. Above a critical temperature product,

$$T_e T_n > \frac{N A_0^2}{16 k_B^2} \,, \tag{10.24}$$

there is only the trivial solution $\langle S^z \rangle = \langle I^z \rangle = 0$, where no spin polarization is formed. If the product $T_e T_n$ is below the critical value, there exist two additional non-trivial solutions. These solutions correspond to the two possible spin polaron states, where the electron spin is aligned in positive or negative z direction and the nuclear spins are antiparallel aligned. In the vicinity of the transition point, the mean-field approach yields its typical square root behavior,

$$\langle |S^z| \rangle, \langle |I^z| \rangle \propto \sqrt{\beta_e \beta_n - \frac{16}{N A_0^2}} \,. \tag{10.25}$$

Interestingly, the mean field approximation predicts a phase transition even for equal temperatures $T_e = T_n$, where the exact single temperature solution (10.22) is continuous. Therefore, the phase transition for a single temperature is an artifact of the mean-field solution.

10.5 Criterion for the polaron formation

The analytic solution of the rate equations Eq. (10.19) offers the possibility to determine a criterion for the polaron formation beyond the mean-field approach. For this purpose, we consider the nuclear spin distribution $g(I^z)$. For high temperatures, the nuclear spins are completely disordered. From a combinatorial point of view, there are more possibilities for a small $|I^z|$ than for a large $|I^z|$. The central limit theorem yields a Gaussian distribution of $g(I^z)$ with its maximum at $I^z = 0$. When the system is cooled, the nuclear spins align antiparallelly to the electron spin so that $g(I^z)$ has a minimum at 0 and two maxima symmetrically around it. These two limiting cases are depicted Fig. 10.1(a). In Fig. 10.1(b), the nuclear spin distribution $g(I^z)$ is color coded as function of the nuclear spin polarization I^z and inverse nuclear spin temperature β_n for a fixed inverse electron spin temperature β_e, where the curves from panel (a) can be extracted as vertical cuts. In between the limiting cases of a single maximum/two maxima, we find a bifurcation point with a transition from a minimum to a maximum at $I^z = 0$ which we will employ as an analytical criterion for the polaron formation. For even N, the criterion demands the ratio

$$\frac{g(1)}{g(0)} \;=\; 1 \tag{10.26}$$

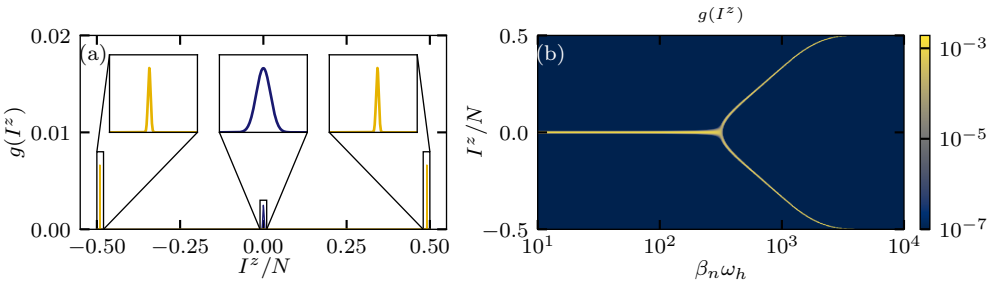

Figure 10.1: Probability distribution $g(I^z)$ of the total nuclear spin I^z in the steady state ($N = 10^5$, $\beta_e\omega_h = 0.05$). (a) Nuclear spin distribution $g(I^z)$ for $\beta_n\omega_h = 10$ (blue) and $\beta_n\omega_h = 3000$ (orange). (b) Nuclear spin distribution $g(I^z)$ as function of I^z and β_n for fixed β_e. The curves in panel (a) can be obtained as vertical cuts from panel (b). The plots are taken from Ref. [173].

at the crossover temperature. By using the analytical solution Eq. (10.19), the implicit condition,

$$1 = \frac{N}{N+2} \frac{\cosh\left(\beta_n A_0/4\right) \cosh\left(\beta_e A_0/2\right)}{\cosh\left(\beta_n A_0/4 - \beta_e A_0/2\right)} , \tag{10.27}$$

can be determined. This condition is fulfilled on the crossover line in the (β_e, β_n) plane. For large electron spin temperatures $\beta_e A_0 \ll 1$, the condition Eq. (10.27) can be rewritten into the explicit form,

$$\beta_n = \frac{4}{A_0} \tanh^{-1}\left(\frac{4}{(2+N)\beta_e A_0}\right) . \tag{10.28}$$

Interestingly, $\tanh^{-1}(x)$ diverges for $|x| = 1$, implying a minimum value $\beta_e > 4/(2+N)A_0$ and thus a maximum upper limit on the electron spin temperature for the polaron formation. Above this maximum temperature, the electron spin fluctuations are so large that the polaron formation is no longer possible. In contrast, the mean-field theory does not include this effect since spin fluctuations are neglected. If many nuclear spins (or small electron spin temperatures) are considered $N \gg (\beta_e A_0)^{-1}$, Eq. (10.28) resorts to the mean field criterion Eq. (10.24).

10.6 Numerical results

The expectation value of a general observable O is expressed by

$$\langle O \rangle = \sum_{S^z} \sum_{I_k^z} \langle S^z, \{I_k^z\} | O | S^z, \{I_k^z\} \rangle \, f(\{I_k^z\}, S^z). \tag{10.29}$$

To study the nuclear-spin polaron formation, we first focus on the electron-nuclear spin correlator $\langle S^z I^z \rangle$. At high spin temperatures, the electron-nuclear correlator yields 0 as all spins are uncorrelated. At low temperatures, the spins minimize their energy by forming an antiparallel alignment considering $A_0 > 0$. In Fig. 10.2(a), $\langle S^z I^z \rangle$ is plotted as function of the two inverse spin temperatures β_e and β_n. The correlator $\langle S^z I^z \rangle$ is color coded, whereby a dark blue corresponds to vanishing correlations and a yellow color corresponds to a strong anticorrelation. When both spin temperatures are low, upper right corner, strong anticorrelations of $-N/4$ form. However, the correlator vanishes for large spin temperatures. We added the transition line from the mean field approach Eq. (10.24) (white line), and the crossover line from the rate equation condition Eq. (10.27) (red dotted line). While both curves agree for large β_e, there are significant discrepancies for small β_e, where the red dotted line is a much better indicator for the spin polaron formation. Note, for asymmetric temperatures $\beta_n \gg \beta_e$ the crossover from a disordered state of the system to a polaron state occurs very rapidly but turns smooth when β_n and β_e become comparable in magnitude. This behavior coincides with the analytical single temperature solution, which is exactly represented in the rate equation approach.

A quantity that behaves similarly is the expectation value of the magnitude of the total spin $\langle |I^z| \rangle$. In the absence of external symmetry breaking, the expectation value $\langle I^z \rangle$ is always 0 due to spin inversion symmetry and, thus, unsuitable for the study of spin polaron formation. Since there is no spontaneous symmetry breaking for finite systems, we study the order parameter $\langle |I^z| \rangle$ instead [203, 207, 208]. The quantity $\langle |I^z| \rangle$ can also be interpreted as the nuclear spin expectation value $\langle I^z \rangle$ of a symmetry-broken distribution

$$g^{(+)}(I^z) = \theta(I^z)[g(I^z) + g(-I^z)]. \tag{10.30}$$

For high temperatures $\langle |I^z| \rangle \propto \sqrt{N}$ holds, so the intensive quantity $\langle |I^z| \rangle / N$ vanishes for $N \to \infty$. For low temperatures, on the other hand, the nuclear spins align antiparallelly to the electron spin so $\langle |I^z| \rangle$ approaches a finite value with a maximum of $\langle |I^z| \rangle = N/2$. In Fig. 10.2(b), $\langle |I^z| \rangle$ is shown as function of β_n and β_e and shows the same generic behavior as $\langle S^z I^z \rangle$.

Qualitative differences arise at the transition line. In Fig. 10.2(c) and Fig. 10.2(d), horizontal cuts for a fixed $\beta_e \omega_h = 0.05$ are shown. While $\langle S^z I^z \rangle$ grows approximately linearly at the transition line, $\langle |I^z| \rangle$ shows a square root-like behavior. This distinction can be understood through the mean-field solution in Eq. (10.25). While the correlator in the mean-field approach (dashed yellow line) is not differentiable at the polaron transition, the rate equations provide a smooth curve since we consider a finite system.

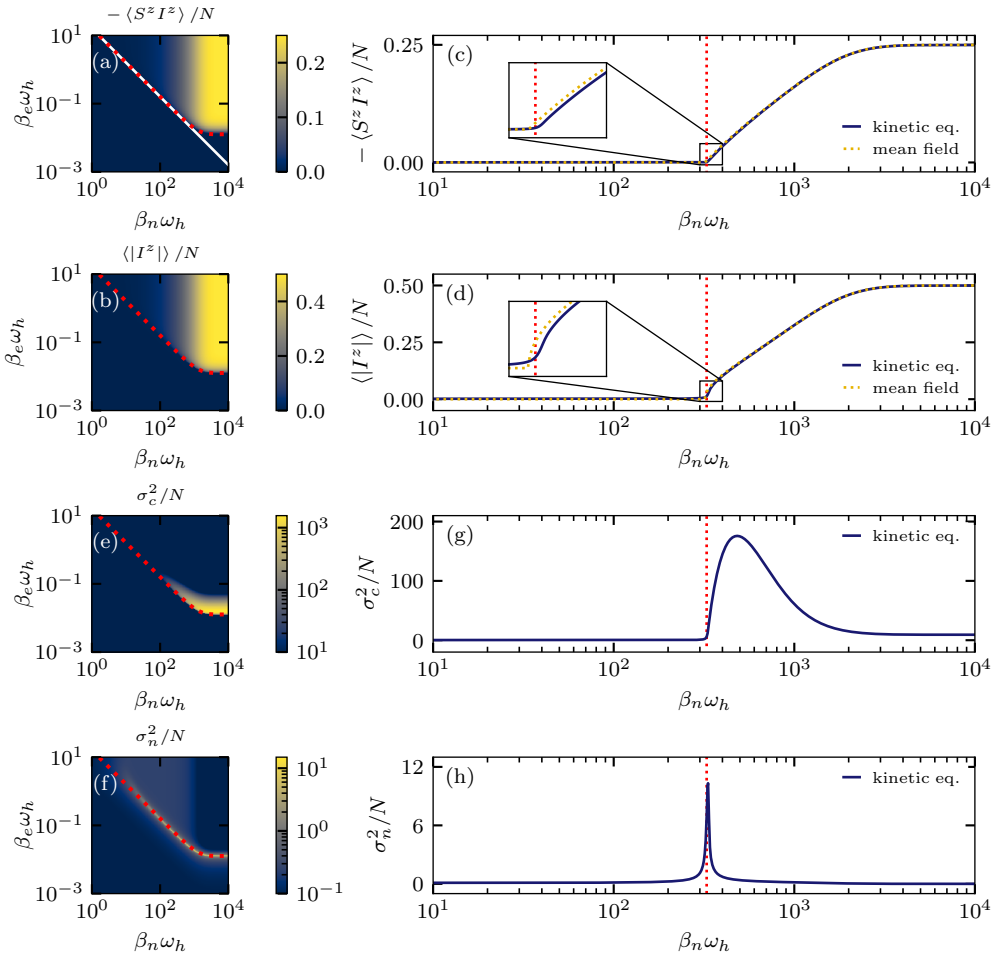

Figure 10.2: (a) and (c) Electron-nuclear spin correlator $\langle S^z I^z\rangle$, (b) and (d) average absolute value of the nuclear spin polarization $\langle|I^z|\rangle$, (e) and (g) fluctuations of the correlator σ_c^2, and (f) and (h) fluctuations of the absolute value of the nuclear polarization σ_n^2. The left panels depict expectation values as function of β_e and β_n while the right panels are horizontal cuts for a fixed electron temperature ($\beta_e\omega_h = 0.05$, $N = 10^5$). The white solid line in panel (a) corresponds to the mean-field critical temperature, Eq. (10.24). The red dotted line marks the transition to the polaron formation, Eq. (10.27)

The features of both quantities at the transition line are transferred to their fluctuations,

$$\sigma_c^2 = \langle (S^z I^z)^2\rangle - \langle S^z I^z\rangle^2\,, \tag{10.31a}$$

$$\sigma_n^2 = \langle (I^z)^2\rangle - \langle |I^z|\rangle^2\,, \tag{10.31b}$$

which are shown in Fig.10.2(e) and Fig. 10.2(f) as color maps and in Fig.10.2(g) and Fig. 10.2(h) as horizontal cuts. The electron-nuclear spin fluctuations σ_c^2 show a broad peak below the transition temperature while the nuclear spin fluctuation σ_n^2 has a sharp peak directly at the transition temperature. To interpret these quantities, we refer to the case of a single temperature. Since $\langle S^z I^z \rangle$ is proportional to the energy of the system, its fluctuations define, except for a prefactor, the heat capacity of the system. In the same way, the fluctuations of $\langle |I^z| \rangle$ can be related to the effective finite-size susceptibility [203, 207, 208]. According to the Landau theory of phase transitions, the heat capacity provides a step at the critical temperature while the susceptibility diverges [209]. As we consider a finite system here, a smoothed behavior can be expected. However, the question arises whether the fluctuations remain smooth for $N \gg 1$.

10.7 Nature of the transition to the polaron state

In this section, we investigate the nuclear polaron formation in the limit of large bath sizes. As starting point, we employ the rate equation (10.16) in the limit $W_e^{(0)} \gg W_n^{(0)}$ and perform a continuum limit for large bath sizes, leading to a Fokker-Planck equation for the nuclear density function. Using this Fokker-Planck equation, we calculate a transition line for the nuclear polaron state and study the nature of the nuclear polaron transition by taking into account thermal fluctuations.

We define the positions $\tilde{I}^z \in \{-N/2+1/2, ..., N/2-1/2\}$ between two possible I^z values and identify the probability current from site $\tilde{I}^z_{\mathrm{tot}} - 1/2$ to $\tilde{I}^z_{\mathrm{tot}} + 1/2$ as

$$J(\tilde{I}^z) = \Gamma^+ \left(\tilde{I}^z - \frac{1}{2}\right) g\left(\tilde{I}^z - \frac{1}{2}\right) - \Gamma^- \left(\tilde{I}^z + \frac{1}{2}\right) g\left(\tilde{I}^z + \frac{1}{2}\right) \tag{10.32}$$

using the transition rates $\Gamma^{\pm}(I^z)$ and probability $g(I^z)$. Consequently, the rate equation reduces to the simple form of a discrete continuity equation

$$\frac{\partial g(I^z_{\mathrm{tot}})}{\partial t} = -J\left(I^z_{\mathrm{tot}} + \frac{1}{2}\right) + J\left(I^z_{\mathrm{tot}} - \frac{1}{2}\right) . \tag{10.33}$$

Now we perform the continuum limit for large bath sizes. For this purpose, we define the intensive variable $i^z = I^z/N$ (with $i^z \in [-1/2, 1/2]$) and define the new quantities using the discretization constant $\Delta = 1/N$:

$$\text{Probability density :} \qquad \tilde{g}(i^z) = \frac{g(i^z/\Delta)}{\Delta} = \frac{g(I^z_{\mathrm{tot}})}{\Delta} \tag{10.34a}$$

$$\text{Transition rate :} \qquad \gamma^{\pm}(i^z) = \Gamma^{\pm}(i^z/\Delta)\Delta = \Gamma^{\pm}(I^z_{\mathrm{tot}})\Delta \tag{10.34b}$$

$$\text{Probability current :} \qquad j(i^z) = J(i^z/\Delta) = J(\tilde{I}^z_{\mathrm{tot}}). \tag{10.34c}$$

Using these definitions, the rate equation turns into the continuity equation

$$\frac{\partial \tilde{g}(i^z)}{\partial t} = \frac{-j(i^z + \frac{\Delta}{2}) + j(i^z - \frac{\Delta}{2})}{\Delta} = -\frac{\partial}{\partial i^z} j(i^z) \; . \tag{10.35}$$

We can further analyze the probability current

$$\begin{aligned} j(i^z) &= \gamma^+ \left(i^z - \frac{\Delta}{2} \right) \tilde{g} \left(i^z - \frac{\Delta}{2} \right) - \gamma^- \left(i^z + \frac{\Delta}{2} \right) \tilde{g} \left(i^z + \frac{\Delta}{2} \right) \\ &\approx \mu(i^z) \tilde{g}(i^z) - D(i^z) \frac{\partial}{\partial i^z} \tilde{g}(i^z) \; . \end{aligned} \tag{10.36}$$

In the last step, we used the mean value

$$\tilde{g}(i^z) \approx \frac{1}{2} \left(\tilde{g} \left(i^z - \frac{\Delta}{2} \right) + \tilde{g} \left(i^z + \frac{\Delta}{2} \right) \right) \; , \tag{10.37}$$

the differential quotient

$$\frac{\partial}{\partial i^z} \tilde{g}(i^z) \approx \frac{1}{\Delta} \left(\tilde{g} \left(i^z - \frac{\Delta}{2} \right) - \tilde{g} \left(i^z + \frac{\Delta}{2} \right) \right) \; , \tag{10.38}$$

as well as introduced the probability drift

$$\mu(i^z) = \gamma^+(i^z) - \gamma^-(i^z) \approx \gamma^+ \left(i^z + \frac{\Delta}{2} \right) - \gamma^- \left(i^z - \frac{\Delta}{2} \right) \tag{10.39}$$

and a diffusion coefficient

$$D(i^z) = \frac{\Delta}{2} \left(\gamma^+(i^z) + \gamma^-(i^z) \right) \approx \frac{\Delta}{2} \left(\gamma^+ \left(i^z - \frac{\Delta}{2} \right) + \gamma^- \left(i^z + \frac{\Delta}{2} \right) \right) \; . \tag{10.40}$$

By inserting $j(i^z)$, Eq. (10.36), into the continuity equation (10.35), we end up with the Fokker-Planck equation

$$\frac{\partial \tilde{g}(i^z)}{\partial t} = -\frac{\partial}{\partial i^z} \left(\mu(i^z) \tilde{g}(i^z) - D(i^z) \frac{\partial}{\partial i^z} \tilde{g}(i^z) \right) \; . \tag{10.41}$$

The diffusion term results from the random nature of the spin flips. The drift term has two origins. On one hand, we have a drift of the probability to the states with the most degeneracy (maximization of entropy). On the other hand, the probability drifts to the states with the lowest energy (minimization of energy). Depending on the electronic and nuclear temperatures, one of these two effects dominates, which defines a transition line between these two regimes.

Transition line

At high (nuclear and electron) spin temperatures, the maximization of entropy dominates, i.e. the states with high degeneracy are predominantly occupied and we obtain a maximum at $\tilde{g}(i^z = 0)$. At low temperatures, the minimization of energy dominates, i.e. the states with low energy are strongly occupied, and we observe a minimum at $\tilde{g}(i^z = 0)$ and two maxima located symmetrically to the right and the left hand. Hence, we establish the extremum at $\tilde{g}(i^z = 0)$ as a criterion to distinguish between a nuclear polaron state and a disordered state. We first study the extremum at $\tilde{g}(i^z = 0)$ in the continuum limit to derive a transition line similar as described before for discrete values of I^z (Sec. 10.5). As a next step, we analyze the fluctuations at the transition line.

At an extremum the derivative $\partial_{i^z}\tilde{g}(i^z) = 0$ vanishes, which in combination with the steady-state condition of a vanishing probability current $j(i^z) = 0$, yields the condition $\mu(i^z) = 0$ for an extremum. From symmetry arguments, we know that there is an extremum at $\tilde{g}(i^z) = 0$, which can either be a maximum or minimum. The condition for a maximum is

$$\frac{\partial}{\partial i^z}\mu(i^z) < 0 \, . \tag{10.42}$$

We insert $\gamma^{\pm}$ into the definition of the probability drift, Eq. (10.39),

$$\begin{aligned}\mu(i^z) = \frac{W_n^{(0)}}{\exp(\frac{A_0\beta_n}{4})\cosh\left(\frac{NA_0\beta_e i^z}{2}\right)}\Bigg[&\left(\frac{1}{2} - i^z\right)\cosh\left(\frac{NA_0\beta_e i^z}{2} + \frac{A_0\beta_n}{4}\right) \\ &- \left(\frac{1}{2} + i^z\right)\cosh\left(\frac{-NA_0\beta_e i^z}{2} + \frac{A_0\beta_n}{4}\right)\Bigg]\end{aligned} \tag{10.43}$$

and calculate its derivative at $i^z = 0$

$$\left.\frac{\partial}{\partial i^z}\mu(i^z)\right|_{i^z=0} = \frac{2W_n^{(0)}}{\exp(\frac{A_0\beta_n}{4})}\left(-\cosh\left(\frac{A_0\beta_N}{4}\right) + \frac{N}{2}\frac{A_0\beta_e}{2}\sinh\left(\frac{A_0\beta_n}{4}\right)\right) \, , \tag{10.44}$$

which yields the transition line

$$\beta_n^c = \frac{4}{A_0}\mathrm{arctanh}\left(\frac{4}{NA_0\beta_e^c}\right) \tag{10.45}$$

in the continuum limit, which coincides with the explicit transition line, Eq. (10.28), in the discrete calculation.

Fluctuations at the transition line

The next step is to analyze the fluctuations $\left(\left\langle (I^z_{\mathrm{tot}})^2 \right\rangle - \left\langle |I^z_{\mathrm{tot}}| \right\rangle^2\right)/N$ at the transition line. For a phase transition, the fluctuations may diverge, while the fluctuations stay finite for a smooth cross-over.

To calculate the expectation values, we first need the probability density $\tilde{g}(i^z)$. In the steady state, we obtain the formal solution of the Fokker-Planck equation

$$\mu(i^z)\tilde{g}(i^z) - D(i^z)\frac{\partial}{\partial i^z}\tilde{g}(i^z) = 0 \tag{10.46}$$

$$\Rightarrow \tilde{g}(i^z) = \exp\left(\int \frac{\mu(i^z)}{D(i^z)}\mathrm{d}i^z\right) . \tag{10.47}$$

Assuming that the distribution $\tilde{g}(i^z)$ becomes very sharp for large N, we can expand $\frac{\mu(i^z)}{D(i^z)}$ in leading order of i^z at $i^z = 0$. At the transition temperature (β_n^c, β_e^c) (defined in Eq. (10.45)), we obtain

$$\mu(i^z) = W_N^{(0)}\frac{\cosh(\frac{A_0\beta_n^c}{4})}{\exp(\frac{A_0\beta_n^c}{4})}\frac{N^3A_0^3(\beta_e^c)^3}{24}\tanh\left(\frac{A_0\beta_n^c}{4}\right)(i^z)^3 + O\left((i^z)^5\right) \tag{10.48}$$

and

$$D(i^z) = W_N^{(0)}\frac{\cosh(\frac{A_0\beta_n^c}{4})}{\exp(\frac{A_0\beta_n^c}{4})}\frac{1}{2N} + O\left((i^z)^2\right) . \tag{10.49}$$

Note, due to symmetry considerations, $\mu(i^z)$ has only odd powers of i^z and $D(i^z)$ has only even contributions. Furthermore, for $\mu(i^z)$, the terms linear in i^z vanish at the transition line, due to the condition $\partial_{i^z}\mu(i^z) = 0$. For the ratio, we obtain

$$\frac{\mu(i^z)}{D(i^z)} = -\xi(i^z)^3 + O\left((i^z)^5\right) \tag{10.50}$$

with the abbreviation for the temperature-dependent prefactor

$$\xi = \frac{N^3A_0^2(\beta_e^c)^2}{3} . \tag{10.51}$$

In this approximation, the probability density can be calculated directly

$$\tilde{g}(i^z) = \frac{\sqrt{2}\sqrt[4]{\xi}}{\Gamma(1/4)}\exp\left(-\frac{\xi}{4}(i^z)^4\right) \tag{10.52}$$

with the gamma function $\Gamma(n)$. Knowing the distribution $\tilde{g}(i^z)$, the expectation values

$$\begin{aligned}\langle|i^z|\rangle &= 2\frac{\sqrt{2}\sqrt[4]{\xi}}{\Gamma(1/4)}\int_0^\infty i^z \exp\left(-\frac{\xi}{4}(i^z)^4\right)\mathrm{d}i^z \\ &= \frac{\sqrt{2}\sqrt[4]{\xi}}{\Gamma(1/4)}\end{aligned} \tag{10.53}$$

and

$$\begin{aligned}\left\langle(i^z)^2\right\rangle &= \frac{\sqrt{2}\sqrt[4]{\xi}}{\Gamma(1/4)}\int_{-\infty}^\infty (i^z)^2 \exp\left(-\frac{\xi}{4}(i^z)^4\right)\mathrm{d}i^z \\ &= \frac{2\,\Gamma(3/4)}{\sqrt{\xi}\Gamma(1/4)}\end{aligned} \tag{10.54}$$

can be calculated analytically. Combining Eqs. (10.53) and (10.54), we obtain the total nuclear spin fluctuations

$$\frac{\left\langle(I^z_{\mathrm{tot}})^2\right\rangle - \langle|I^z_{\mathrm{tot}}|\rangle^2}{N} = \underbrace{\frac{\left(\sqrt{2}-1\right)\sqrt{3}\,\Gamma^2(3/4)}{\pi}}_{\approx 0.343}\frac{1}{\sqrt{N}A_0\beta_e^c}\,. \tag{10.55}$$

As a last step, we use the transition line, Eq. (10.45), to eliminate the A_0 dependency. In the limit $N \gg A_0\beta_e^c$, we can substitute the explicit expression

$$A_0 = \frac{4}{\sqrt{N\beta_e^c\beta_n^c}} \tag{10.56}$$

which yields

$$\frac{\left\langle(I^z_{\mathrm{tot}})^2\right\rangle - \langle|I^z_{\mathrm{tot}}|\rangle^2}{N} = \underbrace{\frac{\left(\sqrt{2}-1\right)\sqrt{3}\,\Gamma^2(3/4)}{4\pi}}_{\approx 0.086}\sqrt{\frac{\beta_n^c}{\beta_e^c}}\,. \tag{10.57}$$

This is a simple and interesting result. Besides a numerical prefactor, the fluctuations only depend on the ratio of the electronic and nuclear temperature. Hence, the transition is more rapid for asymmetric temperatures $\beta_e \gg \beta_n$. On the other hand, the fluctuations are not N dependent, which is an indicator for cross-over rather than a phase transition in the limit $N \gg 1$.

Emergence of the two maxima

The analysis of the nuclear spin fluctuation demonstrates that the polaron formation is expected to be continuous for equal $\beta_e = \beta_n$ and becomes more rapid for asymmetric temperatures $\beta_e \gg \beta_n$. To support this result, we consider the emergence of

the two maxima of the distribution $\tilde{g}(i^z)$ below the polaron transition temperature. At the transition temperature, the single maximum at $i^z = 0$ splits symmetrically into two maxima at $i^z \neq 0$ and a minimum at $i^z = 0$. Since we are only interested in extrema close to $i^z = 0$ we can expand the probability drift $\mu(i^z)$ around $i^z = 0$ in third order

$$\begin{aligned}\mu(i^z) \approx \frac{2W_n^{(0)}}{\exp\left(\frac{A_0\beta_n}{4}\right)} \Bigg[-i^z \cosh\left(\frac{A_0\beta_n}{4}\right) + i^z \frac{NA_0\beta_e}{4} \sinh\left(\frac{A_0\beta_n}{4}\right) \\ -(i^z)^3 \frac{N^3 A_0^3 \beta_e^3}{48} \sinh\left(\frac{A_0\beta_n}{4}\right) \Bigg] + \mathcal{O}\left((i^z)^5\right)\end{aligned} \tag{10.58}$$

and evaluate $\mu(i^z) = 0$. As a result, we obtain a trivial extremum at $i_0^z = 0$ and, for temperatures below the transition line, two additional extrema at the positions

$$i_\pm^z = \pm\sqrt{12}\frac{T_e^c}{A_0 N}\sqrt{-\frac{T_e - T_e^c}{T_e^c} - (T_n - T_n^c)\frac{T_e^c}{N(T_n^c)^2}\left(\frac{N^2A_0^2}{16(T_e^c)^2} - 1\right)} \tag{10.59}$$

appear. We analyze Eq. (10.59) in the limit of large bath sizes $N \gg A_0/T_e^c$, which yields

$$\begin{aligned} i_\pm^z &= \pm\sqrt{12}\frac{T_e^c}{A_0 N}\sqrt{-\frac{T_e - T_e^c}{T_e^c} - (T_n - T_n^c)\frac{T_e^c}{N(T_n^c)^2}\frac{N^2A_0^2}{16(T_e^c)^2}} \\ &= \pm\sqrt{\frac{4}{3N}}\sqrt{\frac{T_e^c}{T_n^c}}\sqrt{-\frac{T_e - T_e^c}{T_e^c} - \frac{T_n - T_n^c}{T_n^c}}\,. \end{aligned} \tag{10.60}$$

For the last step, we employed the simplified transition line $T_e^c T_n^c = \frac{NA_0^2}{16}$ from Eq. (10.24), which is valid in the same limit ($N \gg A_0/T_e^c$). Introducing the reduced temperatures $\tau_{e/n} = \frac{T_{e/n}}{T_{e/n}^c} - 1$, we end up with

$$i_\pm^z = \pm\sqrt{\frac{3}{4N}}\sqrt{\frac{T_e^c}{T_n^c}}\sqrt{|\tau_e| + |\tau_n|}\,. \tag{10.61}$$

On the one hand, the two maxima $i_\pm^z$ diverge more rapidly the larger the ratio T_e^c/T_n^c, on the other hand, the two maxima diverge less rapidly for larger N. If we neglect spin fluctuations, Eq. (10.61) implies a mean-field like phase transition with a critical exponent $\beta = 1/2$.

As the last step, we examine the effect of spin fluctuations. We take into account the width of the maxima $i_\pm^z$ and calculate the temperature interval $\Delta\tau$ starting from the critical temperature to a temperature where the maxima have no substantial

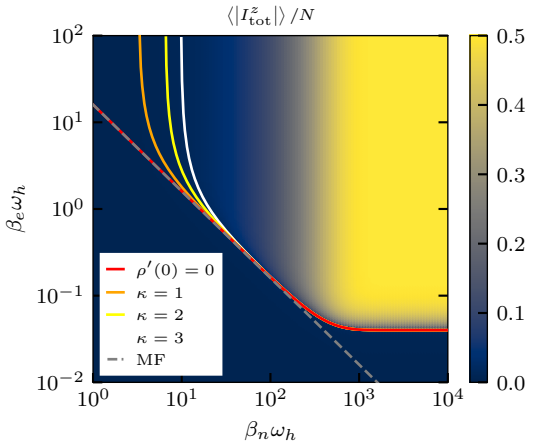

Figure 10.3: Order parameter $\langle |I^z_{\mathrm{tot}}| \rangle$ calculated from the analytic expression, Eq. (10.19) ($N = 10^4$, $A_0 = 1/\sqrt{N}$). The red line indicates where the transition from one maximum to two maxima in $\tilde{g}(i^z)$ takes place, i.e. Eq. (10.45). The orange, yellow and white lines indicate when the two maxima have a distance of κ standard deviations (calculated with Eq. (10.64)). The grey dashed line corresponds to the mean-field critical temperature.

overlap. This temperature interval $\Delta\tau$ can be interpreted as the cross-over region from a disordered to an ordered state. If the cross-over region vanishes for large N, we obtain a discontinuity and a phase transition can be expected. However, if the cross-over region stays finite for large N, we can expect a smooth cross-over.

We assume that the maxima have a standard deviation of

$$\sigma = \sqrt{\frac{1}{2N}} \,. \tag{10.62}$$

The overlap of the two maxima is exponentially suppressed when they have a distance of κ standard deviations (e.g. $\kappa = 1$ corresponds to a single standard deviation). Comparing the distance of the two maxima, to their width, we obtain

$$\sqrt{\frac{3}{4N}} \sqrt{\frac{T_e^c}{T_n^c}} \sqrt{\Delta\tau} = \kappa \sqrt{\frac{1}{2N}} \tag{10.63}$$

$$\Rightarrow \Delta\tau = \frac{2}{3} \frac{T_n^c}{T_e^c} \kappa^2 \,. \tag{10.64}$$

As we can see, $\Delta\tau$ is independent of N which indicates a smooth cross-over between the unpolarized regime and the nuclear polaron regime for $N \gg 1$. On the other

hand, the cross-over region decreases strongly for asymmetric electronic and nuclear temperatures. In Fig. 10.3, the findings of the continuum approach are shown in the phase diagram of $\langle |I^z_{\mathrm{tot}}| \rangle / N$. The red line depicts the transition line, Eq. (10.45). The orange, yellow and white lines indicate when the two maxima have a distance of κ standard deviations (calculated with Eq. (10.64)). We observe a smooth cross-over at high nuclear temperatures while the transition is more rapid at lower nuclear temperatures.

For the experimentally relevant regime, the electron spin has a cryostatic temperature of $T_e \approx 1\,\mathrm{K}$, which corresponds to a nuclear temperature of $T_n^c \approx 10^{-7}\,\mathrm{K}$ at the critical point. This yields a cross-over region of $\Delta T_n = \Delta\tau T_n^c \approx 10^{-14}\,\mathrm{K}$, which is far below the expected temperature resolution in experiments. Hence, in a strongly asymmetric temperature regime, we can expect to observe a mean-field like transition, though formally the system obeys a cross-over.

10.8 Distribution of the hyperfine coupling constants

The box-model approximation is a substantial simplification of the CSM as nuclear spins are subject to the same Knight field and remain synchronized when coupling to the environment is neglected. In this section, we discuss the effect of an A_k distribution. As the coupling of the system to thermal reservoirs breaks the artificial synchronization of the nuclear spins, the main result will be that a system with a A_k distribution behaves as a box-model system with a smaller number of nuclear spins.

We introduce a distribution of coupling constants as it could occur in a realistic QD. The hyperfine coupling constants are proportional to the residence probability of the electron at the location of the nuclear spins. We assume that the electron wave function has the exponential form

$$\psi(\vec{r}) \propto \exp\left[-r^m/(2L_0^m)\right] \,, \tag{10.65}$$

where L_0 is the characteristic length of the QD and m modifies the shape of the wave function. This wave function yields the distribution [210]

$$p(A_k) = \frac{d}{m}\frac{L_0^d}{A_k R^d}\left[\ln\left(\frac{A_{\max}}{A_k}\right)\right]^{d/m-1} \,, \tag{10.66}$$

where d is the dimension of the QD, $A_{\max}$ is the maximum hyperfine coupling constant, and R is an artificial cut-off radius that determines the smallest hyperfine coupling constant.

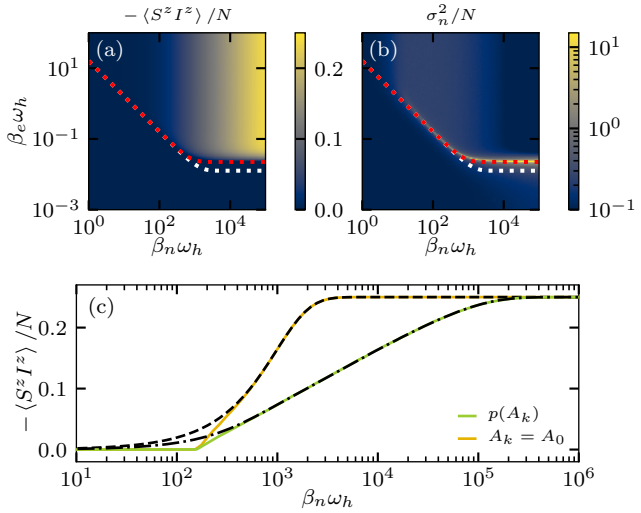

Figure 10.4: Polaron formation in a system ($N = 10^5$) with realistic hyperfine-coupling constants, see Eq. (10.66). (a) Electron-nuclear spin correlator and (b) fluctuations of the absolute value of the nuclear spin polarization as a function of β_e and β_n. The white dotted line presents the transition line with N. The red dotted line indicates the transition temperature, Eq. (10.27), adjusted with N_{eff}. (c) Correlator for a fixed electron temperature ($\beta_e\omega_h = 0.1$). The black dashed/dash-dotted lines correspond to the approximation in Eq. (10.68). The plot is taken from Ref. [173]

In the following, we assume a Gaussian wave function ($m = 2$) in a flat QD ($d = 2$). This results in the distribution $p(A_k) \propto 1/A_k$, where the maximum and minimum values of A_k are regulated by the parameters R and $A_{\max}$. For our calculations, we set the cutoff radius to $R = 2.5L_0$ and adjust $A_{\max}$ in such a way that $\omega_h = (\sum_k A_k^2)^{1/2}$ holds.

To determine the steady-state solution, we employ a Markov chain Monte Carlo method. We use the rates, Eqs. (10.10) and (10.11), to determine the acceptance probability for a spin flip, which coincides with the Metropolis-Hastings algorithm. After a sufficient simulation time, the system is equilibrated in the steady state and various expectation values can be calculated by averaging over several simulation steps.

In Fig. 10.4(a), the correlator $\langle S^z I^z\rangle$ is plotted as a function of the two inverse temperatures β_e and β_n for a spin flip ratio $W_e^{(0)}/W_n^{(0)} = 10^5$. The general behavior of the polaron formation is very similar to the box model, although the transition does not occur at the same temperature line. The analytical curve for the polaron

transition in the box model according to Eq. (10.27) is shown as a white dotted curve. While all nuclear spins contribute equally to the dynamics in the box model, depending on the distribution of A_k, there may be nuclear spins that contribute weakly to the dynamics or even factorize for the extreme case of $A_k = 0$. We quantify this behavior by defining an effective number of nuclear spins, N_{eff}, [17, 211] over the first two moments of the A_k distribution

$$\frac{N_{\text{eff}}}{N} = \frac{\langle A_k \rangle^2}{\langle A_k^2 \rangle} \,. \tag{10.67}$$

While for the box model $N = N_{\text{eff}}$ holds, the distribution used in Fig. 10.4 results in the ratio $N_{\text{eff}}/N \approx 0.32$. We employ N_{eff} to determine a corrected transition line, by replacing N by N_{eff} in Eq. (10.27), which is shown as a red dotted line. Fig. 10.4(b) depicts the nuclear spin fluctuation σ_n^2 where the polaron formation can be seen by a sharp peak, which coincides with the corrected transition line. In essence, the effect of the A_k distribution is parameterized by the statistical quantity N_{eff}.

For temperatures below the transition line, the distribution of the hyperfine constants becomes relevant, since weakly coupled nuclear spins align to the electron spin only at very low temperatures. This is illustrated in Fig. 10.4(c), where the electron-nuclear spin correlator $\langle S^z I^z \rangle$ for a fixed inverse electron spin temperature $\beta_e \omega_h = 0.1$ is plotted against the inverse nuclear spin temperature β_n. The maximum absolute value of the correlator for a distribution $p(A_k)$ is reached at lower temperatures than in the box model. This behavior can be understood analytically in a low-temperature approximation. Below the polaron transition temperature, electron spin flips are strongly suppressed due to the large energy difference. Assuming a fully frozen electron spin, the system factorizes into independent subproblems for each nuclear spin, and the electron-nuclear correlator

$$\langle S^z I^z \rangle \approx -\sum_k \tanh\left(A_k \beta_n / 4\right) / 4 \tag{10.68}$$

can be determined exactly. This approximation is added in Fig. 10.4(c) for the box model (black dashed line) and the distribution Eq. (10.66) (black dash-dotted line). Apart from deviations at the transition temperature, which is dominated by spin fluctuations, the correlator is accurately predicted. In the polaron regime, each nuclear spin aligns individually with its A_k, while the details of the coupling constant distribution are irrelevant for the polaron transition.

10.9 Time evolution of the cooled system

The rate equations do not only provide the two-temperature steady state but also allow the investigation of the temporal evolution to the nuclear-spin polaron state. For this purpose, we consider the rate Eq. (10.12) in matrix form

$$\partial_t \vec{g} = W\vec{g}, \tag{10.69}$$

where the vector $\vec{g}$ has the entries $g(I^z, S^z)$ and the elements of the transition matrix W entail the transition rates Eq. (10.13a) and Eq. (10.13b). The analytical solution is formally given by the matrix exponential function

$$\vec{g} = \exp(Wt)\vec{g}_0 \,, \tag{10.70}$$

with the initial condition $\vec{g}(0) = \vec{g}_0$. While W is a sparse matrix, $\exp(Wt)$ is dense, so the exact solution is not suitable for numerical evaluations with $N = 10^5$. Instead, we use the Trotter decomposition

$$\vec{g} = (\exp(W\Delta t))^n \vec{g}_0 \tag{10.71}$$

with $n = t/\Delta t$ and approximate

$$\exp(W\Delta t) \approx \sum_{k=0}^{4} \frac{W^k}{k!} \,. \tag{10.72}$$

In this approximation, $\exp(W\Delta t)$ is sparse and can be used to determine the time evolution.

In the following, we will consider a cooling scenario where the system starts in a high-temperature state and is cooled by the coupling to the reservoirs. At high temperatures, the $g_0(I^z, S^z)$ are weighted only by their degeneracy, yielding

$$g_0(I^z, S^z) = 2^{-N-1} \binom{N}{N_+(I^z)} \tag{10.73}$$

with $N_+(I^z) = N/2 + I^z$. In Fig. 10.5(a), the time evolution of the correlator $\langle S^z I^z \rangle$ is shown for temperatures deep in the polaron regime, $\beta_n \omega_h = 10^4$ and $\beta_e \omega_h = 5$. It can be seen that all curves, regardless of the rate $W_e^{(0)}$ and $W_n^{(0)}$, match with the exponential function

$$\langle S^z I^z \rangle / N = -(1 - \exp(-W_n^{(0)} t))/4 \tag{10.74}$$

and, thus, only depend on the rate $W_n^{(0)}$. This is explained by the fact that at low temperatures electron spin flips are exponentially suppressed by the large energy

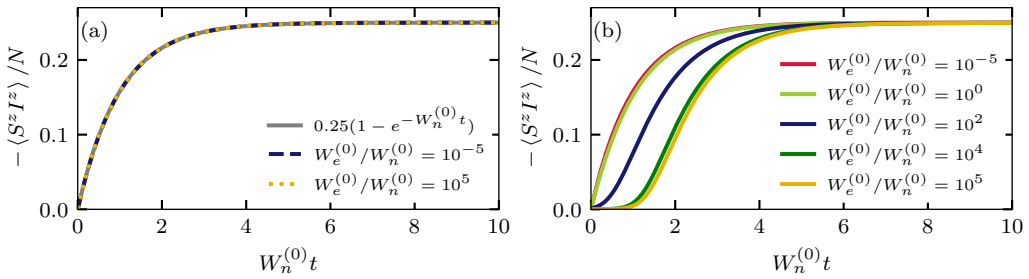

Figure 10.5: Temporal evolution from disordered to nuclear polaron state ($N = 10^5, \beta_n\omega_h = 10^4$) for two inverse electron spin temperatures, (a) $\beta_e\omega_h = 5$ and (b) $\beta_e\omega_h = 0.05$. The plot is taken from Ref. [173].

difference while a nuclear spin flip requires only a small energy exchange. In addition, the maximally anticorrelated spin polaron state can be reached without a single electron spin flip while about half of the nuclear spins must flip when the system starts in a disordered state. In combination, the formation time is determined solely by the nuclear flip rate $W_n^{(0)}$.

In Fig. 10.5(b), the time evolution of the correlator $\langle S^z I^z\rangle$ for a higher electron temperature, $\beta_e\omega_h = 0.05$, is shown. For very slow electron flip rates $W_e^{(0)} < W_n^{(0)}$, there is almost no electron spin flip on the polaron formation time scale and the universal exponential behavior, Eq. (10.74), is preserved. For $W_e^{(0)} > W_n^{(0)}$, on the other hand, there are deviations from the purely exponential growth. The electron spin flips disturb the polaron formation, which initially leads to a delayed growth of the correlator. Only when a sufficiently large nuclear spin polarization has formed and electron spin flips are suppressed again, the further polaron formation takes place in an exponential curve. For very large $W_e^{(0)}$, there is saturation for this effect and a further increase of $W_e^{(0)}$ has no effect. This is the case when the electron spin distribution follows the nuclear spins almost instantaneously.

10.10 Anisotropic hyperfine interaction

So far we have restricted ourselves to a hyperfine interaction of the Ising type while charge carriers in QDs are generally described by an anisotropic hyperfine interaction, Eq. (3.3) with anisotropy factor λ. While heavy holes with $\lambda = 0$ are subject to an Ising interaction, for light holes $\lambda = -2$ holds. For mixed states between heavy and light holes, a value in between is possible. Electron spins are subject to an isotropic hyperfine interaction $\lambda = 1$.

Since the hyperfine Hamiltonian Eq. (3.3) for $\lambda \neq 0$ is no longer diagonal, the rate equation (10.9) has to be extended to a Lindblad master equation which also includes non-diagonal elements. For this purpose, we assume that the eigenstates $H_{\mathrm{HF}} |\psi_n\rangle = \epsilon_n |\psi_n\rangle$ of the system Hamiltonian are accessible. We use the eigenbasis to define the complete operator basis $X_{mn} = |\psi_m\rangle \langle\psi_n|$. Considering a possible degeneracy of the eigenstates, the general Lindblad operator for a transition between the energy levels $\epsilon_n \to \epsilon_m$ is given by

$$L^{k,\alpha}_{m,n} = \sqrt{\Gamma^{k,\alpha}_{m,n}} \sum_{a,b} \delta_{\epsilon_a,\epsilon_m} \delta_{\epsilon_b,\epsilon_n} \langle\psi_a| s^\alpha_k |\psi_b\rangle X_{ab} \,, \tag{10.75}$$

where $\Gamma^{k,\alpha}_{m,n}$ is a rate not yet specified and $\langle\psi_a| s^\alpha_k |\psi_b\rangle$ is the transition matrix element of the spin operator s^α_k. Here $\alpha \in \{x, y, z\}$ is the spatial axis and the index $k \in \{0, ..., N_I\}$ counts all spins in the system, where $k = 0$ corresponds to the electron spin $s^\alpha_0 = S^\alpha$ and $k \geq 1$ corresponds to a nuclear spin $s^\alpha_k = I^\alpha_k$. The corresponding Lindblad master equation reads

$$\partial_t \rho = -i[H_{\mathrm{HF}}, \rho] - \sum_{k,\alpha,m,n} (L^{k,\alpha}_{m,n})^\dagger L^{k,\alpha}_{m,n} \rho + \rho (L^{k,\alpha}_{m,n})^\dagger L^{k,\alpha}_{m,n} - 2 L^{k,\alpha}_{m,n} \rho (L^{k,\alpha}_{m,n})^\dagger \,. \tag{10.76}$$

Finally, the rate $\Gamma^{k,\alpha}_{m,n}$ must be specified in such a way that the Boltzmann form is attained in thermal equilibrium. We choose

$$\Gamma^{k,\alpha}_{m,n} = \frac{W^\alpha_k h^\alpha_k(\epsilon_m - \epsilon_n)}{g(\epsilon_m) g(\epsilon_n)} \,, \tag{10.77}$$

where W^α_k is a phenomenological rate, $h^\alpha_k(\epsilon_m - \epsilon_n)$ is a dimensionless but energy-dependent prefactor, and $g(\epsilon_n)$ is the degeneracy of the energy level ϵ_n, which prevents double counting. We choose the rates for the electron spin $W^\alpha_0 = W^{(0)}_e$ and the nuclear spins $W^\alpha_k = W^{(0)}_n$ following Sec. 10.2. The energy dependent prefactor $h^\alpha_k(\Delta_{mn})$ with $\Delta_{mn} = \epsilon_m - \epsilon_n$ guarantees the Boltzmann form if the ratio $h^\alpha_k(\Delta_{mn})/h^\alpha_k(\Delta_{nm}) = \exp(-\Delta_{mn}\beta_k)$ with $\beta = \beta_k$ is satisfied. Following Sec. 10.2, we choose

$$h^\alpha_k(\epsilon) = \min(1, e^{-\beta_k \epsilon}) \,. \tag{10.78}$$

Consistently, we set $\beta_0 = \beta_e$ for the electron and $\beta_k = \beta_n$ for the nuclear spins.

To demonstrate that the Lindblad approach (10.76) coincides with the rate equations (10.9), we derive the Lindblad Eq. (10.76) for a diagonal density matrix in energy

eigenbases $\rho = \sum_m \rho_{mm} |\psi_m\rangle \langle\psi_m|$. We obtain the rate equation for the diagonal elements ρ_{mm}

$$\begin{aligned}\partial_t \rho_{mm} =& 2 \sum_{k,\alpha,n} W_k^\alpha h_k^\alpha (\epsilon_m - \epsilon_n) |\langle\psi_m| s_k^\alpha |\psi_n\rangle|^2 \rho_{nn} \\ & - 2 \sum_{k,\alpha,n} W_k^\alpha h_k^\alpha (\epsilon_n - \epsilon_m) |\langle\psi_n| s_k^\alpha |\psi_m\rangle|^2 \rho_{mm}.\end{aligned} \tag{10.79}$$

We can replace the operators s_k^α with the ladder operators s_k^τ

$$s_k^\tau = \begin{cases} s_k^+/\sqrt{2}, & \tau = 1 \\ s_k^z, & \tau = 0 \\ s_k^-/\sqrt{2}, & \tau = -1 \end{cases}, \tag{10.80}$$

and identifying $|\psi_m\rangle$ with the Ising basis, which is applicable for $\lambda = 0$. The contribution of s_k^z cancels out in both sums and the operators $s_k^\pm$ generate exactly one spin flip. We can use the definitions of W_k^α and h_k^α in this section and derive the rate equation (10.9) from our more general approach, Eq. 10.76.

While we recover the Ising case exactly, the Lindblad formalism allows studying a general anisotropic hyperfine interaction. The approach relies on the exact knowledge of the energy eigenbasis and is limited this way by the size of the considered Hilbert state. However, by using the box-model approximation, a realistic number of spins can be considered [204]. For a general anisotropy factor, the polaron state forms along the axis with maximal hyperfine interaction, i.e., for $|\lambda| < 1$ along the z-axis and for $|\lambda| > 1$ in the (xy) plane. These two regimes are separated by a quantum phase transition at $|\lambda| = 1$, where the polaron forms isotropically. For $|\lambda| \geq 1$ all ground states are connected by spin flips without increasing the energy barriers, which results in a significantly reduced autocorrelation time. For $|\lambda| < 1$, there are two possible ground states, corresponding to the two polaron states along the z-axis, which are separated by an energy barrier. In the later case, including the Ising limit, the polaron formation is indicated by a bifurcation of the nuclear spin distribution, which significantly increases the correlation time [204].

10.11 Outlook

We demonstrated the formation of a nuclear-spin polaron state at low temperatures. The polaron state is characterized by a strong correlation between the electron spin and nuclear spins. We modeled the system by a CSM for the electron-nuclear spin system in the Ising limit and coupled the electron and nuclear spins to reservoirs

with different temperatures. Interestingly, the exact solution for equal temperatures yields a cross-over to the polaron state while the mean-field approach predicts a phase transition. With the rate equation approach used here, we can unify both results. While we reproduce the exact thermodynamic solution for equal temperatures, the polaron transition becomes sharper for asymmetric temperatures and approaches the mean-field behavior asymptotically.

While this minimal model provides relevant results, it is expected that, for a realistic consideration, further interactions have to be included. For example, nuclear-electric quadrupolar interactions generate disorder in the nuclear spin bath, which compete with the hyperfine interaction in the polaron formation. Another interesting aspect is provided by an interaction between different electron spins. In the case of donor-bound electrons with high donor density, this can be an exchange interaction [89, 90, 212] while for QDs a long-range RKKY interaction is expected [59]. In the case of ferromagnetic coupling and a negative effective nuclear spin temperature, a long-range ferromagnetic state involving the electron spins and the nuclear spins has already been predicted [86]. In contrast, in the case of a mixed ferromagnetic and antiferromagnetic interaction, as it occurs in an RKKY-type interaction, geometric frustration may occur in the electronic subsystem, allowing a potential spin glass phase of the QD ensemble.

Both the quadrupolar interactions, which lift the artificial synchronization of the box model approximation, and the inter-QD interactions, which couple multiple CSMs, generate a significant increase of the complexity, which makes an exact treatment no longer feasible. However, due to the large spin number, the SCA offers a promising route to investigate this issue. While the dynamics at low temperatures are still given by the EOMs (4.32a) and (4.32b), the coupling to the reservoirs can be realized by the quantum jump approach, Sec. 5.4. In this case, the rate of quantum jumps is given by the phenomenological rates $W_e^{(0)}$ and $W_n^{(0)}$, while the temperature of the reservoirs can be included by an additional temperature-dependent acceptance rate $h_k(\Delta\epsilon)$.

Chapter 11

Conclusion

In this thesis, we provide an in-depth analysis of inter-QD spin-spin interactions in self-assembled QD ensembles. We based our theoretical investigations on available experimental data [57, 58, 69] and revealed signatures and effects of the inter-QD interactions relevant for potential future experiments [193]. We present methods to extend the coherence time, such as optical cooling or spin mode-locking, and methods for coherent spin manipulation, such as two-color pumping, where the inter-QD interaction enables strong correlations of electron spins and nuclear spins.

To this end, we developed a cluster model for the QD ensemble in which each individual QD is described by a CSM capturing the hyperfine interaction between the localized electron spin and the surrounding nuclear spins. The model for the individual QDs was extended to include several additional effects, such as nuclear-electric quadrupolar interactions, spin-lattice interactions, and light-matter interactions. The inter-QD interactions are modeled by an effective Heisenberg interaction between the electron spins. For a realistic QD ensemble, around 10^{10} spins have to be included in the theoretical description. Using scaling properties for the coupling constants, we reduced the number of electron spins and nuclear spins required to accurately capture the spin dynamics of the full QD ensemble. For the reduced system, we employed an SCA based on spin-coherent states: Each spin is parameterized by a classical vector. Mapping the time evolution to a quaternionic representation, we preserve quantum effects on the single-spin level. We developed a hybrid approach of the SCA and a quantum jump approach which allows for describing open quantum systems while preserving the bijective mapping between spin vectors and spin-coherent states. The hybrid approach enables the incorporation of spin-lattice interactions, optical excitations, and radiative trion decay.

The experiments of Spatzek et al. [57] served as a basis for the presented theoretical investigations. By a spectral selection of the QDs with two laser pulses, two disjoint subsets of QDs can be optically excited and read out separately. It was found that [57] the subsets interact coherently with each other. Depending on the pulse protocol, phase shifts or changes in the dephasing time can be detected. While the

experimental results can be explained by a Heisenberg interaction between the electron spins of different QDs, the underlying microscopic mechanism of the inter-QD interactions initially remained unclear [57]. We demonstrated that the experimental results are compliant with an RKKY interaction mediated by charge carriers in the wetting layer. For this purpose, we performed a semiclassical simulation of the spin dynamics employing the distance-dependent interaction strength obtained by NRG calculations. Our findings reproduce the key results in Ref. [57], such as the linearly increasing phase shift. Moreover, we developed a simple picture explaining how phase shifts and dephasing times emerge. We discuss the influence of the different electron g factors of the QD subsets.

In pump-probe experiments with tailored laser spectra, the spectral width of the laser pulse can be used to determine the number of excited QDs. In the absence of inter-QD interaction, it is expected that when the spectral laser width increases, the variation of electron g factors also increases. This produces a reduced dephasing time. However, the experimentally determined dephasing times are almost independent of the spectral laser width [69]. To explain this observation, we identified the three relevant mechanisms producing the electron spin dephasing on the time scale of a few nanoseconds: the Overhauser field fluctuations, the electron g-factor variations, and the inter-QD interactions. We found that the inter-QD interactions counterbalance the effect of the g-factor variation. When the laser bandwidth increases, the inter-QD interaction leads to a stabilizing synchronization of the electron spins which suppresses the dephasing. The pump-probe experiments demonstrated that the inter-QD interaction becomes relevant on the time scale of a few nanoseconds and can be utilized to efficiently influence the dephasing time.

Based on the findings for the pump-probe experiments, we developed a concept to identify signatures of the inter-QD interactions in experimental setups with tailored optical excitations. We propose two-color spin-noise measurements to study the inter-QD interactions in equilibrium. By construction, the cross-correlation spectrum vanishes if the spin dynamics in the individual QDs are independent of each other. Therefore the cross-correlation spectrum is especially sensitive to inter-QD interactions. In the autocorrelation spectrum, in contrast, the inter-QD interactions only lead to a broadening of the spectrum which is indistinguishable from other single-QD features. We examined the influence of the different interactions in the QD on the cross-correlation spectrum. For example, the quadrupolar interactions suppress the low-frequency contributions to the spectrum, while electron g-factor variations attenuate the cross-correlation spectrum in the presence of a strong transverse magnetic field. There is a wide window of magnetic fields where the cross-correlation spectrum exhibits profound contributions of the inter-QD interaction. The cross-correlation spectrum in a longitudinal magnetic field is particularly interesting since it is sensitive to the distribution of coupling constants.

Moreover, we studied the influence of periodic pulse trains on the interacting QDs. The repetition frequency of the optical pulses imprints on the spin dynamics and leads to nuclear-induced frequency-focusing. The nuclear spins in the QDs reorient in such a way that the electron spins perform a half-integer or integer number of revolutions for the Larmor precession in a repetition period. This effect can be explained by a hyperfine feedback mechanism between the electron spin and the nuclear spins. We showed that the inter-QD interactions lead to a modification of these dynamics and identify a new resonance condition induced by the inter-QD interaction. Whenever two electron spins favor the same mode, the hyperfine feedback mechanism is bypassed. As a result, two electron spins do not precess in the same mode. This mode repulsion generates strong correlations of the Overhauser fields of adjacent QDs. We demonstrated that the cross-correlations bi-spectrum reveals the correlations in the Overhauser fields.

Aside from the inter-QD interactions, we also investigated the intertwined spin dynamics of the electron spin and the nuclear spins in a single QD or for a donor-bound electron at low temperatures. Through optical cooling, effective nuclear spin temperatures significantly below cryostatic temperatures can be achieved. In this regime a strongly correlated nuclear-spin polaron state should form. Since the electron spin is strongly coupled to the environment, a two-temperature mean-field approach was proposed by Merkulov [44]. We extended the two-temperature approach to a fully quantum-mechanical treatment. We developed kinetic rate equations for the two-temperature scenario that reproduce the exact thermodynamic solution in the case of equal temperatures. From the rate equations, we obtain an analytic temperature line for the polaron formation, which coincides with the mean-field critical temperatures in certain temperature regimes. We derived a Fokker-Planck equation in the limit of large nuclear spin baths which implies that the polaron formation is a crossover phenomenon that becomes sharper for asymmetric temperatures. In this thesis, we restricted ourselves to the nuclear-spin polaron formation in a single QD. However, we expect that the inter-QD interactions have a significant influence on the polaron formation in a QD ensemble as they allow for long-range order or geometric frustration depending on the sign of the coupling constants. Since this complex spin system can no longer be treated exactly, we propose to extend the QJ-SCA developed in this thesis by a temperature-dependent spin-flip rate to efficiently address the polaron formation in an interacting QD ensemble.

In this thesis, we developed a versatile understanding of the inter-QD interactions in self-assembled QD ensembles. However, many questions remain open. The semiclassical approach developed allows for studying large spin systems but, by construction, prevents the formation of quantum entanglement. A systematic

extension of the SCA including quantum corrections that allow for quantum effects beyond the single-spin level is desirable.

Bibliography

[1] W. Gerlach and O. Stern, *Der experimentelle Nachweis der Richtungsquantelung im Magnetfeld*, Zeitschrift für Physik **9**, 349 (1922).

[2] G. E. Uhlenbeck and S. Goudsmit, *Ersetzung der Hypothese vom unmechanischen Zwang durch eine Forderung bezüglich des inneren Verhaltens jedes einzelnen Elektrons*, Die Naturwissenschaften **13**, 953 (1925).

[3] G. E. Uhlenbeck and S. Goudsmit, *Spinning Electrons and the Structure of Spectra*, Nature **117**, 264 (1926).

[4] P. A. M. Dirac and R. H. Fowler, *The quantum theory of the electron*, Proceedings of the Royal Society of London. Series A, Containing Papers of a Mathematical and Physical Character **117**, 610 (1928).

[5] S. A. Wolf, D. D. Awschalom, R. A. Buhrman, J. M. Daughton, S. von Molnár, M. L. Roukes, A. Y. Chtchelkanova, and D. M. Treger, *Spintronics: A Spin-Based Electronics Vision for the Future*, Science **294**, 1488 (2001).

[6] I. Žutic, J. Fabian, and S. Das Sarma, *Spintronics: Fundamentals and applications*, Rev. Mod. Phys. **76**, 323 (2004).

[7] D. Pesin and A. H. MacDonald, *Spintronics and pseudospintronics in graphene and topological insulators*, Nature Materials **11**, 409 (2012).

[8] D. D. Awschalom and M. E. Flatté, *Challenges for semiconductor spintronics*, Nature Physics **3**, 153 (2007).

[9] R. Landauer, *Irreversibility and Heat Generation in the Computing Process*, IBM Journal of Research and Development **5**, 183 (1961).

[10] M. N. Baibich, J. M. Broto, A. Fert, F. N. Van Dau, F. Petroff, P. Etienne, G. Creuzet, A. Friederich, and J. Chazelas, *Giant Magnetoresistance of (001)Fe/(001)Cr Magnetic Superlattices*, Phys. Rev. Lett. **61**, 2472 (1988).

[11] G. Binasch, P. Grünberg, F. Saurenbach, and W. Zinn, *Enhanced magnetoresistance in layered magnetic structures with antiferromagnetic interlayer exchange*, Phys. Rev. B **39**, 4828 (1989).

[12] G. Li, S. Sun, R. J. Wilson, R. L. White, N. Pourmand, and S. X. Wang, *Spin valve sensors for ultrasensitive detection of superparamagnetic nanoparticles for biological applications*, Sensors and Actuators A: Physical **126**, 98 (2006).

[13] L. Berger, *Emission of spin waves by a magnetic multilayer traversed by a current*, Phys. Rev. B **54**, 9353 (1996).

[14] J. Slonczewski, *Current-driven excitation of magnetic multilayers*, Journal of Magnetism and Magnetic Materials **159**, L1 (1996).

[15] N. P. Vasil'eva and S. I. Kasatkin, *Magnetic Random Access Memory Devices*, Automation and Remote Control **64**, 1369 (2003).

[16] D. Loss and D. P. DiVincenzo, *Quantum computation with quantum dots*, Phys. Rev. A **57**, 120 (1998).

[17] J. Schliemann, A. Khaetskii, and D. Loss, *Electron spin dynamics in quantum dots and related nanostructures due to hyperfine interaction with nuclei*, Journal of Physics: Condensed Matter **15**, R1809 (2003).

[18] C. Kloeffel and D. Loss, *Prospects for Spin-Based Quantum Computing in Quantum Dots*, Annual Review of Condensed Matter Physics **4**, 51 (2013).

[19] T. D. Ladd, F. Jelezko, R. Laflamme, Y. Nakamura, C. Monroe, and J. L. O'Brien, *Quantum computers*, Nature **464**, 45 (2010).

[20] A. Chatterjee, P. Stevenson, S. De Franceschi, A. Morello, N. P. de Leon, and F. Kuemmeth, *Semiconductor qubits in practice*, Nature Reviews Physics **3**, 157 (2021).

[21] F. Bloch, *Nuclear Induction*, Phys. Rev. **70**, 460 (1946).

[22] J. Schliemann, A. V. Khaetskii, and D. Loss, *Spin decay and quantum parallelism*, Phys. Rev. B **66**, 245303 (2002).

[23] R. P. Feynman, *Simulating physics with computers*, International Journal of Theoretical Physics **21**, 467 (1982).

[24] P. Shor, *Algorithms for quantum computation: discrete logarithms and factoring*, in Proceedings 35th Annual Symposium on Foundations of Computer Science (1994).

[25] L. K. Grover, *A Fast Quantum Mechanical Algorithm for Database Search*, in Proceedings of the Twenty-Eighth Annual ACM Symposium on Theory of Computing (1996).

[26] P. Shor, *Fault-tolerant quantum computation*, in Proceedings of 37th Conference on Foundations of Computer Science (1996).

[27] E. Knill, R. Laflamme, and W. H. Zurek, *Resilient Quantum Computation*, Science **279**, 342 (1998).

[28] A. Kitaev, *Fault-tolerant quantum computation by anyons*, Annals of Physics **303**, 2 (2003).

[29] D. Aharonov and M. Ben-Or, *Fault-Tolerant Quantum Computation with Constant Error Rate*, SIAM Journal on Computing **38**, 1207 (2008).

[30] E. T. Campbell, B. M. Terhal, and C. Vuillot, *Roads towards fault-tolerant universal quantum computation*, Nature **549**, 172 (2017).

[31] F. Arute, K. Arya, R. Babbush, D. Bacon, J. C. Bardin, R. Barends, R. Biswas, S. Boixo, F. G. S. L. Brandao, D. A. Buell, et al., *Quantum supremacy using a programmable superconducting processor*, Nature **574**, 505 (2019).

[32] E. R. MacQuarrie, C. Simon, S. Simmons, and E. Maine, *The emerging commercial landscape of quantum computing*, Nature Reviews Physics **2**, 596 (2020).

[33] M. Brooks, *Beyond quantum supremacy: the hunt for useful quantum computers*, Nature **574**, 19 (2019).

[34] L. Postler, S. Heußen, I. Pogorelov, M. Rispler, T. Feldker, M. Meth, C. D. Marciniak, R. Stricker, M. Ringbauer, R. Blatt, et al., *Demonstration of fault-tolerant universal quantum gate operations*, Nature **605**, 675 (2022).

[35] D. P. DiVincenzo, *The Physical Implementation of Quantum Computation*, Fortschritte der Physik **48**, 771 (2000).

[36] A. V. Khaetskii, D. Loss, and L. Glazman, *Electron Spin Decoherence in Quantum Dots due to Interaction with Nuclei*, Phys. Rev. Lett. **88**, 186802 (2002).

[37] I. A. Merkulov, A. L. Efros, and M. Rosen, *Electron spin relaxation by nuclei in semiconductor quantum dots*, Phys. Rev. B **65**, 205309 (2002).

[38] R. de Sousa and S. Das Sarma, *Electron spin coherence in semiconductors: Considerations for a spin-based solid-state quantum computer architecture*, Phys. Rev. B **67**, 033301 (2003).

[39] W. Yao, R.-B. Liu, and L. J. Sham, *Theory of electron spin decoherence by interacting nuclear spins in a quantum dot*, Phys. Rev. B **74**, 195301 (2006).

[40] G. S. Uhrig, *Keeping a Quantum Bit Alive by Optimized π-Pulse Sequences*, Phys. Rev. Lett. **98**, 100504 (2007).

[41] G. S. Uhrig, *Exact results on dynamical decoupling by π pulses in quantum information processes*, New Journal of Physics **10**, 083024 (2008).

[42] B. Urbaszek, P.-F. Braun, T. Amand, O. Krebs, T. Belhadj, A. Lemaítre, P. Voisin, and X. Marie, *Efficient dynamical nuclear polarization in quantum dots: Temperature dependence*, Phys. Rev. B **76**, 201301 (2007).

[43] A. Högele, M. Kroner, C. Latta, M. Claassen, I. Carusotto, C. Bulutay, and A. Imamoglu, *Dynamic Nuclear Spin Polarization in the Resonant Laser Excitation of an InGaAs Quantum Dot*, Phys. Rev. Lett. **108**, 197403 (2012).

[44] I. A. Merkulov, *Formation of a nuclear spin polaron under optical orientation in GaAs-type semiconductors*, Physics of the Solid State **40**, 930 (1998).

[45] M. Vladimirova, S. Cronenberger, D. Scalbert, I. I. Ryzhov, V. S. Zapasskii, G. G. Kozlov, A. Lemaître, and K. V. Kavokin, *Spin temperature concept verified by optical magnetometry of nuclear spins*, Phys. Rev. B **97**, 041301 (2018).

[46] A. Greilich, D. R. Yakovlev, A. Shabaev, A. L. Efros, I. A. Yugova, R. Oulton, V. Stavarache, D. Reuter, A. Wieck, and M. Bayer, *Mode Locking of Electron Spin Coherences in Singly Charged Quantum Dots*, Science **313**, 341 (2006).

[47] A. Greilich, A. Shabaev, D. R. Yakovlev, A. L. Efros, I. A. Yugova, D. Reuter, A. D. Wieck, and M. Bayer, *Nuclei-Induced Frequency Focusing of Electron Spin Coherence*, Science **317**, 1896 (2007).

[48] M. M. Glazov, I. A. Yugova, and A. L. Efros, *Electron spin synchronization induced by optical nuclear magnetic resonance feedback*, Phys. Rev. B **85**, 041303 (2012).

[49] G. S. Uhrig, *Quantum Coherence from Commensurate Driving with Laser Pulses and Decay*, SciPost Phys. **8**, 40 (2020).

[50] A. Greilich, S. E. Economou, S. Spatzek, D. R. Yakovlev, D. Reuter, A. D. Wieck, T. L. Reinecke, and M. Bayer, *Ultrafast optical rotations of electron spins in quantum dots*, Nature Physics **5** (2009).

[51] S. E. Economou, L. J. Sham, Y. Wu, and D. G. Steel, *Proposal for optical U(1) rotations of electron spin trapped in a quantum dot*, Phys. Rev. B **74**, 205415 (2006).

[52] S. E. Economou and T. L. Reinecke, *Theory of Fast Optical Spin Rotation in a Quantum Dot Based on Geometric Phases and Trapped States*, Phys. Rev. Lett. **99**, 217401 (2007).

[53] C. P. Williams, *Explorations in Quantum Computing* (Springer London, London, 2011).

[54] M. Veldhorst, C. H. Yang, J. C. C. Hwang, W. Huang, J. P. Dehollain, J. T. Muhonen, S. Simmons, A. Laucht, F. E. Hudson, K. M. Itoh, et al., *A two-qubit logic gate in silicon*, Nature **526**, 410 (2015).

[55] T. F. Watson, S. G. J. Philips, E. Kawakami, D. R. Ward, P. Scarlino, M. Veldhorst, D. E. Savage, M. G. Lagally, M. Friesen, S. N. Coppersmith, et al., *A programmable two-qubit quantum processor in silicon*, Nature **555**, 633 (2018).

[56] K. Takeda, A. Noiri, T. Nakajima, J. Yoneda, T. Kobayashi, and S. Tarucha, *Quantum tomography of an entangled three-qubit state in silicon*, Nature Nanotechnology **16**, 965 (2021).

[57] S. Spatzek, A. Greilich, S. E. Economou, S. Varwig, A. Schwan, D. R. Yakovlev, D. Reuter, A. D. Wieck, T. L. Reinecke, and M. Bayer, *Optical Control of Coherent Interactions between Electron Spins in InGaAs Quantum Dots*, Phys. Rev. Lett. **107**, 137402 (2011).

[58] S. Varwig, A. René, S. E. Economou, A. Greilich, D. R. Yakovlev, D. Reuter, A. D. Wieck, T. L. Reinecke, and M. Bayer, *All-optical tomography of electron spins in (In,Ga)As quantum dots*, Phys. Rev. B **89**, 081310 (2014).

[59] F. Vonhoff, A. Fischer, K. Deltenre, and F. B. Anders, *Microscopic Origin of the Effective Spin-Spin Interaction in a Semiconductor Quantum Dot Ensemble*, Phys. Rev. Lett. **129**, 167701 (2022).

[60] S. A. Crooker, J. Brandt, C. Sandfort, A. Greilich, D. R. Yakovlev, D. Reuter, A. D. Wieck, and M. Bayer, *Spin Noise of Electrons and Holes in Self-Assembled Quantum Dots*, Phys. Rev. Lett. **104**, 036601 (2010).

[61] W. Beugeling, G. S. Uhrig, and F. B. Anders, *Quantum model for mode locking in pulsed semiconductor quantum dots*, Phys. Rev. B **94**, 245308 (2016).

[62] N. Jäschke, A. Fischer, E. Evers, V. V. Belykh, A. Greilich, M. Bayer, and F. B. Anders, *Nonequilibrium nuclear spin distribution function in quantum dots subject to periodic pulses*, Phys. Rev. B **96**, 205419 (2017).

[63] I. Kleinjohann, E. Evers, P. Schering, A. Greilich, G. S. Uhrig, M. Bayer, and F. B. Anders, *Magnetic field dependence of the electron spin revival amplitude in periodically pulsed quantum dots*, Phys. Rev. B **98**, 155318 (2018).

[64] P. Schering, J. Hüdepohl, G. S. Uhrig, and B. Fauseweh, *Nuclear frequency focusing in periodically pulsed semiconductor quantum dots described by infinite classical central spin models*, Phys. Rev. B **98**, 024305 (2018).

[65] M. Gaudin, *Diagonalisation d'une classe d'hamiltoniens de spin*, Journal de Physique **37**, 1087 (1976).

[66] J. S. Dai, *Euler–Rodrigues formula variations, quaternion conjugation and intrinsic connections*, Mechanism and Machine Theory **92**, 144 (2015).

[67] B. L. V. D. Waerden, *Hamilton's Discovery of Quaternions*, Mathematics Magazine **49**, 227 (1976).

[68] B. A. Rosenfeld, *A History of Non-Euclidean Geometry - Evolution of the Concept of a Geometric Space* (Springer New York, Berlin-Heidelberg, 2012).

[69] A. Fischer, E. Evers, S. Varwig, A. Greilich, M. Bayer, and F. B. Anders, *Signatures of long-range spin-spin interactions in an (In,Ga)As quantum dot ensemble*, Phys. Rev. B **98**, 205308 (2018).

[70] E. Aleksandrov and V. Zapasskii, *Magnetic resonance in the Faraday-rotation noise spectrum*, Zh. Eksp. Teor. Fiz **81**, 132 (1981).

[71] V. S. Zapasskii, *Spin-noise spectroscopy: from proof of principle to applications*, Adv. Opt. Photon. **5**, 131 (2013).

[72] M. M. Glazov and E. L. Ivchenko, *Spin noise in quantum dot ensembles*, Phys. Rev. B **86**, 115308 (2012).

[73] P. Glasenapp, D. S. Smirnov, A. Greilich, J. Hackmann, M. M. Glazov, F. B. Anders, and M. Bayer, *Spin noise of electrons and holes in (In,Ga)As quantum dots: Experiment and theory*, Phys. Rev. B **93**, 205429 (2016).

[74] J. Hackmann, P. Glasenapp, A. Greilich, M. Bayer, and F. B. Anders, *Influence of the Nuclear Electric Quadrupolar Interaction on the Coherence Time of Hole and Electron Spins Confined in Semiconductor Quantum Dots*, Phys. Rev. Lett. **115**, 207401 (2015).

[75] N. A. Sinitsyn, Y. Li, S. A. Crooker, A. Saxena, and D. L. Smith, *Role of Nuclear Quadrupole Coupling on Decoherence and Relaxation of Central Spins in Quantum Dots*, Phys. Rev. Lett. **109**, 166605 (2012).

[76] R. Dahbashi, J. Hübner, F. Berski, J. Wiegand, X. Marie, K. Pierz, H. W. Schumacher, and M. Oestreich, *Measurement of heavy-hole spin dephasing in (InGa)As quantum dots*, Applied Physics Letters **100**, 031906 (2012).

[77] D. Roy, L. Yang, S. A. Crooker, and N. A. Sinitsyn, *Cross-correlation spin noise spectroscopy of heterogeneous interacting spin systems*, Scientific Reports **5**, 9573 (2015).

[78] R.-B. Liu, S.-H. Fung, H.-K. Fung, A. N. Korotkov, and L. J. Sham, *Dynamics revealed by correlations of time-distributed weak measurements of a single spin*, New Journal of Physics **12**, 013018 (2010).

[79] A. Bechtold, F. Li, K. Müller, T. Simmet, P.-L. Ardelt, J. J. Finley, and N. A. Sinitsyn, *Quantum Effects in Higher-Order Correlators of a Quantum-Dot Spin Qubit*, Phys. Rev. Lett. **117**, 027402 (2016).

[80] F. Li, S. A. Crooker, and N. A. Sinitsyn, *Higher-order spin-noise spectroscopy of atomic spins in fluctuating external fields*, Phys. Rev. A **93**, 033814 (2016).

[81] L. M. Norris, G. A. Paz-Silva, and L. Viola, *Qubit Noise Spectroscopy for Non-Gaussian Dephasing Environments*, Phys. Rev. Lett. **116**, 150503 (2016).

[82] P. Szańkowski, G. Ramon, J. Krzywda, D. Kwiatkowski, and Ł. Cywiński, *Environmental noise spectroscopy with qubits subjected to dynamical decoupling*, Journal of Physics: Condensed Matter **29**, 333001 (2017).

[83] D. Hägele and F. Schefczik, *Higher-order moments, cumulants, and spectra of continuous quantum noise measurements*, Phys. Rev. B **98**, 205143 (2018).

[84] N. Fröhling, N. Jäschke, and F. B. Anders, *Fourth-order spin correlation function in the extended central spin model*, Phys. Rev. B **99**, 155305 (2019).

[85] R. Oulton, A. Greilich, S. Y. Verbin, R. V. Cherbunin, T. Auer, D. R. Yakovlev, M. Bayer, I. A. Merkulov, V. Stavarache, D. Reuter, et al., *Subsecond Spin Relaxation Times in Quantum Dots at Zero Applied Magnetic Field Due to a Strong Electron-Nuclear Interaction*, Phys. Rev. Lett. **98**, 107401 (2007).

[86] M. Vladimirova, D. Scalbert, M. S. Kuznetsova, and K. V. Kavokin, *Electron-induced nuclear magnetic ordering in n-type semiconductors*, Phys. Rev. B **103**, 205207 (2021).

[87] G.-W. Deng, N. Xu, and W.-J. Li, *Quantum Dot Optoelectronic Devices*, edited by P. Yu and Z. M. Wang (Springer International Publishing, Cham, 2020).

[88] J. R. Maze, J. M. Taylor, and M. D. Lukin, *Electron spin decoherence of single nitrogen-vacancy defects in diamond*, Phys. Rev. B **78**, 094303 (2008).

[89] R. I. Dzhioev, K. V. Kavokin, V. L. Korenev, M. V. Lazarev, B. Y. Meltser, M. N. Stepanova, B. P. Zakharchenya, D. Gammon, and D. S. Katzer, *Low-temperature spin relaxation in n-type GaAs*, Phys. Rev. B **66**, 245204 (2002).

[90] K. V. Kavokin, *Spin relaxation of localized electrons in n-type semiconductors*, Semiconductor Science and Technology **23**, 114009 (2008).

[91] M. I. Dyakonov, ed., *Spin Physics in Semiconductors* - (Springer Science & Business Media, Berlin Heidelberg, 2008).

[92] C. Kittel, *Einführung in die Festkörperphysik* - (Oldenbourg, Deutschland, 2002).

[93] A. Babiński, J. Borysiuk, S. Kret, M. Czyż, A. Golnik, S. Raymond, and Z. R. Wasilewski, *Natural quantum dots in the InAs/GaAs wetting layer*, Applied Physics Letters **92**, 171104 (2008).

[94] D. Gammon, E. S. Snow, B. V. Shanabrook, D. S. Katzer, and D. Park, *Homogeneous Linewidths in the Optical Spectrum of a Single Gallium Arsenide Quantum Dot*, Science **273**, 87 (1996).

[95] A. Zrenner, L. V. Butov, M. Hagn, G. Abstreiter, G. Böhm, and G. Weimann, *Quantum dots formed by interface fluctuations in AlAs/GaAs coupled quantum well structures*, Phys. Rev. Lett. **72**, 3382 (1994).

[96] A. Cho and J. Arthur, *Molecular beam epitaxy*, Progress in Solid State Chemistry **10**, 157 (1975).

[97] S. Lüscher, A. Fuhrer, R. Held, T. Heinzel, K. Ensslin, M. Bichler, and W. Wegscheider, *Quantum wires and quantum dots defined by lithography with an atomic force microscope*, Microelectronics Journal **33**, 319 (2002).

[98] C. R. Kagan, L. C. Bassett, C. B. Murray, and S. M. Thompson, *Colloidal Quantum Dots as Platforms for Quantum Information Science*, Chemical Reviews **121**, 3186 (2021).

[99] X.-X. Song, D. Liu, V. Mosallanejad, J. You, T.-Y. Han, D.-T. Chen, H.-O. Li, G. Cao, M. Xiao, G.-C. Guo, et al., *A gate defined quantum dot on the two-dimensional transition metal dichalcogenide semiconductor WSe2*, Nanoscale **7**, 16867 (2015).

[100] S. Sanguinetti, K. Watanabe, T. Tateno, M. Wakaki, N. Koguchi, T. Kuroda, F. Minami, and M. Gurioli, *Role of the wetting layer in the carrier relaxation in quantum dots*, Applied Physics Letters **81**, 613 (2002).

[101] R. V. N. Melnik and M. Willatzen, *Bandstructures of conical quantum dots with wetting layers*, Nanotechnology **15**, 1 (2003).

[102] S. Lee, O. L. Lazarenkova, P. von Allmen, F. Oyafuso, and G. Klimeck, *Effect of wetting layers on the strain and electronic structure of InAs self-assembled quantum dots*, Phys. Rev. B **70**, 125307 (2004).

[103] J. N. Stranski, *Zur Theorie der orientierten Ausscheidung von Ionenkristallen aufeinander*, (1938).

[104] A. Schwan, B.-M. Meiners, A. B. Henriques, A. D. B. Maia, A. A. Quivy, S. Spatzek, S. Varwig, D. R. Yakovlev, and M. Bayer, *Dispersion of electron g-factor with optical transition energy in (In,Ga)As/GaAs self-assembled quantum dots*, Applied Physics Letters **98**, 233102 (2011).

[105] M. M. Glazov, *Electron & Nuclear Spin Dynamics in Semiconductor Nanostructures* (Oxford University Press, New York, 2018).

[106] G. L. Bir, G. E. Pikus, P. Shelnitz, and D. Louvish, *Symmetry and strain-induced effects in semiconductors* (Wiley, New York, 1976).

[107] R. J. Warburton, *Single spins in self-assembled quantum dots*, Nat Mater **12**, 483 (2013).

[108] M. M. Glazov, I. A. Yugova, S. Spatzek, A. Schwan, S. Varwig, D. R. Yakovlev, D. Reuter, A. D. Wieck, and M. Bayer, *Effect of pump-probe detuning on the Faraday rotation and ellipticity signals of mode-locked spins in (In,Ga)As/GaAs quantum dots*, Phys. Rev. B **82**, 155325 (2010).

[109] I. A. Yugova, M. M. Glazov, E. L. Ivchenko, and A. L. Efros, *Pump-probe Faraday rotation and ellipticity in an ensemble of singly charged quantum dots*, Phys. Rev. B **80**, 104436 (2009).

[110] N. O. Urs, B. Mozooni, P. Mazalski, M. Kustov, P. Hayes, S. Deldar, E. Quandt, and J. McCord, *Advanced magneto-optical microscopy: Imaging from picoseconds to centimeters - imaging spin waves and temperature distributions (invited)*, AIP Advances **6**, 055605 (2016).

[111] A. Greilich, R. Oulton, E. A. Zhukov, I. A. Yugova, D. R. Yakovlev, M. Bayer, A. Shabaev, A. L. Efros, I. A. Merkulov, V. Stavarache, et al., *Optical Control of Spin Coherence in Singly Charged (In,Ga)As/GaAs Quantum Dots*, Phys. Rev. Lett. **96**, 227401 (2006).

[112] E. Evers, N. E. Kopteva, I. A. Yugova, D. R. Yakovlev, M. Bayer, and A. Greilich, *Shielding of external magnetic field by dynamic nuclear polarization in (In,Ga)As quantum dots*, Phys. Rev. B **104**, 075302 (2021).

[113] E. Evers, N. E. Kopteva, I. A. Yugova, D. R. Yakovlev, D. Reuter, A. D. Wieck, M. Bayer, and A. Greilich, *Suppression of nuclear spin fluctuations in an InGaAs quantum dot ensemble by GHz-pulsed optical excitation*, npj Quantum Information **7**, 60 (2021).

[114] V. V. Belykh, A. Y. Kuntsevich, M. M. Glazov, K. V. Kavokin, D. R. Yakovlev, and M. Bayer, *Quantum Interference Controls the Electron Spin Dynamics in n-GaAs*, Phys. Rev. X **8**, 031021 (2018).

[115] E. Evers, V. V. Belykh, N. E. Kopteva, I. A. Yugova, A. Greilich, D. R. Yakovlev, D. Reuter, A. D. Wieck, and M. Bayer, *Decay and revival of electron spin polarization in an ensemble of (In,Ga)As quantum dots*, Phys. Rev. B **98**, 075309 (2018).

[116] S. Spatzek, S. Varwig, M. M. Glazov, I. A. Yugova, A. Schwan, D. R. Yakovlev, D. Reuter, A. D. Wieck, and M. Bayer, *Generation and detection of mode-locked spin coherence in (In,Ga)As/GaAs quantum dots by laser pulses of long duration*, Phys. Rev. B **84**, 115309 (2011).

[117] S. A. Crooker, L. Cheng, and D. L. Smith, *Spin noise of conduction electrons in n-type bulk GaAs*, Phys. Rev. B **79**, 035208 (2009).

[118] J. Hackmann and F. B. Anders, *Spin noise in the anisotropic central spin model*, Phys. Rev. B **89**, 045317 (2014).

[119] N. Fröhling and F. B. Anders, *Long-time coherence in fourth-order spin correlation functions*, Phys. Rev. B **96**, 045441 (2017).

[120] L. Yang, P. Glasenapp, A. Greilich, D. Reuter, A. D. Wieck, D. R. Yakovlev, M. Bayer, and S. A. Crooker, *Two-colour spin noise spectroscopy and fluctuation correlations reveal homogeneous linewidths within quantum-dot ensembles*, Nature Communications **5**, 4949 (2014).

[121] D. Press, K. De Greve, P. L. McMahon, T. D. Ladd, B. Friess, C. Schneider, M. Kamp, S. Höfling, A. Forchel, and Y. Yamamoto, *Ultrafast optical spin echo in a single quantum dot*, Nat Photon **4**, 367 (2010).

[122] A. Bechtold, D. Rauch, F. Li, T. Simmet, P.-L. Ardelt, A. Regler, K. Müller, N. A. Sinitsyn, and J. J. Finley, *Three-stage decoherence dynamics of an electron spin qubit in an optically active quantum dot*, Nature Physics **11**, 1005 (2015).

[123] J. Harrison, M. Sellars, and N. Manson, *Measurement of the optically induced spin polarisation of N-V centres in diamond*, Diamond and Related Materials **15**, Diamond 2005, 586 (2006).

[124] G. Balasubramanian, P. Neumann, D. Twitchen, M. Markham, R. Kolesov, N. Mizuochi, J. Isoya, J. Achard, J. Beck, J. Tissler, et al., *Ultralong spin coherence time in isotopically engineered diamond*, Nature Materials **8**, 383 (2009).

[125] C. F. Wang, R. Hanson, D. D. Awschalom, E. L. Hu, T. Feygelson, J. Yang, and J. E. Butler, *Fabrication and characterization of two-dimensional photonic crystal microcavities in nanocrystalline diamond*, Applied Physics Letters **91**, 201112 (2007).

[126] M. V. G. Dutt, L. Childress, L. Jiang, E. Togan, J. Maze, F. Jelezko, A. S. Zibrov, P. R. Hemmer, and M. D. Lukin, *Quantum Register Based on Individual Electronic and Nuclear Spin Qubits in Diamond*, Science **316**, 1312 (2007).

[127] P. Neumann, N. Mizuochi, F. Rempp, P. Hemmer, H. Watanabe, S. Yamasaki, V. Jacques, T. Gaebel, F. Jelezko, and J. Wrachtrup, *Multipartite Entanglement Among Single Spins in Diamond*, Science **320**, 1326 (2008).

[128] W. A. Coish and D. Loss, *Hyperfine interaction in a quantum dot: Non-Markovian electron spin dynamics*, Phys. Rev. B **70**, 195340 (2004).

[129] A. Abragam, *The Principles of Nuclear Magnetism* (Clarendon Press, Oxford, 1961).

[130] E. Fermi, *Über die magnetischen Momente der Atomkerne.* Z. Phys. **60**, 320 (1930).

[131] C. Testelin, F. Bernardot, B. Eble, and M. Chamarro, *Hole–spin dephasing time associated with hyperfine interaction in quantum dots*, Phys. Rev. B **79**, 195440 (2009).

[132] R. Hanson, L. P. Kouwenhoven, J. R. Petta, S. Tarucha, and L. M. K. Vandersypen, *Spins in few-electron quantum dots*, Rev. Mod. Phys. **79**, 1217 (2007).

[133] B. Urbaszek, X. Marie, T. Amand, O. Krebs, P. Voisin, P. Maletinsky, A. Högele, and A. Imamoglu, *Nuclear spin physics in quantum dots: An optical investigation*, Rev. Mod. Phys. **85**, 79 (2013).

[134] P. Philippopoulos, S. Chesi, and W. A. Coish, *First-principles hyperfine tensors for electrons and holes in GaAs and silicon*, Phys. Rev. B **101**, 115302 (2020).

[135] E. A. Chekhovich, A. Ulhaq, E. Zallo, F. Ding, O. G. Schmidt, and M. S. Skolnick, *Measurement of the spin temperature of optically cooled nuclei and GaAs hyperfine constants in GaAs/AlGaAs quantum dots*, Nature Materials **16**, 982 (2017).

[136] W. Beugeling, G. S. Uhrig, and F. B. Anders, *Influence of the nuclear Zeeman effect on mode locking in pulsed semiconductor quantum dots*, Phys. Rev. B **96**, 115303 (2017).

[137] R. K. Sundfors, *Exchange and Quadrupole Broadening of Nuclear Acoustic Resonance Line Shapes in the III-V Semiconductors*, Phys. Rev. **185**, 458 (1969).

[138] C. Bulutay, *Quadrupolar spectra of nuclear spins in strained InGaAs quantum dots*, Phys. Rev. B **85**, 115313 (2012).

[139] C. P. Slichter, *Principles of Magnetic Resonance* - (Springer Science & Business Media, Berlin Heidelberg, 2013).

[140] G. Czycholl, *Theoretische Festkörperphysik Band 2 - Anwendungen: Nichtgleichgewicht, Verhalten in äußeren Feldern, kollektive Phänomene* (Springer-Verlag, Berlin Heidelberg New York, 2017).

[141] M. A. Ruderman and C. Kittel, *Indirect Exchange Coupling of Nuclear Magnetic Moments by Conduction Electrons*, Phys. Rev. **96**, 99 (1954).

[142] T. Kasuya, *A Theory of Metallic Ferro- and Antiferromagnetism on Zener's Model*, Progress of Theoretical Physics **16**, 45 (1956).

[143] K. Yosida, *Magnetic Properties of Cu-Mn Alloys*, Phys. Rev. **106**, 893 (1957).

[144] F. Eickhoff, B. Lechtenberg, and F. B. Anders, *Effective low-energy description of the two-impurity Anderson model: RKKY interaction and quantum criticality*, Phys. Rev. B **98**, 115103 (2018).

[145] F. Eickhoff and F. B. Anders, *Strongly correlated multi-impurity models: The crossover from a single-impurity problem to lattice models*, Phys. Rev. B **102**, 205132 (2020).

[146] F. Eickhoff and F. B. Anders, *Kondo holes in strongly correlated impurity arrays: RKKY-driven Kondo screening and hole-hole interactions*, Phys. Rev. B **104**, 045115 (2021).

[147] J. R. Schrieffer and P. A. Wolff, *Relation between the Anderson and Kondo Hamiltonians*, Phys. Rev. **149**, 491 (1966).

[148] B. Fischer and M. W. Klein, *Magnetic and nonmagnetic impurities in two-dimensional metals*, Phys. Rev. B **11**, 2025 (1975).

[149] R. Žitko and J. Bon ča, *Multiple-impurity Anderson model for quantum dots coupled in parallel*, Phys. Rev. B **74**, 045312 (2006).

[150] H. R. Krishna-murthy, J. W. Wilkins, and K. G. Wilson, *Renormalization-group approach to the Anderson model of dilute magnetic alloys. I. Static properties for the symmetric case*, Phys. Rev. B **21**, 1003 (1980).

[151] R. Bulla, T. A. Costi, and T. Pruschke, *Numerical renormalization group method for quantum impurity systems*, Rev. Mod. Phys. **80**, 395 (2008).

[152] C. Piermarocchi, P. Chen, L. J. Sham, and D. G. Steel, *Optical RKKY Interaction between Charged Semiconductor Quantum Dots*, Phys. Rev. Lett. **89**, 167402 (2002).

[153] M. Gaudin, *La fonction d'onde de Bethe* (Masson, 1983).

[154] M. Bortz and J. Stolze, *Exact dynamics in the inhomogeneous central-spin model*, Phys. Rev. B **76**, 014304 (2007).

[155] M. Bortz and J. Stolze, *Spin and entanglement dynamics in the central-spin model with homogeneous couplings*, Journal of Statistical Mechanics: Theory and Experiment **2007**, P06018 (2007).

[156] M. Bortz, S. Eggert, C. Schneider, R. Stübner, and J. Stolze, *Dynamics and decoherence in the central spin model using exact methods*, Phys. Rev. B **82**, 161308 (2010).

[157] A. Faribault and D. Schuricht, *Integrability-Based Analysis of the Hyperfine-Interaction-Induced Decoherence in Quantum Dots*, Phys. Rev. Lett. **110**, 040405 (2013).

[158] A. Faribault and D. Schuricht, *Spin decoherence due to a randomly fluctuating spin bath*, Phys. Rev. B **88**, 085323 (2013).

[159] V. V. Dobrovitski and H. A. De Raedt, *Efficient scheme for numerical simulations of the spin-bath decoherence*, Phys. Rev. E **67**, 056702 (2003).

[160] V. V. Dobrovitski, H. A. De Raedt, M. I. Katsnelson, and B. N. Harmon, *Quantum Oscillations without Quantum Coherence*, Phys. Rev. Lett. **90**, 210401 (2003).

[161] H.-P. Breuer, D. Burgarth, and F. Petruccione, *Non-Markovian dynamics in a spin star system: Exact solution and approximation techniques*, Phys. Rev. B **70**, 045323 (2004).

[162] J. Fischer and H.-P. Breuer, *Correlated projection operator approach to non-Markovian dynamics in spin baths*, Phys. Rev. A **76**, 052119 (2007).

[163] E. Ferraro, H.-P. Breuer, A. Napoli, M. A. Jivulescu, and A. Messina, *Non-Markovian dynamics of a single electron spin coupled to a nuclear spin bath*, Phys. Rev. B **78**, 064309 (2008).

[164] W. A. Coish, J. Fischer, and D. Loss, *Free-induction decay and envelope modulations in a narrowed nuclear spin bath*, Phys. Rev. B **81**, 165315 (2010).

[165] E. Barnes, Ł. Cywi ński, and S. Das Sarma, *Nonperturbative Master Equation Solution of Central Spin Dephasing Dynamics*, Phys. Rev. Lett. **109**, 140403 (2012).

[166] W. M. Witzel, R. de Sousa, and S. Das Sarma, *Quantum theory of spectral-diffusion-induced electron spin decoherence*, Phys. Rev. B **72**, 161306 (2005).

[167] R. Röhrig, P. Schering, L. B. Gravert, B. Fauseweh, and G. S. Uhrig, *Quantum mechanical treatment of large spin baths*, Phys. Rev. B **97**, 165431 (2018).

[168] D. Stanek, C. Raas, and G. S. Uhrig, *Dynamics and decoherence in the central spin model in the low-field limit*, Phys. Rev. B **88**, 155305 (2013).

[169] L. B. Gravert, P. Lorenz, C. Nase, J. Stolze, and G. S. Uhrig, *Increased coherence time in narrowed bath states in quantum dots*, Phys. Rev. B **94**, 094416 (2016).

[170] K. A. Al-Hassanieh, V. V. Dobrovitski, E. Dagotto, and B. N. Harmon, *Numerical Modeling of the Central Spin Problem Using the Spin-Coherent-State P Representation*, Phys. Rev. Lett. **97**, 037204 (2006).

[171] G. Chen, D. L. Bergman, and L. Balents, *Semiclassical dynamics and long-time asymptotics of the central-spin problem in a quantum dot*, Phys. Rev. B **76**, 045312 (2007).

[172] B. Fauseweh, P. Schering, J. Hüdepohl, and G. S. Uhrig, *Efficient algorithms for the dynamics of large and infinite classical central spin models*, Phys. Rev. B **96**, 054415 (2017).

[173] A. Fischer, I. Kleinjohann, F. B. Anders, and M. M. Glazov, *Kinetic approach to nuclear-spin polaron formation*, Phys. Rev. B **102**, 165309 (2020).

[174] H. Feldmeier and J. Schnack, *Molecular dynamics for fermions*, Rev. Mod. Phys. **72**, 655 (2000).

[175] A. Polkovnikov, *Phase space representation of quantum dynamics*, Annals of Physics **325**, 1790 (2010).

[176] P. Schering and G. S. Uhrig, *Nuclear magnetic resonance spectroscopy of nonequilibrium steady states in quantum dots*, EPL (Europhysics Letters) **133**, 57003 (2021).

[177] E. Fradkin, *Field Theories of Condensed Matter Physics*, 2nd ed. (Cambridge University Press, 2013).

[178] A. Altland and B. D. Simons, *Condensed Matter Field Theory*, 2nd ed. (Cambridge University Press, 2010).

[179] A. M. Perelomov, *Coherent states for arbitrary Lie group*, Communications in Mathematical Physics **26**, 222 (1972).

[180] E. Fradkin and M. Stone, *Topological terms in one- and two-dimensional quantum Heisenberg antiferromagnets*, Phys. Rev. B **38**, 7215 (1988).

[181] A. Auerbach, *Interacting Electrons and Quantum Magnetism* - (Springer Science & Business Media, Berlin Heidelberg, 2012).

[182] H. J. Carmichael, *Statistical Methods in Quantum Optics 1* (Springer Verlag, Berlin Heidelberg, 1999).

[183] S. Attal, A. Joye, and C.-A. Pillet, *Open Quantum Systems II - The Markovian Approach* (Springer, Berlin, Heidelberg, 2006).

[184] R. Alicki and K. Lendi, *Quantum Dynamical Semigroups and Applications* (Springer Berlin Heidelberg, 2007).

[185] E. B. Davies and E. W. Davies, *Quantum Theory of Open Systems* - (Academic Press, Amsterdam, Boston, 1976).

[186] R. S. Ingarden, A. Kossakowski, and M. Ohya, *Information Dynamics and Open Systems - Classical and Quantum Approach* (Springer Science & Business Media, Berlin Heidelberg, 2013).

[187] C. Lindblad, *Non-Equilibrium Entropy and Irreversibility* - (Springer Science & Business Media, Berlin Heidelberg, 2001).

[188] U. Weiss, *Quantum Dissipative Systems (Fifth Edition)* - (World Scientific, Singapur, 2021).

[189] K. Mølmer, Y. Castin, and J. Dalibard, *Monte Carlo wave-function method in quantum optics*, J. Opt. Soc. Am. B **10**, 524 (1993).

[190] R. Dum, P. Zoller, and H. Ritsch, *Monte Carlo simulation of the atomic master equation for spontaneous emission*, Phys. Rev. A **45**, 4879 (1992).

[191] S. Spatzek, *Kohärente Kontrolle und Wechselwirkung von Elektronenspins in einem (In,Ga)As/GaAs Quantenpunktensemble*, Dissertation (TU Dortmund, 2011).

[192] A. Greilich, D. R. Yakovlev, and M. Bayer, *Optical tailoring of electron spin coherence in quantum dots*, Solid State Communications **49**, Fundamental Phenomena and Applications of Quantum Dots, 1466 (2009).

[193] A. Fischer, I. Kleinjohann, N. A. Sinitsyn, and F. B. Anders, *Cross-correlation spectra in interacting quantum dot systems*, Phys. Rev. B **105**, 035303 (2022).

[194] P. Schering, P. W. Scherer, and G. S. Uhrig, *Interplay of spin mode locking and nuclei-induced frequency focusing in quantum dots*, Phys. Rev. B **102**, 115301 (2020).

[195] D. S. Smirnov, M. M. Glazov, and E. L. Ivchenko, *Effect of exchange interaction on the spin fluctuations of localized electrons*, Physics of the Solid State **56**, 254 (2014).

[196] N. Patanasemakul, S. Panyakeow, and S. Kanjanachuchai, *Chirped InGaAs quantum dot molecules for broadband applications*, Nanoscale Research Letters **7**, 207 (2012).

[197] Z. M. Wang, Y. I. Mazur, J. L. Shultz, G. J. Salamo, T. D. Mishima, and M. B. Johnson, *One-dimensional postwetting layer in InGaAs GaAs(100) quantum-dot chains*, Journal of Applied Physics **99**, 033705 (2006).

[198] T. Sugaya, R. Oshima, K. Matsubara, and S. Niki, *InGaAs quantum dot superlattice with vertically coupled states in InGaP matrix*, Journal of Applied Physics **114**, 014303 (2013).

[199] G. G. Kozlov, *Exactly solvable spin dynamics of an electron coupled to a large number of nuclei; the electron-nuclear spin echo in a quantum dot*, Journal of Experimental and Theoretical Physics **105**, 803 (2007).

[200] N. Jäschke, F. B. Anders, and M. M. Glazov, *Electron spin noise under the conditions of nuclei-induced frequency focusing*, Phys. Rev. B **98**, 045307 (2018).

[201] M. Y. Petrov and S. V. Yakovlev, *Comparison of quantum-mechanical and semiclassical approaches for an analysis of spin dynamics in quantum dots*, Journal of Experimental and Theoretical Physics **115**, 326 (2012).

[202] A. Vezvaee, G. Sharma, S. E. Economou, and E. Barnes, *Driven dynamics of a quantum dot electron spin coupled to a bath of higher-spin nuclei*, Phys. Rev. B **103**, 235301 (2021).

[203] D. Scalbert, *Nuclear polaron beyond the mean-field approximation*, Phys. Rev. B **95**, 245209 (2017).

[204] I. Kleinjohann, A. Fischer, M. M. Glazov, and F. B. Anders, *Nuclear-spin polaron formation: Anisotropy effects and quantum phase transition*, Phys. Rev. B **105**, 195309 (2022).

[205] R. P. Feynman, *Statistical Mechanics, A Set of Lectures* (Benjamin, Reading, MA, USA, 1972).

[206] A. Greilich, A. Pawlis, F. Liu, O. A. Yugov, D. R. Yakovlev, K. Lischka, Y. Yamamoto, and M. Bayer, *Spin dephasing of fluorine-bound electrons in ZnSe*, Phys. Rev. B **85**, 121303 (2012).

[207] K. Binder, *Finite size scaling analysis of ising model block distribution functions*, Zeitschrift für Physik B Condensed Matter **43**, 119 (1981).

[208] D. P. Landau and K. Binder, *A Guide to Monte Carlo Simulations in Statistical Physics*, 4th ed. (Cambridge University Press, 2014).

[209] L. Landau and E. Lifshitz, *Statistical Physics, Part 1* (Butterworth-Heinemann, Oxford, 2000).

[210] J. Hackmann, D. S. Smirnov, M. M. Glazov, and F. B. Anders, *Spin noise in a quantum dot ensemble: From a quantum mechanical to a semi-classical description*, physica status solidi (b) **251**, 1270 (2014).

[211] E. T. Güldeste and C. Bulutay, *Loschmidt echo driven by hyperfine and electric-quadrupole interactions in nanoscale nuclear spin baths*, Phys. Rev. B **98**, 085202 (2018).

[212] G. Garcia-Arellano, F. Bernardot, G. Karczewski, C. Testelin, and M. Chamarro, *Longitudinal spin relaxation time of donor-bound electrons in a CdTe quantum well*, Phys. Rev. B **102**, 165314 (2020).

Acknowledgments

First of all, I would like to thank Prof. Dr. Frithjof B. Anders for supervising my PhD project and for the valuable support throughout the last years. Furthermore, I would like to express my gratitude to Prof. Dr. Götz S. Uhrig for accepting the role of the second reviewer. I am deeply grateful to Prof. Mikhail M. Glazov not only for the great scientific cooperation but also for making me feel welcome during my stays in Saint Petersburg. I am also grateful to Dr. Eiko Evers, PD Dr. Alex Greilich, and Prof. Dr. Manfred Bayer for the scientific cooperation and the experimental insights. Moreover, I thank Dr. Nikolai A. Sinitsyn for the fruitful collaboration. I also thank my colleagues in Dortmund for the pleasant working environment, especially my former office mates Nina and Natalie for the endless discussions on physics and beyond. I highly appreciate the careful proofreading by Kira, Frederik, and Lisa. My sincere thanks go to Iris for the encouragement, suggestions, and comments on all stages of this thesis. Last but not least, I am extraordinarily grateful for the endless backing of my family.